UNIVERSITY OF SOUTHAMPTON

Characterising the Structure and Fluvial Drag of Emergent Vegetation

by

Grigorios Vasilopoulos

A thesis submitted for the
degree of Doctor of Philosophy (PhD)

in the
Faculty of Social Human and Mathematical Sciences
Geography and Environment

Supervisors:
Julian Leyland and Joanna M. Nield

October 2017

ABSTRACT

UNIVERSITY OF SOUTHAMPTON
FACULTY OF SOCIAL HUMAN AND MATHEMATICAL SCIENCES
GEOGRAPHY AND ENVIRONMENT

Doctor of Philosophy (PhD)

Characterising the Structure and Fluvial Drag of Emergent Vegetation

by Grigorios Vasilopoulos

Plants function as large-scale, flexible obstacles that exert additional drag on surface water flows, affecting local scale turbulence and the structure of the boundary layer. Hence, vegetation plays a significant role in controlling flood water and modulating geomorphic change. This makes it an important, but often under-considered, component when undertaking flood or erosion control actions or designing river restorations strategies. Vegetative drag varies depending on flow conditions and the associated vegetation structure and temporary reconfiguration of the plant. Whilst several approaches have been developed to describe this relationship, they have been limited due to the difficulty of accurately and precisely characterising the vegetation itself, especially during flow. In practice, vegetative drag is commonly expressed through bulk parameters that are typically derived from lookup tables. Terrestrial Laser Scanning (TLS) has the ability to capture the surface of *in situ* objects as 3D point clouds, at high resolution (mm), precision and accuracy, even when submerged in water. In this study, the potential for characterising the 3D structure of vegetation from high resolution TLS data is explored. Novel methods capable of converting unstructured TLS 3D point clouds to structured 2D and 3D grid arrays are developed enabling the accurate representation of plant structure. These methods are adapted and combined with physical modelling experiments to investigate a series of structurally variable plants at a range of flow scenarios, including the collection of precise hydraulic measurements and capturing of plant deformation during flow. Models capable of predicting vegetation's fluvial drag from the combination of bulk porous plant structure and extent are developed. Small scale flow characteristics in the vicinity of plant elements, including adjustments of the velocity profile, the extent and intensity of the wake region, the development of secondary flow and adjustments of the turbulent kinetic energy, are quantified and associated with the explicitly characterised plant structure. The results show a promising potential for transferring the methods to field studies. They highlight the potential of employing vegetation in natural flood management applications and can help to inform decisions regarding the choice of plant types to be used for the reforestation of floodplains as well as the optimal plant spacing for a satisfactory control of flood water during floods.

Contents

List of Figures

List of Tables

Nomenclature

Lower-case Roman

f	Darcy-Weisbach roughness coefficient
g	Gravitational acceleration
h	Flow depth
m_s	Channel sinuosity
n	Manning's roughness coefficient
n_r	Refractive index
p	Pressure
t	Time
u	Longitudinal velocity vector
u_*	Shear velocity
v	Transverse velocity vector
w	Vertical velocity vector
x	1^{st} Horizontal Cartesian coordinate vector
y	2^{nd} Horizontal Cartesian coordinate vector
z	Vertical Cartesian coordinate vector
z_0	Roughness height

Upper-case Roman

A_b	Planar area
A_c	Cross-sectional area
A_f	Frontal area
A_l	Frontal area of foliage
A_s	Frontal area of stems
B	Breadth
B^A	Surface area blockage factor
B^V	Volumetric blockage factor
B^X	Frontal area blockage factor
C	Chézy roughness coefficient
C_D	Drag coefficient
D_{50}	Median of grain diameter

D_s	Cylinder diameter
F_D	Form drag
F_{SF}	Friction drag
H	Element height
L	Element length
L_s	Mixing length
LAI	Leaf Area Index
M	Mixing
N	Stem number
OP	Optical Porosity
P	Wetted perimeter
P_{2D}	2D Porosity
P_{2Dpf}	Planform 2D Porosity
P_{3D}	3D Porosity
Q	Discharge
R^2	Coefficient of determination
R_h	Hydraulic radius
Re	Reynolds number
S	Slope
S_f	Friction slope
TKE	Turbulent Kinetic Energy
U	Velocity
VP	Volumetric Porosity
W	Element width

Lower-case Greek

δ	Boundary layer thickness
ϵ	Error
ζ	Earth's angular rotation
θ_w	Refraction angle
θ_a	Incidence angle
κ	Von Karman constant
λ_s	Stem density
μ	Dynamic viscosity
ν	Kinematic viscosity
ρ	Fluid density
τ	Stress
χ	Vogel exponent

Upper-case Greek

Φ	Latitude

Abbreviations

aDcp	Acoustic Doppler Current Profiler
ADV	Acoustic Doppler Velocimeter
ALS	Airborne Laser Scanning
CMOS	Complementary Metal Oxide Semiconductor
FOV	Field Of View
GPS	Global Positioning System
IMU	Inertial Measurement Unit
LiDAR	Light Detection and Ranging
MLS	Mobile Laser Scanning
NDVI	Normalised Difference Vegetation Index
PIV	Particle Image Velocimetry
RMSE	Root Mean Square Error
RMSD	Root Mean Square Deviation
RTK	Real Time Kinematic
TLS	Terrestrial Laser Scanning
UAV	Unmanned Aerial Vehicle

Declaration of Authorship

I,

Grigorios Vasilopoulos

declare that the thesis entitled

Characterising the Structure and Fluvial Drag of Emergent Vegetation

and the work presented in the thesis are both my own, and have been generated by me as the result of my own original research. I confirm that:

- this work was done wholly or mainly while in candidature for a research degree at this University;
- where any part of this thesis has previously been submitted for a degree or any other qualification at this University or any other institution, this has been clearly stated;
- where I have consulted the published work of others, this is always clearly attributed;
- where I have quoted from the work of others, the source is always given. With the exception of such quotations, this thesis is entirely my own work;
- I have acknowledged all main sources of help;
- where the thesis is based on work done by myself jointly with others, I have made clear exactly what was done by others and what I have contributed myself;

Signed: .....

Date: .....

Acknowledgements

It is a pleasure to thank all those who have helped me for the duration of my studies. Firstly, I would like to express my gratitude to my supervisors Julian and Joanna for their valuable time, guidance and support. I would also like to thank Mark Smith who kindly advised me on the employment of through-water TLS and offered his MATLAB code for the through-water TLS refraction correction. Thanks to Arjan Reesink for helping me with the 3D flow visualisations and Hal Voepel for the countless conversations on hydraulics. A special thanks is owed to all my fellow postgraduate students both for helping with my work and in taking my mind off it. Above all, I would like to thank my mother Konstantina and my sister Eliza for their endless love, encouragement and support.

Chapter 1

The Significance of Emergent Vegetation in Surface Water Flows

1.1 Rationale

Vegetation is ubiquitous in nature and has recreational, aesthetic and environmental value. In riverine environments, emergent plants function as large-scale, quasi-stable obstacles that affect local-scale turbulence and the structure of the boundary layer. In this way, riparian vegetation may provide erosion control (Andrews, 1984; Hey and Thorne, 1986), geomorphic stability due to the increased flow resistance (Thorne, 1990), land stability due to buttressing, arching and root reinforcement (Waldron, 1977; Gray and Leiser, 1982; Abernethy and Rutherfurd, 2001), reduction of soil moisture content due to enhanced evapotranspiration and reduced infiltration as well as promotion of the entrapment and deposition of suspended sediment (Abt et al., 1992). On the other hand, riparian vegetation has also been associated with flooding due to increased flow resistance and localised erosion due to surcharge, piping and tree falling due to wind, as well as local turbulent scour around isolated elements (Darby, 1999; Bywater-Reyes et al., 2017). Although the effect of vegetation on surface water flows has long been acknowledged (*e.g.* Hoover, 1944), a practical, yet scientifically robust, method of quantifying the additional drag exerted by plants has not yet been developed. Thus, the influence of vegetation is frequently not explicitly accounted for when undertaking flood or erosion control actions, or designing river restoration strategies, but instead it is lumped together with other surface perturbations as 'roughness', with practitioners resorting to using variations in Manning's n for example to parameterise the effects of vegetation on flow. This research will focus on the effects that vegetative roughness has on the flow field, which is highly pertinent to understanding eco-geomorphic relationships.

Previous research has demonstrated that vegetation exerts a drag resistance into the flow field. This vegetative drag extracts mean flow kinetic energy converting it to turbulent kinetic energy (Yagci and Kabdasli, 2008) and imposes a significant influence on the

total boundary shear stress and mean flow velocity (Abt et al., 1994; Thorne and Furbish, 1995; Musick et al., 1996; Lancaster and Baas, 1998; Griffin and Smith, 2004; Griffin et al., 2005; Huai et al., 2012; Gillies et al., 2014) which may affect sediment transport processes and is associated with increased flow depth. Early attempts to represent vegetation's interference on flows using a roughness approach were based on linear models (Cowan, 1956), combined with field observations and lookup tables (Arcement and Schneider, 1989). Other attempts, acknowledging that plants essentially constitute blockage elements, employed blockage factors incorporated into experimentally derived formulas to estimate vegetative roughness (Huntington and Whitehead, 1992; Green, 2005). However, these are bulk parameters that can only be related to average flow measurements and fail to capture vegetation's effect on local scale turbulence. Numerous studies have adopted Prandtl's (1904) boundary layer theory and Von Karman's (1930) law of the wall, incorporating a roughness height to describe the bulk flow characteristics above the vegetation canopy. However, the dynamics of the flow among vegetation elements cannot be sufficiently described from averaged logarithmic profiles. More recent approaches partition the flow profile in a region above the canopy, which can be sufficiently characterised by a logarithmic profile, and a region below, which is primarily affected by the wake-induced vegetative drag (Nepf and Ghisalberti, 2008). In the special, but wide-spread, consideration of emergent vegetation, which is the focus of this study, the logarithmic part of the velocity profile is abolished and the total extent of the velocity profile is shaped by the vegetative drag.

The vegetative drag is directly influenced by the three dimensional form and structure of the vegetation element producing it, which is difficult to characterise. This is partly because of the high complexity and diversity of natural vegetation along with a lack of appropriate survey methods, as well as vegetation's continuously changing form due to seasonality (e.g. plant growth, shedding) and its tendency to reconfigure (i.e. deform) during active flow. In many studies vegetation elements are substituted by 3D objects of simple geometry (commonly cylinders) in numerical models (*e.g.* Raupach, 1992) and physical modelling experiments (*e.g.* Brown et al., 2008). Whilst these experiments have offered useful insights, such analogies are not sufficient to capture the combined effects of many individual stems and leaves on the flow interference induced by their distinct wakes. Other studies, following a 2D approximation, have employed surveying techniques to measure vegetation's frontal area and associate it with hydraulic parameters (*e.g.* Västilä and Järvelä, 2014). However, this disregards any spatial variability on the streamwise direction both at the plant and the reach scale and therefore, can only be related to the bulk hydraulic roughness.

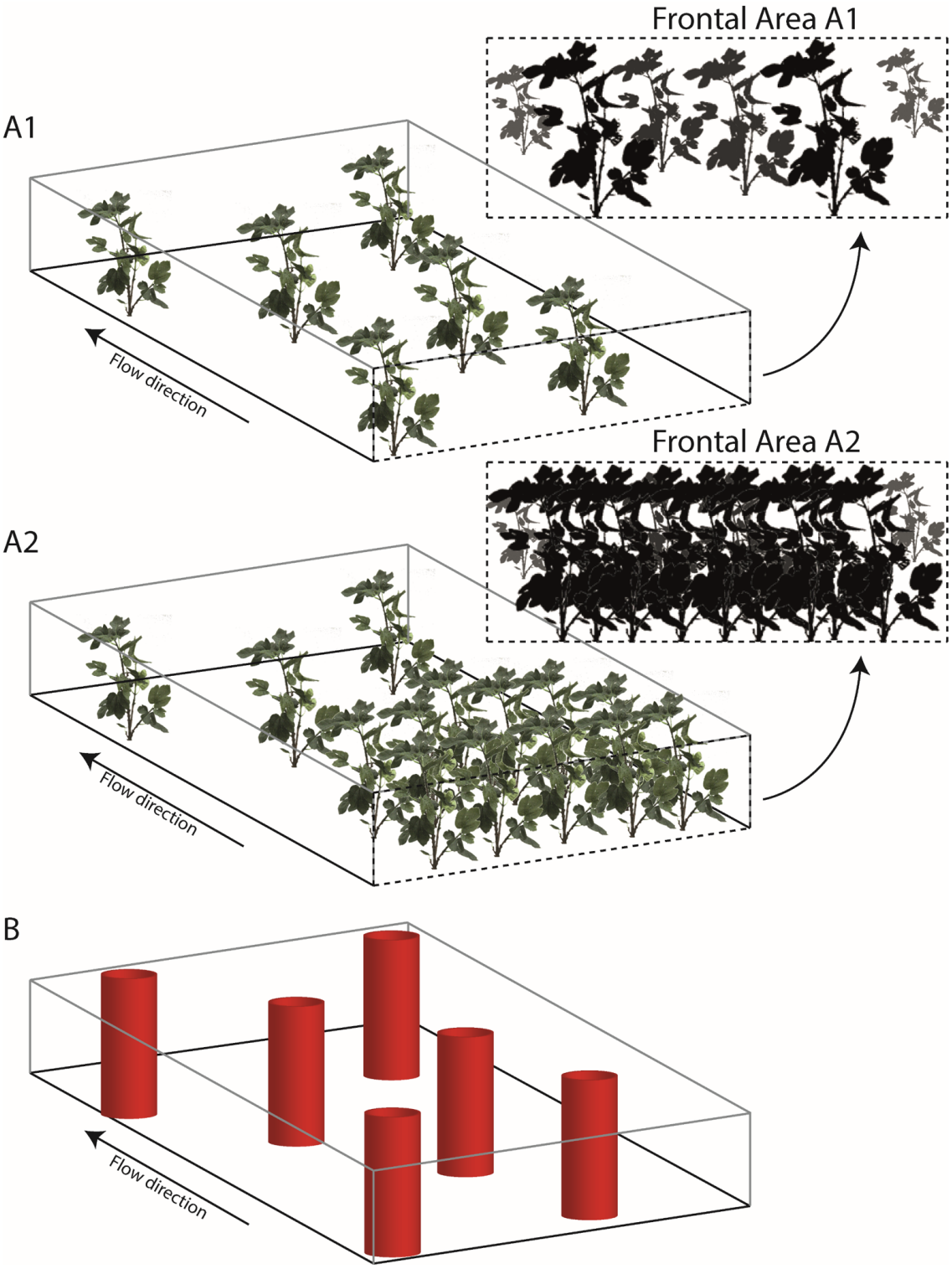

FIGURE 1.1: Example sketch of typical methods for the modelling of vegetation-flow interactions. Many studies, following a 2D approach, employ survey techniques to extract some kind of frontal area measurement. If the spatial distribution of the plant elements within the reach is homogeneous (A1), the extracted metric can be associated with bulk hydraulic parameters in a meaningful way. If the plant distribution is skewed (A2) then the extracted metric may be biased. Other studies sacrifice the spatial heterogeneity of plants, substituting them with simple geometrical objects (B).

1.2 Problem statement

There are two ways to assess the characteristics of surface water flows that interact with vegetation and both are useful depending on scale and the context of the project undertaken. The first seeks to characterise bulk flow attributes and employs bulk hydraulic roughness parameters such as the Manning's n, while the second focuses on the detailed characterisation of spatiotemporal variations of flow velocity and turbulence. In both cases, it is important that plant structure and deformation during flow is accurately and precisely measured and described in 3D. However, this measurement has proven to be difficult to obtain because of the diverse and very complex form of natural vegetation, along with a lack of appropriate survey methods. The current state of the art is to consider the changing nature of vegetation's frontal area as it deforms during flow. This is a 2D measure which neglects the streamwise variation in vegetative roughness and therefore, oversimplifies the vegetation-flow interactions (Figure 1.1, A1 and A2). Alternatively, vegetation's spatial variability is sacrificed and plants are treated as simple 3D geometrical objects, most commonly cylinders (Figure 1.1, B), oversimplifying the mechanics. Significant advances in surveying technology have been made during the last decade and now provide the opportunity of obtaining 3D measurements at high resolution (mm), precision and accuracy in the form of point clouds. Similarly, flow monitoring devices allow the characterisation of flow at high spatial and temporal resolution. However, because the extraction of meaningful metrics to characterise vegetation-flow interactions from 3D point clouds and flow data is complex and requires significant processing that involves computer-heavy calculations, the potential of this method has not yet been fully explored.

1.3 Research aims

The aim of this research is to exploit advanced surveying and flow measuring techniques, and processing methods, in order to accurately quantify the roughness effects of vegetation by developing relationships between 3D porous plant structures and their influence on flow conditions. High resolution survey methods and workflows will be developed to allow the extraction of physically meaningful three dimensional metrics of vegetative structure. These will be coupled with flow measurements obtained through physical modelling to link the effects of vegetative structure with the fluvial drag exerted by plants and the impacts on the flow field. The above can be summarised into the following research objectives:

(O1) Develop survey and processing methods capable of extracting quantitative vegetative structure metrics at suitable scales from 3D point cloud data.

(O2) Couple extracted metrics from O1 with hydraulic measurements acquired through physical modelling of flows through emergent vegetation elements, to link bulk vegetative structure to hydraulic roughness.

(O3) Assess the effects of vegetation on the flow field and link it to the spatial heterogeneity of vegetation.

1.4 Thesis outline

The present Chapter outlines the objectives of this research. Chapter 2 introduces the broad background theory governing fluid flows and their interactions with natural surfaces while Chapter 3 focuses on the specific case of flow encountering vegetation elements, which is pertinent for this research. Chapter 4 outlines the state of the art on surveying technology and processing methods in relation to previous attempts to quantify plant structure. Chapter 5 describes a novel method to characterise plant structure using Terrestrial Laser Scanning (TLS) and a porosity-based approach, fulfilling the first objective of this research. The second objective is fulfilled in Chapter 6 which is involved with vegetation-flow interactions and focuses on the relation between bulk metrics of plant structure and vegetative roughness, quantified through physical modelling. Chapter 7 focuses on adjustments of the flow characteristics generated by the presence of spatially heterogeneous plant elements fulfilling the third objective. Chapter 8 synthesises the findings stemming from the work undertaken and discusses their wider implications.

Chapter 2

Introduction to the Hydraulics of Surface Water Flow

Chapter 1 provided a brief outline of the background content and highlighted the aims and objectives of this research. In the present Chapter the broad theory describing fluid flow and its interactions with natural surfaces is introduced.

2.1 Introduction to fluid mechanics

In order to understand how flowing water interacts with Earth's surface, shaping the contemporary landscapes, the basic concepts governing fluid flows need to be considered.

2.1.1 Basic concepts

The term fluid is used to describe a subset of the states of matter. It includes gases and liquids; the other being solid (although plasma is also a fluid, it is not considered in this study). The fundamental attribute differentiating solids from fluids is that the latter cannot permanently resist a shearing force (Massey, 1998). Instead, they constantly deform under even the smallest deforming forces, flowing under their influence for the period that these forces are applied and adopting the shape of the solid with which they come into contact (Douglas et al., 2005).

All fluids are comprised of discrete fluid particles that can move freely relative to each other. If a very small unit volume is considered, the number of fluid particles within this volume constantly changes making the definition of fluid properties, such as density, problematic. However, in fluid mechanics, and in the present study, every fluid is treated as a continuum. Properties such as pressure and velocity are considered to vary continuously throughout the fluid and any changes rising from molecular motion are disregarded (White, 2011).

Before elaborating on fluid and flow properties, an important distinction must be made. There are two ways to observe any problem in mechanics, the Langrangian and the Eulerian. The former is better suited for the mechanics of solids and it studies the change of an object's property moving through the field. An example would be continuously measuring the speed of an individual sand grain that is transported by the flow. The latter is better suited to fluid mechanics and it focuses on the change of the field properties at a given constant position through time. An example would be the continuous measurement of the water flow velocity at a fixed position using a flow meter. In this study the Eulerian method is followed. The velocity of a fluid at a given point within the flow is presented by its three-dimensional (3D) vectors (u,v,w) varying over time (t), or by their average U. It must also be noted that all other fluid properties rising from thermodynamics, such as temperature, pressure, density and viscosity are considered to remain constant.

2.1.2 Characterising fluid flow

As noted in subsection 2.1.1 fluids will flow under the influence of shearing forces, rising from gravity or changes in pressure. A fluid flow may be categorised in many different groups based on various characteristics. Typical flow characterisations are summarised in Table 2.1.

Table 2.1: Summary of typical flow characterisations.

Parameter	Flow characterisation
Conduit type	Internal External Open channel
Change over time	Steady Unsteady
Compressibility	Incompressible Compressible
Viscosity	Viscous Inviscid
Reynold's Number	Laminar Turbulent

A fluid flow can be characterised as internal or external. Internal flows are constrained by solid boundaries (e.g. water flowing through a pipe). Conversely, external flows are not constrained by boundaries (e.g. wind flowing around a building) (White, 2011). A flow may also be categorised as an open channel flow. In this case the fluid is flowing within a conduit which has solid boundaries as well as a free surface (e.g. rivers and streams). A flow is characterised as steady when its attributes at a fixed point remain constant through time. The opposite of a steady flow is a transient (or unsteady) flow.

Because the movement of a body can only be described with reference to another body, the observer's position must be considered when distinguishing steady and unsteady flows. Although it is significantly easier to model steady flows, in reality the majority of fluid flows are unsteady. However, in flow modelling problems the reference axes are usually chosen in such a way that the flow will appear steady (Massey, 1998). Another parameter to be considered is the compressibility of a fluid. Incompressible flows are characterised from variations of the fluid density within the flow region. For that reason, laws of thermodynamics need to be involved in the modelling of compressible flows, increasing the model complexity. Nevertheless, all fluids are treated as incompressible in the present study, this is justified based on the fact that water has insignificant compressibility (Massey, 1998). A flow can be also characterised as viscous or inviscid and as laminar or turbulent. These flow characterisations are very important for the scope of this study and are discussed separately in subsections 2.1.2.1 and 2.1.2.3 below.

2.1.2.1 Viscous and inviscid flow

Although fluids are incapable of permanently resisting a shear force, they still exert resistance to such forces. The viscosity of a fluid is the property describing the fluid's resistance to shear forces, relating the stress emanating from the applied force to the rate of shear deformation. The stress (τ) rising from an applied force shears a fluid unit, as shown in Figure 2.1. The outcome is the deformation of the fluid with a rate equal to $\frac{d\theta}{dt}$. The viscosity (μ) of the fluid can be related to the shear stress (τ) using:

$$\tau = \mu \frac{d\theta}{dt} = \mu \frac{du}{dy} \tag{2.1}$$

Not all fluids have the same viscosity, for example honey is more viscous than water. Viscosity is affected by pressure and temperature. Although changes in pressure only slightly affect the viscosity of a fluid, changes in temperature have a strong effect. Liquids become less viscous in higher temperatures (White, 2011).

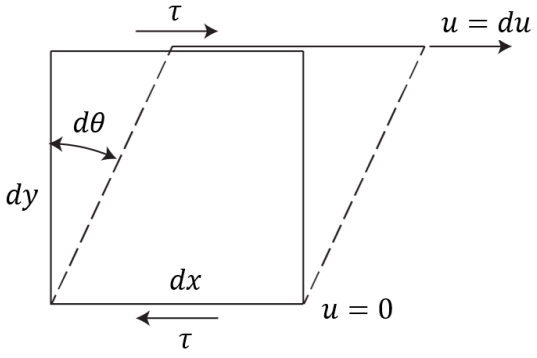

FIGURE 2.1: The deformation of a fluid by $\frac{d\theta}{dt}$ due to shearing stress τ. The no slip condition rising from viscosity keeps the bottom part of the fluid stationary while the upper part moves with velocity u (after White, 2011).

Viscosity effects are more important in the flow regions lying close to a solid surface. Therefore, in flow modelling it is useful to divide the flow into two regions, one close to the solid surface where the viscous forces must be considered, and one far from the solid surface where the viscous forces can be neglected, permitting the flow to be treated as inviscid (Massey, 1998). Partitioning the flow in a viscous and an inviscid region will be further discussed in Section 2.2.

2.1.2.2 Reynolds number

The balance between inertial and viscous forces is an important factor governing the behaviour of a fluid in motion. This idea of the ratio of inertial to viscous forces as an indicator of flow behaviour was originally introduced by Stokes (1851) and later made popular by Reynolds (1883) as the dimensionless Reynolds number (Re) given by:

$$Re = \frac{\rho U L}{\mu} = \frac{U L}{\nu} \tag{2.2}$$

where ρ is the fluid density and U, L are the characteristic velocity and length scales, respectively. In Reynolds number the term kinematic viscosity (ν) is introduced as the ratio of viscosity (μ), also called dynamic viscosity for differentiation, over the density (ρ).

2.1.2.3 Laminar and turbulent flow

Reynolds (1883), using an experimental apparatus, showed that the ratio of inertial to viscous forces is the governing factor making a flow laminar or turbulent. Laminar (or viscous, or streamlined) flows are characterised by the movement of the fluid particles along parallel, straight lines. Laminar flows are usually observed under low flow velocities. Turbulent flows are characterised by the movement of the fluid particles in sinusoidal streamlines which are crossing each other. Turbulent flows are more common under higher flow velocities (Massey, 1998). From equation (2.2) the Reynolds number was defined as the ratio of inertial over viscous forces. When Re is low the viscous forces are sufficiently strong, restraining the fluid particles forcing them to flow along straight parallel routes, maintaining a laminar flow. As the inertial forces increase (e.g. by an increase in velocity) the viscous forces become less sufficient to maintain the laminar flow. The fluid particles start to follow sinusoidal routes, leading to turbulence. The importance of the transition from laminar to turbulent flow is further discussed in Section 2.2.

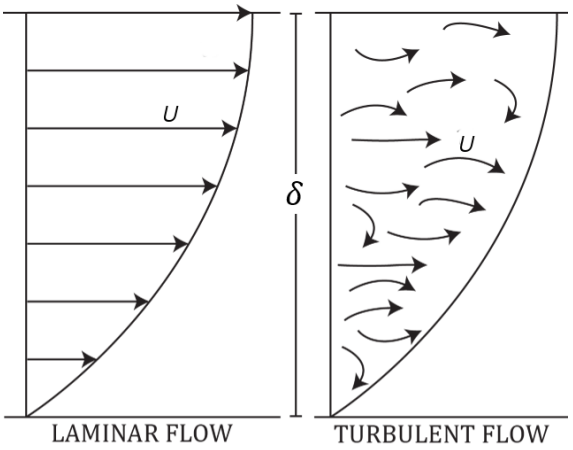

FIGURE 2.2: Typical velocity profiles for laminar and turbulent flow. U is the flow velocity (vertical scale greatly enlarged) (after Knighton, 1998).

2.1.3 Numerical modelling of fluid flow

Despite the obvious importance of characterising the nature and magnitude of fluid flow velocity, it is notoriously difficult to directly measure (Bates et al., 1997; Lane et al., 1998). In fact, numerical modelling remains a useful and necessary technique to quantify fluid flow dynamics. The background to modelling techniques is introduced below. As a general rule, in the numerical modelling of fluid flows it is assumed that the fluids are Newtonian and incompressible, meaning that the density and viscosity of the fluid are constant, providing that there is no change in the fluid's state. This proves convenient as the basic principles of mass and momentum conservation can then be used to underpin modelling approaches.

2.1.3.1 The Navier-Stokes equations

Due to the Newtonian and incompressible nature of the fluid flows, three-dimensional momentum conservation equations can be used such as the ones described below:

$$\frac{\partial}{\partial t}(\rho u)+\frac{\partial}{\partial x}(\rho u^2)+\frac{\partial}{\partial y}(\rho uv)+\frac{\partial}{\partial z}(\rho uw)-2\rho u\zeta\sin\Phi+\frac{\partial p}{\partial x}-\frac{\partial \tau_{xx}}{\partial x}-\frac{\partial \tau_{xy}}{\partial y}-\frac{\partial \tau_{xz}}{\partial z}=0 \quad (2.3)$$

$$\frac{\partial}{\partial t}(\rho v)+\frac{\partial}{\partial x}(\rho uv)+\frac{\partial}{\partial y}(\rho v^2)+\frac{\partial}{\partial z}(\rho vw)-2\rho v\zeta\sin\Phi+\frac{\partial p}{\partial y}-\frac{\partial \tau_{xy}}{\partial x}-\frac{\partial \tau_{yy}}{\partial y}-\frac{\partial \tau_{yz}}{\partial z}=0 \quad (2.4)$$

$$\frac{\partial}{\partial t}(\rho w)+\frac{\partial}{\partial x}(\rho uw)+\frac{\partial}{\partial y}(\rho vw)+\frac{\partial}{\partial z}(\rho w^2)+\rho g+\frac{\partial p}{\partial z}-\frac{\partial \tau_{xz}}{\partial x}-\frac{\partial \tau_{yz}}{\partial y}-\frac{\partial \tau_{zz}}{\partial z}=0 \quad (2.5)$$

The second order non-linear partial differential equations(2.3)-(2.5) are known as the Navier-Stokes equations. Here ρ is the fluid density, g the gravitational acceleration, p the pressure and μ the viscosity, ζ is Earth's angular rotation, Φ the latitude and τ_{ij} the components of the stress tensor. u,v,w are the components of the three dimensional velocity vector in the x,y,z dimension, respectively. The Navier-Stokes equations contain

four unknowns, the pressure (p) as well as the three velocity vectors (u,v,w). For that reason they are combined with equation (2.6) originating from the continuity of mass.

$$\frac{\partial u}{\partial x} + \frac{\partial v}{\partial y} + \frac{\partial w}{\partial z} = 0 \tag{2.6}$$

Despite the lack of an analytical solution capable of solving the Navier-Stokes equations, they still remain very useful as they provide the basis for the modelling of turbulent flows.

2.1.3.2 The Saint-Venant equations

The Navier-Stokes equations may be simplified by averaging them for the vertical dimension, thereby providing the Saint-Venant (or shallow water) equations. They provide a simplified method of modelling turbulent flows which is appropriate for many natural environments. This is because in common natural flows the vertical dimension (i.e. depth) is much smaller than the length scale.

$$\frac{\partial h_w}{\partial t} + \frac{\partial h_w u}{\partial x} + \frac{\partial h_w u}{\partial y} = 0 \tag{2.7}$$

$$\frac{\partial h_w u}{\partial t} + \frac{\partial}{\partial x}\left(u^2 h_w + \frac{g h_w^2}{2}\right) + \frac{\partial}{\partial y}(uv h_w) + S_f = 0 \tag{2.8}$$

$$\frac{\partial h_w v}{\partial t} + \frac{\partial}{\partial x}(uv h_w) + \frac{\partial}{\partial y}\left(v^2 h_w + \frac{g h_w^2}{2}\right) + S_f = 0 \tag{2.9}$$

here u and v are the components of the two dimensional velocity vectors in the x and y dimensions, respectively and h_w is the flow depth. The advantage of the Saint-Venant equations is that they are easier to solve than the Navier-Stokes equations. However, averaging of the vertical dimension disregards the detail of the vertical velocity component. Whilst for many purposes this may be a suitable compromise, for studying vertical arrays of complex, three-dimensional roughness (e.g. vegetative flows; see Chapter 3) it is an oversimplification of the mechanics. Nevertheless, the Saint-Venant equations are mentioned here due to the introduction of a friction slope term (S_f). This friction slope is a bulk representation of the total energy loss due to friction or other resistance exerted to the flow, including resistance arising from surface roughness, topography and protruding elements such as vegetation.

2.1.3.3 Bulk roughness coefficients

The friction slope (S_f), introduced in equations (2.8) and (2.9), is a bulk parameter accounting for the sum of external forces applied to the flow. This key factor represents the total energy loss and flow retardation due to various reasons including friction

between the fluid and the boundary, and drag emanating from topographic features or protruding obstacles. Because the friction slope incorporates the effects of many different interactions between a flowing fluid and the boundary that it is in contact with, it is difficult to directly measure. Many attempts have been made to empirically link it with measurable surface properties resulting in the availability of various different equations such as the Chézy, the Manning and the Darcy-Weisbach formulae.

According to the Chézy formula:

$$u = C\sqrt{R_h S} \tag{2.10}$$

the velocity of a steady turbulent, open channel flow is a function of the slope (S), the hydraulic radius ($R_h = \frac{A_c}{P}$) and the Chézy coefficient of roughness (C). For the hydraulic radius, which is a measure of the efficiency of the channel flow, A_c is the cross-sectional area of the flow and P is the wetted perimeter. If the flow width is much greater than the flow depth, the hydraulic radius can be replaced by the flow depth (GiMey et al., 1991).

The Chézy coefficient of roughness represents the total resistance to the flow exerted by all external forces. It was found to have a tendency to depend on flow depth, this led to the formulation of the Manning's equation which is independent of the flow depth within the reach (Ferguson, 2010).

The Manning's equation calculates the flow velocity (u) as a function of the hydraulic radius (R_h), the slope (S) and the Manning's roughness coefficient (n) as shown below:

$$u = \frac{R_h^{2/3} S^{1/2}}{n} \tag{2.11}$$

Similarly to the Chézy coefficient of roughness, the Manning's roughness coefficient is also a bulk parameter not distinguishing among the different external forces influencing the flow. It is commonly related to grain size through the relation proposed by Strickler, where:

$$n \approx 0.047 D_{50}^{1/6} \approx 0.039 D_{84}^{1/6} \tag{2.12}$$

here D_{50} is the median of the sediment's grain diameter and D_{84} is the diameter of the grain for which 84% are finer (Ferguson, 2010). Equation (2.12), directly linking grain size with n value, proposes that there is only one prominent external force affecting the flow and it is associated with grain roughness, disregarding any other influencing factors such as channel sinuosity, topographic roughness, vegetation or other protruding features.

Although the Manning's roughness coefficient was proposed as an independent to depth

alternative to the Chézy coefficient, it has been reported that n has a tendency to decrease when stage increases in a variety of water flows such as gravel-bed (Chow, 1959; Sargent, 1979; Richards, 1982; Dingman, 2009; Ferguson, 2010), sand-bed and boulder-bed rivers (Ferguson, 2010). An alternative to the previous two coefficients is the Darcy-Weisbach friction slope given by:

$$S_f = \frac{fQ^2}{8gR_h A_b^2} \tag{2.13}$$

here Q is the discharge, g the acceleration due to gravity, A_b is the planar area and f is the Darcy-Weisbach roughness coefficient given by:

$$f = \frac{8gR_h S}{u^2} \tag{2.14}$$

The Darcy-Weisbach friction factor was proposed because in contrast to the Manning's and Chézy coefficients, the Darcy-Weisbach friction factor is dimensionless. Nevertheless, in practical applications the Manning's roughness coefficient is most commonly used (Järvelä, 2002b). The three bulk flow resistance parameters presented above can be related to each other according to equations (2.15), (2.16) and (2.17).

The Chézy coefficient (C) and the Manning's n value can be related using (Martin and Myers, 1991):

$$C = \frac{R_h^{1/6}}{n} \tag{2.15}$$

Manning's and Darcy-Weisbach coefficients are related using (GiMey et al., 1991):

$$n = \left(f \frac{R_h^{1/3}}{8g} \right)^{1/2} \tag{2.16}$$

Therefore, the Manning's n value can be also used for the calculation of the friction slope using the Darcy-Weisbach equation with (Martin and Myers, 1991):

$$S_f = \left(\frac{nQ}{A_b R_h^{2/3}} \right)^2 \tag{2.17}$$

In summary, all three friction slope coefficients described above, namely Chézy, Manning's and Darcy-Weisbach, represent the total resistance exerted on the flow. Therefore, they do not distinguish between the friction of the fluid on the solid surface and the resistance rising from other irregularities that are present, such as large-scale topographic features, vegetation or other above-surface obstacles. Furthermore, all three

friction slope coefficients are estimated using empirical relationships instead of the physical properties of the surface characteristics. For example Strickler's equation (2.12) for the determination of Manning's n relies on empirically derived constants. In practice Manning's n values are commonly used as a means of calibration between model-based and real-world measurements (Lane, 2005).

The simple representation of flow resistance using one bulk parameter, such as the ones described above, is likely not adequate to characterise the complex resisting forces resulting from near bed interactions. In fact, the flow near a solid surface has been studied for many years and is the subject of a well-established theory that is presented further in Section 2.2 below.

2.2 Boundary layer flow

A fluid flow is significantly affected by the characteristics of the surface that is in contact with. However, this effect does not have the same magnitude throughout the flow depth and it is important to distinguish the flow layer that is affected by the surface characteristics from the rest of the flow. This is elaborated through the boundary layer theory.

2.2.1 Introduction to boundary layer theory

Prandtl (1904) was the first to introduce the concept of a boundary layer theory. When a fluid flows across a solid surface, which from now on will be called 'the wall', the flow can be divided into two regions. The first region consists of a thin layer lying close to the wall and is governed by significant viscous forces and rotation. In the second, outer, region the viscous force is insignificant and therefore can be neglected.

The velocity at the lower layer of the fluid, that is adjacent to the wall, is zero (Richardson, 1973). This no-slip condition is due to the shear stress (τ_0) at the wall, rising from the friction of the fluid against the solid surface. This motionless layer exerts a viscous drag against the layer of the fluid right above it, gradually slowing it down. The second layer is losing momentum and therefore exerts a drag on the third layer and so on. The flow velocity increases rapidly as the distance from the wall becomes greater, until it reaches the velocity of the main stream ($U = 0.99U_m$) (Figure 2.3) (Douglas et al., 2005).

The equation that describes the increase of the flow velocity in accordance to the increase on the distance from the wall is given by Von Karman's (1930) 'law of the wall':

$$U = \frac{1}{\kappa} u_* \ln \frac{z}{z_0} \tag{2.18}$$

here κ is the Von Karman constant, u_* is the shear velocity, z is the distance from the wall and z_0 is the roughness height, which is the distance from the wall within which the velocity remains zero (Figure 2.3).

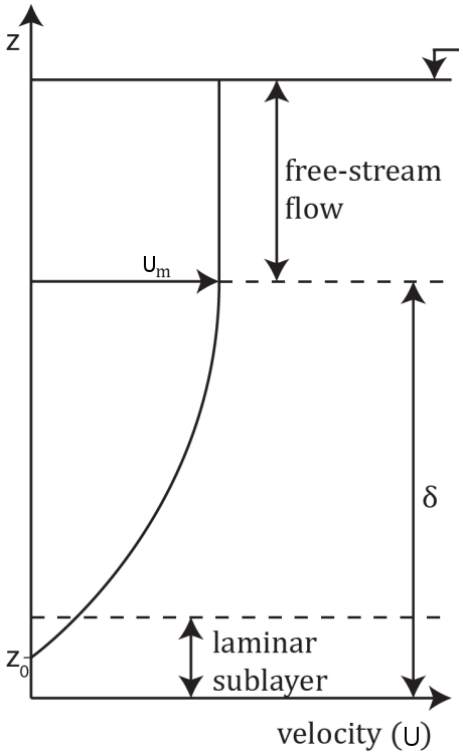

FIGURE 2.3: Boundary layer profile of deep flow, noting the boundary layer of thickness δ, the laminar (or viscous) sublayer and the free stream outside the boundary layer zone. U_m is the free stream velocity and z_0 the roughness height, the vertical scale is greatly enlarged (after Knighton, 1998).

The layer of the fluid within which the rapid increase of the flow velocity is observed is called the boundary layer. The thickness (δ) of the boundary layer increases along the streamwise length of the flow, until it reaches its maximum extent (Figure 2.4). From this point on, the flow is considered to be fully developed Massey (1998). The shear stress (τ_0) follows the same pattern as the thickness of the boundary layer; it increases from zero at the start of the wall and reaches a maximum when the flow is fully developed, from this point on the value of the shear stress remains constant.

As explained above, the higher parts of the boundary layer have higher flow velocities than the lower parts. Therefore, the fluid flowing in the higher parts of the flow region drags the fluid flowing nearer to the wall with two types of mechanism. If the thickness (δ) of the boundary layer is thin, the velocity gradient normal to the surface ($\partial u/\partial y$) is large, meaning that from equation (2.1) the shear stress is also large. Therefore, the drag caused by the shear stress at the wall extends the effect close to the surface keeping the fluid in laminar flow (Figure 2.4 left side). As the thickness of the boundary layer becomes greater, the velocity gradient decreases until it can no longer drag the slow fluid near the wall. This means that if the viscous force was the only action, then the fluid would come to a rest. However, the second mechanism occurs at this point. As the

thickness (δ) of the boundary layer increases, the viscous forces as well as the velocity gradient become smaller. Therefore, they are no longer able to sustain the laminar flow and the motion of the fluid particles become rapidly turbulent (Figure 2.4 right side). Fluid from the fast moving higher regions of the flow moves into the slower zone, transferring momentum and thus maintaining the fluid by the wall in motion. Conversely, fluid from the slow moving region moves to the faster moving region slowing it down. The net effect of the above mechanism is the increase of the momentum in the boundary layer. The transition of the flow from laminar to turbulent is not instant but instead it occurs within a short transition region (Massey, 1998).

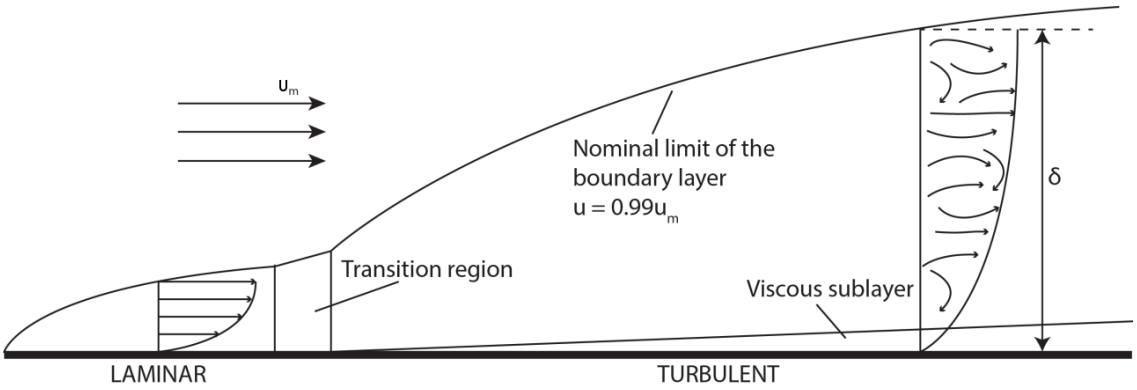

FIGURE 2.4: Fluid flowing along a solid flat plate creates a laminar boundary layer which quickly transitions into a turbulent one. The transition region is pointed out as well as the viscous sublayer that is developed within the turbulent boundary layer region (after Massey, 1998).

2.2.2 Flow over a protruding obstacle

In subsection 2.2.1 the wall was assumed to be flat, which is an idealised case. The current section will focus on the flow over a curved surface, setting the necessary background for the study of natural surfaces which are rarely flat and frequently included topographic or above-surface protrusions (e.g. dunes, bars, vegetation). These protruding obstacles have a significant effect on the flow field which is examined herein.

Figure 2.5 shows the changes of net forces, velocity and pressure gradients as a flow passes over a protruding obstacle. As the flow meets the protruding feature, the flow velocity drops significantly. According to Bernoulli's principle, this decrease in velocity is accompanied by an increase in pressure. As the flow travels downstream, a boundary layer is developed due to the friction force (F_{SF}) between the solid surface and the viscous fluid, following the mechanisms described in subsection 2.2.1. In this region the flow velocity increases gradually, while the pressure decreases until the flow reaches the middle of the protruding object. At this point the flow has achieved maximum flow velocity while the pressure has minimised. As the fluid continues travelling downstream the opposite effect occurs, with the pressure gradually increasing accompanied by a decrease in the flow velocity. This allows the recognition of two distinct flow regions, one

upstream, related to a favourable pressure gradient and one downstream, where the pressure gradient is adverse. This pressure difference creates a drag force which is known as pressure (or form) drag (F_D). The adverse pressure gradient, in combination with the shear forces at the surface of the wall, may cause flow reversal and thus flow separation leading to the development of a wake region characterised by large eddies and significant turbulence. The pressure within the wake region is low due to high energy dissipation because of turbulence. Therefore, the pressure on the front of the protrusion is much greater than the pressure at the rear of the body. This difference significantly increases the form drag (Douglas et al., 2005).

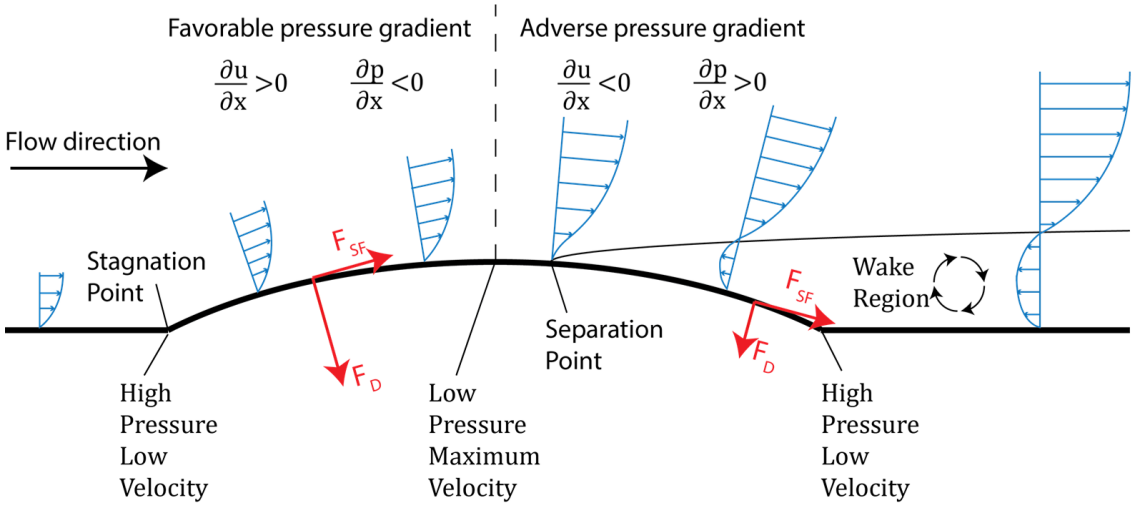

FIGURE 2.5: Flow over a protruding obstacle. Showing the streamwise changes of pressure and velocity gradients, the development of a boundary layer, the flow separation and the development of a wake region and the forces emanating from skin friction (F_{SF}) and pressure (F_D). Direction of flow is from left to right (combination of figures 11.11, 12.1 and 12.2 of Douglas et al., 2005).

2.2.3 Skin and form drag

To summarise, there are two key forces affecting the interaction between a flowing fluid and a solid surface, namely skin (or friction, or viscous) drag (F_{SF}) and form (or pressure) drag (F_D). The former is the result of friction between the flowing fluid and the contacting solid surface while the latter is the outcome of pressure forces, arising from surface topography and the existence of any above-surface features such as vegetation. From the two components of the total drag, the stress emanating from the skin drag (τ_{SF}) is related to sediment transport (Smith and McLean, 1977) but the from drag stress (τ_D) is usually the dominant component of the total boundary shear stress (Thorne and Furbish, 1995; Darby et al., 2010), which has the effect of limiting the values of the skin drag and consequently controlling sediment transport (Darby et al., 2010). Therefore, when studying geomorphological processes, it is important to partition the total boundary shear stress into its skin drag and form drag components. For the correct estimation of skin and form drag, the physical characteristics of vegetation and other

above-surface features must be carefully and precisely measured, and incorporated in the fluid flow modelling. This however, has proven to be particularly difficult because of the complexity and diversity of the plethora of above-surface features such as vegetation.

2.3 Roughness

Section 2.2 highlighted the interaction between boundary and flow and the key role of boundary and above boundary geometry. The small-scale surface characteristics such as micro-topography and above-surface features interacting with the lower layers of flow are commonly dubbed as roughness. Although the concept of roughness is intuitive, it is also difficult to define. The term has been applied extensively and with great diversity in a plethora of disciplines (Smith, 2014). Examples can be found in medicine (*e.g.* Deligianni et al., 2001), biology (*e.g.* Hallab et al., 2001), material science (*e.g.* Miwa et al., 2000), engineering (*e.g.* Webb et al., 1971), acoustics (*e.g.* Law and Zhu, 2005), planetary sciences (*e.g.* Pommerol et al., 2012) and remote sensing (*e.g.* Anderson et al., 2012), among others.

In the Earth sciences the term roughness is used extensively. In tectonics the roughness of fault surfaces is a key factor influencing stress distribution, fault slip and in turn earthquake characteristics (Candela et al., 2009; Power et al., 1987). In marine geosciences sea floor roughness has been identified as a key parameter influencing numerous phenomena such as the dissipation of eddy kinetic energy on the water surface (Gille et al., 2000), interactions between sea floor and acoustic waves (Lyons et al., 2002), or the velocity profile and in turn sediment transport (Siwabessy, 2001). In glaciology the roughness of the substrate has been related to subglacial processes including ice stream flows (Siegert et al., 2004) and glacier sliding (Kamb, 1970). Parameters describing surface roughness have been used for the relative dating of alluvial fans (Frankel and Dolan, 2007). In the study of landslides, roughness is used for the differentiation of the various landslide elements and the identification of active zones (McKean and Roering, 2004; Glenn et al., 2006). In the study of soils, roughness has been found to be a key component affecting the rate of water run-off and infiltration (Burwell and Larson, 1969), the reflection of sun's radiation and thus soil temperature, which directly affects evaporation rates (Allmaras et al., 1977), as well as water routing and skin friction drag related to erosion and sediment transport (Engman, 1986). When studying the motion of a fluid over a solid surface, momentum roughness height is used to describe momentum loss due to surface irregularities. Momentum and surface roughness are referring to related, but not identical, parameters (Smith, 2014).

The vast and diverse application of the term roughness not only in cognate fields of the Earth sciences but in other disciplines as well, causes terminological issues that hinder communication between scientists (Smith, 2014). Subsections 2.3.1-2.3.3 will elaborate on the different meanings of roughness in relation to fluid flows and boundary layer theory.

2.3.1 Roughness as a surface property

Perhaps the most common and intuitive meaning of roughness is that of surface roughness. As a surface property, roughness characterises the relatively high-frequency, short-wavelength irregularities that define surface texture. In this sense, surface roughness has been also called micro-topography (Brayshaw, 1985; Frei et al., 2010; Dunne et al., 2013), rugosity (Jenness, 2004), ruggedness (Beasom et al., 1983) or micro-relief (Lyford and MacLean, 1966; Stone and Dugundji, 1965).

2.3.1.1 Scale considerations

From the above definition is evident that the role of parameterising surface roughness is to highlight those surface characteristics that are too subtle to be considered as topography. However, this depends on measurement scale and method resolution. Various landforms have different sizes, meaning that they must be examined at different scales. When the landforms of interest are identified in advance, they determine the appropriate survey scale. All remaining features that are smaller and not explicitly described are considered as roughness (Smith, 2014). On the other hand, different methods of measurement have different maximum resolutions over which the noise of the method cannot be distinguished from the real value. Leyland et al. (2015) demonstrate that increased survey resolution may enable the identification of smaller roughness elements, increasing the measured values of topographic surface roughness. However, as the authors point out, after a certain threshold any further increase of resolution does not have a significant effect on the estimated surface roughness value. Therefore, surface roughness represents a scale window (Figure 2.6) the lower limit of which is defined by measurement capabilities, primarily linked to technological advances. The upper limit, namely partitioning between topography and roughness, is case-specific and frequently arbitrarily defined (Smith, 2014). Several roughness scales exist inside the roughness window, they are the signatures of various geomorphological processes (Morris et al., 2008; Kreslavsky et al., 2013) changing through time(Smith, 2014).

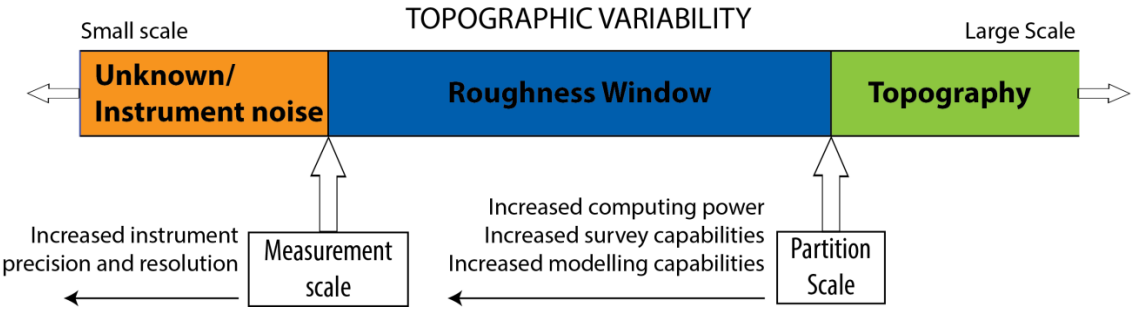

FIGURE 2.6: Schematic outlining the roughness window. Its upper limit is the scale over which topographic features are explicitly identified. Its lower limit is the scale below which measurement and method's noise cannot be distinguished (after Smith, 2014).

2.3.1.2 Measuring surface roughness

The enormous complexity of Earth's surface hinders the derivation of a unique set of parameters capable of describing it in its fullest (Gadelmawla et al., 2002). This, in conjunction to the necessity for a better description of complex, highly diverse, surfaces (Smith, 2014) and technological advances in the field of surface metrology led to an over-abundance of roughness metrics from which only a few are useful (Whitehouse, 1982). Even worse, the plethora of roughness metrics is characterised by a severe lack of standardisation, not only because of the high diversity of geomorphic forms that they aim to describe, but also due to the various international and national standards (Smith, 2014). The various surface roughness metrics, may be classified into four broad categories all of which are summarised in Table 2.2 and further elaborated herein.

Amplitude parameters

Surface roughness is frequently estimated using some sort of elevation measurement for the roughness elements. It can be estimated from discrete particles based on their size distribution(*e.g.* Bathurst, 1993; Hey, 1979; Nikuradse, 1950) or protrusion (Gomez, 1993). Neighbour analysis compares the elevation of a unit cell with the elevation of neighbouring cells and the roughness is estimated either based on the maximum or the root-mean-square elevation difference (Riley et al., 1999). Statistical parameters may be employed for the estimation of roughness such as the mean height of the roughness elements above a reference level (Takken and Govers, 2000), the range of elevation (*e.g.* Haubrock et al., 2009; Pelletier et al., 2009; Torri et al., 2012), or most commonly the standard deviation of elevations (*e.g.* Kuipers, 1957; Banke and Smith, 1973; Kamphorst et al., 2000; Glenn et al., 2006; Sankey et al., 2010; Grohmann et al., 2011; Nield et al., 2011). Alternatively, estimates of surface roughness along a profile can be derived through the comparison of each element's highest elevation point to the lowest elevation of the transect (*e.g.* Courtwright and Findlay, 2011).

Spacing parameters

Instead of relying on elevation differences, spacing parameters aim to describe surface roughness by focusing on measurements along the horizontal dimension. In comparison to amplitude parameters, spacing parameters are less common in the domain of earth sciences (Smith, 2014). Examples include the zero crossing analysis method developed by Lettau (1969) and later adopted by Munro (1989). The L-M method requires the derivation of a zero-mean baseline, subsequently the roughness is calculated based on the number of times that this baseline is crossed along the transect, in an upward direction. Alternatively, surface roughness can be estimated using the length of roughness features (*e.g.* Courtwright and Findlay, 2011) or the spacing between subsequent features (*e.g.* Werner and Zedler, 2002).

Hybrid parameters

Hybrid parameters rely on a combination of vertical and horizontal measurements. Surface roughness can be related to tortuosity (*e.g.* Moser et al., 2007), to the ratio of the actual distance between two points along a profile over the distance along a straight line (*e.g.* Morgan et al., 1998), or to the ratio of surface area per unit planar area (Jenness, 2004). Roughness has been related to porosity measurements of gravel-bed rivers (*e.g.* Aberle, 2007) or vegetation (Grant and Nickling, 1998). The employment of porosity measurements as a means to estimate vegetative roughness is a promising approach which will be further explored in subsection 3.3.3. Roughness may also be estimated through statistical parameters of slope such as RMS slope (Shepard et al., 2001), standard deviation of slope (Grohmann et al., 2011) or mean square slope (Hwang, 2008). McKean and Roering (2004) demonstrate that rough surfaces are related to higher variability of slope and aspect which can be estimated with the introduction of eigenvalues. They also propose an alternative method based on the measurement of topographic curvature via Laplacian operators. Kean and Smith (2006a,b) propose the modelling of subsequent roughness elements with fitted Gaussian curves and estimate roughness using the protrusion height and stream wise length of the distribution as well as the residuals to subsequent fitted curves. Their model has been adopted to calculate bank roughness and relate it to erosion rates (Darby et al., 2010; Leyland et al., 2015). In general, hybrid parameters offer a better overall representation of surface roughness, in comparison to amplitude or spacing derived ones. But they also demonstrate a significant scale dependency as the estimated roughness value appears to increase with increasing survey resolution (Smith, 2014). For that reason, it is a good practice to accompany roughness estimates with a scale sensitivity analysis (*e.g.* Leyland et al., 2015).

Multi-scale parameters

As discussed in subsection 2.3.1.1, surface roughness estimates are significantly affected by the chosen scale. These effects can be defined through sensitivity analysis where profiles are either gradually smoothed by the application of filters (*e.g.* Bergeron, 1996) or resampled at coarser resolutions (*e.g.* Leyland et al., 2015) and roughness estimates are derived after each filtering or resampling step. Alternatively, multi-scale parameters can be employed. Examples of multi-scale parameters include metrics adopted from fractal analysis (Mandelbrot, 1983; Perfect and Kay, 1995; Turcotte, 1997) and geostatistics, such as the sill (Oliver and Webster, 1986; Robert, 1988) calculated from semi-variograms, and the profile's correlation length. The correlation length is defined as the required lag for the decrease of the normalised correlation to approximately 37%, smooth profiles have a larger correlation length value than rough ones (Shepard et al., 2001). The basic concern related to these multi-scale parameters is that their statistical nature makes them less intuitive and detached from the physical meaning of surface roughness (Smith, 2014). Spectral analysis, such as Fourier decomposition, can be employed to identify the different frequency wavelengths that describe various groups of roughness features along a profile or area (*e.g.* Aberle et al., 2010; Banke and Smith,

1973; Briggs, 1989; Hubbard et al., 2000; Lampkin and VanderBerg, 2011; Lyons et al., 2002; McKean and Roering, 2004; Taylor et al., 2004). Wavelet analysis calculates spectra locally, following a similar fashion to spectral analysis. Because of its localised nature, wavelet analysis is more appropriate for heterogeneous surfaces (Nield et al., 2013).

TABLE 2.2: Classification of common surface roughness metrics (after Smith, 2014).

1. Amplitude parameters	1.1 Discrete form parameters	a) Grain size percentiles	Nikuradse (1950); Hey (1979); Bathurst (1993)
		b) Protrusion measures	Gomez (1993)
	1.2 Neighbour elevation differences	a) Nearest neighbour elevation difference	Ergnezinger and Stuve (1989) (cited in Smith (2014))
		b) RMS difference of all adjacent points	Riley et al. (1999)
	1.3 Elevation probability distribution statistics	a) Mean	Takken and Govers (2000)
		b) Standard deviation	Kuipers (1957); Banke and Smith (1973); Kamphorst et al. (2000); Glenn et al. (2006); Sankey et al. (2010); Grohmann et al. (2011); Nield et al. (2011)
		c) Skewness	Aberle and Nikora (2006); Aberle et al. (2010)
		d) Kurtosis	Aberle and Nikora (2006); Aberle et al. (2010)
		e) Range	Pelletier et al. (2009); Haubrock et al. (2009); Torri et al. (2012)
	1.4 Extreme characteristics	a) Height of peaks or depths of pits	Bergeron (1996); Courtwright and Findlay (2011)
2. Spacing parameters	2.1 Zero crossing analysis		Lettau (1969); Munro (1989)
	2.2 Feature spacing		Gadelmawla et al. (2002); Werner and Zedler (2002)
	2.3 Feature length		Courtwright and Findlay (2011)
3. Hybrid parameters	3.1 Complexity ratios	a) Profile tortuosity	Moser et al. (2007)
		b) Total surface area per unit planar area	Jenness (2004)
		c) Measured and straight line distance	Morgan et al. (1998)
		d) Porosity	Grant and Nickling (1998); Aberle (2007)
	3.2 Slope	a) Standard deviation of slope	Grohmann et al. (2011)
		b) RMS slope	Shepard et al. (2001)
		c) Mean square slope	Hwang (2008)
	3.3 Aspect variability	a) Eigenvalue ratios	McKean and Roering (2004)
		b) Laplacian operators	McKean and Roering (2004)
	3.4 Fitted geometry	a) Parameters of fitted Gaussian distribution	Kean and Smith (2006a,b); Darby et al. (2010); Nield et al. (2011); Leyland et al. (2015)
4. Multi-scale parameters	4.1 Space-scale analysis		Bergeron (1996); Leyland et al. (2015)
	4.2 Geostatistics / fractal analysis	a) Correlation length	Shepard et al. (2001)
		b) Limiting distance (sill)	Shepard et al. (2001); Rosenburg et al. (2011); Oliver and Webster (1986); Clifford et al. (1992)
		c) Hurst exponent	Robert (1988)
		d) Fractal dimension	Mandelbrot (1983); Perfect and Kay (1995); Turcotte (1997)
	4.3 Spectral analysis	a) Slope of power spectral density function	Banke and Smith (1973); Briggs (1989); Lyons et al. (2002); McKean and Roering (2004); Aberle et al. (2010)
		b) Fourier decomposition	Lampkin and VanderBerg (2011)
		c) Integral of normalised spectral power density	Hubbard et al. (2000); Taylor et al. (2004)
	4.4 Wavelet analysis	a) Scale-averaged variance at different bonds	Foufoula-Georgiou and Kumar (1994); Lindsay et al. (1996); Torrence and Compo (1998); Nyander et al. (2003); Kalbermatten et al. (2012)
		b) Space-averaged global wavelet spectra	Cataño-Lopera and García (2006); Fraccascia et al. (2011)

2.3.2 Roughness as a flow property

Surface roughness is commonly used as a proxy for other properties that are difficult to directly measure, such as the resistance when a fluid flows over a solid surface. Roughness height (z_0), introduced in Von Karman's law of the wall (Equation (2.18)), can be linked to the momentum loss due to surface roughness. The roughness height can be determined from flow measurements, but this is notoriously difficult because of the method's susceptibility to errors (Munro, 1989), especially in remote locations (Nield et al., 2013). The roughness height can be related to surface roughness, but the two properties are not identical (Smith, 2014). Although this relationship is useful, as it allows the derivation of roughness height from surface roughness metrics, it also inherits the uncertainty about the most appropriate roughness metric to be related with flow attributes.

Perhaps the simplest relation between surface roughness and roughness height is the one proposed by Bagnold (1938) where the roughness height is taken to be equal to $1/30^{th}$ of the height of the roughness element or mean grain diameter. This relationship was later questioned, for example Greeley and Iversen (1985) found Bagnold's ratio to fluctuate for various distances between particles. Moreover, the employment of grain size for the parameterisation of roughness height neglects packing structures such as grain overlapping or other topographic features (Powell, 2014). Various relationships have been proposed, relating the roughness height to the frontal and the total surface area of the roughness elements. For example, Lettau (1969) relates roughness height with average element height (H) and frontal area (A_f) by equation (2.19), with A_b being the surface area and 0.5 representing an empirically derived drag coefficient:

$$z_0 = \frac{0.5 H A_f}{A_b} \tag{2.19}$$

Although these models describe more thoroughly the loss of flow momentum, their application to natural, complex surface features or vegetation can be challenging (Smith and Vericat, 2014).

Nield et al. (2013), for bare, complex, small-scale roughness elements, relate roughness height (z_0) and shear velocity (u_*), measured directly from wind measurements, to surface roughness derived from high resolution TLS data using various surface roughness metrics. Their correlation analysis shows that, for uniform areas, the roughness height (z_0) is best correlated with the mean height ($\bar{H}$) of the roughness elements or the volumetric roughness density, introduced by Grant and Nickling (1998) (see also 3.3.3). But when non-uniform areas are in question then the best predictor appears to be the maximum height of the roughness elements. Although no single surface roughness metric appeared to be universally adequate, Nield et al. (2013) show that all metrics that include some sort of height measurement can sufficiently predict z_0.

2.3.2.1 Impediments in shallow flow

Von Karman's logarithmic velocity profile provides a good representation of the flow field when the height of the roughness element is much smaller than the flow depth. However, its application is problematic in cases where the height of the roughness elements is comparable or even greater that the flow depth (Katul et al., 2002). This is very common in shallow water flows, or flows through fully or partly submerged vegetation. In deep flows, the flow is dominated by skin friction drag, but in the latter case it is the form drag that governs flow behaviour, associated with the wake triggered by the presence of large-scale roughness elements (Powell, 2014). Therefore, an alternative to the classic boundary layer theory is required for the study of shallow flows.

One such alternative is the mixing layer model described by Katul et al. (2002), based on the examples of turbulent flow over terrestrial canopies of Raupach et al. (1996). When the flow depth is comparable to the protrusion height of the roughness elements, the velocity profile is 'S'-shaped with the inflection point being above the roughness element, as shown in Figure2.7. Subsequently, Katul et al. (2002) calculate the vertical velocity profile using equation (20):

$$\frac{U_z}{U_{ref}} = 1 + \tan h\left(\frac{z - D}{L_s}\right) \tag{2.20}$$

where U_z is the mean flow velocity at distance z from the bed, U_{ref} is the reference velocity which is the velocity at distance $z = D_{84}$ (D_{84} is the mean grain diameter of the 84% finer sediment), h is the flow depth and L_s is the mixing length for a given particle size D.

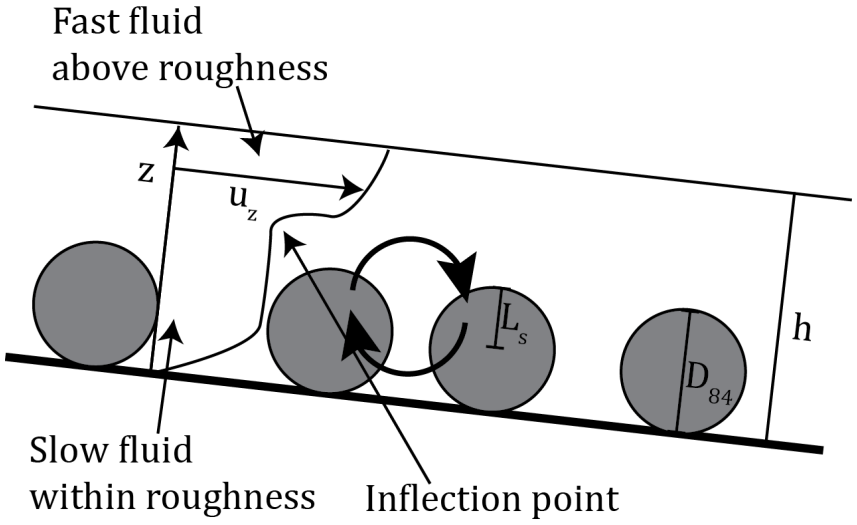

FIGURE 2.7: Velocity profile developed in the case of shallow flow with large roughness elements. The flow between the roughness elements is significantly slower than the flow above, resulting to an 'S'-shaped velocity profile and a mixing layer characterised by significant turbulence (after Katul et al., 2002).

Alternatively, velocity and stress distributions near the boundary may be explicitly accounted through applications of the Navier-Stokes equations. Specifically, the double averaged type of the Navier-Stokes equations (Raupach and Shaw, 1982; Wilson and Shaw, 1977) introduces three terms describing flow resistance arising from skin drag, form drag and stresses due to spatial variations in the flow field (Powell, 2014).

2.3.2.2 The spatial arrangement of the roughness elements

Another parameter that must be taken into account when investigating the relation between surface and boundary layer roughness is the spatial arrangement of the roughness elements. This should be considered not only in relation to surrounding roughness features but also in relation to the flow direction, due to the geometric anisotropy of most roughness elements (Smith, 2014). Regarding the spacing between members of a sequence of protruding obstacles, Morris (1955) identified three individual cases, namely isolated roughness flow, wake interference flow and skimming flow (Figure 2.8). In the first case (Figure 2.8, a) the distance between subsequent roughness elements is large enough to allow for wake attenuation. Each roughness feature is isolated and remains unaffected by the wake developed by the existence of the upstream obstacle. As the distance between subsequent roughness elements decreases (Figure 2.8, b), the wake region affects the interactions between flow and subsequent roughness feature downstream. But the characteristics of the wake are strongly related to the geometric characteristics of the roughness element that produces it. This means that a small obstacle immediately downstream of a large one will be affected significantly by the wake product (Figure 2.8, b. ii), conversely the existence of a small roughness element upstream of a large one will create a small wake that will have an insignificant effect to the larger element downstream (Figure 2.8, b. i) (Kean and Smith, 2006b). In the third case (Figure 2.8, c), the distance between subsequent features is so small that the wake region is significantly suppressed by the roughness elements. This creates skimming flow characterised by stable vortices (Wolfe and Nickling, 1993).

Raupach et al. (1993) define roughness density as a function of the amount (N), breadth (B) and height (H) of the roughness elements and the surface area that they occupy (A_b) (equation (2.21)):

$$\lambda_d = \frac{NBH}{A_b} \tag{2.21}$$

Brown et al. (2008), based on wind tunnel experiments, show that there is a log-linear relationship between roughness density and average drag. This indicates that the key factor governing drag stress is the amount of roughness elements per unit area, regardless of their spatial configuration. However, all of the roughness features used in their experiments was of identical shape and size. This could potentially affect their results as

it is not taking into account the examples of different sized obstacles depicted in Figure 2.8, b.

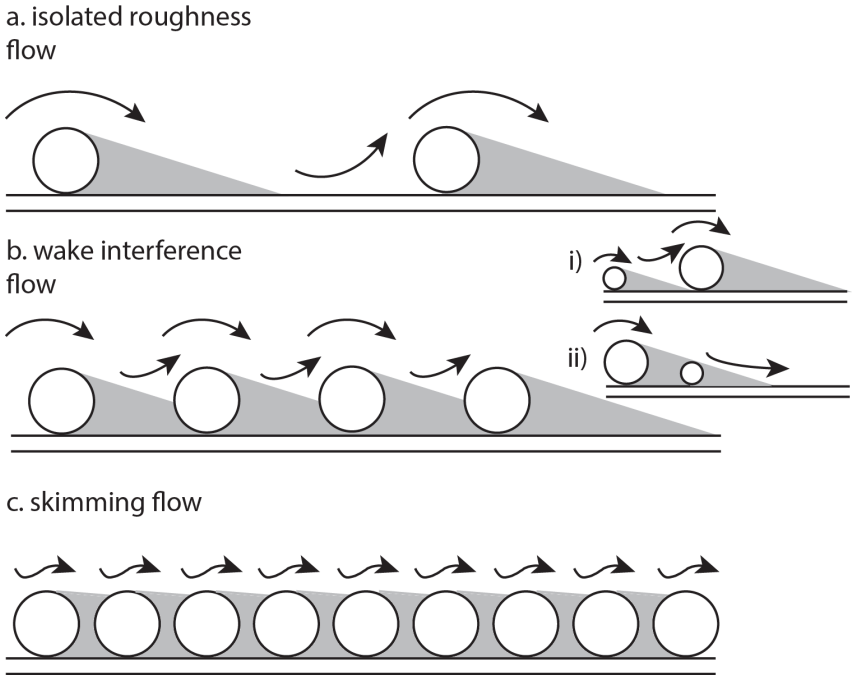

FIGURE 2.8: Sketch showing the types of potential spatial arrangement of roughness elements and resulting wake regions (modified from Wolfe and Nickling, 1993).

2.3.3 Roughness as a modelling parameter

The third use of the term roughness was introduced in Section 2.1.3. It is used in reference to the bulk representation of the cumulative mechanisms that dissipate flow energy and momentum, and are not explicitly accounted for (Morvan et al., 2008; Smith, 2014). Numerical modelling of fluid flows, using the Navier-Stokes equations for example, relies on explicit representations of all individual mechanisms responsible for energy or momentum loss (e.g. turbulence, drag). However, when these equations are simplified into 1 or 2-D equivalents (e.g. the Saint-Venant equations), terms such as the Darcy-Weisbach friction factor, the Manning's coefficient of roughness or the Chézy coefficient of roughness are employed to account for the aggregate of all potential momentum and energy dissipation mechanisms. In this sense roughness is frequently detached from the physical properties of surface or above-surface features, and flow conditions. Instead, it is employed as a means to calibrate numerical models, based on physical experiments (Morvan et al., 2008).

2.3.4 Section summary

Section 2.3 focused on roughness highlighting the pluralism of the term's meanings in relation to fluid flows and their interaction with natural surfaces. Roughness may be

associated with the shape and form of surface and above surface features (subsection 2.3.1). It can be employed as a surrogate for the estimation of energy and momentum loss in fluid flows (subsection 2.3.2) or it can be used as a tuning parameter calibrating numerical modelling results to physically measured flow attributes (subsection 2.3.3). This pluralism is accompanied by ambiguous definitions and unclear boundaries for the different meanings of roughness. As a surface parameter and thus as a flow property, roughness is highly scale dependent. The appropriate scale is determined based on the size of the features of interest and the resolution capabilities of available measuring methods.

2.4 Chapter summary

The present Chapter introduced the broad background theory governing fluid flow and its interaction with the Earth's surface. Section 2.1 highlighted the fundamental principles governing fluid mechanics and the numerical modelling of fluid flows, Section 2.2 outlined the boundary layer theory that describes the interactions between fluids and solid surfaces while Section 2.3 dealt with the characterisation of surface properties that affect flow. Chapter 3 below will focus and elaborate on the specific, but widespread, case where water flows encounter and interact with vegetation elements, which is of relevance to this research.

Chapter 3

Introduction to the Hydraulics of Flow through Vegetation

Plants cover many natural surfaces fully or partially and function as large-scale, flexible obstacles affecting flow characteristics such as large scale turbulence and the structure of the boundary layer. Previous studies have attempted to characterise vegetative roughness and relate it to flow measurements. However, a comprehensive understanding of the effects of vegetation on surface water flow has been hindered by the diverse and complex structure of natural plants.

3.1 Bulk parameters for the vegetative roughness

A number of attempts to incorporate the effect of vegetation in flow models rely on bulk parameters, such as the Manning's roughness coefficient (n). Cowan (1956) developed one of the earliest mathematical models introducing the vegetation effect in the flow pattern in an explicit way:

$$n = (n_0 + n_1 + n_2 + n_3 + n_{veg})m_s \tag{3.1}$$

In the above equation n is the total Manning's roughness coefficient for a vegetated channel calculated as a function of the channel's sinuosity (m_s) and the aggregate of various roughness values, each one accounting for a different type of external interference. n_0 is the Manning's roughness coefficient if the channel was straight, smooth and uniform, n_1 represents surface irregularities, n_2 accounts for variations on the shape and size of the channel's cross-section, n_3 accounts for other obstructions and n_{veg} incorporates the effect of vegetation.

Cowan's model generated an interest of estimating the vegetative roughness component from field measurements. Acknowledging that plants essentially function as obstructions

blocking part of the flow, n_{veg} has often been estimated using a blockage factor. For example, Huntington and Whitehead (1992) proposed the estimation of n_{veg} using an experimental formula:

$$n_{veg} = 0.037 + 0.0239\frac{B^A}{UR_h} \tag{3.2}$$

Here R_h is the hydraulic radius, U is the mean flow velocity and B^A is the surface area blockage factor which is the proportion of the reach surface area covered by vegetation. The authors also proposed alternative ways of estimating the blockage factor by using a volume ratio instead of the surface area ratio, but they concluded that from a practical perspective the surface area is the easiest to measure. However, as Green (2005) points out, when the surface area is used in the blockage factor of Equation (3.2), the effect of water depth and blockage variations along the vertical dimensions are neglected. Therefore, they propose the use of the volumetric (B^V) or a cross-sectional ($B^X = A_{c,p}/A_{c,tot}$) blockage factor, where $A_{c,p}$ is the area covered by plants in a cross-section and $A_{c,tot}$ is the total cross-sectional area. Based on field measurements, (Green, 2005) supports the use of B^X because Equation (3.3) showed the highest correlation (R^2=0.658)

$$n_{veg} = 0.0043B^X - 0.0497 \tag{3.3}$$

Equations that relate a Manning's value with some vegetation characteristic, such as the examples of Equations (3.2) and (3.3), are empirically derived and based on measurements with a finite number of vegetation types. Therefore, they are unlikely to be accurate for dissimilar plant species and should be carefully used. Moreover, Equation (3.3) would yield a negative result for n_{veg} if all vegetation was completely removed from the reach.

3.2 Effects of vegetation on the velocity profile

Numerous studies have employed boundary layer theory and roughness height to describe the velocity profile for vegetated flows. These efforts employ modified versions of Von Karman's law of the wall (Equation (2.18)) that incorporate the plant height (*e.g.* Plate and Quraishi, 1965; Kouwen et al., 1969; El-Hakim and Salama, 1992; Stephan and Gutknecht, 2002). However, using the plant height in the logarithmic law implies a zero velocity between the vegetation elements. This approximation may be acceptable for large scale studies (e.g. when looking at the atmospheric boundary layer) but it is not appropriate for finer scales where plant height and flow depth are comparable, and the plant significantly affects the flow velocity profile. In these cases the mixing layer

approach (see also 2.3.2.1) seems to be a more appropriate alternative and is discussed herein.

3.2.1 Structure of the vegetative velocity profile

When a flowing fluid encounters fully submerged vegetation, the flow field can be divided into two regions; a fast moving region above the vegetation elements where the velocity profile is logarithmic and a slow moving one below, governed by the wake-induced drag force. The product of these two regions is a mixing layer profile, originally introduced by Raupach et al. (1996). The fast and slow regions are joined at the inflection point. The zone surrounding the inflection point is characterised by high shear due to great difference in the flow velocity above and below the inflection point. This leads to significant turbulence propagating through Kelvin-Helmholtz (K-H) instability (Ghisalberti and Nepf, 2002). The large-scale vortices developed through the K-H instability grow downstream and infiltrate between the vegetation elements by δ_e until they reach their maximum size (Figure 3.1). This is achieved when the dissipation of turbulent kinetic energy into the canopy and production at the shear layer become equal (Ghisalberti and Nepf, 2004).

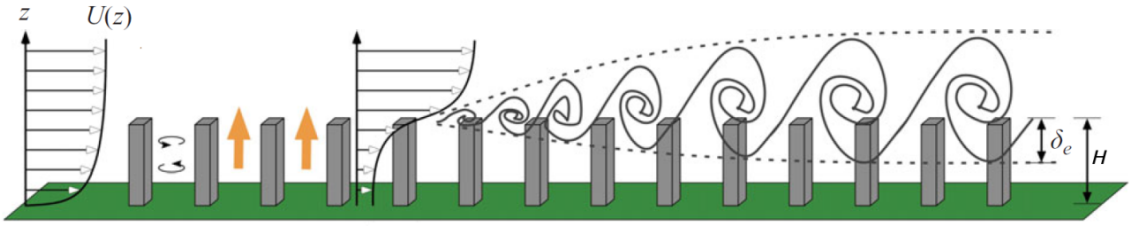

FIGURE 3.1: Mean flow velocity profile over roughness elements of height H. Showing the development of Kelvin-Helmholtz instability vortices infiltrating through the roughness elements by distance δ_e (Source: Figure 3 from Ghisalberti, 2009).

The penetration of the vegetated region by the large-scale K-H vortices means that the slow moving region of the flow may be further partitioned into two sub-layers. One close to the upper vegetation boundary, affected by the wake-induced drag force due to the presence of vegetation and also by the shear-scale vortices, and one close to the surface where the flow field is primarily affected by the vegetative drag (Figure 3.2).

The fast moving region is following the logarithmic law of the wall. But this requires equilibrium between turbulence production (due to the vegetation right below) and dissipation (due to viscosity effects). This condition is not satisfied immediately above the upper vegetation boundary, but some distance is required instead. The zone between the upper vegetation boundary and the height of equilibrium is called the roughness sub-layer (Figure 3.2) (Nepf and Ghisalberti, 2008). In cases where the vegetation is fully submerged but its height is comparable to the flow depth, the upper, logarithmic, zone of the fast moving region cannot be developed and the roughness sub-layer extends to the flow surface (Nepf and Vivoni, 2000).

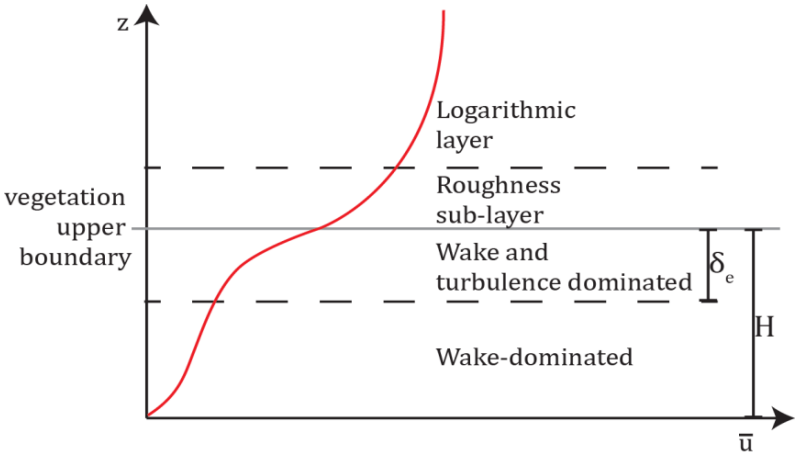

FIGURE 3.2: Mean velocity profile affected by the presence of fully submerged vegetation of height H (after Nepf and Ghisalberti, 2008).

In cases of emergent vegetation, the mean velocity profile is dominated by the drag force emanating from the vegetation elements (Nepf, 1999). Wakes are developed on the lee of the plant elements generating vortices at the stem scale which convert form drag to turbulent kinetic energy while all skin drag quickly dissipates into heat (Nepf, 2012). The form drag is directly related to the geometric characteristics of the protruding obstacle (see 2.2.2). Therefore, the mean flow velocity varies with height, following the variation of the form drag which in turn is the product of the varying plant geometry. Figure 3.3 shows such an example sketch where the plant geometry, characterised using a ratio of frontal area per volume (α), affects the vertical variation of the longitudinal velocity ($\langle\bar{u}\rangle$).

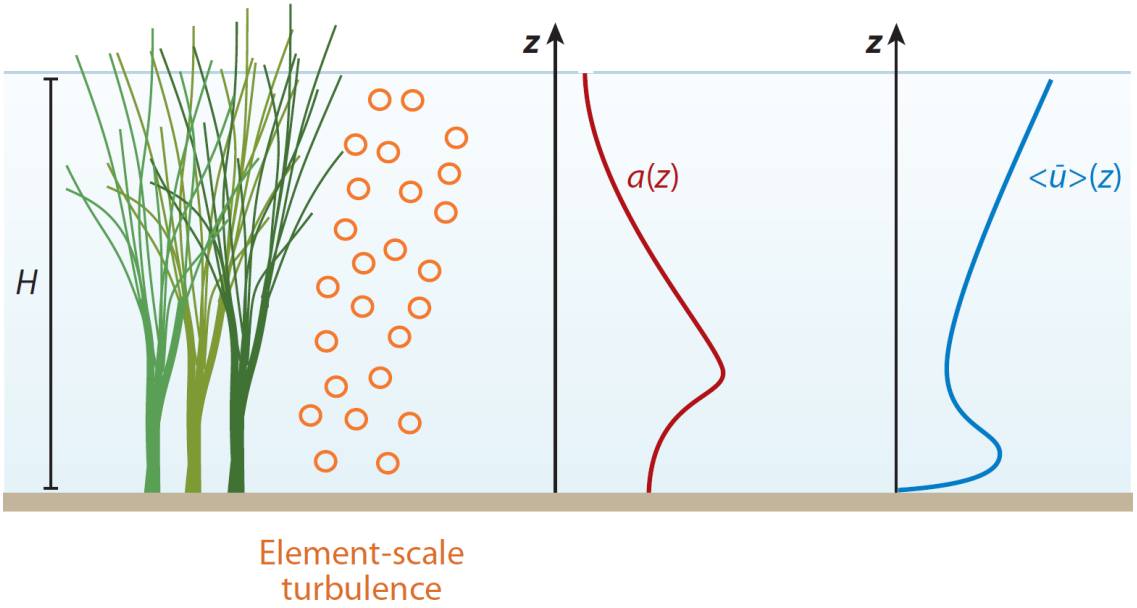

FIGURE 3.3: Schematic showing emergent plant with the vertical profile of frontal area per volume (α) and longitudinal velocity ($\langle\bar{u}\rangle$). The velocity profile varies with height, due to the variation of the plant geometry (Source: Figure 1 from Nepf, 2012).

3.3 Estimating vegetative drag based on the physical characteristics of plants

As highlighted in subsection 3.2.1, the estimation of the drag force exerted by plants is of crucial importance for vegetated flows. The hurdle in this approach lies in the high complexity and diversity of natural vegetation; making it difficult to establish a universally accepted attribute as a key factor influencing the velocity profile. Vegetation density, diameter, shape, flexibility, orientation, concentration and submergence all play an important role (Bennett et al., 2008). Moreover, different vegetation types and their combinations have effects of different magnitudes on the flow field (Järvelä, 2002b).

3.3.1 Modelling vegetation elements using simple, rigid, geometric objects

The simplest method of modelling vegetation elements relies on the use of solid elements of simple geometry. For example, Griffin et al. (2005) modelled vegetation stems as rigid, vertical cylinders and estimated the drag force exerted by a stem by adapting the drag equation to their cylindrical analogy:

$$F_D = \frac{1}{2}\rho U_{ref}^2 C_D \left(\frac{\overline{D_s}}{\lambda_s^2}\right) \tag{3.4}$$

here U_{ref} is the velocity if the element was removed from the flow, C_D is the drag coefficient, $\overline{D_s}$ is the cylinder diameter, equal to the mean stem diameter, and λ_s is the stem density. A similar approach was followed by Manners et al. (2013) who derived vegetation metrics, using TLS data, based on a cylinder analogy. A rigid cylinder analogy was also used by Raupach (1992) and Raupach et al. (1993), who estimated roughness density from the height and breadth of their cylindrical approximations using Equation (2.21).

Modelling plants using rigid objects of simple geometry is a useful approach permitting the direct estimation of drag using Equation (3.4). However, it is based on three important assumptions. Firstly, that the plants are solid and therefore there is no flow between individual stems or leaves. Secondly, that the vegetation's breadth is constant regardless of height. Thirdly, that the vegetation elements are rigid. These assumptions may be true in limited cases of natural conditions, such as a flow through large, woody, vertical vegetation elements (e.g. tree trunks). However, in most natural settings, vegetation is comprised of either a mixture of rigid (e.g. main stem) and flexible (e.g. foliage, small branches) parts, or flexible parts only (e.g. grass). Vegetation's flexibility means that under the flow influence it will reconfigure, changing its geometry and therefore exerting a different amount of drag force.

3.3.2 Accounting for vegetation's biomechanical properties

As previously mentioned, in many cases natural vegetation is, at least partly, flexible. The flow kinetic energy dissipates through the bending, swaying and fluttering of leaves, needles, or even stems, because these activities absorb a portion of the flow momentum (Gillies et al., 2002). When flexible plants encounter large-scale K-H vortices they move in a wave-like pattern. This behaviour was first described by Inoue (1955) for terrestrial vegetation and called 'honami'. Later the mechanism was adopted for aquatic plants from Ackerman and Okubo (1993) and was dubbed 'monami' for differentiation. Although honami and monami differ because of variations in the biomechanical properties of terrestrial and aquatic plants, nevertheless, they are essentially the product of the same mechanism. As the K-H vortices encounter vegetation, the flexible plants bend parallel to the flow direction due to an increase in pressure. This converts part of the flow turbulent kinetic energy to potential elastic energy in the form of stem strain. As a vortex passes over the bended plant, the plant releases part of the stored elastic potential energy moving in the opposite to the flow direction. This movement exerts a drag force to the flow thus converting the elastic potential energy to turbulent kinetic energy. This mechanism is very important as it assists the dissipation of the turbulent kinetic energy from the shear layer. Based on previous observations with rigid and flexible models of vegetation, Nepf and Ghisalberti (2008) suggest that rigid plants produce larger K-H vortices that rotate faster than the ones produced by flexible ones.

Vogel (1984, 1989) introduced an exponent (χ) relating the form drag exerted by a plant to flow velocity as well as the plant's flexibility:

$$F_D \propto U^{2+\chi} \tag{3.5}$$

For a rigid vegetation element the Vogel exponent is equal to zero and from Equation (3.5) the form drag is analogous to the square of the flow velocity. For all other cases its value is negative and decreases with increased flexibility. The Vogel exponent was adapted by Järvelä (2004), who calculates the resistance exerted by a plant in terms of the Darcy-Weisbach friction factor using:

$$f_{veg} = 4C_{D\chi}LAI\left(\frac{U}{U_\chi}\right)^{\chi}\frac{h}{H} \tag{3.6}$$

where the Vogel exponent (χ) and the drag coefficient ($C_{D\chi}$) are species specific, LAI is the leaf area index defined as $LAI = \dfrac{A_L}{A_b}$ with A_L being the one-sided area of foliage and A_b being the ground unit area. h is the flow depth and H the height of the plant. Finally U_χ is the lowest velocity, used to determine the value of χ. The ratio $\dfrac{h}{H}$ accounts for the level of submergence; for a fully submerged plant it is equal to 1 and can be discarded, for emergent plants it assumes a linear increase of LAI with height.

Västilä and Järvelä (2014) further developed Järvelä's model. They assume that the drag forces exerted by the vegetation's stems and foliage follow a linear superposition principle written in terms of Darcy-Weisbach friction factor as

$$f_{veg_T} = f_{veg_S} + f_{veg_F} \tag{3.7}$$

where f_{veg_S} is the friction factor allocated to the rigid stems, f_{veg_F} is allocated to the flexible foliage and f_{veg_T} is the total friction factor for the plant. Each one of the components of the right side of Equation (3.7) can be written using Equation (3.6). Then the friction factor for the plant's foliage is given by:

$$f_{veg_F} = 4C_{D\chi F}\frac{A_L}{A_b}\left(\frac{U}{U_{\chi F}}\right)^{\chi F} \tag{3.8}$$

The friction factor for the plant stems is calculated with:

$$f_{veg_S} = 4C_{D\chi S}\frac{A_S}{A_b}\left(\frac{U}{U_{\chi S}}\right)^{\chi S} \tag{3.9}$$

where the $LAI = \frac{A_L}{A_b}$ term is replaced by the stem frontal area index given by $\frac{A_S}{A_b}$, with A_S being the stem area. This yields Equation (3.10) calculating the friction factor for the plant:

$$f_{veg_T} = \frac{4}{A_b}\left[A_L C_{D\chi F}\left(\frac{U}{U_{\chi F}}\right)^{\chi F} + A_S C_{D\chi S}\left(\frac{U}{U_{\chi S}}\right)^{\chi S}\right] \tag{3.10}$$

Equation (3.10), allows for the partitioning of the stem and foliage originating resistance to the flow. The total resistance of a plant (f_{veg_T}) may be measured using laboratory or field data. Defoliating the plant and repeating the measurements allows for the direct measurement of f_{veg_S} and the indirect estimation of f_{veg_F} from Equation (3.7). Subsequently, f_{veg_T}, f_{veg_S} and f_{veg_F} can be estimated for other plants of the same species incorporating measurements of A_b, A_L and A_S in Equation (3.10). Although the method developed by Västilä and Järvelä (2014) employs a bulk roughness parameter, it is useful as it does not treat the plant as a homogeneous bluff object, but instead as an aggregate of rigid and flexible elements that react differently under the flow influence. However, plant biomechanical properties are not only species-specific, but also vary with plant age and environmental parameters. Therefore, care must be taken when this model is widely applied to multiple plants, even of the same species. Moreover, as the authors point out, the model is designed for individual plants and therefore, the effect of wake shading from neighbouring plants (see 2.3.2.2) is not accounted for.

3.3.3 Modelling vegetation elements as porous media

An alternative way of modelling the complex geometry of natural vegetation is using a porous medium approach. The relationship between an object's porosity and exerted drag force has been extensively studied through two-dimensional approaches, mostly related to the effectiveness of porous windbreak fences (*e.g.* Perera, 1981; Borges and Viegas, 1988; Raju et al., 1988; Lee and Park, 1998). However, it has also been applied in studies focusing on vegetation-flow interactions.

Grant and Nickling (1998) distinguish between two different porosity metrics, namely optical porosity (OP) and volumetric porosity (VP). The former is a two dimensional measure related to plant frontal area and the latter is a three dimensional measure related to plant volume. According to the authors, who used an artificial scotch pine, the two metrics are strongly correlated (R^2=0.996). However, the relation that they propose is unlikely to be applicable for plants of different species of varying structure and size. The underlying problem when using a 2D porosity estimate, such as the optical porosity of Grant and Nickling, is the assumption that the flow direction concurs with the line of sight connecting the plant and point of observation. In other words, it assumes that the flow 'sees' what the observer saw when they estimated the plant's porosity. Nevertheless, the authors demonstrate that if a plant is modelled as a porous medium, the drag coefficient (C_D), is quite different to that of a solid object of equivalent shape and size. In more detail, their findings show an increase in the drag coefficient with increasing porosity values until a threshold is reached, after which any further increase in porosity results in a decrease in the value of the drag coefficient. This behaviour is reasonable if the porous plant is thought of as an aggregate of many bluff obstacles (e.g. leaves, branches) the wakes of which are interfering with the downstream obstacles. Such an aggregate will exert a greater drag force to the flow compared to a solid body. However, as the plant's porosity becomes greater, an increasing part of the flow passes through the plant without being interfered by wakes and thus without losing momentum.

A porosity approach has been also adopted by Hoffmann (2004) who estimated porosity using vegetation's structural parameters and coupled his porosity term into a computational flow model. Shucksmith et al. (2011) estimate porosity for a vegetated flume using the ratio $PlantArea/FlowArea$. But their plant measurement is based on an average plant stem diameter. In other words, instead of estimating the porosity of their flume based on the actual plants, they use cylindrical analogues. Nevertheless, the authors show that there is a strong relationship between porosity and drag coefficient.

A consideration about porosity applications is that, as discussed in subsection 3.3.2, plants tend to reconfigure under the flow influence reducing their frontal area. This means that values of porosity are likely to vary under different flow velocities. Gillies et al. (2002) found that normalising the OP values using the still air OP value, significantly improved the accuracy of their drag coefficient estimates. A second consideration is in regards to plant shape and structure. If porosity is calculated as a

single value of an individual plant aggregate, then variations of plant structure and configuration (for example at various heights) are disregarded. This means that various plant types with dissimilar structures may yield similar porosity estimates. These average porosities can only be related to average flow attributes, inhibiting the in depth study of flow variation at finer scales.

3.4 Physical modelling of surface water flow through vegetation

Efforts to develop the background theory that governs vegetation-flow interactions (outlined in sections 3.1-3.3) have been frequently based on physical modelling experiments. These experiments are usually undertaken in artificial channels (flumes). Flumes allow for the various flow attributes such as discharge, flow velocity, flow depth and channel bed slope to be carefully measured and adjusted with the use of pumps, valves and tailgates, in conjunction with monitoring equipment such as flow velocimeters and water surface recorders.

3.4.1 Representing vegetation in flumes

In physical modelling experiments the role of vegetation has been commonly represented by cylindrical analogues. Nepf (1999) represented vegetation in her laboratory experiments using arrays of wooden cylindrical dowels. Rigid cylindrical dowels as vegetation surrogates have also been used by Nepf and Koch (1999), Ghisalberti and Nepf (2006), Tanino and Nepf (2008), Malcangio and Mossa (2016), Zhao et al. (2016) and Yan et al. (2016), among others. Although the employment of rigid cylindrical surrogates in physical modelling experiments is a good starting point, as previously discussed in subsection 3.3.1, a cylindrical analogy neglects vegetation's structure and biomechanical properties and as such it might be an oversimplification of the mechanics. To assess this, Chapman et al. (2015) compare the drag forces measured in a flume with rigid cylindrical dowels and flexible ones. They employ Young's modulus of elasticity (E) to account for the deformation of their surrogates and compare it with values calculated using Vogel's exponent (see also 3.3.2). They conclude that flexible bluff bodies are exposed to different drag forces in comparison to rigid bluff bodies of identical shape and size. They also argue that the employment of Young's modulus of elasticity provides more consistent results than the ones obtained using Vogel's exponent.

A different approach to represent vegetation in physical models is by the use of real plants. For example, Fathi-Maghadam and Kouwen (1997) used pine and cedar saplings because of their symmetry, stiffness and resistance to withering during testing. Järvelä (2002b) employed sedges (*Carex acuta*), willows (*Salix sp.*) and grasses which were placed in a flume using different combinations and densities. Stephan and Gutknecht

(2002) used three types of real aquatic macrophytes (*Ranunculus trichophyllus*, *Groenlandia densa L.* and *Berula erecta*) collected from a small river situated near their laboratory and positioned inside the flume in an arrangement similar to what they observed at the collection site. Yagci and Kabdasli (2008) classify vegetation using the volume/height ratio and chose three species that fall into three different categories; *Pinus Pinea*, *Thuja Orientalis* and *Cupressus Macrocarpa*. Shucksmith et al. (2011) conducted flume experiments with two semiaquatic vegetation species, common reed (*Phragmites australis*) and *Carex*. They planted the selected species in two identical channels in staggered rows using a spacing similar to the plants' spacing in nature. Västilä and Järvelä (2014) used four woody vegetation species; common osier (*Salix viminalis*), hybrid crack willow (*Salix x rubens*), common alder (*Alnus glutinosa*) and silver birch (*Betula pendula*). The saplings were collected randomly and stored in water until they were used.

Using real plants in physical modelling experiments is a much more realistic approach in comparison to the employment of cylindrical analogues, as it allows replication of the structural and biomechanical plant properties. However, plant husbandry in hydraulic laboratories can be a very demanding process. The environmental conditions in hydraulic laboratories (i.e. water salinity, temperature, light and nutrient concentration) are frequently dissimilar to the natural environmental conditions (Frostick et al., 2014). This means that plants might be under stress which will affect their biomechanical properties. For example Stephan and Gutknecht (2002) report that during their experiments plants would decay within 7-10 days and could not be used after that period. But plant biomechanical properties, such as stiffness, may be altered due to plant stress before any visual signs of decay are observed. On the other hand, subjecting plants to optimal conditions would lead to thriving organisms which seldom occur in nature (Frostick et al., 2014). Therefore, it is important to take into account all factors affecting plant stress, aiming to reflect the variability of environmental variables occurring in natural systems. Although methods for measuring plant stress have been established, these protocols have not been adopted yet in ecohydraulic studies. This means that it is uncertain if the plant biomechanical properties, and their effects on surface water flow, observed during ecohydraulic experiments, replicate reality.

An alternative to the problems arising by the usage of real plants may be the employment of realistic plant surrogates. Nepf and Vivoni (2000) employed flexible seagrass surrogates fabricated from thick vinyl plastic blades with similar geometry and flexural rigidity to aquatic vegetation. Lee et al. (2001) used nylon ribbons to mimic seagrass (*Zostera japonica*). Vionnet et al. (2004) used plastic ornamental plants to replicate the effects of flexible vegetation. Folkard (2005) fabricated artificial seagrass (*Posidonia oceanica*) using polyethylene sheeting of similar dimensions, density and elasticity to real samples. Ghisalberti and Nepf (2006) fabricated flexible seagrass-like blades from wooden dowels and thin strips of polyethylene film. They modelled their surrogates after eelgrass (*Zostera Marina*) and chose the blade thickness accordingly so

that they would accurately mimic the motion of real seagrass. A similar seagrass surrogate was also employed by Le Bouteiller and Venditti (2015). Wilson et al. (2003) designed artificial plant prototypes fabricated from flexible rods to which they attached frond foliage. Their simulated plants were 1/10 scale replicas of kelp (*Laminaria Hyperborean*) and both plant geometric and kinematic parameters were scaled using the Froude law. Artificial plastic plants have also been used by Fathi-Maghadam et al. (2011) to replicate shrubs and hedges commonly grown in rivers and floodplains.

3.4.2 Measuring flow characteristics during physical modelling experiments

Typical measurements involved in ecohydraulic experiments include flow discharge, stage, flow velocity and form drag. Discharge is either measured directly using weirs or calculated, using Equation (3.11), from the flume cross-sectional area (A_c), which can be measured directly, and the average flow velocity ($\overline{U}$), which can be estimated by velocity measurements

$$Q = A_c \times \overline{U} \tag{3.11}$$

Stage can be measured directly using, point gauges (*e.g.* Rhee et al., 2008), resistance-type water surface recorders (*e.g.* Nepf, 1999) or ultrasonic distance recorders (see 6.1.3.5).

A plethora of techniques for measuring flow velocity have been employed in previous ecohydraulic studies, including flowmeters (*e.g.* Fathi-Maghadam and Kouwen, 1997), Acoustic Doppler Velocimetry (ADV) (*e.g.* Nepf, 1999; Nepf and Vivoni, 2000; Wilson et al., 2003; Yagci and Kabdasli, 2008), Laser Doppler Anemometry/Velocimetry (LDA) (*e.g.* Nepf, 1999; Nepf and Vivoni, 2000), Particle Image Velocimetry (PIV) (*e.g.* Moulin et al., 2007; Tinoco and Cowen, 2009), Hot Film/Wire Anemometry (HFA/HWA) (*e.g.* Biggs et al., 1998). The method used in this study is Acoustic Doppler Velocimetry and is further discussed in Chapter 6 (6.1.1.1) (for an extensive review of the techniques for flow velocity measurement see (Frostick et al., 2014 pp. 50-67).

The methods for estimating drag can be classified to direct and indirect. Direct methods rely on bespoke apparatus that directly measures the force applied to a vegetation element that is mounted on it. Examples include the system load cells designed by Fathi-Maghadam and Kouwen (1997) and the force drag plate designed by Tinoco and Cowen (2013). Indirect methods rely on estimation of drag from other flow parameters that can be obtained from standard flow measurements. For example Nepf (1999) measured water surface elevation upstream and downstream of an array of modelled vegetation elements and calculated water surface slope $\partial h/\partial x$, where h is the flow depth and x the distance between the location of the two measurements. This is then used to

estimate the total bulk drug of the flume section. Calibrating these measurements with base measurements obtained without any modelled vegetation arrays in the flume provided the bulk drag of the modelled vegetation array.

3.5 Chapter summary

The effect of vegetation on fluid flow dynamics is directly related to the form and structure of plants. Various approaches have been employed in attempts to describe the relationship between flow attributes and vegetation characteristics, all of which have significant advantages and limitations. Vegetative drag can be estimated using bulk parameters, through geometric analogies, or by using a porous medium approach. Regardless of method of choice, it is important that vegetation structure is accurately and precisely measured and discretised to enable better interpretations of ecogeomorphic relationships. However, this is difficult due to the high complexity and diversity of natural plants coupled with a historical lack of appropriate survey methods. Chapter 4 will review the state of the art in surveying methods and explore their potential applications in flows through vegetation.

Chapter 4

Survey Methods for the Characterisation of Vegetation

4.1 Introduction

Over the last two decades our ability to acquire measurements that describe surface and above-surface features has been revolutionised because of technological advances in both instruments and associated processing software (Brasington et al., 2012). A plethora of survey techniques have emerged and continue to develop, allowing for the collection of data over large areas at high resolution. However, there is still a trade-off to be made between resolution and coverage. Figure 4.1 shows the typical extent and resolution that various survey techniques are capable of delivering, and their applicability in measuring landforms of various scales. Surveying of above-surface features, such as vegetation, requires those techniques capable of achieving ultra-high resolution, while it is less reliant on maximum coverage. Therefore, this review of survey methods focuses on terrestrial photogrammetry and terrestrial laser scanning.

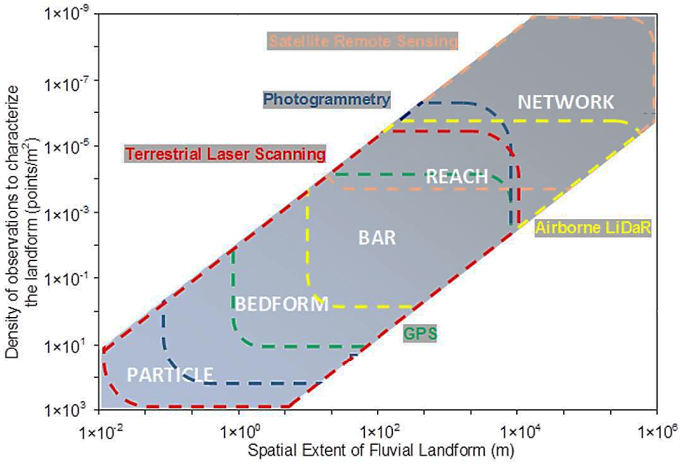

FIGURE 4.1: Coverage and density (resolution) of different survey techniques and their applicability in fluvial landforms (Source: Figure 1 from Brasington et al., 2012).

4.2 Photogrammetry

The field of photogrammetry includes a range of techniques aiming to obtain measurements, such as exact position of points, from photographs (ITC., 2011). Photogrammetric surveys can be distinguished to aerial and terrestrial. The former are conducted from airborne platforms, such as aeroplanes, helicopters and more recently unmanned aerial vehicles (UAVs), the latter are conducted from the ground level. Both approaches rely on the acquisition of overlapping imagery of features and surfaces allowing for their stereoscopic representation.

A recent development in photogrammetric techniques is Structure-from-Motion (SfM). Similarly to other photogrammetric approaches, SfM utilises overlapping images to extract 3D geometries from 2D images. SfM relies on iterations of a bundle adjustment procedure, which identifies features appearing in multiple images for the estimation of the sensor's position and orientation (Westoby et al., 2012). Therefore, external ground control points (GCPs) are not required for scene reconstruction. However, lens distortions, combined with parallel flight paths, produce a significant 'doming' effect in reconstructed scenes (James and Robson, 2014). This can be corrected using GCPs, which are also essential for the geo-location of the reconstructed scenes, pertinent for studies concerned with change detection (for example for the derivation of DEMs of difference [DoDs]). In the next step, the measured image coordinates are transformed to 3D points resulting in a sparse point cloud which can be intensified using multi-view stereo techniques (Micheletti et al., 2015). SfM has two main advantages. Firstly, it does not require specific or expensive equipment. Although a good quality camera is desirable for the acquisition of high quality imagery, consumer-level cameras or even smartphones can be employed to obtain useful data (Micheletti et al., 2014). Secondly, there is a plethora of software capable of conducting the required image processing for the development of 3D models. Some software packages are both fully automated and free to use, either in the form of online platforms (e.g. Autodesk, Photosynth) or desk-based applications (e.g. VisualSFM). On the other hand, a few considerations arise when using SfM techniques, related both to data acquisition and post processing. Firstly, appropriate coverage must be ensured during the photogrammetric survey. Every point within the area of interest must appear in multiple images (three at least). Secondly, consistent light and exposure for the obtained imagery is necessary to produce accurate results during the matching process, but flash photography is not advised because it creates inconsistent textures that may result in errors. Thirdly, a static scene is necessary. A survey protocol with key points has been provided by Micheletti et al. (2014). Because plant elements often move due to wind, the requirement of a static scene might pose a significant limitation when surveying vegetated areas. In regards to processing tools, and especially the fully automated packages mentioned earlier, the limitation lies on the fact that usually they function in a black-box manner, prohibiting any user interference, and thus hindering the quality control of the final product (Micheletti et al., 2015).

4.2.1 Extracting vegetation metrics from imagery

The photogrammetric approaches outlined above, can be useful for the extraction of topographic features which are inherently 2.5D (only a single z-coordinate is assigned to each pair of x,y-coordinates) and usually have simple structure. However, the complex three-dimensional structure of vegetation hinders attempts to reconstruct accurate 3D vegetation models from 2D imagery. Attempts are commonly focused into the production of real-looking but not accurate models, mostly used in computer graphics applications (*e.g.* Shlyakhter et al., 2001; Tan et al., 2007). Nevertheless, other image analysis techniques have been employed to characterise plan attributes and are discussed herein.

A common method employed in forestry studies involves the acquisition of hemispherical or fisheye photographs of trees along a vertical (bottom-up) direction (Figure 4.2). Subsequent analysis of the obtained imagery provides estimates of plant area index, canopy cover or leaf area index of the forest plot (*e.g.* Brown and Forest, 1962; Anderson, 1964; Jones and Campbell, 1979; Lakso, 1980; Chan et al., 1986; Chen et al., 1991).

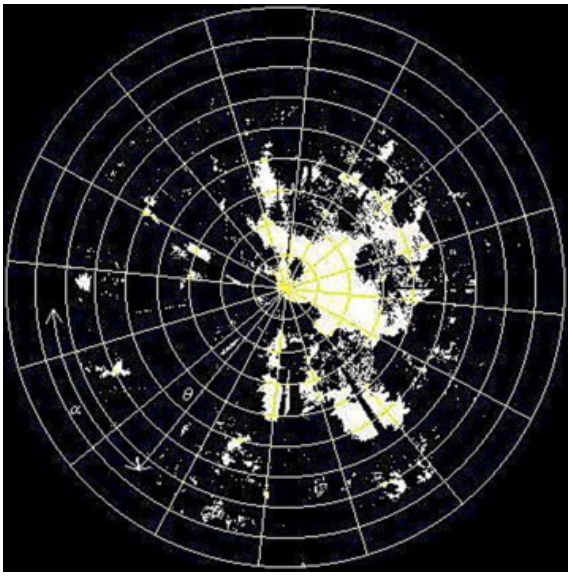

FIGURE 4.2: Hemispherical image of tree canopy divided in angular sectors for further gap fraction analysis (Source: Figure 1 from Montes et al., 2008).

Grant and Nickling (1998) obtained standard black and white photographs of an artificial scots pine positioned in front of a white backdrop. Using Java-based software they converted the images to a binary format and estimated plant porosity by measuring the amount of white pixels within the plant area (Figure 4.3 left). Their method was adopted by Gillies et al. (2000) who obtained multiple images from various positions, allowing for a more complex estimation of plant porosity. Gillies et al. (2002) coupled the method of Grant and Nickling with wind tunnel experiments. Obtaining plant images under various wind velocities provided useful information regarding the effect of plant reconfiguration on porosity estimates. They found a non-linear relationship between wind velocity and plant frontal area. In more detail, for leafy vegetation, a decrease of the plant's frontal

area is observed. However, as the wind velocity increases leaves show a tendency to align themselves with their maximum projected area perpendicular to the flow direction. This leads to higher frontal area estimates which may be higher than the still air values. Further increases of the wind velocity over a threshold forces the plant to a configuration state that is characterised by decreased frontal area. Straatsma et al. (2008) analysed mosaicked images, obtained using parallel photography techniques in front of a high-contrast backdrop, and estimated tree and herbaceous vegetation densities in a floodplain (Figure 4.3 middle and right). The above image analysis techniques are useful because they provide vegetation metrics that can be implemented in the study of vegetation-flow interactions. However, their 2D nature prohibits capturing of the plant structure fully. Additionally, as previously mentioned, a 2D model assumes that the view angle and flow direction coincide, but this is likely not accurate in many cases. An alternative method of data acquisition, capable of capturing the form and structure of features in 3D, is that of terrestrial laser scanning, as discussed further in Section 4.3.

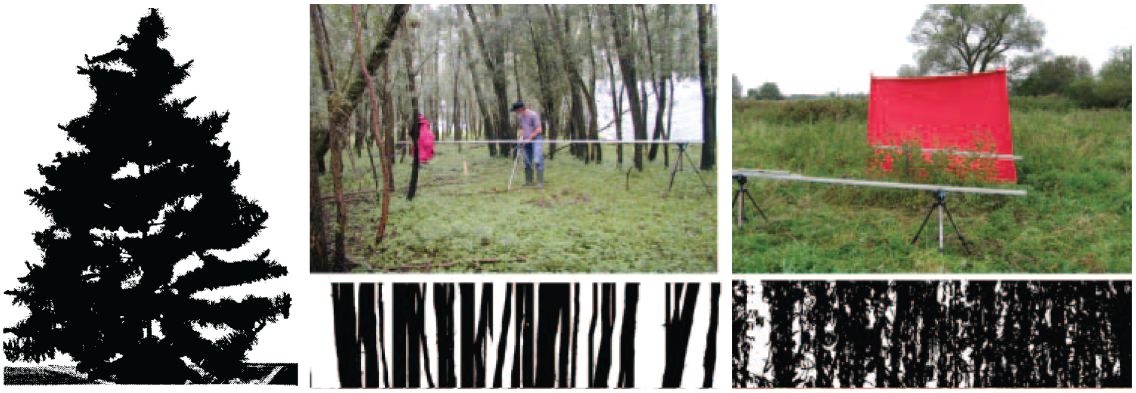

FIGURE 4.3: Binary image of artificial scots pine taken in front of white backdrop. The amount of white pixels within the plant area provides a 2D plant porosity estimate (left) (Source: Figure 3 from Grant and Nickling, 1998). Collection of parallel photography images against a high contrast backdrop for tree (middle) and herbaceous (right) vegetation of a floodplain, and derived binary images (Source: Figure 2 from Straatsma et al., 2008).

4.3 Laser scanning

Laser scanning is a non-invasive, active method of data acquisition. It relies on the fundamental principle that the speed of light in a given medium is constant. Therefore, measuring the time required for an emitted light pulse to travel from a source to a reflective surface and back to a sensor is a convenient way to calculate distance (Vosselman and Maas, 2010).

There are two key types of laser technology that scanners employ, namely pulsed laser and continuous wave (or phase-based) systems (Beraldin et al., 2010). The former emit short, distinct pulses of a single wavelength; subsequently, one or multiple echoes of each pulse are captured and recorded by the scanner receiver. Phase-based systems emit a

continuous laser beam of varying wavelength; the phase difference between emitted and received laser beam provides the time difference and hence the distance between the sensor and the reflective surface.

Laser scanners may be mounted on moving platforms such as aeroplanes or helicopters and cars or boats. In the former case the method is referred to as airborne LiDAR (Light Detection and Ranging) and in the latter is usually called mobile laser scanning (MLS) (Lemmens, 2011). Both airborne LiDAR and MLS require additional inputs regarding the platform's relative position and orientation. This information is obtained simultaneously with the scanning survey using a DGPS (Differential Global Positioning System) and an IMU (Inertial Measurement Unit), respectively (Vosselman and Maas, 2010).

Laser scanners can also be operated from stationary positions. In that case the technique is called terrestrial laser scanning (TLS). Because of its stationary nature and its often relatively shorter range, the extent of the area that a TLS system can cover is limited in comparison to airborne or mobile systems. However, because of the small footprint size of the TLS laser beam and the small angular steps between subsequent pulses, coupled with the lack of movement inherent in mobile systems, TLS has the ability of achieving much higher spatial resolution and of better accuracy, providing datasets of superior detail in comparison to other survey methods (Béland et al., 2014). Recent advances in laser scanning technology have made possible the development of miniature, lightweight laser scanning devices that can be mounted on unmanned aerial vehicles (UAVs) and are available off the shelf (e.g. RIEGL miniVUX-1UAV). Although these new systems are still inferior to standard TLS systems in terms of spatial resolution and accuracy, they show a trend in technological advances that shows a promising potential of bridging the gap between resolution and coverage in the near future. Nevertheless, at the moment TLS remains a particularly suitable approach for measuring the highly complex structure associated with some vegetation and as such TLS is the main method of data capture employed in the present study, and is further discussed herein.

4.3.1 Terrestrial laser scanning

TLS follows the basic laser scanning principles outlined above. The scanner emits a short laser pulse or a continuous laser beam which is reflected from surrounding objects. The instrument's sensor captures the reflected laser echoes, deriving the time-of-flight distance between the object and the scanner. Additionally, the system records the horizontal and vertical scan angles. This, in conjunction with the measured distance, provides the means to calculate the 3D coordinates of the reflected point within an arbitrary 3D coordinate system (Figure 4.4). The procedure is fully automated and repeated at very high speed, enabling the measurement of millions of points in a short amount of time (e.g. the Leica P20 TLS is technically capable of collecting 1M points per second). The obtained data are recorded in the form of 3D point clouds, often characterised by a very

high resolution (mm scale) (Hodge et al., 2009b). The scan survey of a feature or area can be repeated from multiple positions and the individual datasets can be co-registered with the use of tie points. This is typically achieved through a bundle-adjustment algorithm based on a least-squares method, and allows for the complete representation of features in 3D with minimum occlusions and shadowing effects. If the scanner's position is defined in a real-world coordinate system (e.g. using a GPS system) the arbitrary coordinates of the point cloud data can be converted accordingly.

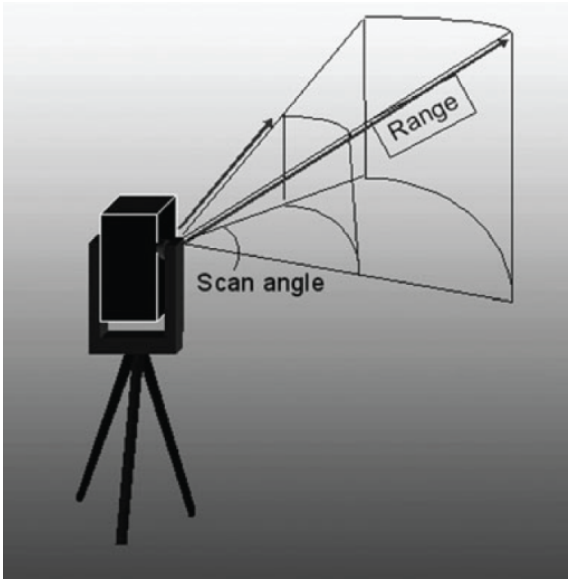

FIGURE 4.4: Sketch showing the principle of TLS measurement. Combination of estimated range, angle and scanner position and orientation allows for the estimation of 3D coordinates of the points reached by the laser beam (Source: Figure 6.2 from Lemmens, 2011).

There are two main types of terrestrial laser scanners in terms of field of view (FOV); window-like and panoramic. Window-like scanners have a fixed rectangular field of view, much like a conventional camera. Panoramic scanners have a field of view of 360^o on the horizontal plane, achieved by the instrument's rotation around its vertical axis. On the vertical plane a wide field of view is achieved through the use of a polygonal, rotating mirror. Combination of the vertical and horizontal rotation means that the scanner is basically limited only by self-occlusions. Examples of the two types of TLS instruments are shown in Figure 4.5.

FIGURE 4.5: Examples of different types of TLS instruments. Optech ILRIS 3D, window-like system with field of view 40^o x 40^o (left); Leica ScanStation C10 with rotating polygonal mirror with field of view 360^o x 270^o (right).

4.3.2 Errors in TLS data

3D point clouds obtained with TLS are prone to a variety of errors which, similar to all survey methods, can be broadly categorised into random, systematic and blunders (Hodge et al., 2009b). Blunders are the result of human error or malfunctioning equipment. They can be constrained by ensuring the good state of all instruments prior to surveying and by following carefully designed survey and data processing protocols. Sources of random and systematic errors in TLS data affect the precision and accuracy of measurement and include instrument design, surface reflectivity and imaging geometry. The resulting errors include angular displacement, mixed pixels, detector saturation, blooming and multipath, all of which are discussed here. The difficulty of quantifying and tackling the receptivity of errors in TLS lies in the lack of independent measurement methods of comparable resolution (Hodge, 2010).

4.3.2.1 Laser footprint size

Because of divergence effects, the laser beam of TLS systems has a conical shape. When it illuminates a surface, it creates a footprint of finite size with the size of the footprint increasing with distance. Regardless of the part of the surface that reflects the emitted light, the point is assigned to the coordinates of the centre of the footprint. This however creates disagreement between the real and the apparent location of a point, leading to an angular displacement. Lichti et al. (2005) demonstrated this effect by scanning a tensioned vertical plumb line with 0.5 mm diameter using a Leica HDS2500. The diameter of the laser footprint for this instrument is approximately 6 mm. The plumb line was illuminated at several sample locations and enough light was reflected in order for its position to be registered, leading to the artefacts presented in Figure 4.6. Essentially the maximum resolution that a scanner is capable of delivering is limited by the footprint size of its laser beam, rather than the sampling interval (minimum point spacing) (Hodge et al., 2009b).

4.3.2.2 Imaging geometry

Mixed pixels are another type of error associated with the footprint size and surface geometry. When the laser beam illuminates two overlapping surfaces, both of them will reflect part of the emitted pulse. If the distance between the two surfaces is less than half of the pulse length, the scanner cannot tell the two apart. In this case the scanner will integrate the two echoes into one, registering the coordinates of a point located somewhere between the two surfaces that were illuminated (Figure 4.7) (Lichti et al., 2005).

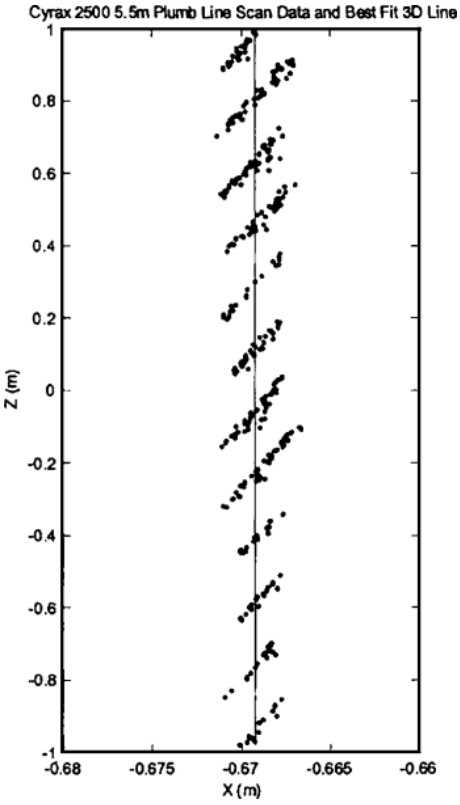

FIGURE 4.6: TLS point cloud obtained by scanning a tensioned vertical plumb line of 2 m length and 0.0005 m diameter, and best-fit 3D line. Used to demonstrate angular displacement errors (Source: Figure 2 from Lichti et al., 2005).

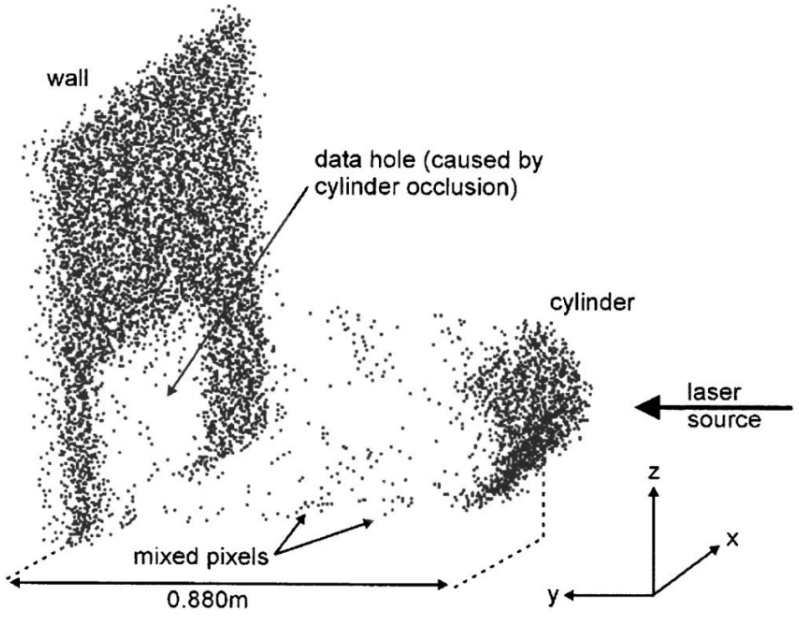

FIGURE 4.7: Example of a TLS point cloud derived from a single scan of a horizontal cylinder placed in front of a wall using a Riegl LMS-Z210 TLS. The pulse length of this instrument (2 m) is larger than the distance between the wall and the cylinder leading to the appearance of mixed pixels. The chosen scanning position also creates a gap in the dataset due to shadowing effects (Source: Figure 4 from Lichti et al., 2005).

4.3.2.3 Surface reflectivity

If a highly reflective area is surveyed from close range, the reflected echo may have higher energy than the detector's dynamic range. In such cases, the detector will be saturated faster from a more reflective part of a surface in comparison to a less reflective one. This will introduce bias on the time of flight estimate, leading to the appearance of trails of points in front and behind the object. Similarly, high object reflectivity in combination with the finite width of the laser footprint may result in a blooming effect were highly reflective objects appear larger in scan datasets. Associated with surface reflectivity is also the effect of multipath. In this case artefacts appear because of backscattered laser light which has been reflected by multiple surfaces before reaching the sensor (Lichti et al., 2005).

4.3.2.4 Shadowing effects

Another parameter that must be considered when conducting TLS surveys has to do with data completeness. When surveying complex scenes, areas may be omitted because of occlusions caused by overlapping features (example presented in Figure 4.7). This is common in vegetated areas where various plant elements are located in front of each other, and constitutes an important limitation of TLS applications to vegetation studies. Currently, the only solution for controlling occlusions is by conducting repeated scans of objects from a variety of locations and angles, although a full coverage is not always achieved (Pueschel, 2013).

4.3.2.5 Error filtering

Removing the artefacts appearing in TLS data is frequently hindered by the lack of comparable validation data. Hodge et al. (2009b) propose scanning the area of interest multiple times from one position before moving to the next. Subsequently, the multiple scan datasets are compared to each other and averaged. Points that do not appear in all datasets are assumed to be erroneous and are discarded. In the next step, the averaged scan data from each scanning position are co-registered which each other with the use of tie points. The authors found that this method is capable of filtering out part of the erroneous points and quantified the error reduction to be approximately $1/\sqrt{m}$ with m being the number of individual scans. However, scanning repeatedly the same area can be laborious and time consuming. Moreover, this method is likely to remove only random erroneous points. Points appearing due to systematic errors are likely to be present in all scan datasets and therefore will not be detected. The authors suggest further point cloud filtering using a cone and a local high point filter. These filters are specifically designed for the derivation of 2.5D surfaces such as DEMs (Digital Elevation Models) and cannot be applied to 3D objects such as vegetation; therefore, they will not

be further discussed. Alternatively, a sparse outlier removal (SOR) filter may be used (Rusu et al., 2008). Because erroneous points appear in sparse, in comparison to true points, aggregates; the filter calculates the distance between each point of the dataset and a user-defined amount of neighbours (k). Assuming that the resultant distribution is Gaussian, a mean (μ) and a standard deviation (σ) of nearest neighbour distances is computed. All points that fall outside the $\mu \pm \alpha \times \sigma$ threshold where α is a user-defined multiplier, are considered as erroneous and discarded.

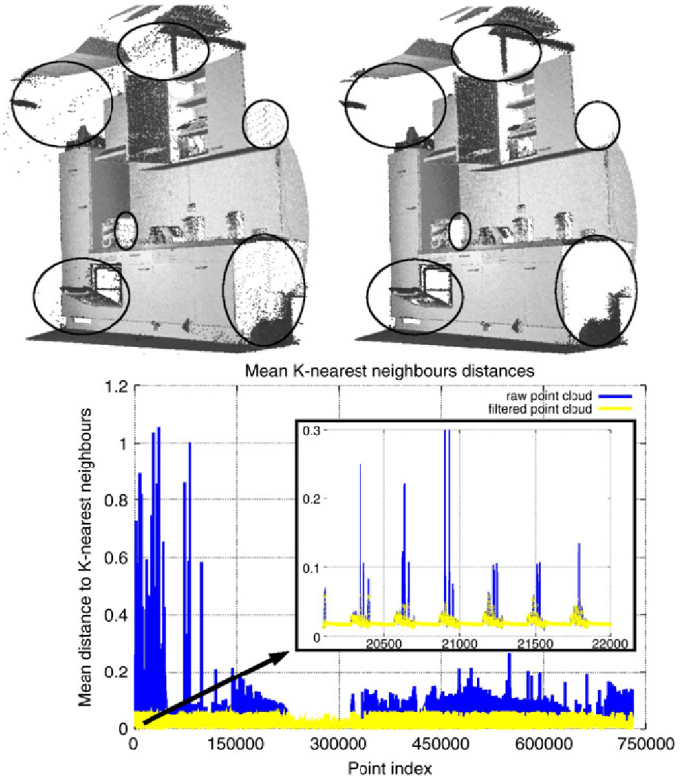

FIGURE 4.8: Example of the application of the SOR filter. Raw point cloud data littered with erroneous pixels in circled areas (top left). In the filtered dataset the majority of the mixed pixels is removed (top right). Mean distances to $k = 30$ neighbours before and after filtering using $\alpha = 1$ (bottom) (Source: Figure 5 from Rusu et al., 2008).

4.3.3 TLS applications

TLS was originally developed for applications related to structural engineering. However, the potential of laser scanning in environmental applications was quickly recognised because of its ability to remotely capture data of high precision and resolution (Hodge et al., 2009b). Early applications include processing of TLS point cloud data to derive DEMs (Heritage and Hetherington, 2005), to detect and quantify channel change from subtraction of subsequent DEMs (Milan et al., 2007), and to extract surface roughness metrics (Large and Heritage, 2007) in fluvial systems. Multiple examples can be found in the study of surface-flow interaction in both fluvial and aeolian settings. TLS has been employed to study spatiotemporal variations of roughness within catchments, relating them to surface run off and erosion processes (Haubrock et al., 2009), debris flow

(McCoy et al., 2010), relations between bed roughness, flow dynamics and sediment transport (Hodge et al., 2009a,b; Milan, 2009), and to quantify the form drag emanating from large-scale roughness features on riverbanks and its effects on flow patterns and erosion processes (Darby et al., 2013; Leyland et al., 2015; Hackney et al., 2015). Within the aeolian domain, TLS has been employed to characterise the aerodynamic roughness of complex features (Nield et al., 2013), to measure surface moisture (Nield et al., 2011, 2014) and to link these surface attributes to sediment transport processes (Nield and Wiggs, 2011; Nield et al., 2017). Other TLS applications include extracting sea ice roughness metrics, assisting the understanding of geothermophysical conditions of snow covered sea ice (Landy et al., 2015); relating glacier surface roughness to ice melt and tephra distribution after volcanic eruptions (Nield et al., 2013); monitoring and quantifying coastal cliff erosion (Rosser et al., 2005). Recently, attempts have been made to use TLS for the acquisition of bathymetric data through clear shallow water (Smith et al., 2012; Smith and Vericat, 2014).

4.3.4 Extracting vegetation characteristics from TLS data

TLS is increasingly used to quantify the form and structure of plants. Various examples come from forestry and crop related studies and include measurements of plant height, biomass, nitrogen estimates, stem position, stem number, tree timber volume and diameter at breast height (*e.g.* Hopkinson et al., 2004; Watt and Donoghue, 2005; Chatzinikos et al., 2013; Eitel et al., 2014; Tilly et al., 2014). Danson et al. (2007) employed TLS to estimate canopy gap fraction, using a ratio of *emitted*/*recorded* pulses. Comparison of their TLS-based estimates with, the well-established in forestry studies, measurements derived from hemispherical photography suggests that TLS can be used for the accurate extraction of canopy features with the additional advantage of delivering information related to the 3D canopy structure. Straatsma et al. (2008), using the same ratio, after converting the 3D point cloud data to a polar grid system, estimated the hydrodynamic density of floodplain vegetation along horizontal slices. This method was also adopted by Manners et al. (2013) who derived 2D stem maps, assuming that the stems have cylindrical shape. These maps were later incorporated into River2D, a 2D CFD (computational fluid dynamics) model (Figure 4.9). However, as Straatsma et al. (2008) point out, laser scanners record the number of returned echoes but not the number of emitted pulses which has to be estimated. Moreover, in both studies the data were derived from single scans which means that the method is susceptible to shadowing and occlusions as discussed above, and as such is more akin to 2D photogrammetric approaches. A single scan also assumes that scan angle and flow direction coincide, which is unlikely in many cases. Manners et al. (2013) use a cylindrical analogy, which, as discussed in subsection 3.3.1, is likely an inadequate assumption.

Hosoi and Omasa (2006) proposed modelling vegetation from TLS-derived data by combining voxel-based (volumetric pixel) and ray tracing approaches. Based on the point

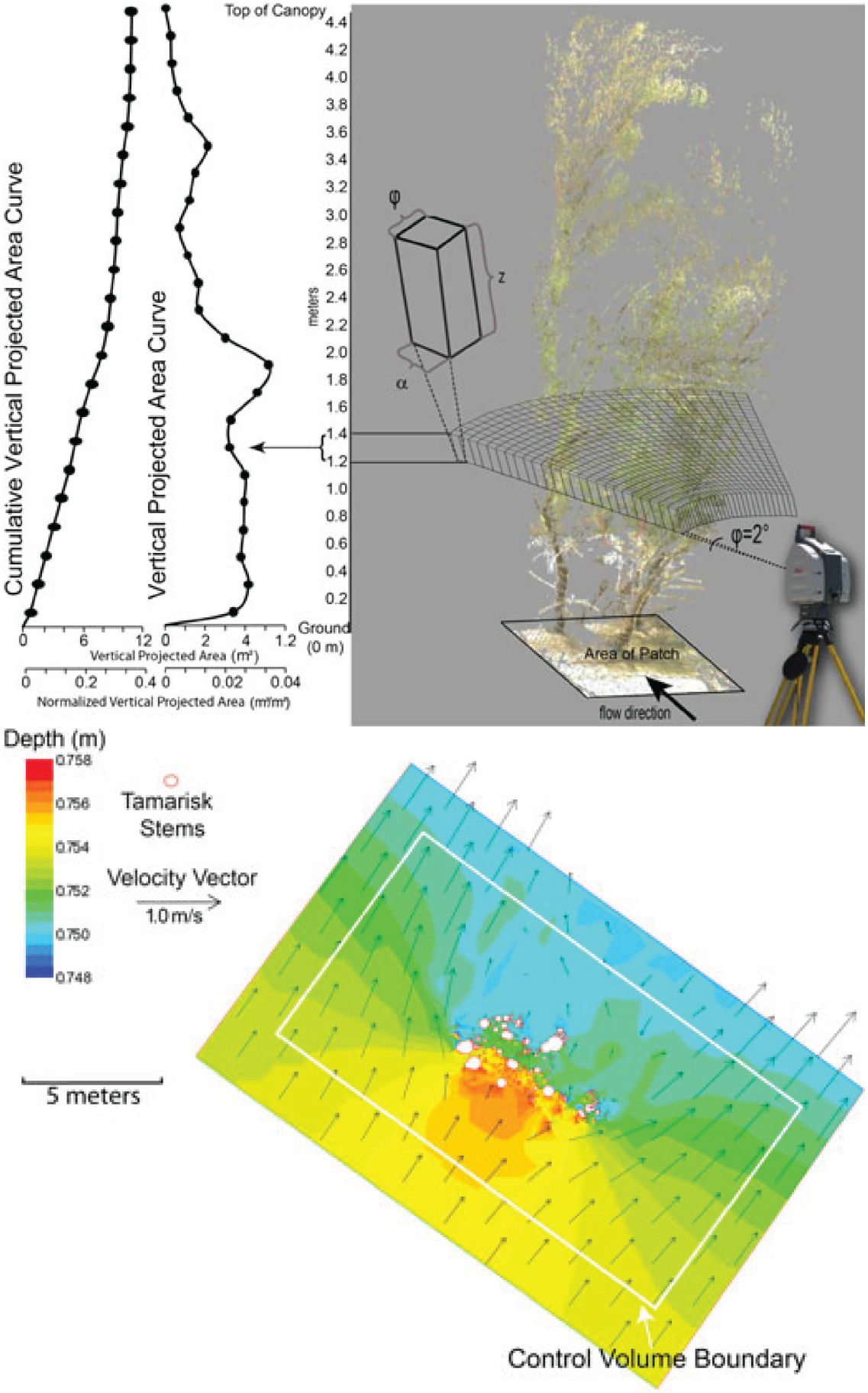

FIGURE 4.9: Schematic demonstrating the method followed by Manners et al. (2013) to extract vegetation density and vertical projected area (top) and implement them to a CFD model (River2D) using a cylindrical analogy (bottom) (Source: Figures 3 and 5 from Manners et al., 2013).

coordinates they derived a 3D grid, the cells (voxels) of which were assigned values depending on the existence or absence of points inside them and the likelihood of points missing due to shadowing effects. Antonarakis et al. (2009) analysed TLS data of leafless trees and extracted tree volume, spacing and projected area using mesh-based and voxel-based analyses. Their measurements were afterwards used for the estimation of drag coefficient of trees and the calculation of Darcy-Weisbach friction factors, using the Järvelä (2004) model (see also 3.3.2) and subsequently Manning's n values. Antonarakis et al. (2010) expanded this method to leafy vegetation by deriving estimates of LAI from 3D point clouds using the method of Danson et al. (2007). However, as the authors point out there is an uncertainty related to the *emitted/recorded* pulses ratio. LAI should be calculated using only those echoes reflected from tree foliage, discarding any echoes reflected from woody plant elements. However, the two types of echoes cannot always be distinguished from the TLS data. Béland et al. (2014) developed a voxel-based algorithm which does not rely on ray tracing. Instead, it employs computational geometry to estimate the theoretical number of points within each voxel. Leaf area density can then be measured by comparing the theoretical amount of TLS echoes per voxel to the measured one. This approach also requires a distinction to be made between echoes reflected from foliage and those reflected from stems. The authors propose the use of TLS instruments equipped with an infrared laser beam, because of the high reflectance of the infrared part of the electromagnetic spectrum from the photosynthetic plant elements.

TLS units equipped with infrared lasers have already been developed (e.g. the RIEGL VZ-400 and the Leica P20 TLS use near infrared lasers [1500 nm and 808 nm, respectively]). Although, scanners capable of conducting multiple wavelength surveys are currently under development (e.g. the Dual Wavelength Echidna LiDAR [DWEL] and the Salford Advanced Laser Canopy Analyser [SALCA]), these instruments are not commercially available, and have limited capabilities in terms of range (e.g. maximum range of the SALCA is 105 m) and spatial resolution (e.g. maximum spatial resolution of the SALCA is 15 cm) (Danson et al., 2014). Nevertheless, their development demonstrates the potential of using a ratio of returned intensities from two distinct wavelengths (Figure 4.10), similarly to the Normalised Difference Vegetation Index ($NDVI$) that is typically used in satellite-based remote sensing applications. This could assist the development of robust automated algorithms for the extraction of vegetation from point cloud datasets as well as the partitioning of the point cloud between photosynthetic (e.g. leaves) and non-photosynthetic (e.g. branches) plant elements.

Raumonen et al. (2013) developed an algorithm capable of reconstructing models of single trees from TLS data using geometric primitives. In their method they partitioned the point dataset into very small patches (approximate diameter 1-3 cm) which conform to the tree surface. Subsequently, neighbour analyses were used to determine the connectivity relation between the individual patches while the identification of various tree elements was accomplished through a geometric-based analysis. In the next step, the various neighbouring patches that belong to the same element (e.g. branch or trunk)

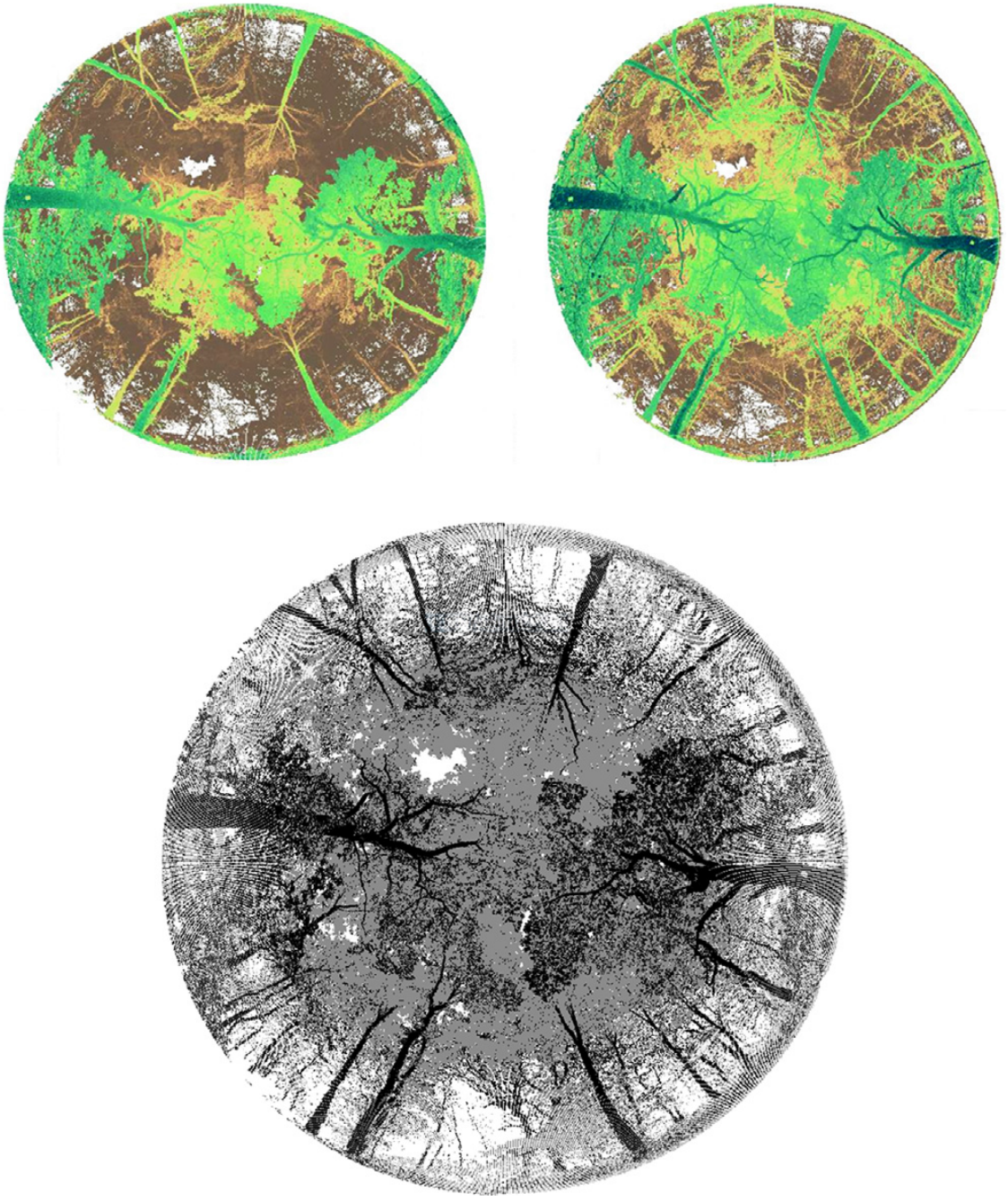

FIGURE 4.10: TLS point clouds of forest canopy acquired using the two different wavelengths of SALCA; 1063 nm (top left) and 1545 nm (top right). Dark green indicates high intensity and brown low intensity values. SALCA Normalised Ratio Index ($SNRI = \frac{p1063 - p1545}{p1063 + p1545}$) product (bottom) low intensity values are darker (Source: Figure 4 from Danson et al., 2014).

were segmented together forming larger segments, each one of which corresponds to an entire, unique, plant element (e.g. branch). In the final step each segmented plant element was reconstructed using successive cylinders with similar orientation and radius to the plant element. Although this method permits a realistic reconstruction of the larger and more distinct tree elements (i.e. trunk and large branches) its limitations are highlighted on the reconstruction of the smaller elements (Figure 4.11). As the authors point out, branches with diameters smaller than 3 cm produce an error in the order of 1 cm. Moreover, needles or other foliage are completely omitted by the reconstruction algorithm. The focus in the study of Raumonen et al. (2013) was to obtain information which is relevant in forestry studies such as tree quality and timber volume. However, the omitted by this method smaller plant elements and, more importantly, foliage are pertinent in the study of vegetation-flow interactions and their exclusion could yield significant errors.

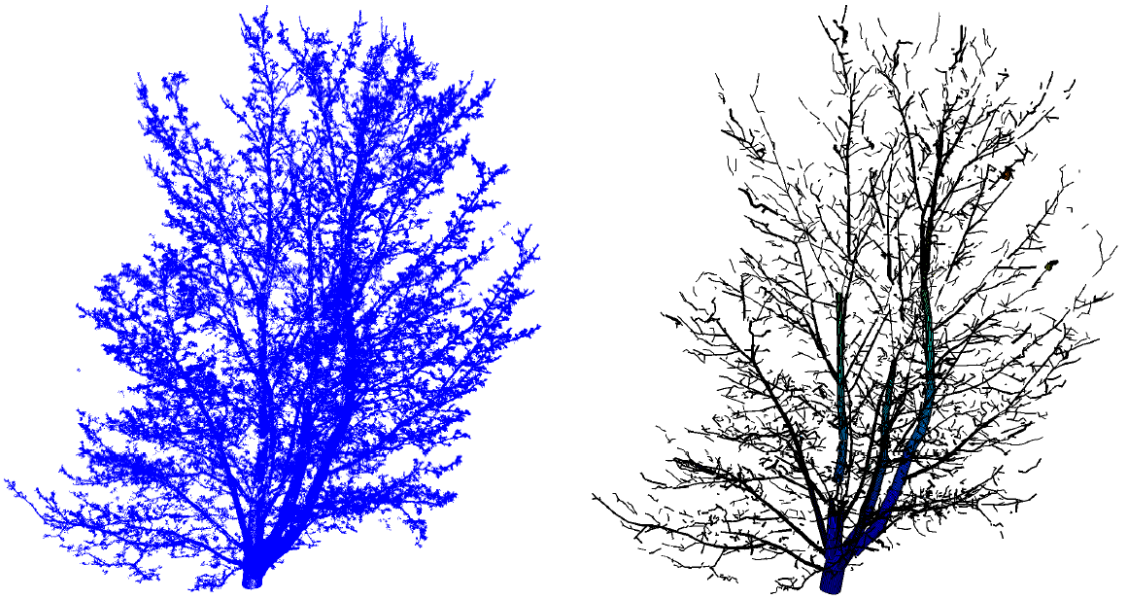

FIGURE 4.11: TLS point cloud (left) and cylinder-based model (right) of a maple tree (*Acer platanoides*) (Source: Figure 2 from Raumonen et al., 2013).

4.4 Chapter summary

In the past decades image-based analysis has been the main approach for capturing information and deriving metrics regarding vegetation's form and structure. This has been mainly based in 2D analysis which is only partly adequate for flow-related problems. Recent advances in the field of photogrammetry and specifically SfM techniques may have a potential to precisely capture the 3D structure of plants. However, this is yet to be accomplished. On the other hand, significant advances have been made in laser scanning technology during the last decade. The development of various TLS instruments generates a potential to characterise the form and structure of plants and derive those metrics required for the study of vegetation-flow interaction. A variety of

methods suited to various vegetation-related problems have emerged that all have both advantages and limitations. Limitations are either due to instrument capabilities (e.g. occlusions, maximum resolution) or post processing methods related to the nature of TLS-based datasets which are of large size (usually many GBs) and require complex, computer-heavy, calculations. A TLS-based workflow for the characterisation of the vegetation form and structure is developed in Chapter 5 to address some of these prior weaknesses, specifically issues with data complexity from porous structured vegetation.

Chapter 5

Extracting Vegetation Metrics from TLS and Digital Imagery

Chapter 3 highlighted the importance of vegetation in terms of its capability to affect surface water flows and underlined that the main factors affecting such flows are the plant structure and reconfiguration. Chapter 4 reviewed the state of the art in surveying technology and data processing routines pertinent to vegetation characterisation. From this review it became evident that TLS is the most appropriate surveying technique capable of capturing vegetation's complex 3D structure at high resolution and that this method has a potential for enabling the discretisation of individual plant elements (e.g. stems, leaves).

As a first step to addressing the identified need of quantifying the effects of vegetation on flow, the present Chapter describes the development and testing of a new method to characterise vegetation's complex morphology. TLS surveying and processing routines are developed to characterise the vegetative structure in bulk employing the concept of porosity that was first introduced by Grant and Nickling (1998). These processing routines are further expanded to derive 3D porosity arrays from the TLS data, enabling the discretisation of individual plant elements and the precise representation of vegetation's spatial heterogeneity. Image surveying and processing methods, typically employed in forestry studies, are adopted and employed in tandem with the TLS surveying and analysis. The data derived from the image-based workflow offer a set of control metrics that are used as a means of comparison to the assess and evaluate the TLS-derived metrics.

5.1 Plant types

Previous studies that have focused on the effects of vegetation on flow dynamics in the context of water or wind flows have investigated a variety of plants, depending upon the

intended scope and context of the research. Examples from the aeolian domain include the artificial scots pine employed by Grant and Nickling (1998) and the estimation of the drag coefficient of a desert shrub (*Sacrobatus vermiculatus*) by Gillies et al. (2000), while Gillies et al. (2002) employed three plants to represent a variety of forms, Burning bush (*Euonymus alatus*), Colorado spruce (*Picea pungens glauca*) and Fountain grass (*Pennisetum setaceum*). Some studies have sought to estimate shallow marine vegetation-flow interactions. For example, Nepf and Vivoni (2000) employed flexible seagrass surrogates. Seagrass has also been used by Lee et al. (2001) (*Zostera japonica*), Folkard (2005) (*Posidonia oceanica*) as well as Ghisalberti and Nepf (2006) and Le Bouteiller and Venditti (2015) (*Zostera Marina*). Wilson et al. (2003) employed scaled surrogates modelled after kelp (*Laminaria hyperborean*). In the fluvial domain, Stephan and Gutknecht (2002) have employed aquatic macrophytes (*Ranunculus trichophyllus*, *Groenlandia densa L.* and *Berula erecta*) as did Marjoribanks (2013) (*Ranunculus penicillatus*). Shucksmith et al. (2011) employed common reed (*Phragmites Australis*) and *Carex* while common reed was also used in the study of Vionnet et al. (2004). Järvelä (2002a) employed sedges (*Carex acuta*), willows (*Salix sp.*) and grasses. Fathi-Maghadam et al. (2011) employed shrubs and hedges while Fathi-Maghadam and Kouwen (1997) used pine and cedar saplings and Kouwen and Fathi-Maghadam (2000) used four species of coniferous trees (cedar, spruce, Austrian pine and white pine). Yagci and Kabdasli (2008) used a stone pine (*Pinus pinea*), a platucladus (*Thuja Orientalis*) and a Monterey cypress (*Cupressus Macrocarpa*), while Västilä and Järvelä (2014) undertook experiments employing common osier (*Salix viminalis*), hybrid crack willow (*Salix x rubens*), common alder (*Alnus glutinosa*) and silver birch (*Betula pendula*). A summary of plant types evaluated in previous work can be found in Table 5.1.

From the above it is apparent that there is a plethora of plant types that encounter fluid flows in different Earth surface domains, all of which have distinct structural characteristics. From the examples presented in Table 5.1, the fluvial domain is associated with many different plant types that include grasses, sedges, shrubs, and trees, which are characterised by a variety of stem and foliage structures. In an attempt to develop methods and metrics that are applicable to the variety of plant types encountered on floodplains, the present study will not focus on a specific vegetation type. Instead, six plants were selected to represent grasses as well as forms that combine stiff woody stems, flexible branches, and a variety of foliage types (i.e. narrow and broad leaves, needle-like and spray foliage) (Figure 5.1). Furthermore, because natural plants can deteriorate after they are removed from their natural environment (see also Section 3.4.1), which may in turn alter their physiological characteristics, artificial plant surrogates were favoured instead. The choice of artificial plants was also necessary for the present study as it allowed the employment of identical vegetation elements at the various stages of this research, assuring consistency. Two grass plants were selected, namely tall grass and short grass. The former was approximately 0.9 m tall and had long, thin grass blades. The later was approximately 0.2 m tall and had short wider ones. A bamboo and a fig were chosen to represent plants that combine flexible leaves and

TABLE 5.1: Examples of plant types employed in previous studies focusing on vegetation-flow interactions.

Domain	**Type**	**Plant**	**Characteristics**	**Author**
Aeolian	Coniferous tree	Scots pine (*Pinus sylvestris*)	Trunk, woody stems, needle-like foliage	Grant and Nickling (1998)
		Colorado spruce (*Picea pungens glauca*)	Trunk, woody stems, needle-like foliage	Gillies et al. (2002)
	Shrub	Burning bush (*Euonymus alatus*)	Woody stems, simple elongated leaves	Gillies et al. (2002)
		Desert shrub (*Sacrobatus vermiculatus*)	Spiny branches, succulent leaves	Gillies et al. (2000)
	Grass	Fountain grass (*Pennisetum setaceum*)	Grass blades with bristles	Gillies et al. (2002)
Marine	Seaweed	Kelp (*Laminaria hyperborean*)	Elongated stems, leaf blades	Wilson et al. (2003)
	Seagrass	*Zostera japonica*	Grass blades	Lee et al. (2001)
		Zostera marina	Grass blades	Ghisalberti and Nepf (2006); Le Bouteiller and Venditti (2015)
		Posidonia oceanica	Grass blades	Folkard (2005)
Fluvial	Aquatic macrophyte	*Ranunculus trichophyllus*	Thin flexible stems	Stephan and Gutknecht (2002)
		Groenlandia densa L.	Thin flexible stems and leaves	Stephan and Gutknecht (2002)
		Berula erecta	Thin flexible stems and leaves	Stephan and Gutknecht (2002)
		Ranunculus penicillatus	Thin flexible stems	Marjoribanks (2013)
	Grass	Grass	Grass blades	Järvelä (2002a)
	Perennial grass	Common reed (*Phragmites australis*)	Woody flexible stems, elongated leaves	Shucksmith et al. (2011); Vionnet et al. (2004)
	Sedge	*Carex*	Stalk, leaves	Shucksmith et al. (2011)
	Shrub	Common osier (*Salix viminalis*)	Woody branches, long slender leaves	Västilä and Järvelä (2014)
	Shrub/tree	Hybrid crack willow (*Salix x rubens*)	Woody branches, elongated leaves	Västilä and Järvelä (2014)
		Willow (*Salix sp.*)	Woody branches, elongated leaves	Järvelä (2002a)
		Common alder (*Alnus glutinosa*)	Woody branches, leaves	Västilä and Järvelä (2014)
	Tree	Silver birch (*Betula pendula*)	Woody branches, leaves	Västilä and Järvelä (2014)
	Coniferous tree	Pine (*Pinus pinea*)	Trunk, woody stems, needle-like foliage	Kouwen and Fathi-Maghadam (2000); Yagci and Kabdasli (2008)
		Cedar	Trunk, woody stems, needle-like foliage	Kouwen and Fathi-Maghadam (2000)
		Spruce	Trunk, woody stems, needle-like foliage	Kouwen and Fathi-Maghadam (2000)
		Platucladus (*Thuja orientalis*)	Trunk, woody stems and spray foliage	Yagci and Kabdasli (2008)
		Monterey cypress (*Cypressus Macrocarpa*)	Trunk, woody stems and spray foliage	Yagci and Kabdasli (2008)

small flexible branches with rigid woody stems. They were both approximately 0.5 m tall. The bamboo had many, simple, narrow, elongated leaves while the fig had fewer, wide leaves of more complex shape. A scots pine and a cedar were selected to represent plants with needle-like and spray foliage, respectively. The height of the cedar was approximately 0.4 m while the height of the scots pine was approximately 0.6 m. The plant types used in this study are summarised in Table 5.2.

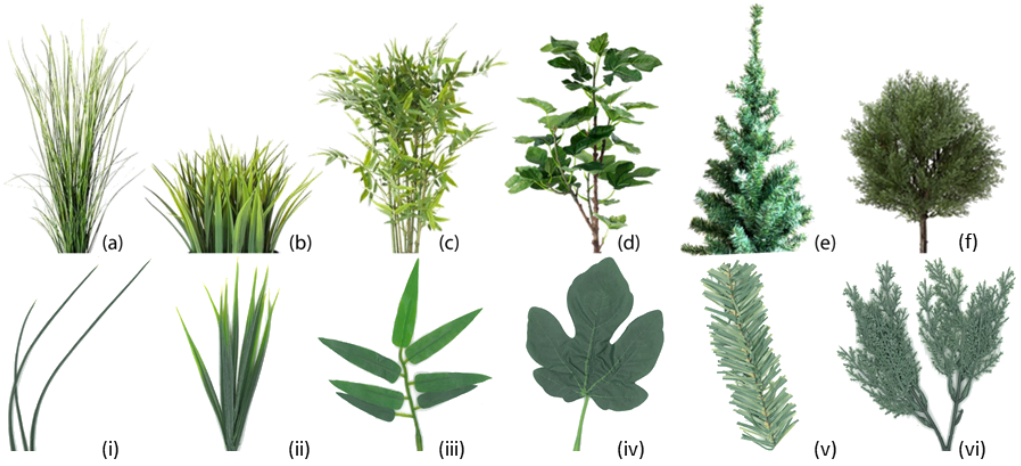

FIGURE 5.1: The artificial plants used in this study. Tall grass (a), short grass (b), bamboo (c), fig (d), scots pine (e), cedar (f) and details of their foliage (i-vi).

TABLE 5.2: Main characteristics of the plants employed in this study

Plant	**Characteristics**
Tall grass	Long, thin grass blades
Short grass	Short, wide grass blades
Bamboo	Woody branches, long slender leaves
Fig	Woody branches, wide leaves
Scots pine	Woody branches, needle-like foliage
Cedar	Woody branches, needle-like, spray, foliage

5.2 Data collection

5.2.1 Plant scanning and imaging

All six plants were scanned using a Leica C10 TLS and imaged with a Canon EOS 350D SLR camera. The Leica C10 is a pulsed (time-of-flight) system that uses a lower power laser beam (3R laser class), of green wavelength (532 nm). The maximum range of the instrument is 300 m and the minimum is 0.1 m. It can acquire up to 50 000 points s^{-1} at a user-defined resolution (the highest is 1×1 mm). The field of view of the scanner is 360^o on the horizontal and 270^o on the vertical axis. For distances up to 50 m the laser footprint size is 4.5 mm, the reported data accuracy is 6 mm for position and 4 mm for distance measurements. The Canon EOS 350D is a digital single-lens reflex (SLR)

camera. It is equipped with an 8.2M pixels CMOS sensor, the size of which is 22.2×14.8 mm (aspect ratio 3:2). The camera was coupled with a Tamron 17-50 mm F/2.8 aspherical lens. Because the size of the camera sensor is smaller than the standard 36×24 mm film format, the effective focal length of the system is 27.2-80 mm.

The survey was conducted indoors to minimise plant movement due to wind and to protect both the plants and the equipment from the elements. Each plant was individually scanned and imaged from four survey positions (Figure 5.2). The distance between surveying position and plant varied between 3 and 3.8 metres, with an average distance equal to 3.4 metres. First each plant was scanned from a surveying position, the point spacing for the TLS was set to the maximum allowed by the proprietary software (Leica Cyclone 9.0), which is 1×1 mm. After a scan was completed, the scanner was unmounted from the tripod, a white backdrop was placed behind the plant and the camera was mounted on the tripod using a Nodal Ninja mount. This allowed plant images to be captured in front of the white backdrop with a viewing angle very close to the scan angle. In order to minimise the radiant distortion of the digital images, which is frequently observed when using wide-angle lenses, the focal length of the camera lens was kept at 50 mm (80 mm equivalent) at all times. After plant scanning and imaging from a survey position was completed, the tripod was moved to the next position and the procedure was repeated. At the end of each survey cycle, when data had been obtained from all four surveying positions, part of the plant's foliage was removed and a new survey cycle followed. Each plant was surveyed under four foliage densities and approximately an equal amount of foliage was removed at each defoliation step.

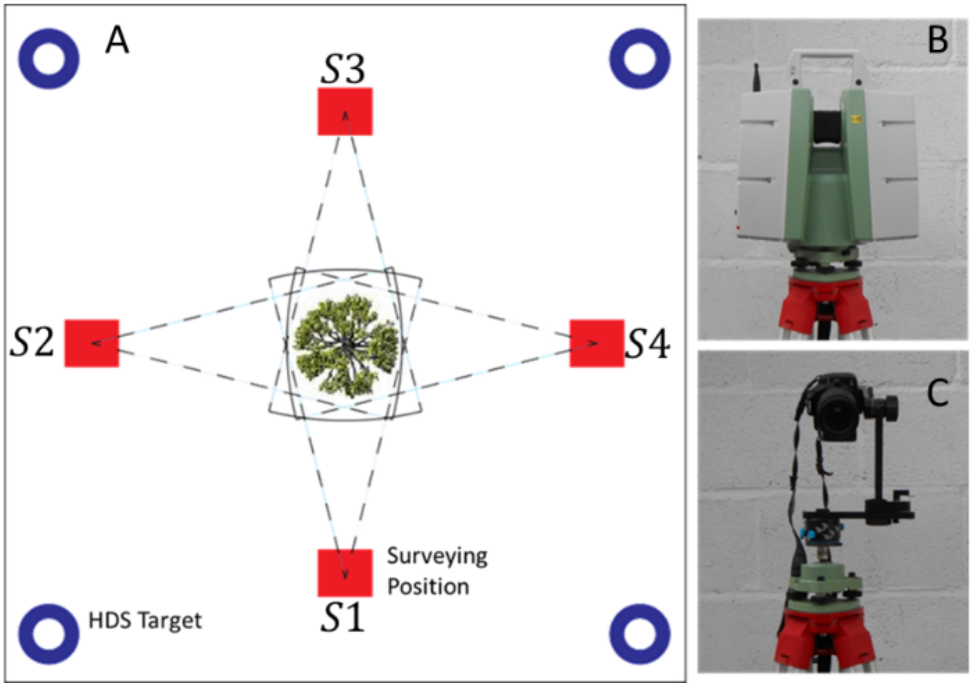

FIGURE 5.2: Schematic showing the top down view of the survey set up, including the four surveying positions, the position of the HDS targets and the survey area (A). Leica C10 TLS mounted on tripod (B) and Canon EOS 350D SLR coupled with Tamron 17-50 mm F/2.8 lens and Nodal Ninja mount (C).

5.3 Data preparation

By the end of the scanning survey, ninety-six individual scans had been acquired (from four surveying positions for each vegetation type). Each scan tetrad corresponded to a plant with a certain foliage density. The datasets were processed following two parallel workflows; the first one involved the processing of individual scans for the extraction of 2D metrics, while the second one involved the processing of registered scans for the extraction of 3D metrics. All of the processing steps are described below (Sections 5.4 and 5.5) and presented in the flowchart of Figure 5.3. Prior to that, pre-processing of the TLS datasets was undertaken to remove unwanted subsets of the point clouds (i.e. parts not representing vegetation) and minimise errors such as mixed pixels. The data preparation procedure, which is also included in the flowchart of Figure 5.3 is described herein.

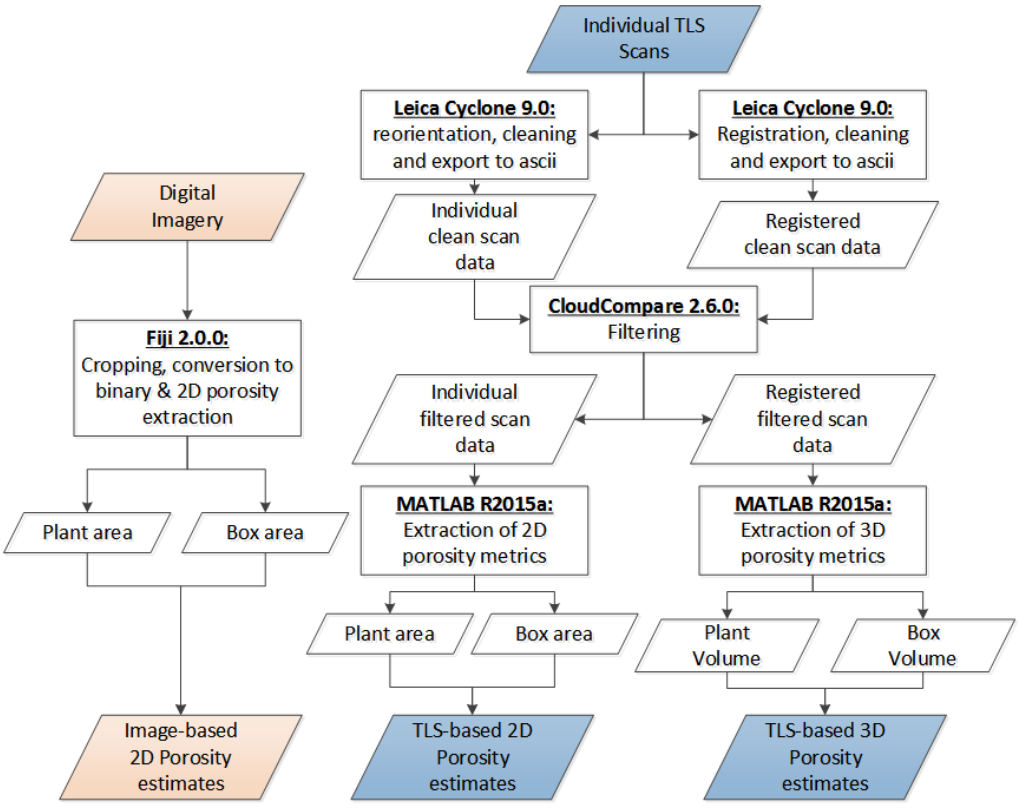

FIGURE 5.3: Flowchart presenting the processing methods of the TLS data and digital imagery.

5.3.1 TLS data pre-processing

5.3.1.1 Single scans

Each single scan was inspected using Leica Cyclone 9.0. The scan data were reoriented to match the viewing angle of the corresponding digital image and the points that did

not represent vegetative parts (such as surrounding built infrastructure) were manually selected and removed from the datasets. Subsequently, the scan datasets were exported in ASCII files containing the 3D coordinates of each point of the dataset.

5.3.1.2 Registered scans

Each tetrad of single scans was registered using four HDS targets, which remained fixed throughout the experiment (Figure 5.2). This was accomplished using an automated bundle adjustment algorithm implemented in Leica Cyclone. For all cases the registration error was 1 mm. The registered point clouds were inspected and the points that did not represent any vegetation were manually selected and removed from the dataset. The clean point clouds were exported in ASCII files containing the 3D coordinates of each point of the dataset.

5.3.2 TLS filtering

For the reasons discussed in subsection 4.3.2, the point cloud data were littered with mixed pixels, especially for example between discrete elements like leaves or stems. All ASCII files were individually imported into the open source software CloudCompare 2.6.0 (Cloudcompare.org, 2015) and filtered using the sparse outlier removal (SOR) filter described in 4.3.2.5. The SOR filter requires user inputs in respect to the amount of neighbours (k), that should be accounted in the assessment of each point, and a multiplier (α) for the standard deviation of the k-nearest neighbour distances. Various combinations of these settings were tested and the results were evaluated by visual inspection. The best filtering result for the single scans was accomplished using $k = 10$ and $\alpha = 1$. For the registered scans $k = 50$ and α =1 generated the best results. Figure 5.4 represents a before and after example of the filtering procedure showing how the extraneous points around a leaf are removed using the filter, whilst the internal points remain intact. All filtered datasets were exported from CloudCompare as ASCII files and further processed in MATLAB R2015a following the method described in Sections 5.4 and 5.5.

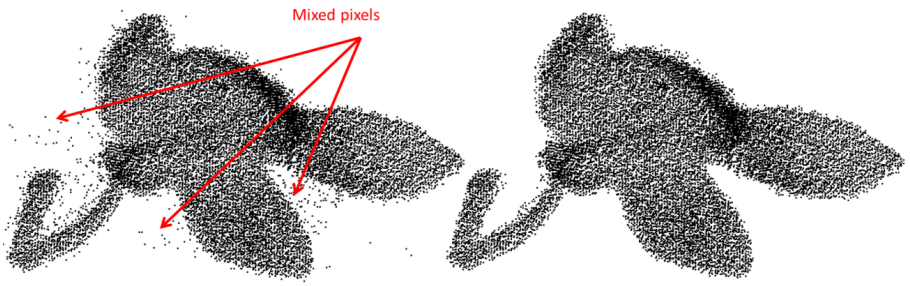

FIGURE 5.4: Application of the SOR filter for a single leaf from the fig. The original point cloud (left) is littered with mixed pixels around the leaf. Most of them are identified by the filter and discarded, producing the filtered dataset (right).

5.4 Extraction of 2D metrics

2D metrics were extracted from the single TLS scan datasets and the acquired digital imagery. The aim was to extract 2D porosity estimates for each plant, as seen from each of the four surveying positions, under various foliage densities and compare them with optical porosity estimates extracted from the digital imagery obtained from an identical point of view.

5.4.1 Extraction of 2D porosity from TLS data

A bespoke MATLAB function (ViPER-2D) (see Appendix A) was developed which undertook the analysis of all single scans to estimate a 2D porosity metric for each one of the datasets. It should be noted that although the TLS point spacing is set during the scan survey (1×1 mm in this example), this is only a nominal value. In reality the point spacing deviates slightly from the nominal value, due to small discrepancies of the angle increments of the mechanism during scanning and due to the varying distance between the scanner and the surveyed feature, with points that are further away from the scanner being spaced further apart. The steps involved in the procedure are described thus:

1. The 3D point cloud of a single scan is converted into 2D by discarding all y-coordinates. This effectively collapses all 3D points onto a vertical 2D plane that is perpendicular to the line of sight (Figure 5.5, A).

2. Based on the smallest and greatest values of the x and z coordinates, the minimum bounding 2D grid, with a cell size equal to the nominal TLS point spacing (i.e. 1×1 mm) is derived (Figure 5.5, B). Each grid cell is defined by the coordinates of its bottom left corner (i,h) and the cell size.

3. Because of the small deviations from the nominal point spacing value described earlier, each point can be situated anywhere within the boundaries of its corresponding grid cell. In order to increase the computational efficiency of the code, each point of the cloud is snapped to its corresponding grid cell. This is achieved by rounding down the point x,z coordinates to their third decimal degree (Figure 5.5, C).

4. The 2D grid is cross-referenced with the TLS dataset by comparing pairs of x,z and i,h coordinate values and is populated in a binary form. If the coordinates of a grid cell match with the coordinates of a point, the cell is assigned a value of 1 (filled) otherwise it is assigned a value of 0 (empty) (Figure 5.5, D).

5. The ratio of empty cells to the total number of cells in the grid is used as a TLS-based estimate of the 2D porosity (P_{2D}) of the dataset.

6. The binary grid is stored in the directory as a text file that contains the coordinates of the grid cells and their binary status.

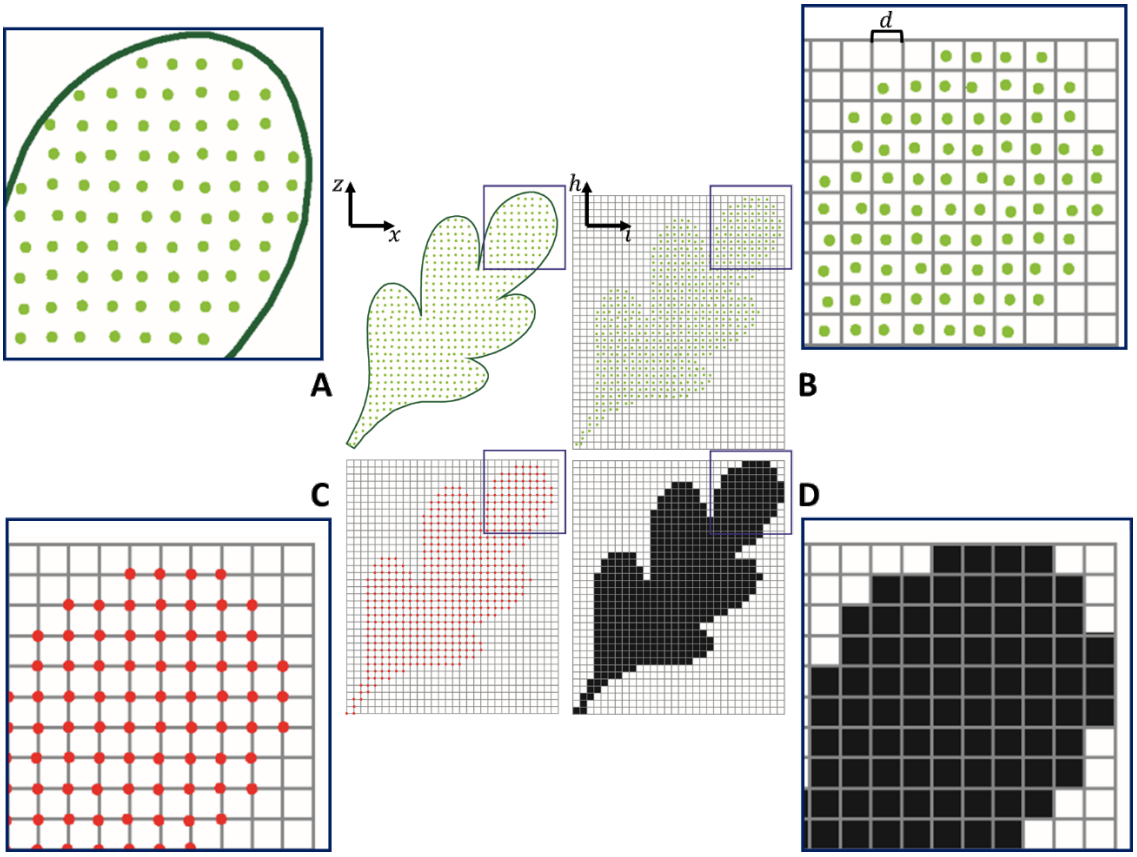

FIGURE 5.5: Example sketch of the 2D porosity extraction routine for a single leaf. The point cloud is converted into 2D by discarding its y-coordinates (A), the minimum bounding grid is derived (B) and the point cloud is being organised to match the derived grid (C). The grid is cross-referenced with the organised point cloud and populated in a binary form (D).

5.4.2 Extraction of optical porosity from digital images

Following the methods of Grant and Nickling (1998), image analysis was undertaken on the obtained digital imagery to extract the plants' optical porosity. Fiji version 2.0.0 (Fiji.sc, 2015), an open source, java-based image processing package, was used for this task. Each image was individually imported into Fiji and cropped to remove any parts not corresponding to vegetation. Subsequently, the image was converted to binary and the minimum bounding rectangle enclosing the plant was automatically derived by the software. In the next step, the amount of white (empty) and black (filled) pixels within the bounding rectangle was counted. The ratio of empty pixels over the total amount of pixels was then used as an image-based estimate of optical porosity (OP). An example of the image-based optical porosity estimate and the corresponding TLS based 2D porosity estimate is presented in Figure 5.6. Figures showing the outputs of the TLS and image analysis routines for all plants are presented in Appendix C (Figures C.1-C.6).

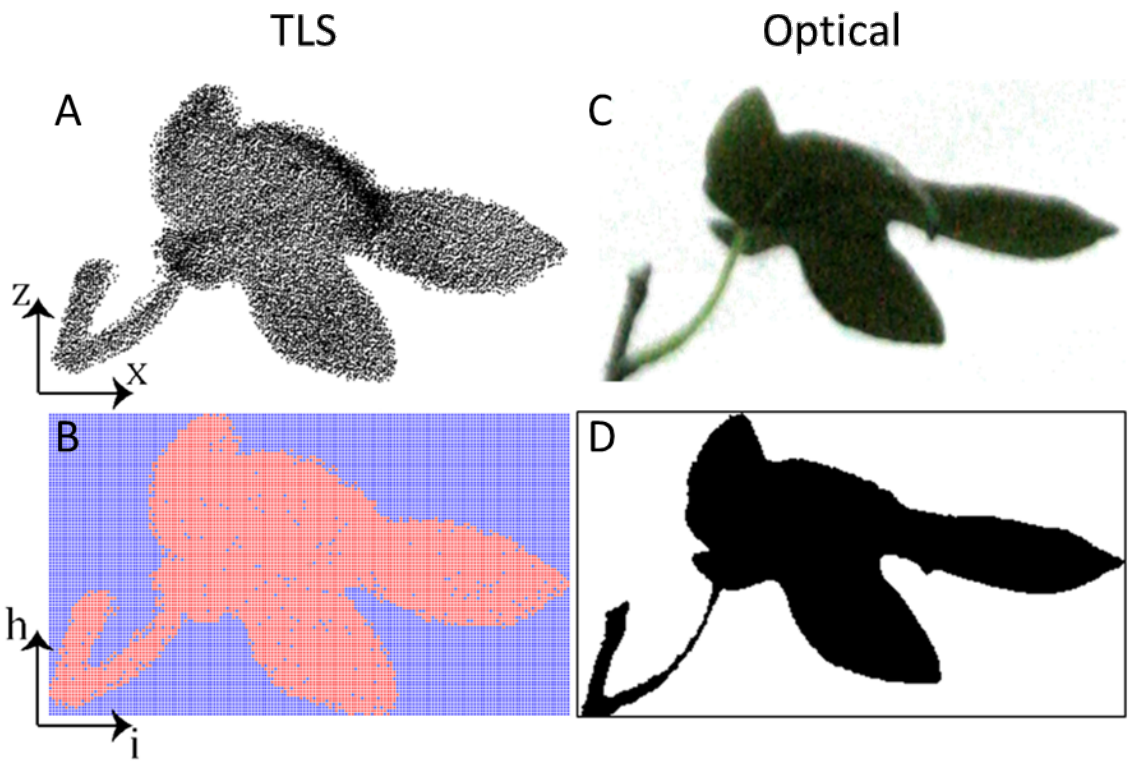

FIGURE 5.6: Example showing the extraction of 2D metrics of a single leaf of the fig. From the TLS data (A) a binary porosity grid is derived (B). The cell size is equal to the TLS nominal point spacing (1×1 mm). Blue cells are empty and red ones are filled. Similarly, from the obtained image (C) a binary image is derived (D). White pixels are empty and black ones are filled.

5.5 Extraction of 3D porosity from TLS data

Following the same principle with the 2D porosity extraction routine described in Section 5.4, a 3D analysis was undertaken to derive estimates of the 3D porosity of each plant under the various foliage scenarios, akin to the volumetric porosity introduced by Grant and Nickling (1998).

A bespoke MATLAB function (ViPER-3D) (see Appendix B) was developed which undertook the analysis of all registered scans to estimate a 3D porosity metric for each dataset. The steps of the procedure are described as follows:

1. Based on the lowest and highest values of x,y,z coordinates of the point cloud, the minimum bounding 3D grid with a voxel size equal to the nominal point spacing of the input data (i.e. 1×1×1 mm) is derived. Each voxel is defined by the coordinates of its bottom, left, front corner (i,j,h) and the cell size (d).

2. Because of the small deviations from the nominal points spacing, each point can be situated anywhere within the boundaries of its corresponding voxel. In order to increase the computational efficiency of the code, each point of the cloud is snapped to its corresponding voxel. This is achieved by rounding down the point

x,y,z coordinates to their third decimal degree.

3. The empty 3D grid is cross-referenced with the input TLS data by comparing triplets of x,y,z and i,j,h coordinate values, and populated in a binary form, identifying the occupied voxels (Figure 5.7, A).

4. The ratio of empty voxels over the total amount of voxels is used as a measure of the 3D porosity (P_{3D}) of the dataset.

5. A final step is added to this procedure where the binary grid is converted to a coarser porosity array. For example Figure 5.7, B shows an array of $1\,cm^3$ 3D cells; each assigned a porosity value based on the number of empty $1\,mm^3$ binary voxels (computed in step 3) that fall within the boundaries of the 3D cell. In this example, each 3D cell contains 10^3 binary voxels, if half of them within a 3D cell are occupied, then the cell's porosity is 0.5. $1\,cm^3$ porosity arrays for all plants are presented in Figure C.7 in Appendix C.

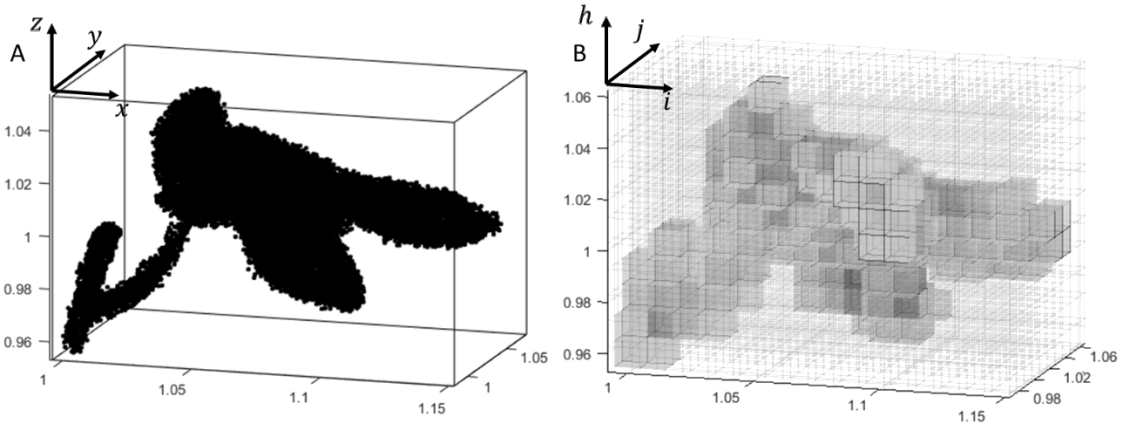

FIGURE 5.7: 3D binary grid ($1\,mm^3$) derived from the TLS data is used to estimate the bulk 3D porosity of the dataset (A). 3D porosity array ($1\,cm^3$) derived from the binary one allows an individual porosity estimation for each 3D grid cell (B). Darker shades correspond to lower porosity values.

5.6 Results

Using the methodological steps outlined in Sections 5.4 and 5.5, metrics of optical porosity (OP), 2D porosity (P_{2D}) and 3D porosity (P_{3D}) were extracted. As plant elements were removed after each survey cycle, the space occupied by the plant each time varied. This means that foliage reduction may be associated with a bounding box of reduced size and as a consequence, in some cases yield lower porosity values. This complicates the comparison between individual results. For this reason, in the data shown in the present Chapter, the size of the bounding box is kept constant between foliage scenarios and varies only between plant scenarios.

5.6.1 Comparison of 2D metrics

Estimates of OP and P_{2D} as they were extracted from each surveying position for all plant-foliage scenario combinations are presented in Figure 5.8, while the residual values ($P_{2D} - OP$) are presented in Table 5.3. As expected both porosity estimates are decreased after each successive defoliation. Comparison between OP and P_{2D} reveals a good agreement although P_{2D} appears to be slightly higher than the OP for the majority of the measurements ($\overline{P_{2D} - OP} = 0.056$, $\sigma = 0.016$). The two metrics gradually converge at higher porosity values and in some cases P_{2D} becomes slightly larger than the OP. The best agreement between the two metrics is found for the fully defoliated fig when its porosity is measured from the S1, S2 and S3 surveying positions (respective residuals equal to 0.002, 0.004 and 0.003) and for the fully defoliated bamboo when its porosity is measured from the S4 surveying position (residual equal to 0.002). The lowest agreement is found for the fully foliated cedar when its porosity is measured from the S1 and S3 surveying positions (respective residuals equal to 0.164 and 0.185) and from the short grass when porosity is measured from the S2 and S4 surveying positions (respective residuals equal to 0.188 and 0.157). If the mean values of all surveying positions, presented in Table 5.3, are taken into account, the best agreement appears to be for the fully defoliated scots pine (residual equal to 0.001) and the lowest for the fully foliated cedar (residual equal to 0.156).

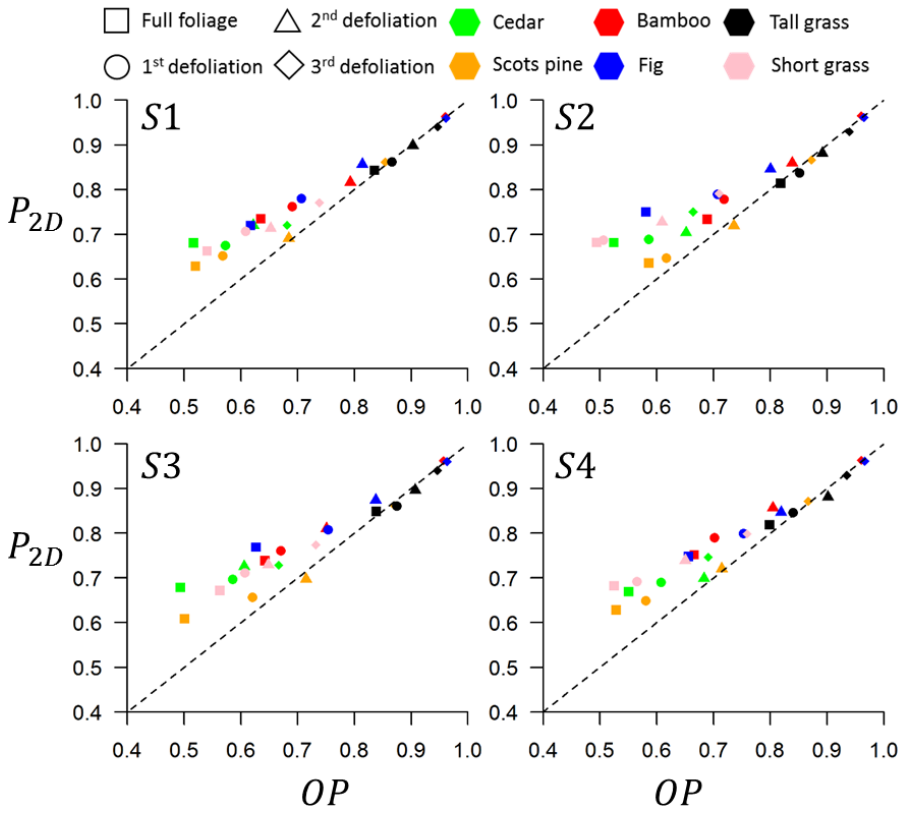

FIGURE 5.8: Comparison between Optical Porosity (OP) and 2D Porosity (P_{2D}) as they were estimated from each one of the four surveying positions (S1 to S4) (see Figure 5.2). The dashed line represents the 1:1 relationship.

TABLE 5.3: Residual values ($P_{2D} - OP$) corresponding to the plots of Figure 5.8 accompanied by the mean and standard deviation (σ)

Plant	**Foliage**	**Surveying position**				**Mean**	$\boldsymbol{\sigma}$
		S1	**S2**	**S3**	**S4**		
Bamboo	Full foliage	0.099	0.044	0.096	0.086	0.081	0.022
	1st defoliation	0.072	0.06	0.091	0.088	0.078	0.012
	2nd defoliation	0.024	0.021	0.059	0.052	0.039	0.017
	3rd defoliation	0.004	0.005	0.005	0.002	0.004	0.001
Cedar	Full foliage	0.164	0.157	0.185	0.119	0.156	0.024
	1st defoliation	0.103	0.103	0.111	0.082	0.1	0.011
	2nd defoliation	0.099	0.052	0.12	0.016	0.072	0.041
	3rd defoliation	0.039	0.086	0.062	0.056	0.061	0.017
Scots Pine	Full foliage	0.108	0.049	0.108	0.1	0.091	0.024
	1st defoliation	0.085	0.03	0.036	0.068	0.055	0.022
	2nd defoliation	0.007	-0.016	-0.017	0.006	-0.005	0.012
	3rd defoliation	0.007	-0.006	-0.009	0.005	-0.001	0.007
Fig	Full foliage	0.102	0.169	0.141	0.091	0.126	0.031
	1st defoliation	0.073	0.082	0.054	0.046	0.064	0.015
	2nd defoliation	0.043	0.046	0.037	0.028	0.038	0.007
	3rd defoliation	-0.002	-0.004	-0.003	-0.005	-0.003	0.001
Tall Grass	Full foliage	0.008	-0.005	0.01	0.02	0.008	0.009
	1st defoliation	-0.003	-0.014	-0.014	0.006	-0.006	0.008
	2nd defoliation	-0.005	-0.01	-0.011	-0.021	-0.012	0.006
	3rd defoliation	-0.006	-0.01	-0.006	-0.005	-0.007	0.002
Short Grass	Full foliage	0.122	0.188	0.109	0.157	0.144	0.031
	1st defoliation	0.099	0.181	0.104	0.127	0.128	0.033
	2nd defoliation	0.061	0.118	0.081	0.089	0.087	0.021
	3rd defoliation	0.032	0.081	0.042	0.039	0.049	0.019

5.6.2 Evaluation of 3D porosity

One key limitation of 2D metrics of plant structure is that their estimated values may vary depending on the viewing angle. For this reason, the approach of Gillies et al. (2000) was followed. OP and P_{2D} were estimated from four surveying positions and the individual estimates were averaged. The extracted mean values along with the standard deviation (σ) and the estimates of 3D porosity (P_{3D}) for all plant-foliage scenarios are presented in Table 5.4.

The estimates of 3D porosity (P_{3D}) are compared with the average values of optical ($\overline{OP}$) and 2D porosity (($\overline{P_{2D}}$) in Figure 5.9. Regression analysis was undertaken using the statistical software R 3.3.2 and a strong power law relationship was found between P_{3D} and the 2D metrics for each individual plant (the regression statistics are shown in Table 5.5). In the comparison between P_{3D} and ($\overline{OP}$) , the strongest correlation was found for the bamboo ($R^2 = 0.993$, P = 0.004) and the lowest for the tall grass ($R^2 = 0.880$, P = 0.062). In the comparison between P_{3D} and $\overline{P_{2D}}$ the bamboo and the short grass show an equally strong correlation between the two metrics ($R^2 = 0.990$, P $<$ 0.001). Notably, the lines corresponding to the different plant types appear to be

TABLE 5.4: Summary of porosity estimates for each plant under various conditions of foliage. Average optical porosity estimates ($\overline{OP}$) and standard deviations (σ) are derived from image processing of the four images for each vegetation scenario. Average 2D porosity estimates ($\overline{P_{2D}}$) and standard deviations (σ) are derived from TLS processing of the four individual scans for each vegetation scenario. 3D porosity estimates (P_{3D}) are derived from the processing of the registered TLS datasets for each vegetation scenario. Because of the high values of P_{3D} it is reported here with four points of precision.

Plant	**Foliage**	$\overline{OP}$	σ	$\overline{P_{2D}}$	σ	P_{3D}
Bamboo	Full foliage	0.658	0.021	0.739	0.007	0.9972
	1^{st} defoliation	0.695	0.017	0.773	0.012	0.9976
	2^{nd} defoliation	0.797	0.031	0.836	0.023	0.9983
	3^{rd} defoliation	0.96	0.002	0.964	0.001	0.9996
Scots pine	Full foliage	0.521	0.02	0.677	0.005	0.9948
	1^{st} defoliation	0.588	0.013	0.688	0.008	0.9951
	2^{nd} defoliation	0.641	0.03	0.712	0.011	0.9955
	3^{rd} defoliation	0.676	0.011	0.736	0.012	0.9959
Cedar	Full foliage	0.534	0.032	0.625	0.01	0.9951
	1^{st} defoliation	0.597	0.023	0.651	0.004	0.9953
	2^{nd} defoliation	0.712	0.018	0.707	0.013	0.9961
	3^{rd} defoliation	0.866	0.007	0.865	0.004	0.9982
Fig	Full foliage	0.62	0.027	0.746	0.017	0.9963
	1^{st} defoliation	0.73	0.023	0.794	0.01	0.9971
	2^{nd} defoliation	0.818	0.013	0.856	0.011	0.998
	3^{rd} defoliation	0.964	0.002	0.961	0.001	0.9995
Tall Grass	Full foliage	0.654	0.284	0.831	0.015	0.9987
	1^{st} defoliation	0.858	0.013	0.852	0.01	0.9989
	2^{nd} defoliation	0.901	0.006	0.889	0.008	0.9995
	3^{rd} defoliation	0.942	0.005	0.935	0.006	0.9995
Short grass	Full foliage	0.531	0.025	0.675	0.008	0.9907
	1^{st} defoliation	0.572	0.042	0.699	0.01	0.9914
	2^{nd} defoliation	0.64	0.018	0.727	0.009	0.9924
	3^{rd} defoliation	0.735	0.018	0.784	0.012	0.9941

grouped together and follow similar trajectories. The only exception appears for the short grass which, in both graphs of Figure 5.9 appears to be isolated, due to lower estimates of P_{3D} in comparison to the other plant types. This particular plant type was associated with high levels of mixed points (due to TLS noise) which could not be sufficiently identified and removed during the filtering process.

Although the R^2 values computed for each individual plant reveal a good agreement between 3D and 2D metrics, the P values computed are relatively large and in some cases (i.e. tall grass) the level of significance is below the threshold of $P<0.05$. Each plant was examined under four levels of foliage, and consequently each regression analysis was undertaken using four points only. This may be a factor affecting the magnitude of the P values. Nevertheless, when the model is computed using the combination of all of the plant types the levels of significance are increased sufficiently revealing that there is a clear relationship between 3D porosity and 2D metrics. When all plant types are used the R^2 values are equal to 0.702 and 0.625 for $\overline{OP}$ and $\overline{P_{2D}}$,

respectively (grey dashed lines in Figure 5.9). If the short grass is treated as an outlier and consequently not taken into account in the regression analysis the R^2 values become equal to 0.914 and 0.915, for $\overline{OP}$ and $\overline{P_{2D}}$, respectively with the P values being smaller than 10^{-10} in both cases (thick black lines in Figure 5.9).

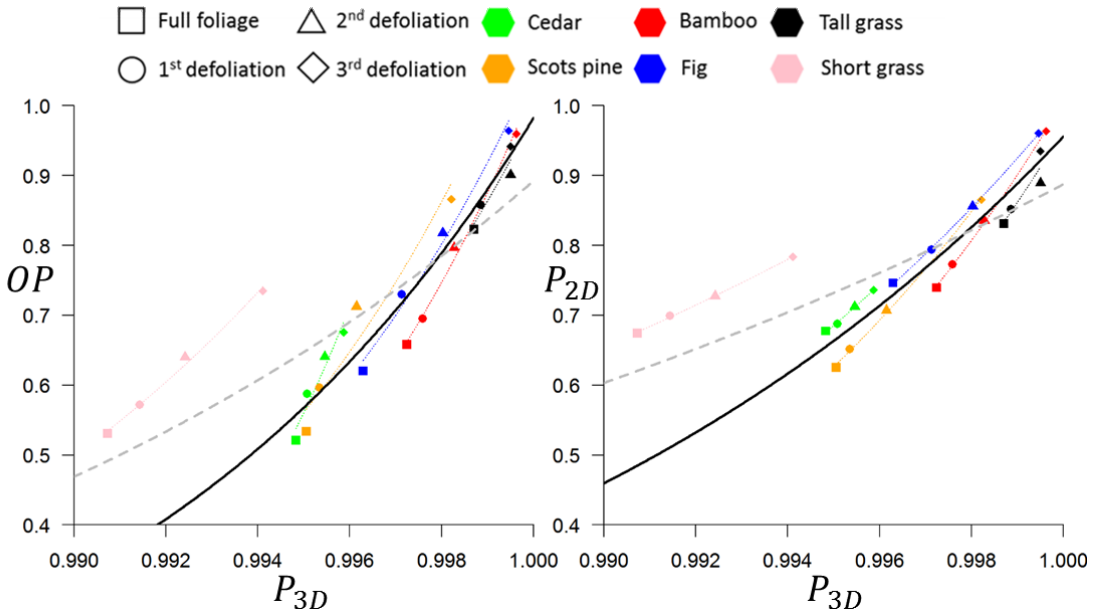

FIGURE 5.9: Comparison between 3D porosity (P_{3D}) with the average optical porosity ($\overline{OP}$) (left) and the average 2D porosity ($\overline{P_{2D}}$) (right). The grey, dashed line is the regression line computed for all of the plant-foliage scenarios, while the thick black line is the regression line computed when the short grass scenarios are excluded. All regression statistics are presented in Table 5.5.

TABLE 5.5: Regression statistics relating 3D porosity with optical and 2D porosity. Asterisks denote the level of significance following: $P < 0.05$ *, $P < 0.01$ **, $P < 0.001$ ***, $P < 0.0001$ ****.

Plant	P_{3D} - OP		P_{3D} - P_{2D}	
	R^2	P	R^2	P
Cedar	0.926	0.0380 *	0.996	0.0019 **
Scots pine	0.928	0.0366 *	0.998	0.0008 ***
Bamboo	0.993	0.0035 **	0.999	0.0006 ***
Fig	0.984	0.0078 **	0.995	0.0002 ***
Tall grass	0.88	0.0617	0.841	0.0832
Short grass	0.932	0.0034 **	0.999	0.0006 ***
All plants	0.702	3×10^{-7} ****	0.625	4×10^{-7} ****
All plants (except short grass)	0.914	5×10^{-11} ****	0.915	4×10^{-11} ****

5.7 Methodological considerations

5.7.1 2D porosity

In Subsection 5.6.1 small discrepancies were observed between OP and P_{2D}, where at low porosity values the P_{2D} metric produces systematically higher values than the OP, while at high porosity values the P_{2D} estimates are lower than the respective OP, although the latter is less accentuated. These discrepancies are likely the result of two distinct reasons. The first is associated to the much higher resolution that the camera is capable of delivering, in comparison to the TLS system. As mentioned in Section 5.2, the average distance between sensor and plant during the data collection varied between 3 and 3.8 metres with an average equal to 3.39 metres. The focal length of the imaging system was set to 80 mm and was kept constant at all times, while a single pixel of the camera sensor has a surface area equal to $41.09\,\mu m^2$ (Digicamdb.com, 2017). Therefore, using Equation (5.1):

$$\frac{PixelArea}{ObjectArea} = \frac{FocalLength}{Distance} \tag{5.1}$$

it is calculated that a single pixel of the camera's CMOS sensor corresponds to approximately $0.0017\,mm^2$ of plant frontal area. This is a much finer resolution than the $1\,mm^2$ achieved from the TLS system and is likely to have an effect on the estimated 2D metrics.

The second reason is associated with limitations of the TLS instrument. In Figure 5.6, on the surface of the leaf reconstructed from TLS data, empty cells can be observed. These gaps, which increase the estimated P_{2D}, could be the outcome of small deviations of the scanning point spacing during data acquisition or the result of overzealous filtering during the application of the SOR filter. On the other hand, the stem on the same figure appears to be larger when reconstructed from TLS data. This is likely related to the finite size of the laser footprint (see also 4.3.2.1). This could potentially overestimate the stem area and generate lower porosity values. The area occupied by leaves is larger than the area occupied by stems at full foliage scenarios but the ratio gradually changes after each successive defoliation. Therefore, the first type of error could potentially have a stronger influence under dense foliage and as the foliage is gradually removed, the influence of the second error type becomes apparent.

5.7.2 3D porosity

When the 3D porosity was compared to the optical and 2D porosities in Subsection 5.6.2, the short grass was characterised by much lower P_{3D} values in comparison to all other plants and appeared as an outlier (Figure 5.9). This is likely due

to increased TLS noise associated with this particular plant, that was not successfully removed when the filtering procedure was undertaken. It highlights that the extracted porosity metrics are inherently affected by limitations of the TLS technology. However, because there are no other surveying techniques capable of capturing the three dimensional plant structure at comparable levels of detail, the errors stemming from the existence of mixed points in the datasets cannot be quantified.

5.7.2.1 Occlusions

TLS is an optical method, and therefore, it is inherently prone to occlusions and shadowing effects. In some cases, this limitation can be negated if surveying is repeated from multiple positions. However, in cases where a solid, or even very dense, object is surveyed, occlusions cannot be avoided in the areas that the laser beam cannot physically penetrate. This means that the 3D porosity extraction routine will erroneously evaluate empty space in areas that are in fact solid and this will affect both the bulk P_{3D} metric as well as the derived 3D porosity array. An extreme example is presented in Figure 5.10 where a thin horizontal slice near the base of the dense tall grass is examined. High plant density prevents the laser beam from reaching the inner parts of the plant creating a hole in the dataset (Figure 5.10, B). In the next step when the binary array is generated this region is erroneously evaluated as empty space (Figure 5.10, C). This error is also propagated during the generation of the porosity array, where empty space is evaluated for some cells while others are assigned porosity values that are higher than the expected ones.

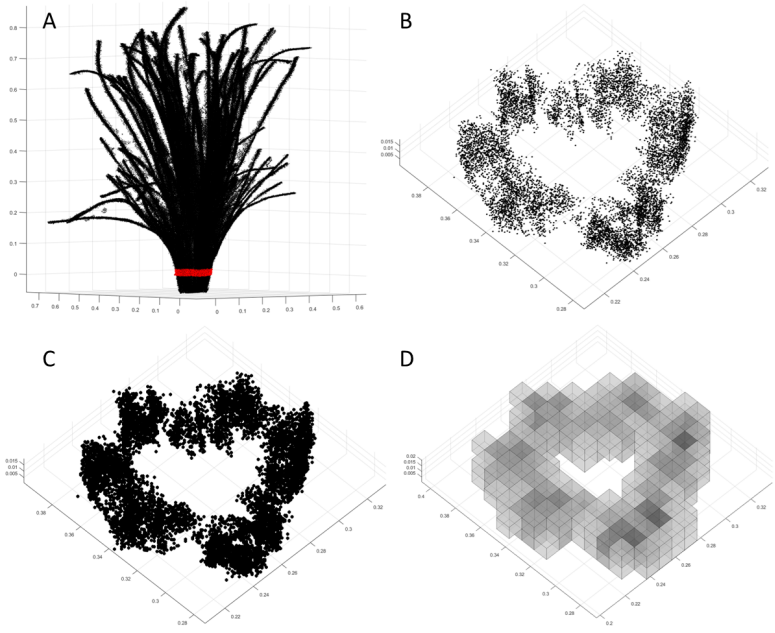

FIGURE 5.10: Thin horizontal slice (marked with red in A) near the base of the TLS point cloud of the tall grass highlights the effect of occlusions in the central region of the point cloud (B) as well as the derived binary grid (C) and porosity array (D). For the porosity array darker shades correspond to lower porosity values.

A method of accounting for these occlusions using a ray tracing approach, similar to the one described by Hosoi and Omasa (2006) was explored. However, implementing it to the large 3D binary grids was found to be computationally intensive and required an extreme amount of processing time, as such it was not employed in this study. However, the technique is worth exploring further. Nevertheless, the plants employed here are characterised by relatively sparse foliage and thin solid stems. Therefore, the amount of occlusions is minimal and assumed to generate only a limited bias in the results. It must be stressed though that if the 3D porosity extraction routine is applied in other studies that involve larger solid elements, for example those that seek to explore the effects of large woody debris dams in rivers, the occlusions of the central region of the solid elements might be greater and must be accounted for.

5.7.3 Computational requirements

The porosity extraction routines described earlier were undertaken using a desktop PC running Windows 7 and MATLAB R2015a, and equipped with an Intel core i7 CPU processor, clocked at 3.40 GHz, 32 GB of memory (RAM) and a standard mechanical Hard Disk Drive (HDD).

The 2D porosity extraction routine involved loading each individual point cloud into the system's memory, processing the point cloud to derive the 2D binary grid and calculating the bulk P_{2D} value (following the steps outlined in Section 5.4), then storing both the P_{2D} estimate as well as the binary grid in the directory. This process was not computationally intensive but the time required for each dataset varied (approximately between 1 and 30 seconds). The key factor affecting the time required is the scanning resolution and the extent of the plant, as they define the size of the bounding grid. This can be seen from Figure 5.12 where the required time increases linearly with the increasing size of the bounding grid, for a constant grid resolution equal to 1 mm. It must be noted that approximately 70% of the required time for the processing of each dataset was consumed into saving the binary grid on the HDD. Therefore, in cases where the spatial distribution of plant elements is not a requirement and a single bulk P_{2D} value would be sufficient, the required processing time is significantly shortened.

The 3D porosity extraction routine involved loading each individual point cloud into the system's memory, processing the point cloud to derive the 3D binary grid, calculating the bulk P_{3D} value (following the steps outlined in Section 5.5), then using the 3D binary grid to derive the 3D porosity array and finally storing the P_{3D} value, 3D binary grid and 3D porosity array in the directory. In contrast to the 2D porosity extraction routine, the 3D one was computationally intensive. The small voxel size (1 mm^3) meant that the amount of voxels consisting the binary grid could easily become too large for the system's RAM memory to handle it, resulting in computer crashes. For example, the binary grid derived for the fully foliated tall grass consists of more than 500 million voxels. For this reason, an additional step was added into the routine, whereby the input point cloud was

partitioned into eight sub-datasets in a spatial manner (example shown in Figure 5.11) and a binary grid derived for each sub-dataset (for more detail see the ViPER-3D function code in Appendix B). In this way for each point cloud input, eight binary grids and eight porosity arrays were derived and saved into the directory in separate files.

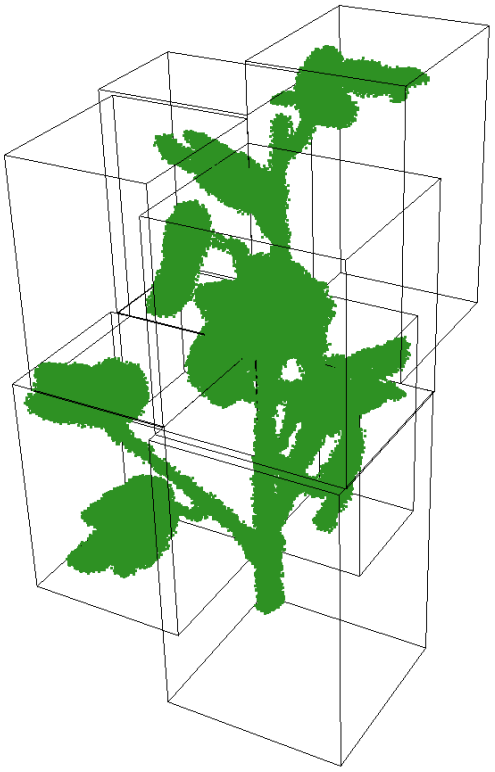

FIGURE 5.11: Example of partitioning the TLS point cloud into eight sub-datasets in spatial manner, in order to increase the code's computational efficiency.

Partitioning the point clouds into sub-datasets improved the code efficiency, however the processing time required was quite large although varied depending on the extent of the dataset (between 2 minutes and 5 hours). The key factor affecting the time required is, as before, the size of the binary grid (Figure 5.12) where for a constant voxel size equal to $1\,\mathrm{mm}^3$ the processing time required increases linearly for increasing grid extent. It must be noted that 97% of processing time was consumed into saving the binary grids into the directory, due to their vast size. Therefore, omitting this step will significantly decrease the required time for the procedure. Although the memory limitation, associated with the size of the binary grid, was resolved in the examples presented here by partitioning the point clouds into eight sub-datasets, this might not be sufficient if much larger point clouds are to be analysed (e.g. large scale trees). In this case further partitioning might be helpful, if for example the point cloud is partitioned into eight sets each one of which is further partitioned into eight subsets, the point cloud is effectively split into sixty-four smaller subsets that can be easily handled by the hardware.

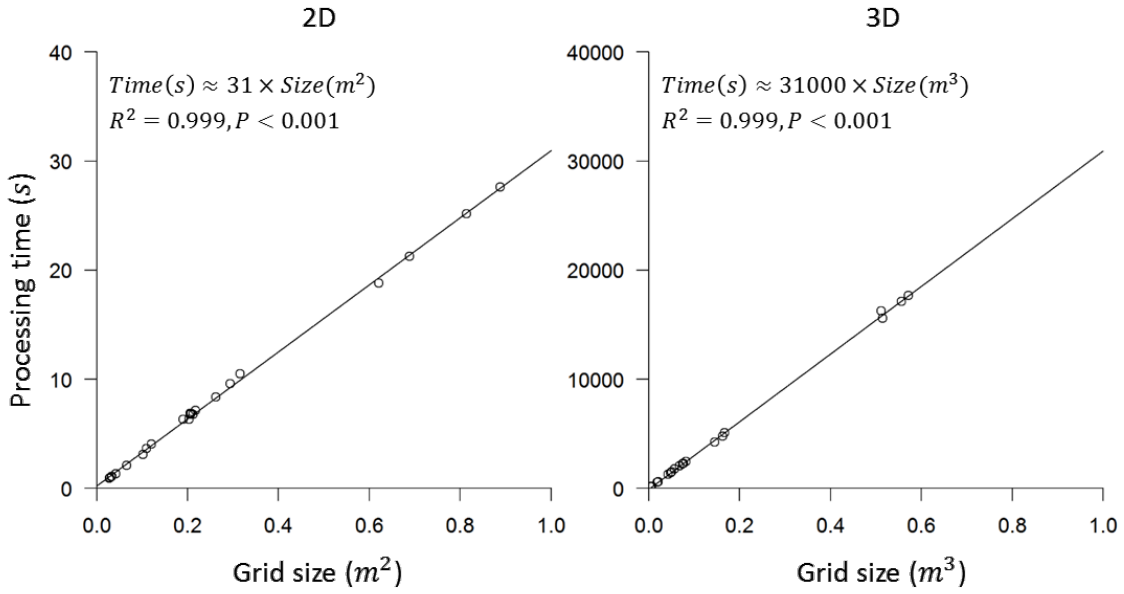

FIGURE 5.12: Computational time required as a function of the size of the binary grid for the 2D porosity (left) and 3D porosity (right) extraction routines.

5.8 Chapter summary

Two bulk metrics to characterise plant structure, based on a porosity approach where developed in the present Chapter, namely 2D porosity (P_{2D}) and 3D porosity (P_{3D}). Comparison between P_{2D} and the optical porosity (OP) shows a good agreement between the two metrics, although the estimates of P_{2D} presented a systematic bias at lower porosity values (i.e. higher foliage densities). However, as the amount of plant foliage is reduced after each successive defoliation step, the two metrics gradually converge with each other.

Comparison between the P_{3D} and the 2D metrics revealed a very good agreement. More importantly, the two types of metrics appear to be related by a universal model that is independent of plant type, at least for the plants examined in this study. The only exception was found for the short grass, which appears to be an outlier. This behaviour is likely the result of increased noise in the datasets associated with this individual plant and highlights a limitation of the TLS technology in terms of the identification and removal of erroneous points. The second limitation is related to the empty areas evaluated in the central region of solid or very dense plant scenarios, as a result of the inability of the laser beam to physically reach these areas. Because the plants used in this study are relatively sparse and are characterised by thin stems, the latter is assumed to have only a minor effect on the extracted P_{3D} metric.

The bulk 3D porosity metric (P_{3D}) is akin to the volumetric porosity (VP) introduced by Grant and Nickling (1998) who measured VP via simple water volumetric displacement. That is a laborious, destructive method and can easily lead to inaccurate

porosity estimates if water volume is not measured precisely. This perhaps explains why, although Grant and Nickling (1998) found a good agreement between VP and drag measurements, the metric has not been employed in more recent work. Instead, the majority of studies (*e.g.* Straatsma et al., 2008; Manners et al., 2013; Bywater-Reyes et al., 2017) have been limited by the employment of 2D metrics only. The development of the 3D bulk porosity extraction routine (ViPER3D) allows for a similar to the VP metric to be extracted, but based on the non-destructive laser scanning technology. Moreover, ViPER3D enables the measurement of additional metrics such as the plant extent on the lateral and streamwise directions. These supplementary metrics will be employed in Chapter 6 to fine-tune the bulk porosity estimates. Additionally, the routine was further expanded to construct 3D porosity arrays. They allow the detailed mapping of the 3D plant form, using discrete porosity values assigned to small unit spaces, and enable the discretisation and accounting of individual plant elements (e.g. stems, leaves) instead of lumping the complete plant structure into a single value. The extraction of 3D porosity arrays may revoke the considerations regarding the relationship between plant shape or structure and bulk porosity estimates that were discussed in subsection 3.3.3. 3D porosity arrays will be employed in Chapter 7.

Chapter 6

Investigating the Relationship between Plant Structure and Hydraulic Roughness

Chapter 5 focused on developing the novel methods needed to characterise plant structure in 2D and 3D using high resolution TLS data. The aim of the present Chapter is to link the novel plant structure metrics with the fluvial drag exerted by plants using a bulk roughness approach. To achieve this, a set of physical modelling experiments was undertaken in a flume, using a series of structurally variable plants. The methods of porosity extraction from TLS data, developed and discussed in Chapter 5, were adopted to characterise plant structure before and also during active flow via the employment of through-water TLS. Additional high resolution hydraulic data were obtained simultaneously, including flow velocity and water surface elevation measurements. The latter was used to extract water surface slope and to thereby estimate drag using a bulk roughness function. The overall setup and workflow of this set of experiments is described in detail in Section 6.1, while Section 6.2 outlines the steps undertaken to analyse the various obtained datasets and the derived outputs.

It was discussed in Chapter 3 that plants tend to reconfigure during flow and this can influence their geometrical characteristics and in turn affect the extracted P_{2D} and P_{3D} metrics. The employment of through-water TLS allows capturing of 'snapshots' of the plant structure during flow, and is used to quantify plant deformation in Section 6.3. Due to an increased amount of erroneous points littering the through-water TLS datasets, Section 6.4 focuses on assessing the quality of the datasets obtained via the through-water method.

The state-of-science of approaches to approximate plant structure and link it to the vegetative drag was reviewed in Chapter 3 and porosity was identified as a potential candidate, with less porous plants exerting a greater drag on the flow. However, plant

size, extent and streamlining may also affect drag. For this reason, an aggregate of supplementary metrics was extracted from the TLS datasets (using ViPER) and employed to fine-tune the P_{2D} and P_{3D} values. Section 6.5 compares the experimentally measured hydraulic roughness with a range of metric combinations extracted from both 'through-water' and standard TLS datasets, identifying the most appropriate combination of plant structure metrics to predict the fluvial drag exerted by plants. The key findings from the present Chapter are summarised in Section 6.7.

6.1 Physical modelling experiment

This section includes a detailed description of the flume experiment. It outlines the apparatus that was employed and how it was used, the scenarios that were investigated and describes in detail the workflow that was followed.

6.1.1 Flume setup

The physical modelling experiment was carried out using a rectangular, glass-walled, Armfield recirculating flume. The flume dimensions are 6.5×0.5×0.4 m (length×depth×width) (Figure 6.1). The flume is equipped with a pump that recirculates water, an overflow weir at the tail end to regulate water level and an inlet valve that regulates discharge.

The flume floor was covered with a false bed that extended from wall to wall. This was fabricated from marine plywood (18 mm thickness) placed on top of a base constructed from elements of timber studwork (38 mm thickness). Marine plywood was chosen due to its water resistance. Additionally, all wood elements were covered with waterproof paint to further minimise the danger of deformation once they were immersed underwater. Three sheets of marine plywood were required to cover a six meter long section, leaving uncovered two small sections (0.25 m long) near the flume inlet and outlet. All three plywood sections were fixed on the studwork base with screws. The upstream and downstream sections of the flume bed were sealed with adhesive, waterproof, sealant. The middle section was sealed using modelling clay. This setup allowed for the middle section to be easily removed when required, so that various plants could be fixed on it.

To assure a quick transition to a fully turbulent flow, three rectangular roughness elements were secured on top of the false bed, near the inlet, perpendicular to the direction of flow and extending from wall to wall. The height of these roughness elements was 38 mm, their width 63 mm and the distance between two individual elements was 25 cm. A rig constructed from aluminium rails was placed above the flume and securely fixed on top of the flume side panels. This allowed for various types of equipment to be mounted on it and used to obtain various measurements (see 6.1.1.1). Finally, a set of four HDS targets was situated at fixed locations surrounding the scene. They provided

tie points for the registration of the TLS datasets. A schematic of the flume set up is presented in Figure 6.1 below.

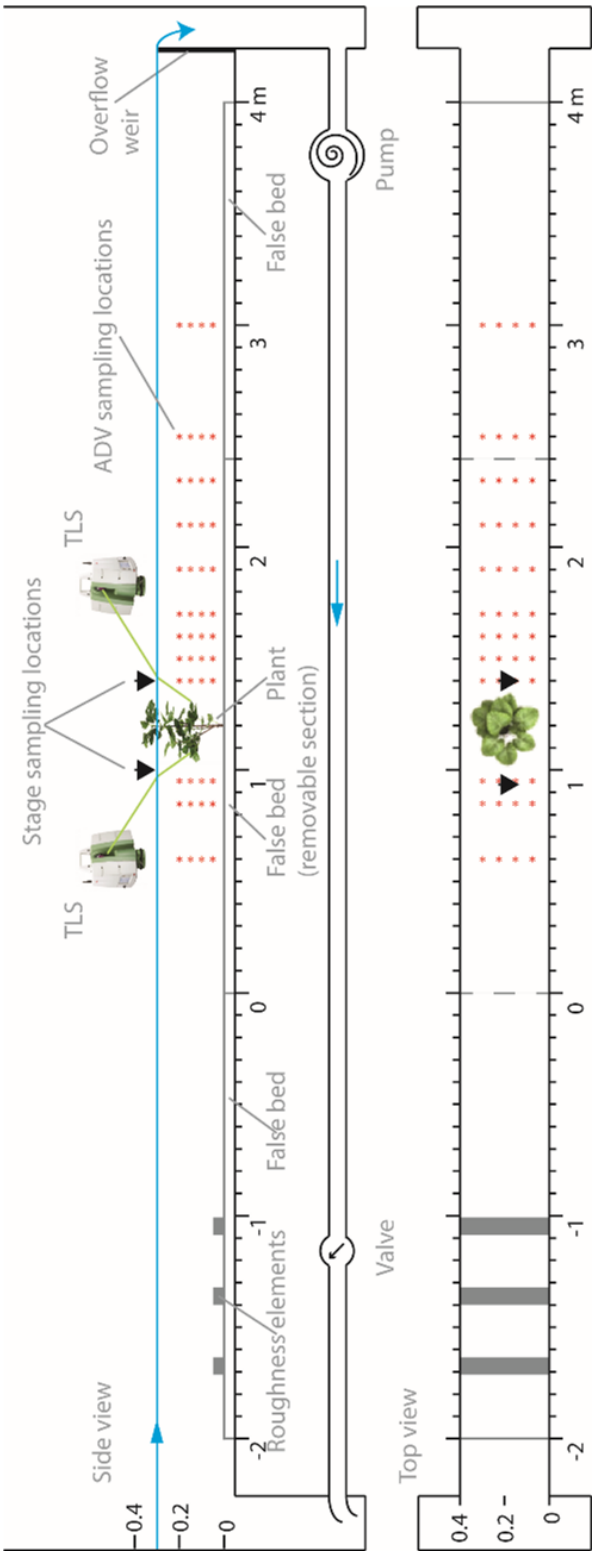

FIGURE 6.1: Schematic outlining the flume setup, showing the convergent scan locations, ADV sampling points and position of ultrasonic water surface measurement devices.

6.1.1.1 Instrumentation

The types of the equipment used are outlined herein. Similar to the workflow described in Chapter 5, a Leica C10 TLS was used to scan the plant elements. The characteristics and specifications of this scanner have been described in Chapter 5 and are not repeated in this section. A detailed description of how the TLS datasets were acquired is provided in subsection 6.1.3.

Acoustic Doppler Velocimetry (ADV)

Acoustic Doppler Velocimeters (ADVs) were employed to collect velocity measurements at high resolution. ADV probes record instantaneous values of the 3D velocity components (u,v,w in the x,y,z dimension, respectively) with a high frequency at a single point. This is achieved by employing the Doppler shift principle on sound waves that are reflected from the surface of small sound scattering particles, assuming that these particles move with a velocity similar to the fluid velocity (Lane et al., 1998). Thus, ADVs are capable of measuring the flow velocity at a single point and discretising this measurement to the three rudimentary velocity components (u,v,w). The point of measurement (sampling volume) is located 5 or 10 cm below the sensor head, ensuring that the interference to the flow field by the sensor itself is minimal. This also permits the acquisition of velocity measurements very near to the bed. Figure 6.1.2 presents the schematic of an ADV sensor head.

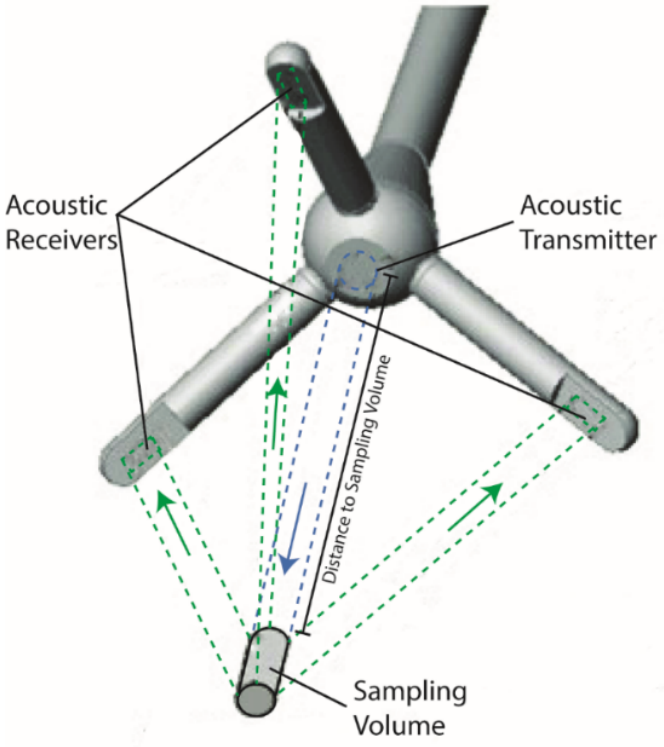

FIGURE 6.2: Schematic showing the principle components of an Acoustic Doppler Velocimetry (ADV) probe. Sound waves are emitted from the acoustic transmitter and are reflected from sound scattering particles that are passing through the sampling volume, while travelling with a similar to the flow velocity (Reproduced from SonTek, 2016).

The ability of ADVs to obtain instantaneous measurements of 3D velocity at high resolution makes them ideal for this study. However, ADV measurements are inherently characterised by a low signal to noise ratio. This means that the sampling duration at each location must be suitably long in order for a sufficient number of recordings to be obtained that can be later filtered in the post processing phase. This makes the acquisition of ADV data time consuming, especially when a large amount of point measurements is desired. For this reason, two identical ADV probes (SonTek 16 MHz MicroADV) were mounted on the ADV rig in a lateral format and were placed at a distance equal to 14 cm away from each other (see also Figure 6.4), permitting the survey of two point locations simultaneously, thus decreasing the surveying duration by 50%. The ADV probes employed are equipped with a downwards looking sensor. The distance from the acoustic transmitter to the sampling volume is 5 cm and the size of the sampling volume is 0.09 cm^3. The probes were carefully oriented to the downstream plane and secured on the ADV rig with ring clamps. The ring clamps were lined with synthetic rubber and were tightened to ensure that the probes would not get misaligned over time. A spirit level was fixed on top of the ADV rig to ensure that the probes were always positioned vertically during sampling. Both ADV probes were connected to a laptop running the vendor's proprietary software Sontek Horizon ADV v1.20.

Ultrasonic distance sensors

Two ultrasonic distance sensors (Senix Toughsonic 14) were used to record water surface elevations. Ultrasonic sensors measure the distance to an object (e.g. water surface) by emitting sound waves towards the object and measuring the time required for the sound echo to return to the sensor. Given that the speed of sound through air has a known, constant value, the sensor can determine the distance between the transmitter and the surface of interest (Figure 6.3).

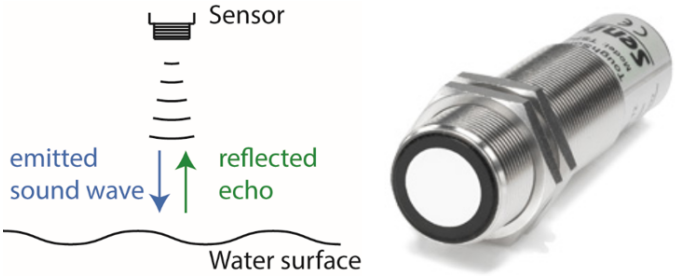

FIGURE 6.3: Schematic presenting the principles of ultrasonic ranging (left). Photograph of Senix Toughsonic 14 ultrasonic distance sensor (right) (Reproduced from Senix, 2015).

The advantages of ultrasonic sensors in comparison to other methods of measuring water surface elevation, such as stage boards, point gauges or capacitance probes are the superior measurement resolution, high signal to noise ratio, durability, easy set up, the ability to obtain multiple measurements over a period of time and that they do not affect the measured properties as they are positioned outside the flow. The models used in these experiments have a maximum sense range of 4.2 m and a minimum of 0.1 m. They can be set up to 0.1 mm resolution of measurement and they can perform one

measurement every second (1 Hz frequency). Both sensors were connected to a data logger (Delta-T Devices, GP1). Photographs of the complete setup during a run are presented in Figure 6.4.

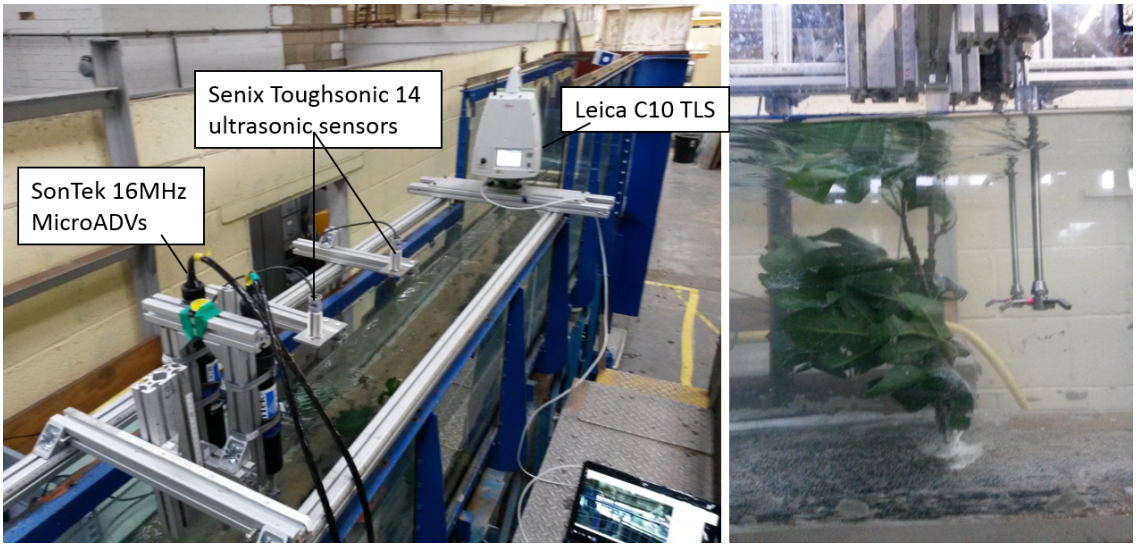

FIGURE 6.4: Photograph of the complete flume setup, the Leica C10 TLS, the Senix Toughsonic 14 ultrasonic distance sensors and the SonTek 16 MHz MicroADV probes in operation (left). Detail of the two ADV sensors obtaining velocity measurements near a plant element which is significantly deformed under active flow (right).

6.1.2 Scenarios

A range of sixty scenarios in total were investigated during this experiment. A series of five structurally variable plants were employed, they were subjected to three different flow scenarios and their foliage was progressively reduced, resulting in four foliage densities for each plant.

6.1.2.1 Plant scenarios

Identical plants to the ones examined in Chapter 5 were used for these experiments, namely fig, bamboo, tall grass, scots pine and cedar. The focus of the present work is on emergent vegetation. The short grass that was investigated in Chapter 5, being only 17 cm tall, would be fully submerged. Therefore, it was omitted from these experiments. The remaining plants were fixed on the flume bed one at a time. After a full set of flume runs was concluded, part of the plant foliage was removed and a new set of flume runs was initiated (see also Section 6.1.3 and flowchart in Figure 6.5). Each plant was progressively defoliated three times, and approximately an equal amount of foliage was removed each time, resulting in four foliage scenarios that are dubbed 'Full Foliage', '1st Defoliation', '2nd Defoliation' and '3rd Defoliation'. After all plants were investigated, a set of runs without any vegetation present in the flume, named 'Empty' was conducted

allowing for flume hydraulic characterisation (a set of base measurements) to be undertaken.

6.1.2.2 Flow scenarios

Flume runs were conducted under three flow scenarios (Table 6.1), named Deep-Slow, Medium, Shallow-Fast. For the Deep-Slow flow scenario the average flow depth was 0.3 m and the average flow velocity was 0.25 m s^{-1}. The Medium flow scenario had an average flow depth equal to 0.25 m and average flow velocity equal to 0.3 m s^{-1}. Finally, the Shallow-Fast flow scenario was characterised by an average flow depth equal to 0.2 m and flow velocity equal to 0.38 m s^{-1}. All three flow scenarios were characterised by subcritical and fully turbulent flows. This is demonstrated by their respective Froude and Reynold numbers shown on Table 6.1. Table 6.2 presents the scenario matrix of all the undertaken flume runs and the datasets that were collected each time.

TABLE 6.1: The flow scenarios that were investigated during the experiments

Flow Scenario	**Depth** (m)	**Velocity** (m s^{-1})	**Reynolds**	**Froude**
Dry	0	0	-	-
Deep - Slow	0.30	0.25	2.2 x 10^4	0.15
Medium	0.25	0.30	2.4 x 10^4	0.19
Shallow - Fast	0.20	0.38	2.8 x 10^4	0.27

6.1.3 Experimental procedure

In subsections 6.1.1 and 6.1.2 the experimental apparatus was described and the various scenarios were outlined. In the current section the workflow of a full experiment cycle is described in detail.

6.1.3.1 Fixing plants on the flume bed

The removable, middle, section of the false bed was perforated, so that an individual plant could be fixed in the gap, secured with screws and cable ties underneath and any gaps between the bed and the stem of the plant were filled with waterproof sealant. Subsequently, the false bed section was placed inside the flume, secured on the base with screws and sealed along the joints with adjoining boards and the flume walls with modelling clay.

6.1.3.2 Plant TLS survey

In the next step the Leica C10 TLS was mounted on the aluminium rig and the plant was surveyed. Similarly to the laser scanning described in Chapter 5, the scanning resolution was set to the highest allowed by the vendor's proprietary software Leica Cyclone 9.0 (i.e. 1 mm). The average distance between the plant and the scanner was approximately two meters. Due to space limitations, plant scanning was undertaken from two positions only, upstream and downstream of the plant element.

6.1.3.3 Collection of acoustic Doppler velocimetry data

Subsequently the flume run was initiated. Using the overflow weir at the tail end, the flow depth was adjusted to 0.3 m (Deep-Slow flow scenario) and sufficient time (approximately twenty minutes) was allowed for the flow to reach equilibrium. ADV measurements were surveyed at twelve cross-sections at various locations along the flume. The first cross-section was located well upstream of the plant element, at a sufficient distance (0.6 m upstream of the plant mounting point) to capture the unaffected inlet conditions. The next two cross-sections were near the plant element (0.35 m and 0.25 m upstream of the plant mounting point), to capture any back water effects produced by the presence of vegetation. The remaining cross-sections were located downstream of the plant at increasing distances (0.2, 0.3, 0.4, 0.5, 0.7, 0.9, 1.1, 1.3 and 1.8 meters downstream of the plant mounting point). Each ADV cross-section consisted of sixteen points (4 vertical $\times$ 4 lateral) at distances equal to 0.05, 0.1, 0.15 and 0.2 meters from the flume bed (at z/h approximately equal to 0.17, 0.3, 0.5 and 0.67, where z is the distance from the flume bed and h the water depth) and 0.09, 0.16, 0.23 and 0.3 metres from the flume's left side panel (see also Figure 6.1).

A velocity range is required as an input for the ADV instrument. If the measured velocity is higher than the user-defined velocity range, data aliasing takes place leading to velocity ambiguities (Wahl, 2000). The ADV sensors employed in these experiments allow the selection of a programmed velocity range from a set of discrete values (i.e. 3, 10, 30, 100 and 250 cm s^{-1}). From the available options, 100 cm s^{-1} was found to be the most appropriate as it was large enough to account for any flow acceleration occurring downstream of the vegetation element.

The second user-defined input that is required for the ADVs is related to the sampling frequency. The instrument collects data as quickly as possible and the collected records are then averaged internally at a user-defined sampling rate (Lane, 1998), ranging between 0.1 and 50 Hz. The 50 Hz option was selected for this experiment. Wahl (2000) suggest that it is best to select the highest possible sampling rate to avoid masking erroneous data when they are averaged with valid data before the sample is written to file.

Finally, each location was sampled for a duration of at least sixty seconds. The effect of the sampling duration on the turbulent statistics calculated has been discussed by Buffin-Bélanger and Roy (2005). Based on extensive analysis of a range of flow velocity data collected using ADVs and ECMs (electromagnetic current meters) they report that the optimal record length falls between 60 and 90 seconds and that it is slightly shorter for ADVs.

6.1.3.4 Plant structure characterisation during active flow

During the first flume run, significant plant reconfiguration was observed (see also photograph in Figure 6.4). This suggested that the plant structure, which had been scanned prior to being subjected to flow, was not a static metric. Therefore, it was imperative to capture 'snapshots' of the plant deformation during active flow. For this reason, through-water TLS was employed (the through-water TLS method is discussed in 6.2.2.1 below). Plant laser scanning was repeated, from the same positions as earlier and with identical scan settings but this time during active flow. This was possible because the Leica C10 TLS is employed with a green laser beam (532 nm). Green colour lasers have the highest water penetration and are typically employed in bathymetric LiDAR systems. Through-water TLS requires additional processing steps that are discussed in 6.2.2.1.

6.1.3.5 Water surface recording

In the following step, the ultrasonic sensors were employed to measure the distance to water surface immediately upstream and downstream of the plant element. Because of fluctuations of the water surface (i.e. ripples) due to the turbulent flow, the recording of the water surface was undertaken for a duration greater than ten minutes at 1 Hz frequency. This allowed for a sufficient number of measurements to be collected from which a mean elevation can be robustly averaged.

6.1.3.6 Preparation for the next run

Recording of the water surface elevation concluded a full set of measurements for the Deep-Slow scenario. Subsequently, using the overflow weir, the water depth was adjusted to 0.25 m for the Medium Scenario and later to 0.20 m for the Shallow-Fast flow scenario. The data collection process described above, was repeated for these two flow scenarios but because of the decreased flow depth as well as time constrains, no ADV data were collected. After the three scenarios had been investigated, the flume was emptied. An additional set of measurements with the ultrasonic sensors was obtained to measure the distance between the sensors and the false bed. Finally, part of the plant foliage was removed (or a new plant was fixed inside the flume) and the whole process was

reinitiated. The flowchart outlining a full working cycle of the flume experiments is presented in Figure 6.5.

6.1.3.7 Flume hydraulic characterisation (base measurements)

After all plant and flow scenarios had been investigated, the total extent of the flume was laser scanned when the flume was dry and one set of flume runs was undertaken without any vegetation being present in the flume. The water surface was recorded for all flow scenarios and ADV data were collected for the Deep-Slow flow scenario at identical cross-section locations. In this way the empty flume hydraulics were fully characterised and a set of base measurements collected for comparison with the experimental scenarios.

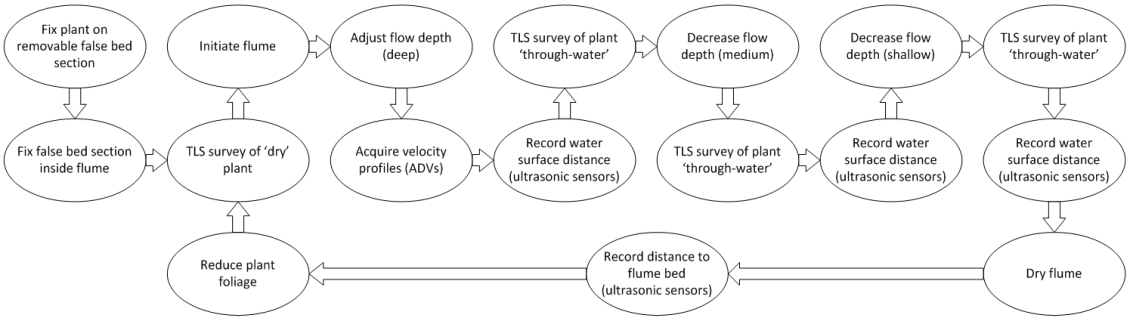

FIGURE 6.5: Flowchart summarising the workflow followed during the experiment for each individual plant type.

TABLE 6.2: Scenario matrix outlining the flume runs and the datasets that were collected each time.

Plant	Foliage Scenario	Flow Scenario	TLS	Ultrasonic	ADV	Plant	Foliage Scenario	Flow Scenario	TLS	Ultrasonic	ADV
Fig	Full Foliage	Dry	✓	✓	✗	Scots Pine	Full Foliage	Dry	✓	✓	✗
		Deep-Slow	✓	✓	✓			Deep-Slow	✓	✓	✓
		Medium	✓	✓	✗			Medium	✓	✓	✗
		Shallow-Fast	✓	✓	✗			Shallow-Fast	✓	✓	✗
	1st Defoliation	Dry	✓	✓	✗		1st Defoliation	Dry	✓	✓	✗
		Deep-Slow	✓	✓	✓			Deep-Slow	✓	✓	✓
		Medium	✓	✓	✗			Medium	✓	✓	✗
		Shallow-Fast	✓	✓	✗			Shallow-Fast	✓	✓	✗
	2nd Defoliation	Dry	✓	✓	✗		2nd Defoliation	Dry	✓	✓	✗
		Deep-Slow	✓	✓	✓			Deep-Slow	✓	✓	✓
		Medium	✓	✓	✗			Medium	✓	✓	✗
		Shallow-Fast	✓	✓	✗			Shallow-Fast	✓	✓	✗
	3rd Defoliation	Dry	✓	✓	✗		3rd Defoliation	Dry	✓	✓	✗
		Deep-Slow	✓	✓	✓			Deep-Slow	✓	✓	✓
		Medium	✓	✓	✗			Medium	✓	✓	✗
		Shallow-Fast	✓	✓	✗			Shallow-Fast	✓	✓	✗
Bamboo	Full Foliage	Dry	✓	✓	✗	Cedar	Full Foliage	Dry	✓	✓	✗
		Deep-Slow	✓	✓	✓			Deep-Slow	✓	✓	✓
		Medium	✓	✓	✗			Medium	✓	✓	✗
		Shallow-Fast	✓	✓	✗			Shallow-Fast	✓	✓	✗
	1st Defoliation	Dry	✓	✓	✗		1st Defoliation	Dry	✓	✓	✗
		Deep-Slow	✓	✓	✓			Deep-Slow	✓	✓	✓
		Medium	✓	✓	✗			Medium	✓	✓	✗
		Shallow-Fast	✓	✓	✗			Shallow-Fast	✓	✓	✗
	2nd Defoliation	Dry	✓	✓	✗		2nd Defoliation	Dry	✓	✓	✗
		Deep-Slow	✓	✓	✓			Deep-Slow	✓	✓	✓
		Medium	✓	✓	✗			Medium	✓	✓	✗
		Shallow-Fast	✓	✓	✗			Shallow-Fast	✓	✓	✗
	3rd Defoliation	Dry	✓	✓	✗		3rd Defoliation	Dry	✓	✓	✗
		Deep-Slow	✓	✓	✓			Deep-Slow	✓	✓	✓
		Medium	✓	✓	✗			Medium	✓	✓	✗
		Shallow-Fast	✓	✓	✗			Shallow-Fast	✓	✓	✗
Grass	Full Foliage	Dry	✓	✓	✗	Empty		Dry	✓	✓	✗
		Deep-Slow	✓	✓	✓			Deep-Slow	✗	✓	✓
		Medium	✓	✓	✗			Medium	✗	✓	✗
		Shallow-Fast	✓	✓	✗			Shallow-Fast	✗	✓	✗
	1st Defoliation	Dry	✓	✓	✗						
		Deep-Slow	✓	✓	✓						
		Medium	✓	✓	✗						
		Shallow-Fast	✓	✓	✗						
	2nd Defoliation	Dry	✓	✓	✗						
		Deep-Slow	✓	✓	✓						
		Medium	✓	✓	✗						
		Shallow-Fast	✓	✓	✗						
	3rd Defoliation	Dry	✓	✓	✗						
		Deep-Slow	✓	✓	✓						
		Medium	✓	✓	✗						
		Shallow-Fast	✓	✓	✗						

6.2 Analysis

Section 6.1 described the experimental setup, the methodological workflow that was followed and the datasets that were collected. The current section outlines the necessary processing steps undertaken to analyse the obtained datasets and the products that were derived. Subsection 6.2.1 focuses on the processing of the water surface recordings, obtained using the ultrasonic distance sensors. Subsection 6.2.2 outlines the processing routines that were followed to characterise the vegetation elements from the TLS data, while Section 6.2.3 describes the analysis undertaken for the ADV data.

6.2.1 Extracting water depth, slope and hydraulic parameters

As described in Section 6.1, ultrasonic distance sensors were used to record water surface elevation immediately upstream and downstream of the plant element for each flow scenario. These recordings were analysed in order for precise estimates of water depth to be derived. This is essential for the derivation of the water surface slope for each flume run, from which pertinent hydraulic parameters can be calculated. Furthermore, a precise estimate of water depth is required for the processing of the through-water TLS datasets that will be described further in 6.2.2.1.

6.2.1.1 Pre-processing

The distance measurements obtained from the ultrasonic sensors were recorded and stored in the data logger. The individual datasets were converted to text files and imported in MS Excel. Upon inspection, outliers were observed in most of the time series. These outliers likely resulted from miscommunications between the sensor and the data logger (dropped bytes). They were easy to identify, as they presented much greater and unrealistic distance values (Figure 6.6), and they were manually discarded. Subsequently, each one of the time series was averaged to obtain two discrete distance measurements for each scenario; upstream and downstream of the plant element.

In the next step the distance measurements recorded during active flow were subtracted from those that were recorded when the flume was dry. In this way accurate estimates of flow depth (h) immediately upstream and downstream of the plant element, as well as estimates of water surface slope ($S = \frac{h_2 - h_1}{\Delta x}$) were calculated. The mean standard error (ϵ) for depth estimates was calculated as $\pm 4 \times 10^{-5} m$. This error is propagated on the estimates of water surface slope, and its magnitude was calculated using the standard statistical method of error propagation and found equal to $\pm 10^{-4}$.

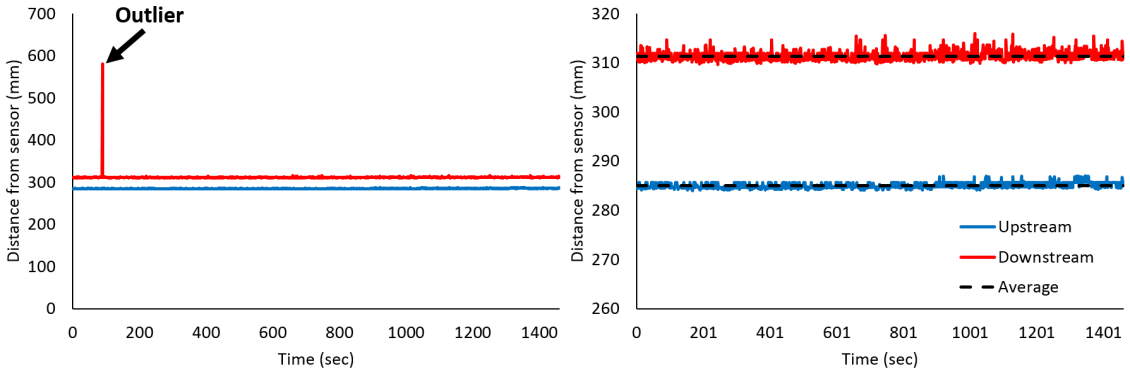

FIGURE 6.6: Time series presenting the recordings of distance between water surface and the ultrasonic sensors positioned immediately upstream and downstream of the plant element. Identified outliers (left) were manually removed. Averaging of the time series data provided the desired distance values (right).

6.2.1.2 Extraction of hydraulic parameters

The water surface slope is an indicator of the total drag exerted on the flow. This can be partitioned into two components; the vegetative drag and the drag exerted by the flume itself (friction of the flume bed and walls). In the 'Empty' scenario there was no vegetation present in the flume. This means that the water surface slope values that were measured during these scenarios were due to the flume drag only. Thus, these slope values were subtracted from the ones measured during all other scenarios, and the differences calculated are representative of the vegetative drag. The estimates of water depth were also used to derive the values of cross-sectional area (A_c) and wetted perimeter (P) and derive the hydraulic radius ($R_h = A_c/P$). Due the changing flow depth between flow scenarios and time constrains, ADV data were not collected for the 'Medium' or 'Shallow - Fast' flow scenarios. From the ADV data collected during the 'Empty', 'Deep - Slow' flume run the mean flow velocity was calculated equal to $U = 0.249\,\mathrm{m\ s^{-1}}$. The cross-sectional area for the same scenario was calculated equal to $A_c = 0.116\,\mathrm{m^2}$. Therefore, the flow discharge was estimated using Equation 3.11 and was found equal to $Q = 0.029\,\mathrm{m^3\ s^{-1}}$. The inlet valve setting was not altered for the duration of the experiments. Thus, the discharge calculated here is taken as constant for all of the flume runs undertaken and is combined with the cross-sectional area (A_c) measured for each individual run to estimate the mean flow velocity for each scenario. With known values of water surface slope, hydraulic radius and mean velocity, the Darcy-Weisbach friction factor (f) was calculated using Equation (2.14). A table containing the calculated hydraulic parameters for each scenario is presented in Appendix D. All of the above hydraulic parameters calculated are affected by the error that is present for the water depth estimates. Using the standard statistical method of error propagation, it is derived that for the estimates of Darcy-Weisbach friction factor an error (ϵ) should be assumed with a mean value equal to ± 0.05. Given that the range of Darcy-Weisbach friction factor values that were estimated is between 0.12 and 4.93 this error was regarded negligible.

6.2.2 Extracting plant porosity from the TLS data

Eighty TLS datasets were obtained from the flume experiments, each dataset corresponding to an individual combination of plant and flow scenario. These datasets can be grouped into two categories, those obtained when the flume was dry and those obtained when through-water TLS was employed. The processing steps undertaken for the extraction of porosity metrics from the TLS data is outlined in the flowchart of Figure 6.7 and described herein.

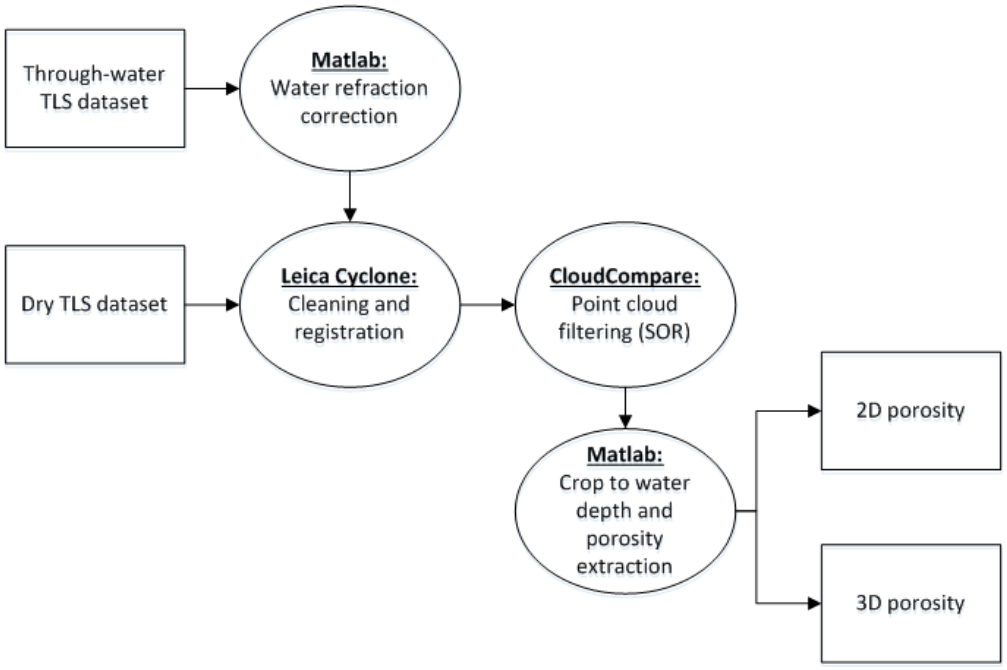

FIGURE 6.7: Flowchart outlining the key parts of the TLS data analysis.

6.2.2.1 Water refraction correction for the through-water TLS data

As described in subsection 6.1.3 during the first flume run it was realised that the vegetation elements are significantly deformed under active flow. Therefore, through-water TLS scanning was applied to capture snapshots of the plant reconfiguration. This was possible because Leica C10 TLS uses a green colour laser beam (wavelength 532 nm) which can penetrate the water column. Datasets that have been obtained with the through-water TLS method are inherently affected by errors arising from the refraction of the laser beam when it passes the boundary between two different media (i.e. air and water). However, the errors produced by the laser refraction are systematic and therefore can be corrected if additional processing steps are undertaken.

Snell's law states that when a wave passes through the boundary of two isotropic media it bends according to:

$$\frac{\sin\theta_a}{\sin\theta_w} = n_r \tag{6.1}$$

where θ_a is the incidence and θ_w the refraction angle, respectively (Figure 6.8). n_r is the refractive index the value of which depends on the properties of the transmission media, temperature and the wavelength of the laser beam. Based on the above, a method to correct through-water TLS data has been developed by Smith et al. (2012) and was used in this study. The processing steps undertaken for the water refraction correction are outlined herein.

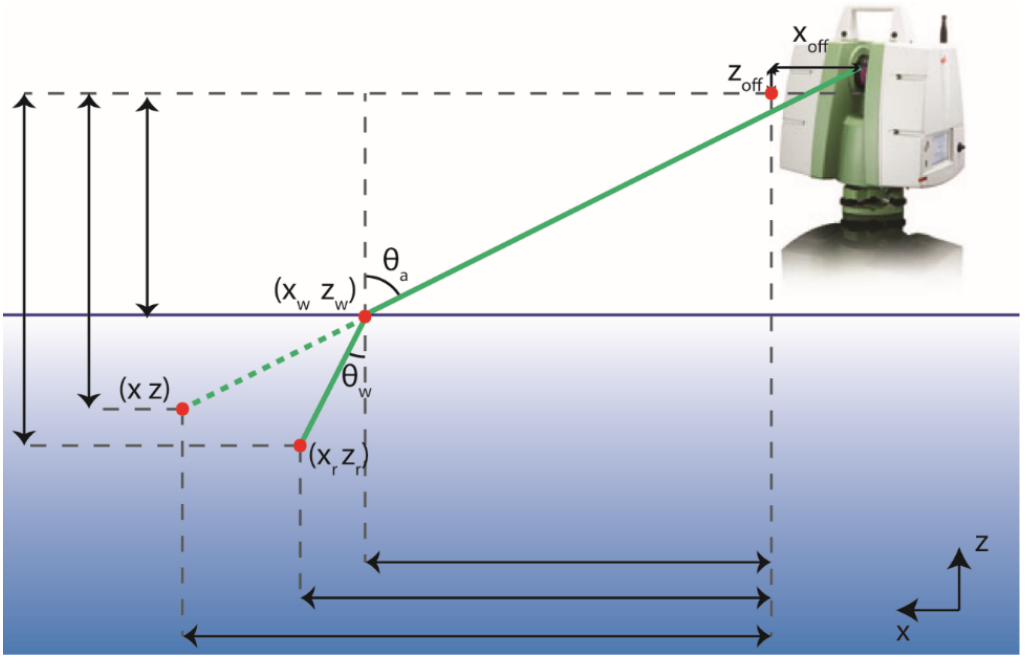

FIGURE 6.8: Geometry of TLS water refraction correction. x, z are the apparent coordinates of the point measured by the scanner and x_r, z_r are the real coordinates of the same point. x_w, z_w are the coordinates of the point where the laser beam meets the water surface and x_{off}, z_{off} are offset values related to the instrument's internal architecture (reproduced from Figure 1 of Smith et al., 2012).

The refraction of the laser beam is related to the scanner's position, the water surface elevation relatively to the scanner and the location of the recorded point. Therefore, the refraction correction must be applied to each point individually at every single scan dataset, prior to registration. All single scan datasets were exported from Leica Cyclone as ASCII text files and imported to MATLAB. In order for the correction procedure to be simplified, each point cloud was transformed from Cartesian to polar grid coordinates. The values of x_{off} and z_{off} was taken equal to the ones reported from Smith and Vericat (2014) ($x_{off} = 0.0168\,\text{m}$ and $z_{off} = 0.012\,\text{m}$), while z_w was derived from the ultrasonic water surface recordings. For the scan datasets obtained from a position upstream of the plant element, the upstream ultrasonic recording was used. Conversely, the downstream ultrasonic reading was used for the scan datasets obtained from a scanning position downstream of the plant element. The refractive index was taken equal to n_r=1.33538 Daimon and Masumura (2007). These inputs combined with the recorded (apparent)

point coordinates allowed for the calculation of the real point coordinates using simple trigonometry. In the last step the point coordinates were converted back to a Cartesian system, stored in ASCII text files and imported into Leica Cyclone for further processing.

6.2.2.2 Further processing of refraction-corrected and dry TLS datasets

The next steps that were undertaken for the processing of the TLS data include both dry and refraction corrected scan datasets and are similar to the routines described in Chapter 5. Using the vendor's proprietary software, Leica Cyclone v9.0, the single scan data were registered using the locations of the HDS targets; the registration error for each dataset was 0.001 m. In the next step the point clouds were reoriented so that the x-axis was horizontal and perpendicular to the flow direction, the y-axis was horizontal and parallel to the flow direction pointing downstream and the z-axis was vertical and pointing upwards. Subsequently, the registered datasets were manually cleaned and any parts of the point clouds that did not depict vegetation elements were discarded. In the next step the point clouds were exported in ASCII text files containing the 3D coordinates of each point.

The ASCII files were subsequently imported into CloudCompare v2.6.2 and were filtered using the Sparse Outlier Removal (SOR) filter. Similarly to the methods outlined in Chapter 5, each point was evaluated using the fifty closest neighbouring points (k) and one standard deviation for the k-nearest neighbour distances. The filtered outputs were inspected visually and exported as ASCII text files.

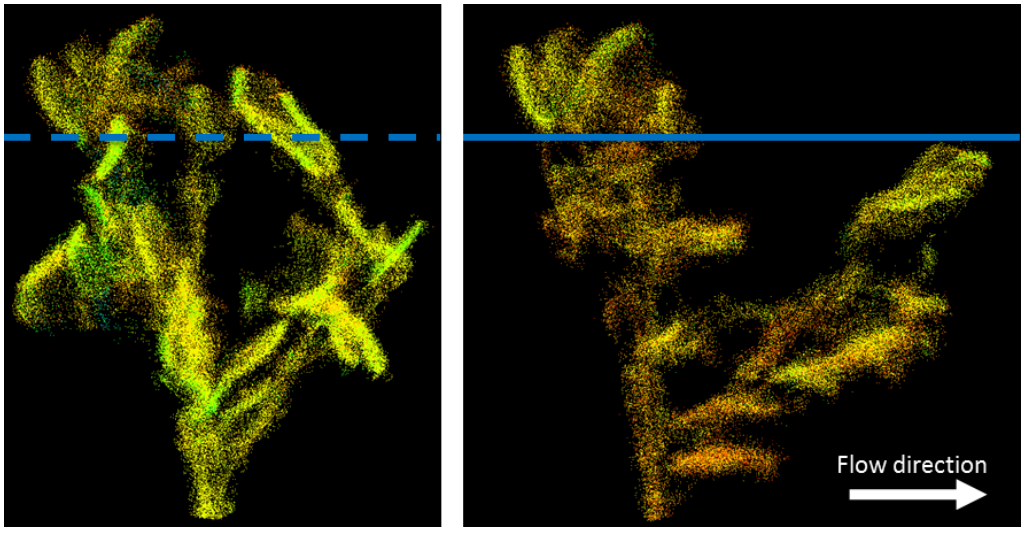

FIGURE 6.9: Side view of TLS scan dataset of fig tree before (left) and during (right) active flow. Blue line represents the approximate position of the water level (deep-slow flow scenario), the flow direction is from left to right.

Subsequently, the filtered point cloud data were imported in MATLAB so that porosity metrics could be extracted. For each flow scenario a different portion of a plant element was subject to flow, depending on the respective flow depth. Therefore, each dataset was

segregated in accordance to the three relevant flow scenarios that were investigated, using the flow depth derived from the ultrasonic measurements (see also 6.2.1).

In the next step bulk 2D (P_{2D}) and 3D (P_{3D}) porosity metrics were extracted and 3D porosity arrays were derived, following the methods described in Chapter 5. Because of the re-orientation of the scan datasets described earlier in this subsection, 2D porosity could be extracted from the point of view of the flow. The minimum bounding box for the estimation of the porosity metrics assigned to each dataset was defined by the plant extent on the streamwise and the cross-stream dimensions and by the water depth on the vertical dimension. Additional metrics that were derived from the TLS data included the streamwise (L) and the cross-stream (W) plant extent (mean, maximum and 80^{th} percentile) and the bulk 2D porosity measured using the plant planform area (P_{2Dpf}). The vegetation metrics extracted for each scenario are presented in Appendix E. From the example presented in Figure 6.9 it is obvious that 'through-water' TLS data are of reduced quality in comparison to the datasets acquired using 'standard' laser scanning techniques. The magnitude of this data degradation and its effect on the plant structure metrics will be further investigated in Section 6.4.

6.2.3 Extracting flow velocity from the ADV data

All ADV data were processed using WINADV32 V2.031. This software was developed by Wahl (2000) for use in the Bureau of Reclamation, US Department of the Interior and has been further improved through collaboration among the Bureau of Reclamation and two principal ADV manufacturers, SonTek and Nortek. WINADV32 has the capability of reading raw ADV files and processing them in a batch mode, involving a variety of filtering options. Outputs are saved both in individual text files as well as in a summary text file containing the average outputs of the entire processed group. The ADV data were grouped in clusters with each cluster corresponding to an individual flume run. These batches were imported into WINADV32 and filtered, using threshold values of the correlation coefficient (70%) and the signal to noise ratio (15 dB). These filtering threshold values are recommended by ADV manufacturers for the measurement of instantaneous velocities and turbulence quantities (Wahl, 2000). In the next step, following Goring and Nikora (2002), phase threshold despiking was undertaken. On average, 5% of each time series was discarded during the filtering and despiking routines.

Subsequently, the datasets underwent Reynolds decomposition. Each time series corresponding to a velocity vector measured at a single point, was partitioned to an average and a fluctuating part following Equation (6.2), where $\bar{u}$ is the time averaged part of the velocity and $u'$is the fluctuating one.

$$u_{(x,y,z,t)} = \overline{u}_{(x,y,z)} + u'_{(x,y,z,t)} \tag{6.2}$$

The outputs were summarised and stored in ASCII text files that included the name of

the respective ADV raw file, the average values of the three velocity vectors and the root-mean-square of the turbulent velocity fluctuations given by:

$$RMS[u'] = \sqrt{\overline{(u')^2}} = \sqrt{\frac{\sum u^2 - (\sum u)^2/n}{n-1}} \tag{6.3}$$

$$RMS[v'] = \sqrt{\overline{(v')^2}} = \sqrt{\frac{\sum v^2 - (\sum v)^2/n}{n-1}} \tag{6.4}$$

$$RMS[w'] = \sqrt{\overline{(w')^2}} = \sqrt{\frac{\sum w^2 - (\sum w)^2/n}{n-1}} \tag{6.5}$$

Here u, v, w are the three velocity components, u', v', w'their fluctuating parts and n is the number of velocity recordings in each time series. Subsequently, each ADV summary file was manually populated with the 3D location coordinates (x, y, z) of the surveyed point. The turbulent kinetic energy (TKE) was calculated from the fluctuating parts of the velocity vectors using Equation 6.6.

$$TKE = \frac{1}{2}\left(u'^2 + v'^2 + w'^2\right) \tag{6.6}$$

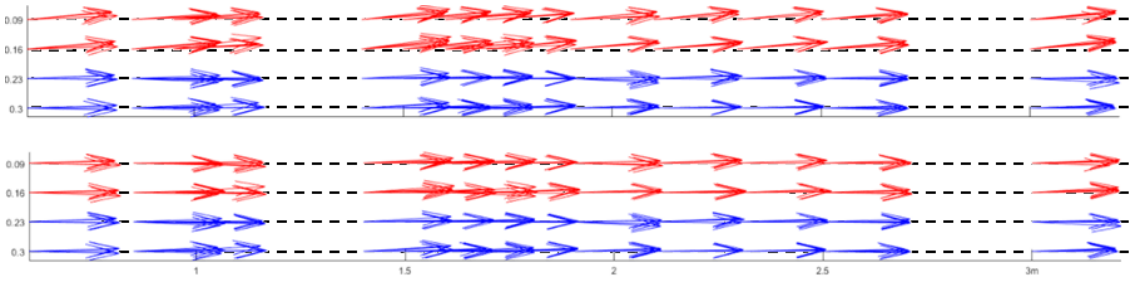

FIGURE 6.10: Top down view of 3D vector plots of the ADV data that were collected during the Empty Flume run. Colours are used here to identify the two individual ADV probes that were used. Red arrows deviate slightly from the horizontal axis due to probe misalignment (top) after applying a rotation on the XY plane both blue and red arrows are correctly aligned (bottom).

In the next step the summary files were imported into MATLAB and 3D vector plots were drawn and visually inspected. The vectors representing the velocity measurements taken at distances 0.09 and 0.16 m from the flume left side panel were deviating slightly towards the left. Although no conclusions could be drawn from the ADV data collected downstream of the plant elements, this tendency was also identified when looking at the ADV data collected during the empty flume run (Figure 6.10 top). This meant that the ADV probe that measured velocities at the respective points was slightly misaligned from the downstream plane. The average angle of deviation was calculated equal to $-3.542\,^{\circ}$, based on the data collected from the Empty Flume scenario, and because the probes were secured tightly on the ADV rig (see also 6.1.1.1) it was assumed that the probe misalignment was constant for the duration of the experiments. Therefore, a single correction was applied to all the velocity measurements that were obtained with the

misaligned probe. The original ADV files corresponding to the misaligned probe were analysed again using WINADV and a rotation of 3.542° on the XY plane was applied. This was followed by the application of identical processing methods with the ones described earlier in this section (filtering, despiking, Reynolds decomposition).

6.3 Plant reconfiguration during flow

As earlier discussed in Chapter 3, most plants tend to reconfigure (i.e. deform) under flow. This affects their structural characteristics such as streamwise and cross-stream extent and frontal area. Therefore, measuring the plant frontal area during different flow scenarios can provide information regarding the plant reconfiguration under active flow. Estimates of plant frontal area, for all flow scenarios, were extracted as a by-product of the bulk 2D porosity metric extraction routine (see also Chapter 5). Figure 6.11 compares the measurements of plant frontal area for each plant scenario under dry conditions and the three flow scenarios. The flow depth was not kept constant between flow scenarios, which means that a different portion of a plant was subject to flow each time. Therefore, for reasons of comparison all of the frontal area measurements presented in this figure correspond to the lower 20 cm portion of each plant (i.e. the minimum flow depth), regardless of the flow scenario that was investigated. These results are further described in the following subsections (6.3.1-6.3.3) and summarised in subsection 6.3.4. The plants are grouped into three categories; leafy plants which include the fig and the bamboo, plants with needle-like foliage including the cedar and the scots pine, and grass.

6.3.1 Leafy plants

When it was fully foliated the fig tree had a frontal area equal to $0.0218\,\mathrm{m}^2$ under dry conditions. As soon as the plant was subjected to Deep-Slow flow ($Re = 2.2 \times 10^4$) its frontal area decreased by 44% due to streamlining. A further increase in Reynolds number ($Re = 2.4 \times 10^4$) resulted in a further decrease of the frontal area by 5%. When the Shallow-Fast flow scenario ($Re = 2.8 \times 10^4$) was conducted the plant frontal area increased by 7%, suggesting that the leaves were slightly reoriented in a way that they presented a larger amount of their area to the flow. After the first defoliation the frontal area of the fig was equal to $0.0217\,\mathrm{m}^2$ under dry conditions. Subjecting the plant to active flow during the Deep-Slow flow scenario caused it to deform decreasing its frontal area by 42%, but a further increase of Reynolds number lead to an increase of the frontal area by 4% and 7% for the Medium and the Shallow-Fast flow scenarios, respectively. After the second defoliation the frontal area of the fig plant was equal to $0.0155\,\mathrm{m}^2$ under dry conditions. After the flume flow was initiated, plant reconfiguration occurred reducing the plant total area by 38% for a Reynolds number equal to 2.2×10^4 and an additional 5% for a Reynolds number equal to 2.4×10^4. A further increase of Reynolds number lead to an increase of frontal area by 12%. The fully defoliated fig shows a

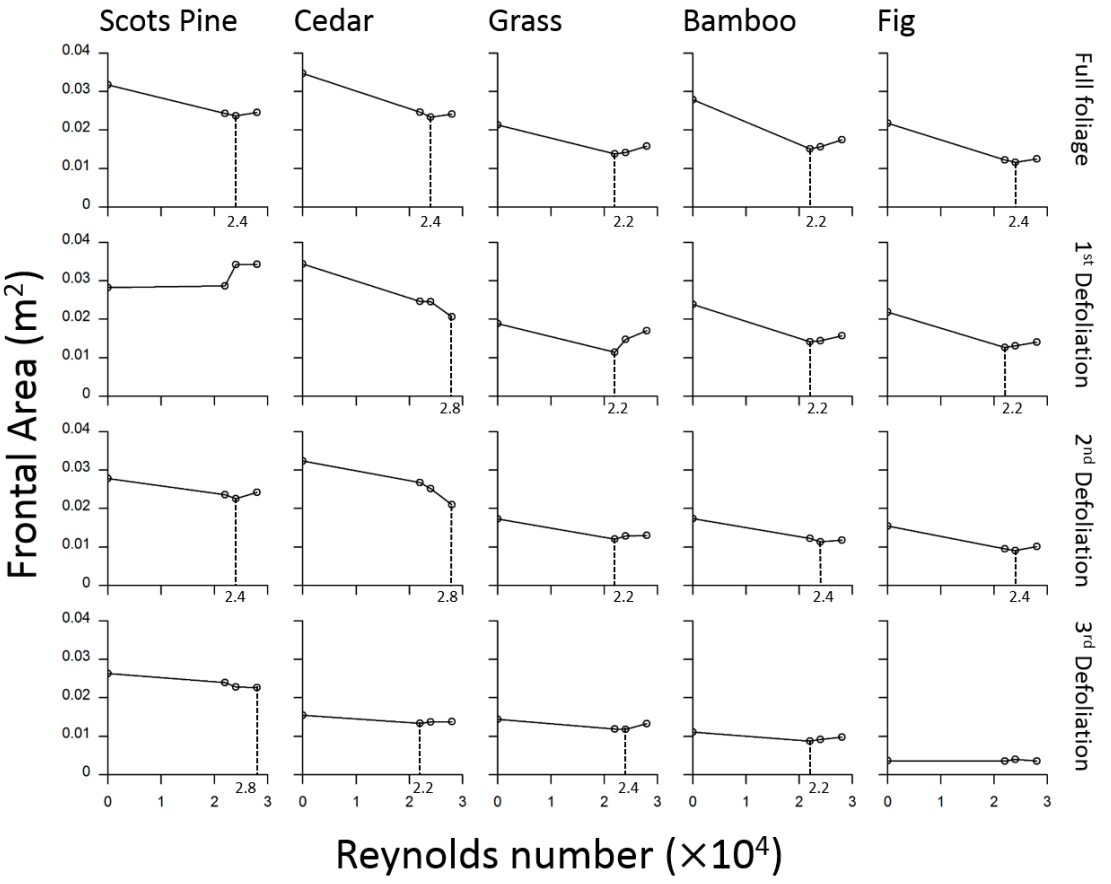

FIGURE 6.11: Changes of plant frontal area for each plant scenario under the various flow scenarios highlighting plant reconfiguration during active flow. Dashed lines show the Reynolds number where maximum plant deformation occurs.

minimal variation of frontal area between flow scenarios. Under dry conditions its frontal area is equal to $0.0036\,\mathrm{m}^2$ and becomes equal to $0.0035\,\mathrm{m}^2$, $0.0040\,\mathrm{m}^2$ and $0.0036\,\mathrm{m}^2$ when it is subjected to the Deep-Slow, Medium and Shallow-Fast flow scenarios, respectively.

The fully foliated bamboo had a frontal area equal to $0.0279\,\mathrm{m}^2$ under dry conditions. When it was subjected to Deep-Slow flow plant reconfiguration occurred, reducing its frontal area by 46%. When the Reynolds number was increased to 2.4×10^4 and subsequently to 2.8×10^4 the plant frontal area increased by 3% and 11%, respectively. A similar behaviour was observed after the first defoliation. The plant frontal area was equal to $0.0239\,\mathrm{m}^2$ and when the flow was initiated it decreased by 41%, while subsequent increase of Reynolds number led to an increase of the frontal area by 2% and 9% for the Medium and Shallow-Fast flow scenarios, respectively. After the second defoliation the frontal area of the Bamboo was equal to $0.0174\,\mathrm{m}^2$ under dry conditions. When it was subjected to flow it reconfigured reducing its frontal area by 30% for $Re = 2.2 \times 10^4$ and 7% for $Re = 2.4 \times 10^4$. A subsequent increase of Reynolds number to $Re = 2.8 \times 10^4$ resulted in an increase of plant frontal area by 4%. The fully defoliated bamboo had a frontal area equal to $0.0111\,\mathrm{m}^2$ which marginally decreased when it was

subjected to flow. The values of frontal area for Deep-Slow, Medium and Shallow-Fast flow were $0.0088\,\mathrm{m}^2$, $0.0092\,\mathrm{m}^2$ and $0.0098\,\mathrm{m}^2$, respectively.

6.3.2 Grass

The frontal area of the fully foliated grass under dry conditions was equal to $0.0213\,\mathrm{m}^2$. Subjecting it to flow with a Reynolds number equal to 2.2×10^4 forced the grass to deform, reducing its frontal area by 35%. Further increases in the Reynolds number led to an increase of the grass's frontal area by 3% and 12% for Re equal to 2.4×10^4 and 2.8×10^4, respectively. A similar behaviour of the grass is observed after the first and second defoliation. When it is initially subjected to flow the frontal area of the plant is reduced but a further increase of Reynolds number leads to an increase of the measured frontal area. This behaviour becomes very prominent after the first defoliation where the initial frontal area is equal to $0.0189\,\mathrm{m}^2$ and although it is reduced by 39% during the Deep-Slow flow scenario, subsequent increases of the Reynolds number are accompanied by increases of the frontal area by 29% and 15%.

6.3.3 Plants with needle-like foliage

The cedar had a frontal area equal to $0.0347\,\mathrm{m}^2$ under dry conditions when it was fully foliated. Active flow forced the plant to reconfigure reducing its frontal area by 29% during the Deep-Slow flow scenario and subsequently by 5% during the Medium flow scenario. Under the Shallow-Fast flow the frontal area of the fully foliated cedar increased by 3%. After the first defoliation the frontal area of the cedar was equal to $0.0344\,\mathrm{m}^2$ under dry conditions. Subjecting the cedar to active flow and the consequent plant deformation caused the frontal area to be reduced by 28%, 0.5% and 16% for the Deep-Slow, Medium and Shallow-Fast scenario, respectively. A similar behaviour was observed after the second defoliation of the cedar plant. The frontal area under dry conditions was equal to $0.0323\,\mathrm{m}^2$ and was reduced by 17%, 6% and 17% when it was subjected to active flow with Reynolds numbers equal to 2.2×10^4, 2.4×10^4 and 2.8×10^4, respectively. The bare cedar had a frontal area equal to $0.0155\,\mathrm{m}^2$ the value of which decreased during the Deep-Slow flow scenario by 13%, and subsequently increased by 2% and 1% during the Medium and Shallow-Fast flow scenario, respectively.

The scots pine had a frontal area equal to $0.0318\,\mathrm{m}^2$ when it was fully foliated under dry conditions. When it was subjected to Deep-Slow flow it reconfigured reducing its frontal area by 24% and subsequently by 2% during the Medium flow scenario. Transitioning to the Shallow-Fast flow scenario lead to an increase of plant frontal area by 4%. After the first defoliation the scots pine had a frontal area equal to $0.0282\,\mathrm{m}^2$, subjecting it to flow scenarios with gradually increasing Reynolds number lead to increase of the frontal area by 2%, 19% and 0.3%, for Reynolds equal to 2.2×10^4, 2.4×10^4 and 2.8×10^4, respectively. This is in juxtaposition with what was observed from the fully foliated scots

pine and also for the other foliage scenarios that will be described further below. It is likely that when the first defoliation took place, the fixtures underneath the false bed that were securing the plant got loosen. This allowed for the plant to become loose during active flow, affecting the estimated frontal area. Therefore, this individual plant scenario is discarded and will not be involved in any further analysis. After the second defoliation the frontal area of the scots pine was equal to $0.0278\,\mathrm{m}^2$ under dry conditions. Under Deep-Slow flow plant reconfiguration reduced the measured frontal by 15% while increasing the Reynolds number from 2.2×10^4 to 2.4×10^4 further reduced the frontal area by 5%. A further increase of the Reynolds number resulted in an increase of the frontal area by 8%. After the scots pine was defoliated for the last time its frontal area was equal to $0.0263\,\mathrm{m}^2$ under dry conditions and decreased when the plant was subjected to flow. Specifically, its frontal area was equal to $0.024\,\mathrm{m}^2$, $0.0229\,\mathrm{m}^2$ and $0.0226\,\mathrm{m}^2$ for the Deep-Slow, Medium and Shallow-Fast flow scenario, respectively.

6.3.4 Summary

In the graphs of Figure 6.11 a general trend can be identified. Comparison between the plant frontal area measured under dry conditions with respective values obtained during active flow for all flow scenarios, revealed that considerable plant deformation occurred. The reconfiguration occurring during the Deep-Slow flow scenario reduced the frontal area by 28% on average. This percentage can be further partitioned to 33% for leafy plants, 19% for plants with needle-like foliage and 31% for grass. Similarly, when the frontal area measurements that were obtained under dry conditions are compared with the values measured under Medium flow reveals an average plant frontal area reduction equal to 27% which can be further partitioned to 32% for leafy plants, 22% for plants with needle-like foliage and 25% for the grass. Comparing the values of frontal area obtained during the Shallow-Fast flow with the one obtained under dry conditions shows an average frontal area reduction equal to 24%, which corresponds to 29% for leafy plants, 24% for plants with needle-like foliage and 17% for grass.

The differences between frontal area values measured under dry conditions and those measured during active flow were expected. It has been previously discussed (subsections 3.3.2 and 3.3.3) that plants tend to deform under active flow, adjusting the amount of frontal area that is presented to the flow each time. In regard to the increased values of frontal area that was found for the Medium and Shallow-Fast flow scenarios, in comparison to the ones measured for the Deep-Slow flow scenario, Gillies et al. (2002) conducted wind tunnel experiments with real plants and found that, for a certain range of velocities, plants showed a tendency to align their leaves with their maximum projected area perpendicular to the flow direction. However, the authors report that this behaviour is observed at much higher Reynolds numbers (between 4.6×10^4 and 19×10^4) than the ones involved in the experiments discussed here, but also for a different medium (i.e. air).

Another possible explanation for the discrepancies of plant frontal area with increasing Reynolds number is related to artefacts originating from TLS noise. At higher flow velocities, and associated turbulence, some leaf fluttering occurred. Moreover, the water surface during the Medium and the Shallow-Fast flow was rougher in comparison to the water surface during the Shallow-Fast flow, especially downstream of the plant elements. This is likely to affect the water-refraction correction routine, as a perfectly horizontal water surface is assumed for this method. Consequently, this is likely to have increased the amount of mixed points in the TLS datasets, affecting the estimated frontal area values. Another possible explanation is that during the Deep-Slow flow scenario the force exerted from the flowing water to the plant elements was large enough to cause them to attain a maximum reconfiguration. The flow scenarios that followed (i.e. Medium, Shallow-Fast) did not vary sufficiently to change the frontal area. Any minor changes are likely to be within the magnitude of the data noise and thus difficult to measure from the methods employed here. The additional TLS noise imposed in the datasets that were acquired with the through-water method will be investigated in Section 6.4 below.

The plants employed in these experiments are artificial plant surrogates, consisting of synthetic materials and so although their physical characteristics are realistic in terms of the shape, size and structure (i.e. leaves or needles, branches), their flexibility may not fully resemble the biomechanical properties of real vegetation. Nevertheless, quantifying the reconfiguration of the plants employed in these experiments is required in order to better understand the relationship between plant structure and hydraulic roughness under various flow conditions (see Section 6.5).

6.4 Assessing the quality of the through-water TLS datasets

The TLS datasets that were obtained following the 'through-water' procedure appear to be of a lower quality (with respect to number of recorded points and the noise in the data) in comparison to the ones acquired using 'standard' laser scanning techniques. This is due to irregularities of the water surface (i.e. ripples), rapid attenuation of the laser beam when it travels through water, suspended material, air bubbles and plant movement due to the water flow (e.g. leaf fluttering). This may have an effect on the extracted plant structure metrics that were derived and will be later presented in Section 6.5. Quantification of the magnitude of this error requires the comparison between 'through-water' and 'standard' TLS datasets. However, this is not possible for the majority of the datasets presented in this study, because of the plant reconfiguration that occurred due to flow. Nevertheless, the fully defoliated fig showed a negligible reconfiguration and thus it is used to investigate the magnitude of error that degrades the 'through-water' TLS data. The scan datasets of the fully defoliated fig tree were cropped at the common flow depth of all flow scenarios (i.e. 0.2 m) (Figure 6.12). Subsequently, the total number of points is derived for each dataset along with the frontal area, 2D and 3D porosity. The results are presented in Figure 6.13.

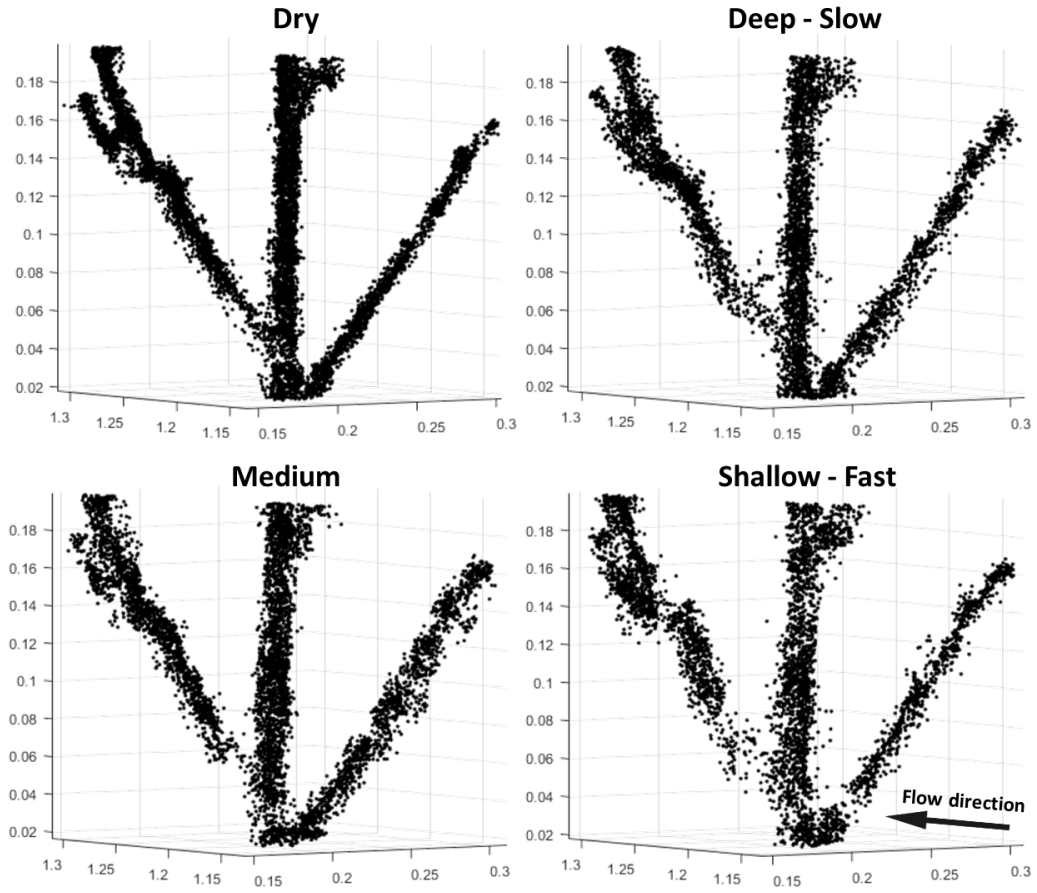

FIGURE 6.12: TLS datasets of the fully defoliated fig obtained using 'standard' and 'through-water' laser scanning procedures.

The total number of points in the dataset obtained using the 'standard' laser scanning procedure is much greater in comparison to the datasets acquired via the employment of 'through-water' TLS. In detail, the 'standard' scan dataset contains 7043 points in total. Under deep flow, the total amount of points is reduced by 27.5%. Under medium flow the total number of points in the 3D point cloud is slightly higher (5326 points) but still remains lower by 24.4% than the original dataset. Finally, shallow flow degrades the dataset even further (by 38.6%). If the rapid attenuation of the laser beam when it travels through the water column was the only factor affecting the quality of the TLS data, the dataset acquired under deep flow would have been the most degraded one. However, there are a number of other factors influencing data quality. Smith and Vericat (2014) undertook a series of experiments to evaluate the magnitude of errors produced by a number of factors in through-water TLS data. They examined the effect of flow velocity, suspended material and surface irregularities, among others. Their findings suggest that the errors arising from each one of these individual factors reduces the data quality but in an acceptable level. However, the authors acknowledge that the combined effect of the examined factors, although it was not tested, may be significant. In the experiments discussed here, shallower flow scenarios were characterised by increased flow velocity and associated turbulence. This means that for shallower and faster flows, the

amount of water surface irregularities (ripples), air bubbles forming in the water as well as stem trembling are likely to be greater. The cumulative effect of these factors has resulted in a greater degradation of the 3D point clouds observed in shallower flow scenarios.

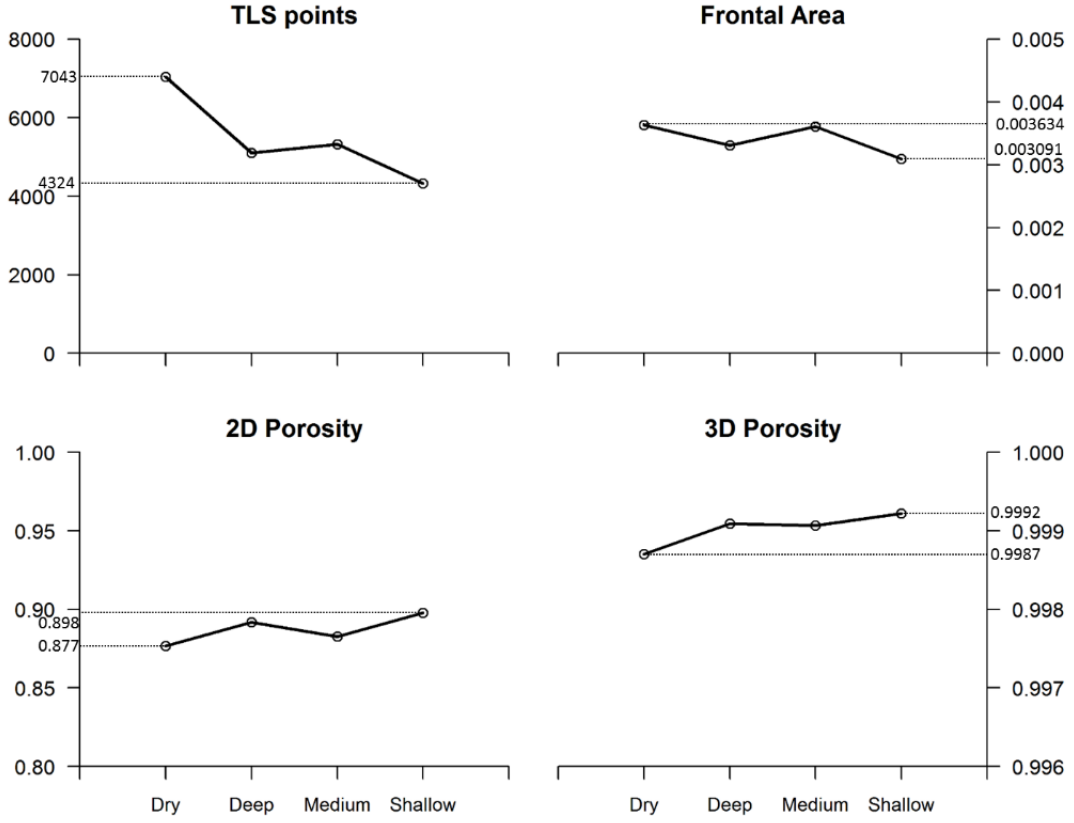

FIGURE 6.13: Total number of points of the TLS dataset for the fully defoliated fig acquired using 'standard' and 'through-water' TLS methods (top left), corresponding frontal area (top right), bulk 2D porosity (bottom left) and 3D porosity (bottom right) estimates.

The reduction of the total number of TLS points has an effect on the estimates of plant structure metrics. However, as shown in Figure 6.13 its propagation is not linear. In more detail, the frontal area estimate under deep flow is reduced from 0.0036 m^2 to 0.0033 m^2 (9%) and subsequently is increased to 0.0036 m^2 under medium flow (0.7% lower than the original frontal area) while under shallow flow it is decreased to 0.0031 m^2 (15% lower than the original frontal area). The bulk 2D porosity estimated using the 'standard' TLS data is equal to 0.877, under deep flow the estimate is increased to 0.892 (1.7%) and subsequently reduced to 0.883 (0.7% higher than the original value) under medium flow, while under shallow flow it becomes equal to 0.898 (2.4% higher than the original value). The estimate of bulk 3D porosity from the 'standard' TLS data is equal to 0.9987, during the deep and medium flow scenarios it is increased to 0.9991 (0.04% increase), while under the shallow flow scenario it becomes equal to 0.992 (0.05% higher than the original value). It must be noted that foliated plants are likely to be also affected by errors related to leaf fluttering due to flow, however this cannot be quantified

by the datasets obtained in this study and will not be further investigated.

6.5 Associating plant structure and hydraulic roughness

One of the vital questions related to this research is in regards to which bulk plant structure metric is the most pertinent to be associated with hydraulic roughness. Factors that are likely to be involved include plant porosity as well as plant extent and streamlining during flow. Therefore, a variety of 2D and 3D metrics were extracted from both 'standard' and 'through-water' TLS data. These metrics include the bulk 2D porosity from the point of view of the flow (P_{2D}) but also using the planform plant area (P_{2Dpf}), the bulk 3D porosity (P_{3D}), the streamwise plant extent (L) and the cross-stream plant extent (W). From the streamwise and the cross-stream plant extents a streamlining factor (SF) can be derived using the ratio $SF = L/W$, as well as a measure of the total plant extent (or planar area) (A_b) using $A_b = L \times W$. The cross-stream and streamwise plant extents were calculated for the mean, maximum and 80^{th} percentile. A sketch showing examples of the vegetation structure metrics that were extracted from the TLS data is presented in Figure 6.14, while all of the metrics and their combinations that are explored herein are presented in Table 6.3. The hydraulic roughness is expressed using the Darcy-Weisbach friction factor (f).

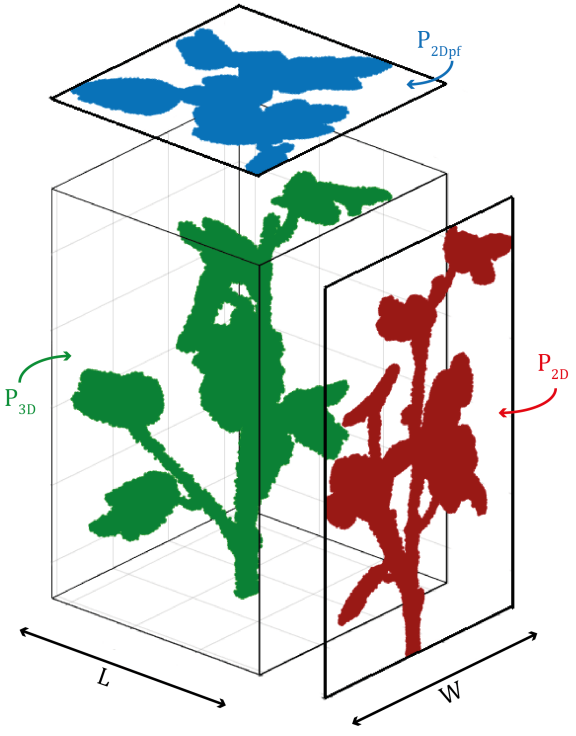

FIGURE 6.14: Sketch showing an example of the vegetation structure metrics that were derived from the TLS data.

Graphs comparing all of the 2D and 3D metrics and their combinations presented in Table 6.3 were created using the statistical software R v3.3.2 and can be found in

TABLE 6.3: Plant structure metrics and their combinations.

2D metrics:	P_{2D}	P_{2D}/W	P_{2D}/L	$P_{2D} \times SF$	P_{2D}/A_b	$P_{2D} \times P_{2Dpf}$
3D metrics:	P_{3D}	P_{3D}/W	P_{3D}/L	$P_{3D} \times SF$	P_{3D}/A_b	$P_{3D} \times P_{2Dpf}$

Appendix F (Figures F.1 to F.12). The relationship between plant structure and hydraulic roughness does not appear to be linear. However, a strong linear relationship was identified when the natural logarithms of some of the plant structure metrics and the natural logarithms of the hydraulic roughness were investigated (the R^2 and the P values for all combinations of plant structure metrics with the hydraulic roughness are presented in Table 6.4). This means that a power function describes the relationship between plant structure and hydraulic roughness more effectively. This finding is further supported by the work of Luhar et al. (2008) who fit power curves to describe the relationship between Manning's n and the blockage factor B^X proposed by Green (2005). From the R^2 values presented herein, some metric combinations show high correlation between plant structure and hydraulic roughness, while others perform poorly. In order for a metric to be considered suitable it must perform equally well in all of the flow scenarios that were investigated using both 'through-water' and 'standard' scan datasets.

TABLE 6.4: R^2 and P values of the regression analysis for each metric that was investigated for all flow scenarios. For simplicity only P values that were equal or greater than 0.001 are stated on this table, in all other cases 'P<0.001' is added instead.

Metric	Deep-Slow		Medium		Shallow-Fast	
	Through-water	Standard	Through-water	Standard	Through-water	Standard
P_{2D}	0.854,P<0.001	0.774,P<0.001	0.887,P<0.001	0.825,P<0.001	0.788,P<0.001	0.772,P<0.001
P_{2D}/W_{max}	0.833,P<0.001	0.651,P<0.001	0.876,P<0.001	0.694,P<0.001	0.840,P<0.001	0.678,P<0.001
P_{2D}/W_{80}	0.825,P<0.001	0.667,P<0.001	0.843,P<0.001	0.731,P<0.001	0.836,P<0.001	0.625,P<0.001
$P_{2D}/\overline{W}$	0.804,P<0.001	0.680,P<0.001	0.858,P<0.001	0.760,P<0.001	0.780,P<0.001	0.657,P<0.001
P_{2D}/L_{max}	0.480,P=0.001	0.510,P<0.001	0.536,P<0.001	0.605,P<0.001	0.538,P<0.001	0.671,P<0.001
P_{2D}/L_{80}	0.479,P=0.001	0.596,P<0.001	0.584,P<0.001	0.743,P<0.001	0.521,P<0.001	0.752,P<0.001
$P_{2D}/\overline{L}$	0.505,P<0.001	0.691,P<0.001	0.578,P<0.001	0.818,P<0.001	0.668,P<0.001	0.781,P<0.001
$P_{2D} \times SF_{max}$	0.622,P<0.001	0.649,P<0.001	0.587,P<0.001	0.553,P<0.001	0.394,P=0.004	0.288,P=0.02
$P_{2D} \times SF_{80}$	0.596,P<0.001	0.580,P<0.001	0.585,P<0.001	0.450,P=0.002	0.309,P=0.01	0.175,P=0.07
$P_{2D} \times \overline{SF}$	0.566,P<0.001	0.457,P=0.001	0.553,P<0.001	0.434,P=0.002	0.398,P=0.004	0.206,P=0.05
P_{2D}/A_{bmax}	0.607,P<0.001	0.519,P<0.001	0.649,P<0.001	0.577,P<0.001	0.695,P<0.001	0.633,P<0.001
P_{2D}/A_{b80}	0.688,P<0.001	0.609,P<0.001	0.711,P<0.001	0.730,P<0.001	0.696,P<0.001	0.693,P<0.001
$P_{2D}/\overline{A_b}$	0.640,P<0.001	0.678,P<0.001	0.692,P<0.001	0.796,P<0.001	0.711,P<0.001	0.722,P<0.001
$P_{2D} \times P_{2Dpf}$	0.783,P<0.001	0.809,P<0.001	0.761,P<0.001	0.774,P<0.001	0.668,P<0.001	0.658,P<0.001
P_{3D}	0.521,P<0.001	0.460,P=0.001	0.512,P<0.001	0.444,P=0.002	0.385,P=0.005	0.266,P=0.02
P_{3D}/W_{max}	0.644,P<0.001	0.451,P=0.002	0.695,P<0.001	0.442,P=0.002	0.649,P<0.001	0.475,P=0.001
P_{3D}/W_{80}	0.716,P<0.001	0.563,P<0.001	0.721,P<0.001	0.607,P<0.001	0.715,P<0.001	0.504,P<0.001
$P_{3D}/\overline{W}$	0.707,P<0.001	0.604,P<0.001	0.769,P<0.001	0.687,P<0.001	0.639,P<0.001	0.571,P<0.001
P_{3D}/L_{max}	0.189,P=0.06	0.252,P=0.03	0.205,P=0.05	0.270,P=0.02	0.327,P=0.01	0.420,P=0.003
P_{3D}/L_{80}	0.225,P=0.04	0.399,P=0.004	0.310,P=0.01	0.525,P<0.001	0.358,P<0.007	0.644,P<0.001
$P_{3D}/\overline{L}$	0.280,P=0.02	0.578,P<0.001	0.328,P=0.01	0.734,P<0.001	0.520,P<0.001	0.721,P<0.001
$P_{3D} \times SF_{max}$	0.149,P=0.1	0.094,P=0.2	0.13,P=0.1	0.050,P=0.4	0.078,P=0.2	0.000,P=1
$P_{3D} \times SF_{80}$	0.246,P=0.03	0.257,P=0.03	0.199,P=0.06	0.101,P=0.2	0.056,P=0.3	0.000,P=1
$P_{3D} \times \overline{SF}$	0.174,P=0.08	0.098,P=0.2	0.115,P=0.2	0.053,P=0.3	0.027,P=0.5	0.001,P=0.9
P_{3D}/A_{bmax}	0.445,P=0.002	0.376,P=0.005	0.467,P=0.001	0.389,P=0.004	0.579,P<0.001	0.495,P<0.001
P_{3D}/A_{b80}	0.565,P<0.001	0.529,P<0.001	0.598,P<0.001	0.642,P=<0.001	0.619,P<0.001	0.635,P<0.001
$P_{3D}/\overline{A_b}$	0.543,P<0.001	0.631,P<0.001	0.584,P<0.001	0.761,P<0.001	0.630,P<0.001	0.687,P<0.001
$P_{3D} \times P_{2Dpf}$	0.680,P<0.001	0.686,P<0.001	0.612,P<0.001	0.655,P<0.001	0.453,P=0.002	0.497,P<0.001

The bulk 2D porosity (P_{2D}) performs well for all flow scenarios using either the 'through-water' or the 'standard' TLS datasets (R^2 values range between 0.772 and 0.887). The ratio of 2D porosity over the cross-stream plant extent (P_{2D}/W) also shows a good correlation. In regards to the most appropriate value of cross-stream plant extent to be used for this ratio, the mean value shows the highest consistency between scenarios (R^2 values range between 0.657 and 0.858). The ratio of 2D porosity over the streamwise

plant extent (P_{2D}/L) shows an average performance when using the 'through-water' TLS datasets with the lowest R^2 being equal to 0.480 and the highest equal to 0.668, but when 'standard' scan datasets are used the performance of the metric is improved (R^2 values ranging between 0.510 and 0.818). The highest correlation for this ratio is achieved when the mean value of the streamwise plant extent is used. The product of bulk 2D porosity and streamlining factor ($P_{2D} \times SF$) shows low to medium correlation (R^2 values range between 0.175 and 0.649). The ratio of bulk 2D porosity over the total plant extent (P_{2D}/A_b) performs well (R^2 values range between 0.519 and 0.796), especially when the mean values of cross-stream and streamwise plant extent are used for the estimation of A_b. Interestingly, 'standard' scan datasets appear to perform better than 'through-water' ones. The combination of bulk 2D porosity and bulk planform 2D porosity ($P_{2D} \times P_{2Dpf}$) shows good correlation for all flow scenarios using both 'through-water' and 'standard' TLS data, with the R^2 values ranging between 0.658 and 0.809.

The bulk 3D porosity (P_{3D}) shows an average to low correlation (R^2 values range between 0.521 and 0.266). The ratio of 3D porosity over the cross-stream plant extent (P_{3D}/W) performs better. Specifically, when the mean value of the cross-stream plant extent is used the R^2 values range between 0.571 and 0.769. The ratio of 3D porosity over the stream wise plant extent (P_{3D}/L) performs poorly with the R^2 values ranging between 0.189 and 0.520 when 'through-water' TLS data are used. However, employment of 'standard' scan datasets improves the performance of the metric (maximum R^2 value is equal to 0.734). The combination of bulk 3D porosity with the streamlining factor ($P_{3D} \times SF$) shows low to no correlation with the highest R^2 value being only 0.257 and the lowest being 0.000. But the ratio of bulk 3D porosity over the total plant extent (P_{3D}/A_b) performs quite well, especially when A_b is derived from the mean values of W and L and 'standard' TLS datasets are used. Finally combining 3D porosity and planform 2D porosity ($P_{3D} \times P_{2Dpf}$) performs averagely with the R^2 values ranging between 0.686 and 0.453.

From the R^2 values that were presented earlier a mean and a standard deviation were derived using all types of scan datasets or after separating those obtained using 'standard' procedures from those acquired via 'through-water' TLS (Table 6 5). Based on the fact that a metric must perform equally well when 'through-water' or standard TLS datasets are used, the metrics that show some potential for associating plant structure and hydraulic roughness are the 2D porosity the ratio of 2D and 3D porosity over the mean value of the plant extent (using either the cross-stream, streamwise or total extent) and the combination of porosity with the planform 2D porosity. All of these metrics will be individually investigated in subsections 6.5.1 and 6.5.2.

TABLE 6.5: Mean and standard deviation values derived from the R^2 values of Table 6.4 using only the TLS datasets that were obtained via the 'through-water' method, or only the ones acquired using 'standard' scanning procedures, or all of the datasets regardless of scanning procedure.

Metric	**Through-water**		**Standard**		**All**	
	Mean	$\boldsymbol{\sigma}$	**Mean**	$\boldsymbol{\sigma}$	**Mean**	$\boldsymbol{\sigma}$
P_{2D}	0.843	0.041	0.790	0.025	0.817	0.043
P_{2D}/W_{max}	0.850	0.019	0.674	0.018	0.762	0.090
P_{2D}/W_{80}	0.835	0.007	0.674	0.044	0.755	0.086
$P_{2D}/\overline{W}$	0.814	0.033	0.699	0.044	0.757	0.069
P_{2D}/L_{max}	0.518	0.027	0.595	0.066	0.557	0.064
P_{2D}/L_{80}	0.528	0.043	0.697	0.072	0.613	0.103
$P_{2D}/\overline{L}$	0.584	0.067	0.763	0.053	0.674	0.108
$P_{2D} \times SF_{max}$	0.534	0.100	0.497	0.153	0.516	0.131
$P_{2D} \times SF_{80}$	0.497	0.133	0.402	0.169	0.449	0.159
$P_{2D} \times \overline{SF}$	0.506	0.076	0.366	0.113	0.436	0.119
P_{2D}/A_{bmax}	0.650	0.036	0.576	0.047	0.613	0.056
P_{2D}/A_{b80}	0.698	0.010	0.677	0.051	0.688	0.038
$P_{2D}/\overline{A_b}$	0.681	0.030	0.732	0.049	0.707	0.048
$P_{2D} \times P_{2Dpf}$	0.737	0.050	0.747	0.065	0.742	0.058
P_{3D}	0.473	0.062	0.390	0.088	0.431	0.087
P_{3D}/W_{max}	0.663	0.023	0.456	0.014	0.559	0.105
P_{3D}/W_{80}	0.717	0.003	0.558	0.042	0.638	0.085
$P_{3D}/\overline{W}$	0.705	0.053	0.621	0.049	0.663	0.066
P_{3D}/L_{max}	0.240	0.062	0.314	0.075	0.277	0.078
P_{3D}/L_{80}	0.298	0.055	0.523	0.100	0.410	0.138
$P_{3D}/\overline{L}$	0.376	0.104	0.678	0.071	0.527	0.175
$P_{3D} \times SF_{max}$	0.119	0.030	0.048	0.038	0.084	0.049
$P_{3D} \times SF_{80}$	0.167	0.081	0.119	0.106	0.143	0.097
$P_{3D} \times \overline{SF}$	0.105	0.060	0.051	0.040	0.078	0.058
P_{3D}/A_{bmax}	0.497	0.059	0.420	0.053	0.459	0.068
P_{3D}/A_{b80}	0.594	0.022	0.602	0.052	0.598	0.040
$P_{3D}/\overline{A_b}$	0.586	0.036	0.693	0.053	0.639	0.070
$P_{3D} \times P_{2Dpf}$	0.582	0.095	0.613	0.083	0.597	0.090

6.5.1 2D metrics

The 2D metrics that were previously identified as potentially suitable to be associated with hydraulic roughness are further investigated in the following paragraphs (6.5.1.1 - 6.5.1.4) for all flow scenarios.

6.5.1.1 2D porosity

The bulk P_{2D} values, estimated from the point of view of the flow, are in good agreement with the values of hydraulic roughness. The relationship seems to follow a power function for all flow scenarios characterised by high R^2 values. The strongest relationship is found for the Medium flow scenario ($R^2 = 0.887$) where all points are grouped tightly around the fitted curve. Importantly, individual lines connecting the points that belong to the same plant type (not drawn in Figure 6.15 for simplicity) follow a similar trajectory with the fitted curve. Due to the plant deformation during active flow, 'Through-water' TLS data show a better fit (R^2 value range 0.789-0.887) in comparison to the 'standard' TLS datasets (R^2 value range 0.772-0.825).

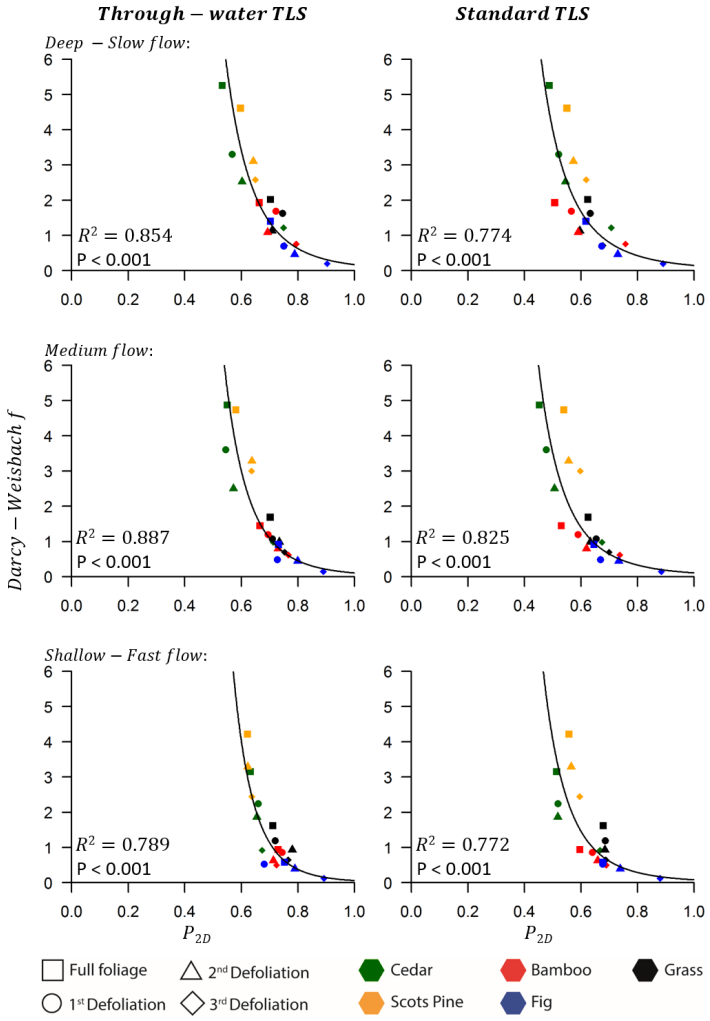

FIGURE 6.15: Plant structure, expressed using the bulk 2D porosity (P_{2D}), versus they hydraulic roughness, expressed using the Darcy-Weisbach friction factor (f), for all flow scenarios, using both 'through-water' and 'standard' TLS data.

6.5.1.2 Combining 2D porosity and cross-stream plant extent

When the bulk 2D porosity values are combined with the mean values of the cross-stream plant extent the relationship between the metric and the hydraulic roughness is slightly weakened. Employment of the 'through-water' TLS data yields R^2 values that are ranging between 0.780 and 0.858, while when 'standard' TLS data are used the R^2 values are slightly decreased due to plant deformation. The points corresponding to the cedar, scots pine, fig and bamboo plants are grouped tightly around the fitted curve and have a similar trajectory. However, the points corresponding to the grass seem to follow a different trajectory, although they remain tightly grouped around the fitted curve.

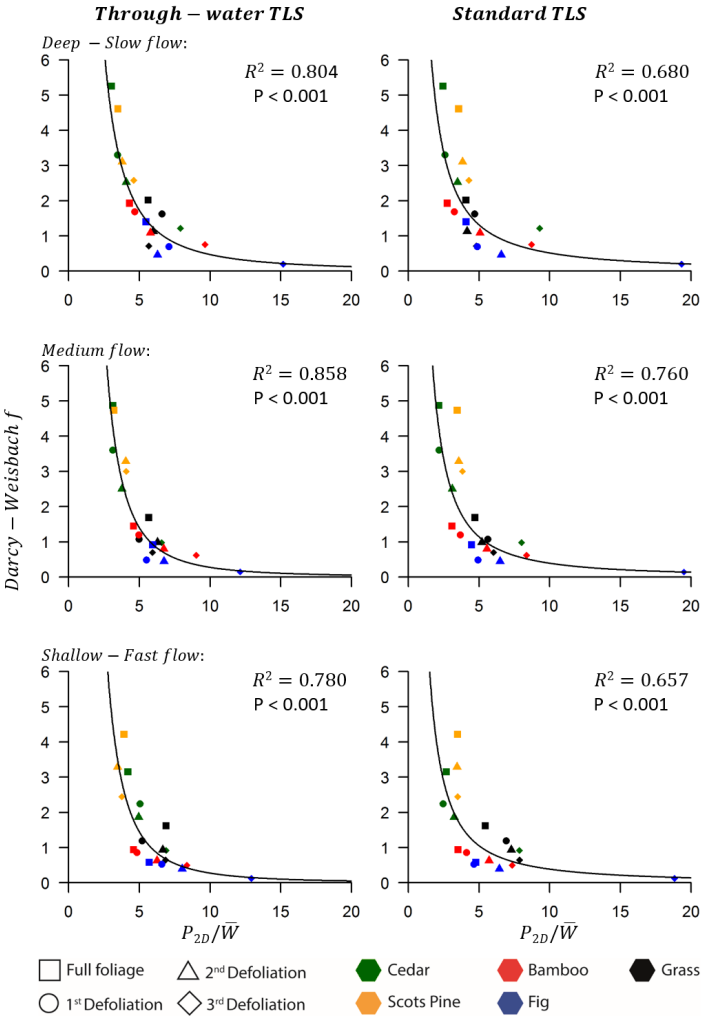

FIGURE 6.16: Plant structure, expressed using the ratio of bulk 2D porosity over the mean value of the cross-stream plant extent ($P_{2_D}/\overline{W}$), versus they hydraulic roughness, expressed using the Darcy-Weisbach friction factor (f), for all flow scenarios, using both 'through-water' and 'standard' TLS data.

6.5.1.3 Combining 2D porosity and streamwise plant extent

Combining the bulk 2D porosity values with the mean values of the streamwise plant extent shows a different picture. 'Standard' TLS data reveal a stronger relationship than the 'through-water' datasets. The strongest relationship is found for the Medium flow scenario ($R^2 = 0.818$) when 'standard' TLS data are used. The trajectories of the lines connecting points that belong to the same plant are similar with the trajectory of the fitted curve.

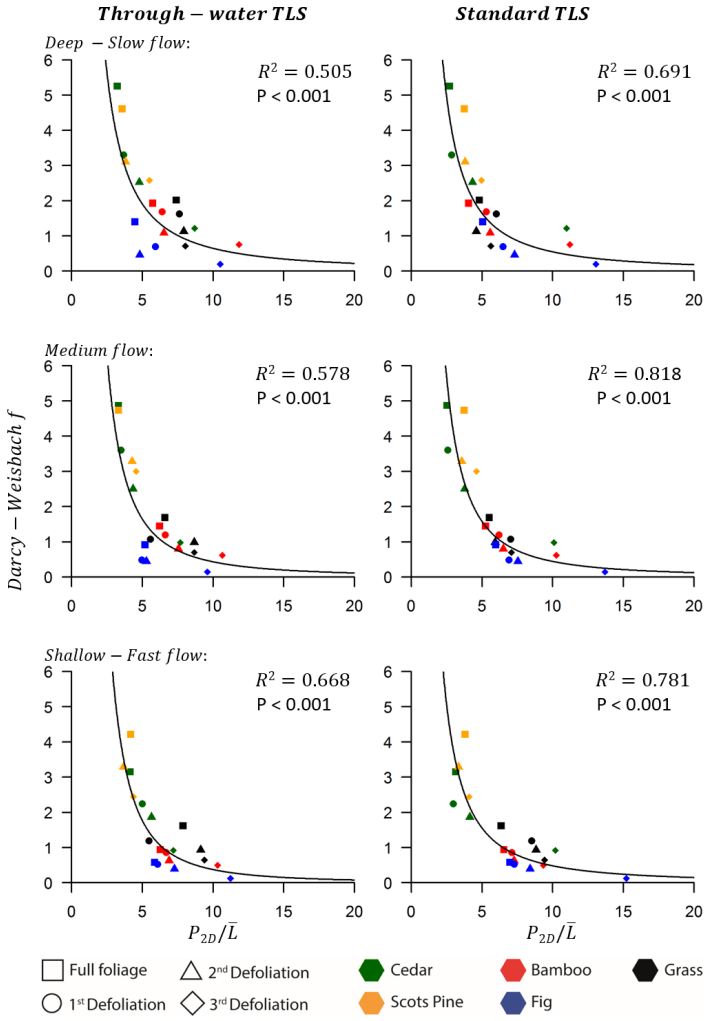

FIGURE 6.17: Plant structure, expressed using the ratio of bulk 2D porosity over the mean value of the streamwise plant extent ($P_{2D}/\overline{L}$), versus they hydraulic roughness, expressed using the Darcy-Weisbach friction factor (f), for all flow scenarios, using both 'through-water' and 'standard' TLS data.

6.5.1.4 Combining 2D porosity and planform 2D porosity

Combining the values of bulk 2D porosity measured from the point of view of the flow with the ones measured using the planform plant area shows a good relationship with the values of hydraulic roughness. Porosity values extracted from the 'standard' TLS data seem to work better for the Deep-Slow and Medium flow scenarios. For the Shallow-Fast flow scenario both datasets perform equally well with the R^2 value being marginally higher when 'through-water' datasets are used. Most of the plant types seem to follow the trajectory of the fitted curve, however the trajectories of the scots Pine and the grass show a slight deviation.

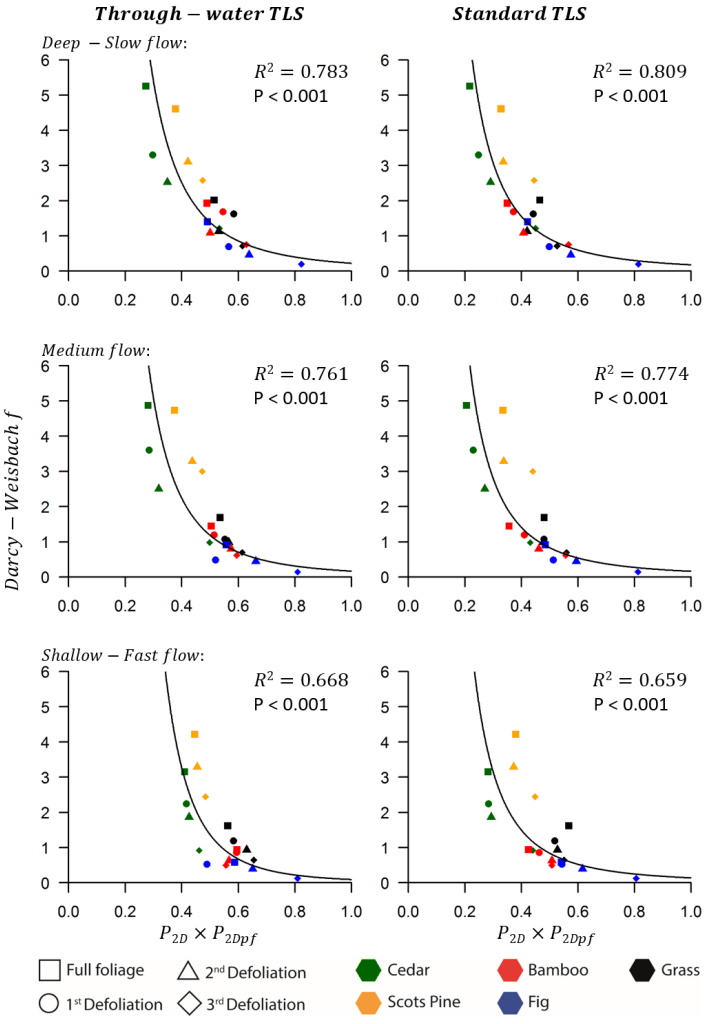

FIGURE 6.18: Plant structure, expressed using the combination of bulk 2D porosity and bulk planform 2D porosity, versus they hydraulic roughness, expressed using the Darcy-Weisbach friction factor (f), for all flow scenarios, using both 'through-water' and 'standard' TLS data

6.5.1.5 Combining 2D porosity with the mean plant extent

The ratio of 2D porosity over the mean value of the total plant extent shows a good agreement with the values of hydraulic roughness. The trajectories of the lines connecting points that belong to the same plant type are similar to the trajectory of the fitted curve. 'Standard' scan datasets show a higher correlation (R^2 values range between 0.678 and 0.796) than the 'through-water' ones (R^2 values range between 0.640 and 0.711).

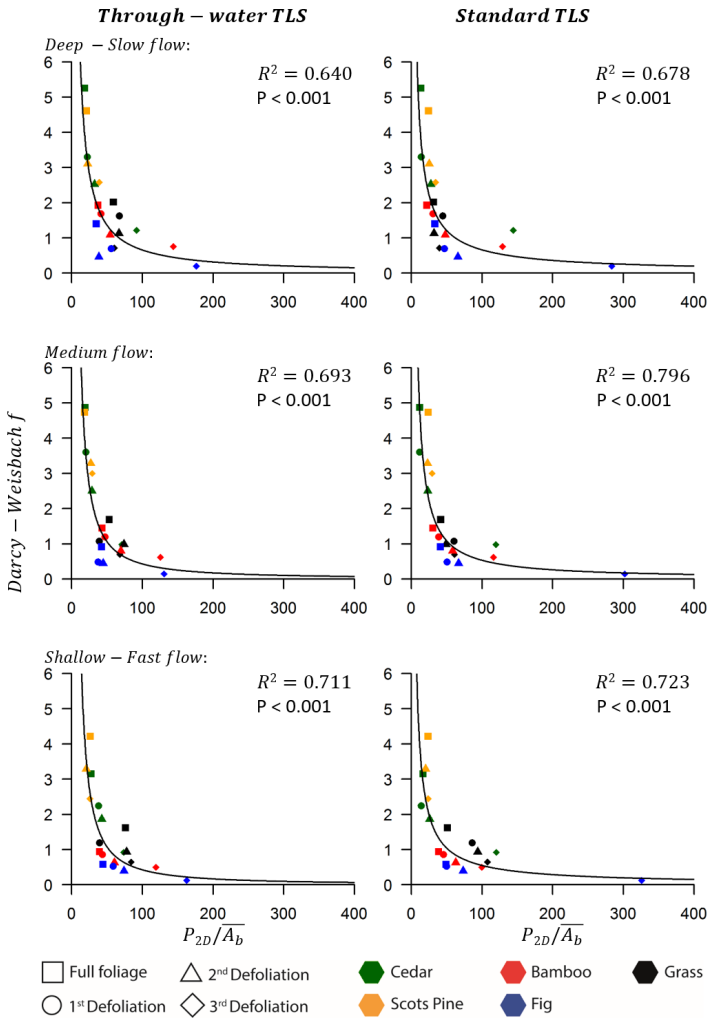

FIGURE 6.19: Plant structure, expressed using the ratio of bulk 2D porosity over the mean value of the total plant extent, versus they hydraulic roughness, expressed using the Darcy-Weisbach friction factor (f), for all flow scenarios, using both 'through-water' and 'standard' TLS data.

6.5.2 3D metrics

The 3D metrics that were previously identified as potentially suitable to be associated with hydraulic roughness are further investigated in the following paragraphs (6.5.2.1 - 6.5.2.4) for all flow scenarios.

6.5.2.1 Combining 3D porosity and cross-stream plant extent

The ratio of bulk 3D porosity over the mean values of the cross-stream plant extent shows a good agreement with the values of hydraulic roughness. Increasing values of the metric lead to a decrease of the respective hydraulic roughness following a power curve. The R^2 value for the Deep-Slow flow scenario is equal to 0.707 when 'through water' TLS data are used and is reduced to 0.603 when 'standard' TLS data are employed. The R^2 values for the Medium flow scenario are equal to 0.770 and 0.687 when 'through water' and 'standard' scan datasets are employed, respectively. The R^2 values corresponding to the Shallow-Fast flow scenario are slightly lower with the 'through-water' TLS data yielding an R^2 value equal to 0.639 while the respective value for the 'standard' TLS data is equal to 0.571. Although the points corresponding to all plant types are grouped tightly around the fitted curves, the points corresponding to the grass seem to deviate slightly from the trajectory defined by the fitted curve.

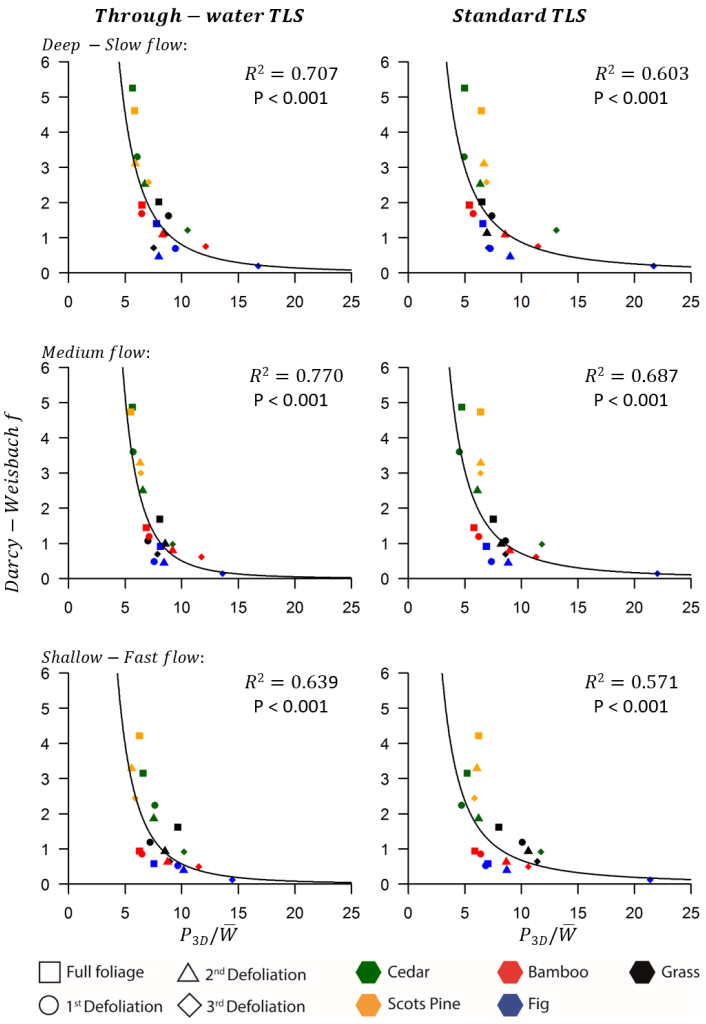

FIGURE 6.20: Plant structure, expressed using the ratio of bulk 3D porosity over the mean value of the cross-stream plant extent ($P_{3_D}/\overline{W}$), versus they hydraulic roughness, expressed using the Darcy-Weisbach friction factor (f), for all flow scenarios, using both 'through-water' and 'standard' TLS data.

6.5.2.2 Combining 3D porosity and streamwise plant extent

The ratio of 3D porosity with the streamwise plant extent shows an average to poor relationship with the hydraulic roughness when 'through-water' TLS data are used, especially for the Deep-Slow flow scenario ($R^2 = 0.270$). However, when 'standard' TLS data are employed the relationship is strengthened as shown by the R^2 values that are equal to 0.577, 0.734 and 0.721 for the Deep-Slow, Medium and Shallow-Fast flow scenarios, respectively.

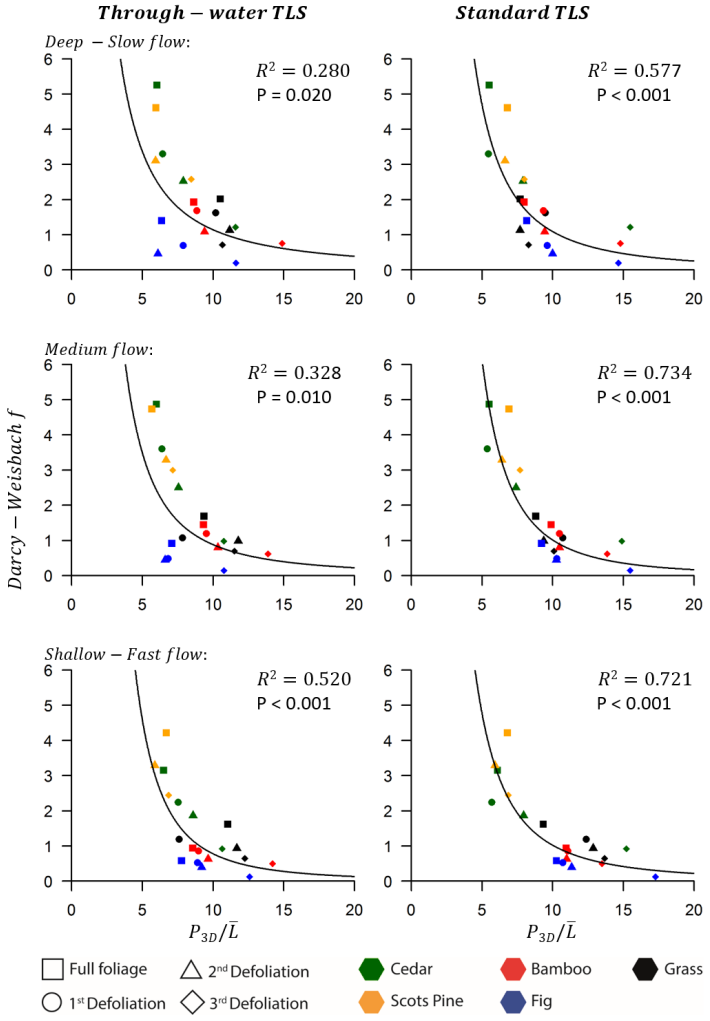

FIGURE 6.21: Plant structure, expressed using the ratio of bulk 3D porosity over the mean value of the streamwise plant extent ($P_{3_D}/\overline{L}$), versus they hydraulic roughness, expressed using the Darcy-Weisbach friction factor (f), for all flow scenarios, using both 'through-water' and 'standard' TLS data.

6.5.2.3 Combining 3D porosity and planform 2D porosity

The combination of 3D porosity and planform 2D porosity values show a strong relationship with the values of hydraulic roughness, especially for the Deep-Slow and Medium flow scenarios. For the Deep-Slow flow scenario the R^2 value is equal to 0.680 when 'through-water' TLS data are employed and is only marginally decreased ($R^2 = 0.686$) when 'standard' TLS data are used instead. When the Medium slow scenario is investigated, 'standard' TLS data perform better than the 'through-water' ones with the R^2 values being equal to 0.612 and 0.655, respectively. The relationship appears weaker for the Shallow-Fast flow scenario with the R^2 being equal to 0.453 and 0.497 for 'through-water' and 'standard' scan datasets, respectively.

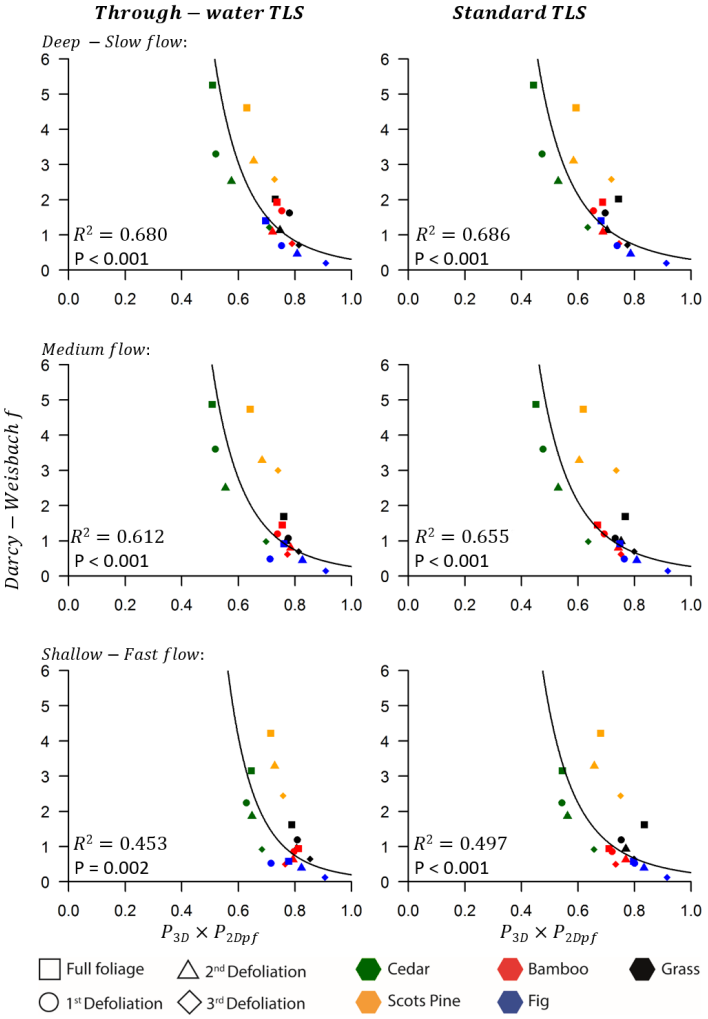

FIGURE 6.22: Plant structure, expressed using the combination of bulk 3D porosity and bulk planform 2D porosity, versus they hydraulic roughness, expressed using the Darcy-Weisbach friction factor (f), for all flow scenarios, using both 'through-water' and 'standard' TLS data.

6.5.2.4 Combining 3D porosity with the mean plant extent

The ratio of 3D porosity over the total plant extent shows a good agreement with the values of hydraulic roughness. 'Standard' scan datasets show a better fit with the R^2 values being greater (between 0.631 and 0.761) than the ones calculated from the 'through-water' datasets (between 0.544 and 0.630). The trajectories of the lines connecting points that belong to the same plant type are similar to the trajectory of the fitted curve and the points are grouped tightly around the fitted curve.

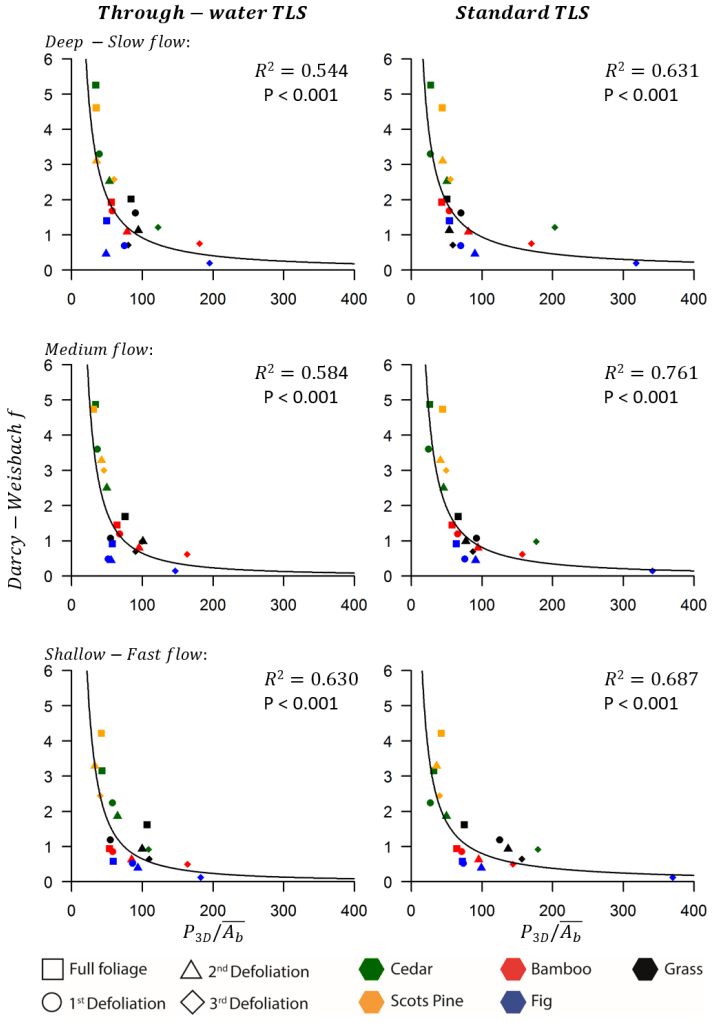

FIGURE 6.23: Plant structure, expressed using the ratio of bulk 3D porosity over the mean value of the total plant extent, versus they hydraulic roughness, expressed using the Darcy-Weisbach friction factor (f), for all flow scenarios, using both 'through-water' and 'standard' TLS data.

6.6 Modelling the vegetative hydraulic roughness

All of the 2D metrics that were investigated in subsection 6.5.1 performed well for all flow scenarios, using either 'through-water' or 'standard' TLS data. The 3D metrics investigated in subsection 6.5.2 also performed well but their respective R^2 values were lower than the ones calculated for the 2D metrics. The comparison between the R^2 values calculated from the 'through-water' scan datasets and those calculated from the 'dry' scans, reveals that most metrics perform better when 'through-water' TLS data are used. This behaviour is expected due to plant reconfiguration (Section 6.3). However, exceptions are observed for the ratio of porosity over the stream-wise or the total plant extent. These metrics appear to perform better when 'standard' TLS datasets are employed. The superiority of 'standard' TLS data for these metrics is likely an advantage. The application of 'through-water' TLS has limitations in regards to the maximum distance within the water column that can be surveyed, due to the rapid attenuation of the laser beam. Furthermore, the method is susceptible to increased noise due to the presence of suspended material (e.g. sediment), ripples on the water surface, air bubbles in the water body and plant movement under the influence of flow. Therefore, the utilization of 'through-water' TLS in field applications is unrealistic, albeit useful in laboratory studies. As such, a plant structure metric that can be easily obtained in field applications and shows a robust relationship with the hydraulic roughness is desirable. Therefore, considering the R^2 values calculated when 'standard' TLS data are used, two bulk structure metrics appear to work best and are suggested here. The ratio of 2D porosity over the mean value of the total plant extent ($P_{2D}/\overline{A_b}$) and the ratio of 3D porosity over the mean value of the total plant extent ($P_{3D}/\overline{A_b}$).

Models employing the above mentioned plant structure metrics to predict the vegetative hydraulic roughness, in terms of Darcy-Weisbach (f), are described by Equations 6.7 and 6.8:

$$f = \alpha_1 \left(\frac{P_{2D}}{\overline{A_b}} \right)^{\beta_1} \tag{6.7}$$

$$f = \alpha_2 \left(\frac{P_{3D}}{\overline{A_b}} \right)^{\beta_2} \tag{6.8}$$

The parameters α_1, β_1, α_2, β_2 do not have a constant value and are a function of Reynold's number. Table 6.6 shows the values of the above parameters estimated for the three flow scenarios that were investigated, Figure 6.24 presents the fitted curves.

TABLE 6.6: Estimated values for the α_1, β_1, α_2, β_2 of equations (6.7) and (6.8) for varying Reynolds number.

Re	α_1	β_1	α_2	β_2
22000	37.315	-0.876	107.329	-1.028
24000	62.016	-1.034	259.875	-1.252
28000	39.925	-0.931	113.081	-1.074

The derived models show that for low values of the plant structure metric (i.e. dense plants and/or large extent) the vegetative hydraulic roughness increases. Conversely, high values of the metric, associated either with very porous vegetation and/or a small plant extent, correspond to lower values of hydraulic roughness. From Equations (6.7) and (6.8), if the plant element is removed from the flow, the vegetative hydraulic roughness becomes equal to zero.

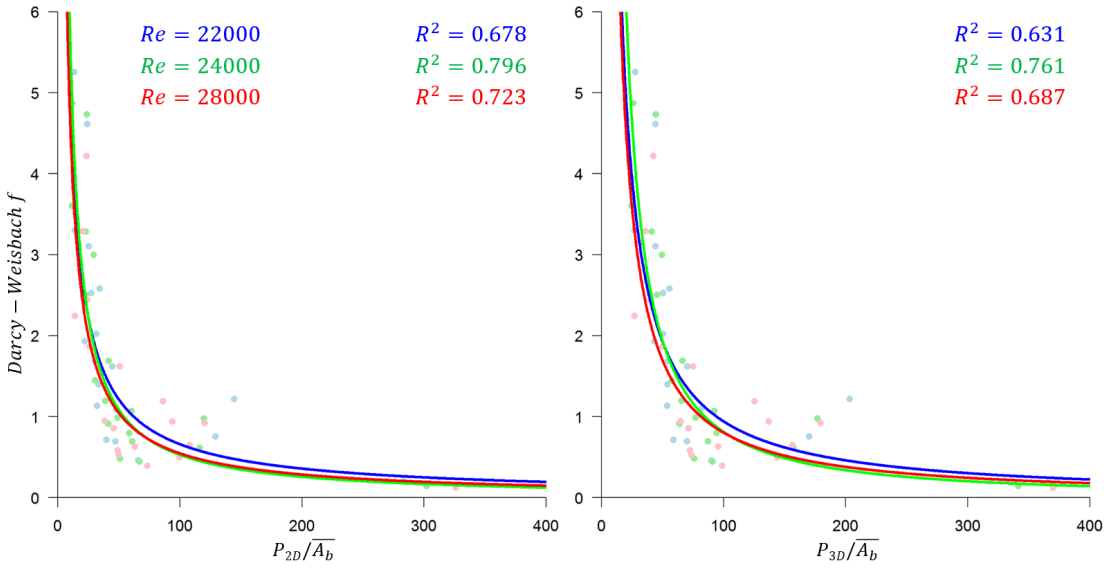

FIGURE 6.24: Fitted curves relating plant structure and bulk hydraulic roughness using Equations (6.7) and (6.8) for the scenarios presented in Table 6.6, for all curves $P < 0.001$.

It is interesting that the values of the parameters α_1, β_1, α_2, β_2 represented in Table 6.6, are relatively similar when Re is equal to 22000 and 28000 but change considerably for $Re = 24000$. Increased values of Re are expected to be associated with decreased values of the friction factor (f). This condition is satisfied when the curves that correspond to $Re = 22000$ and 28000 are considered. However, the curves that correspond to $Re = 24000$ show mixed results. For the 2D metric, the above condition is satisfied within the range of $25 < \frac{P_{2D}}{\overline{A_b}} < 73$ and for the 3D metric within the range of $52 < \frac{P_{3D}}{\overline{A_b}} < 107$, whilst outside of these ranges the predicted values of f are opposed to the expected ones. This is likely due to the combination of two factors; on one hand, outliers within the datasets may be affecting the slope and the intercept of the regression lines. For this reason, a Theil-Sen regression analysis (Theil, 1950; Sen, 1968) was

performed as well (Appendix G). However, it yielded results that were similar to the ones obtained from the, widely-used, least squares regression. On the other hand, the three flow scenarios only offer small variability in Reynolds number, making it difficult to highlight the effect that Re has on the above parameters and separate this from noise of the experiment itself. For this reason, the data from the three flow scenarios were aggregated and a single regression curve was fitted for each metric (Figure 6.25) and new parameters for Equations (6.7) and (6.8) were derived (Table 6.7). It must be stressed however that the values of α_1, β_1, α_2, β_2 are expected to be Re dependent and additional experiments are required to assess this relationship over a greater Re range.

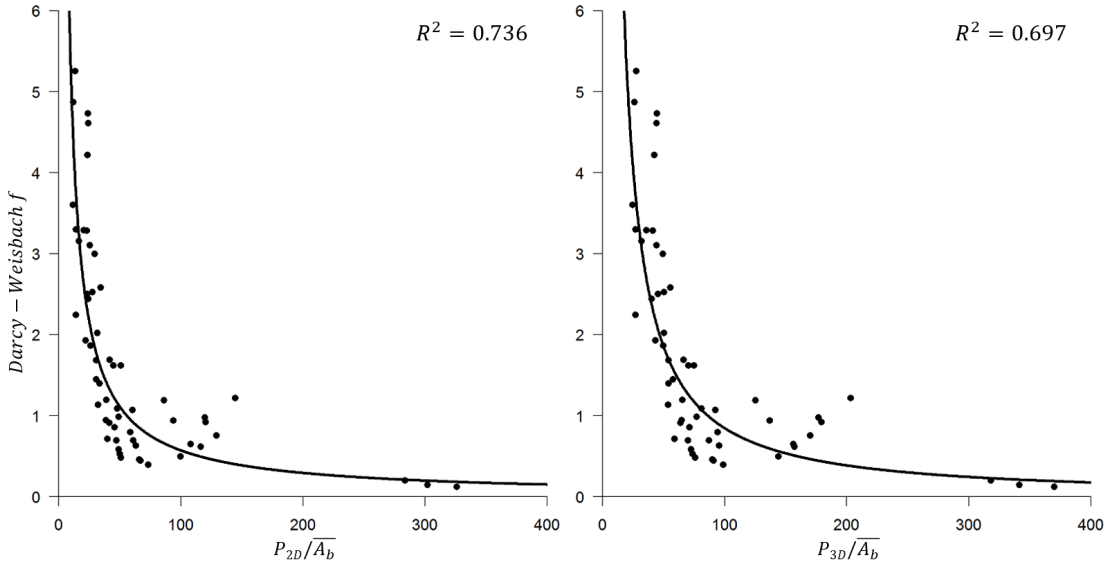

FIGURE 6.25: Fitted curves relating plant structure and bulk hydraulic roughness using Equations (6.7) and (6.8) independent of Reynold's number ($P < 0.001$).

TABLE 6.7: Fitted curves relating plant structure and bulk hydraulic roughness using Equations (6.7) and (6.8) independent of Reynold's number (for $22000 \leq Re \leq 28000$).

$\boldsymbol{\alpha_1}$	$\boldsymbol{\beta_1}$	$\boldsymbol{\alpha_2}$	$\boldsymbol{\beta_2}$
46.744	-0.956	152.186	-1.127

6.7 Chapter summary

Values of hydraulic roughness are typically assigned based on field observations and lookup tables in everyday practice. This can lead to biased estimates of roughness values, disconnecting the hydraulic roughness from the physical properties of the elements obstructing the flow and frequently diminishing it to a calibration parameter set to optimise the agreement between measured and modelled values (Lane, 2005). The present Chapter focused on associating physically meaningful metrics of vegetative structure with the fluvial drag exerted by plants. The employment of

Equations 6.7 and 6.8 can lead to more robust methods of assigning hydraulic roughness values that are directly related to the structure of vegetation.

On the other hand, bulk plant structure metrics are limited by the fact that they do not represent explicitly the spatial arrangement of individual plant elements such as stems or leaves. Therefore, although they are useful for the investigation of bulk hydraulic parameters such as the hydraulic roughness, they are not able to provide the necessary information for the investigation of more detailed flow attributes that are affected by the presence of vegetation, such as adjustments of the flow velocity profile and turbulent structures, that will be the focus of Chapter 7. 3D porosity arrays such as the ones shown in Figure 6.26 present a more appropriate alternative for the study of vegetation-flow interactions at the plant scale.

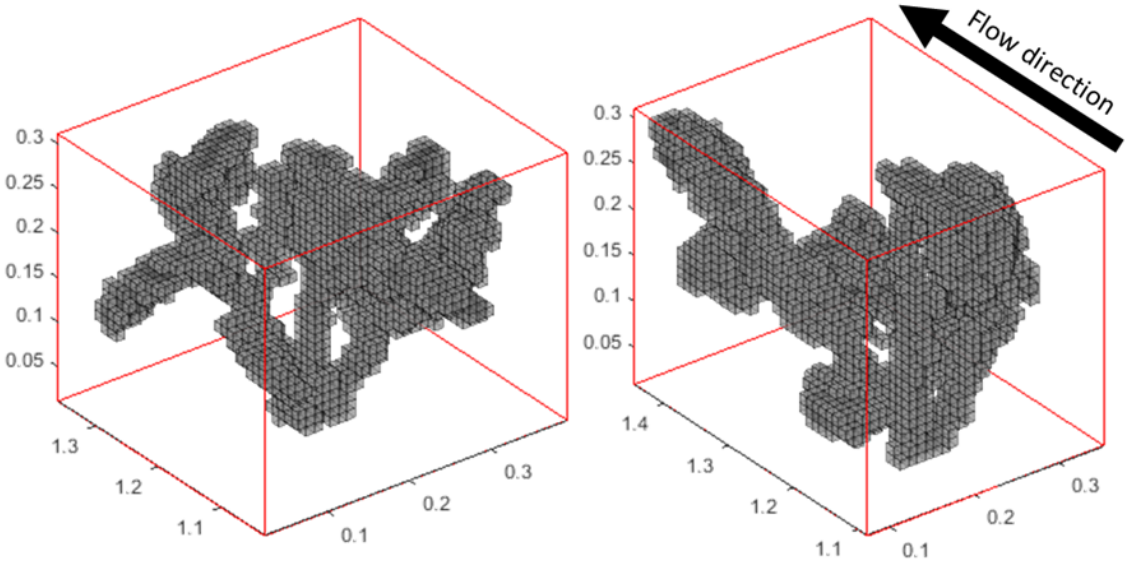

FIGURE 6.26: Comparison of porosity array (1 cm^3 resolution) of the fig tree after the first defoliation, under dry conditions (left) and during active Deep-Slow flow (right). The minimum bounding boxes assigned to each dataset are shown in red, the direction of flow is shown by the arrow.

Chapter 7

Assessment of the Effect of Plant Structure on Flow Attributes

The focus of Chapter 6 was on the characterisation of vegetative structure and its association with the bulk hydraulic roughness, useful in studies that seek to represent the average flow conditions over large areas. When surface water flows encounter plant elements, distinct topographic features (e.g. tail bars, scours) are developed in the vicinity of the plant obstructions which may be linked to channel forms at the reach scale (Bywater-Reyes et al., 2017). These features are the outcome of feedbacks between vegetation and flow operating at the plant scale and include velocity and turbulence adjustments as well as the development of a secondary flow. The extent and magnitude of these topographic features may be associated to the extent of the affected region of the flow (i.e. the wake), as well as the magnitude of the flow adjustment occurring within this region.

The present Chapter assesses the flow characteristics affected by the presence of individual vegetation elements, at the plant scale. These flow characteristics include adjustments of the velocity profile and turbulence, as well as the development of secondary flow downstream of the plant obstruction. The necessary data for this assessment are drawn from the physical modelling experiments that were described in Chapter 6. The vegetative structure is characterised using 3D porosity arrays (example shown in Figure 6.26 of Chapter 6), while the flow attributes are extracted from the dense arrays of the flow velocity measurements that were obtained using Acoustic Doppler Velocimetry (ADV). Section 7.1 presents a generic overview of the observed flow adjustments of the flume flow for the various plant-foliage scenario combinations. Section 7.2 investigates the effects of vegetation on the velocity profile, and highlights the ways that water flow is altered when propagates through the porous plant structure. Averaging the flow velocity vectors, in both space and time, enables the delineation the wake region developed downstream of the plant elements, and highlights the effects of different types of plant structure on the wake region in Section 7.3. Comparison between

the longitudinal and transverse velocity vectors in Section 7.4 highlights the magnitude of secondary flow developed downstream of the plant elements, while the flow turbulent kinetic energy is quantified in Section 7.5. Finally, Section 7.6 summarises the findings of the present Chapter. ADV data was not obtained from the Medium and Shallow-Fast flow scenarios. Therefore, the analysis and discussion undertaken in the present Chapter is focused on the Deep-Slow flow scenario only.

7.1 Overview of the effects of vegetation on the flow structure

The dense arrays of flow velocity measurements obtained using ADV during the Deep-Slow flow scenario, can be used to derive information regarding the 3D structure of the flow field. Datasets containing the time averaged velocity measurements (one for each plant-foliage scenario combination) were imported into MATLAB. Linear 3D interpolation of these scattered datasets (at 0.01 m resolution) enables the estimation of 3D velocity components at every point within the examined region of the flow. In this way, the extraction of velocity slices, flow vectors and stream lines is possible, allowing an overview of the overall 3D structure of the flow field and highlighting any adjustments that occurred downstream of the various plant types. Vegetation has a considerable effect on the flow field and as such, interpolating velocity measurements collected at the opposite sides of a vegetation element (i.e. upstream and downstream) would yield unrealistic results. Therefore, each ADV dataset was partitioned into two sub-datasets; one containing the velocity measurements that were obtained upstream of a plant and one containing measurements obtained downstream. The subsequent 3D interpolation was undertaken for each sub-dataset separately.

The structure of the flow field, during Deep-Slow flow, for all plant foliage combinations is presented in Figure 7.1. When vegetation was absent, the flow field appeared homogeneous. The flow velocity did not show any variations, and its value was approximately 0.25 m s^{-1}. The streamlines and flow vectors were horizontal, parallel to each other and pointing downstream. When vegetation was introduced to the flow, its structure was altered. In most cases, upstream of the vegetation element, the streamlines steered towards the sides of the flume. Immediately downstream of the vegetation element, the velocity field showed a great variation. In the centre region (defined as the zone between 0.16 and 0.23 m from the flume's left side wall) the flow decelerated and in some cases flow separation occurred (scots pine-all foliage scenarios, cedar-full foliage). At the sides and near the bed flow acceleration was observed, with the flow velocity becoming much greater (up to 0.5 m s^{-1}) than the background values observed in the absence of vegetation. At further distances downstream of the vegetation element, the slow and fast regions of flow gradually diffused within each other. In some cases this happened quickly (e.g. fully foliated fig), while in others this was not achieved within the

surveyed section of the flume flow.

The slow regions of flow were situated directly in front of the main body of the plant elements, while the fast regions were located near the bed and at the sides of the flume where the plant obstruction was minimal. This highlights that as the flow reaches the plant obstruction, water is forced through the small openings that are mainly located near the bottom, where it accelerates due to increased pressure. Foliage reduction creates new pathways for the flow and thus decreases the magnitude of the flow field adjustments. For example, although downstream of the fully foliated bamboo some regions of flow acceleration and deceleration were observed, the fully defoliated bamboo appeared to have a minor effect to the flow. The adjustments of the velocity profiles downstream of each plant-foliage scenario combination will be examined in detail in Section 7.2 below.

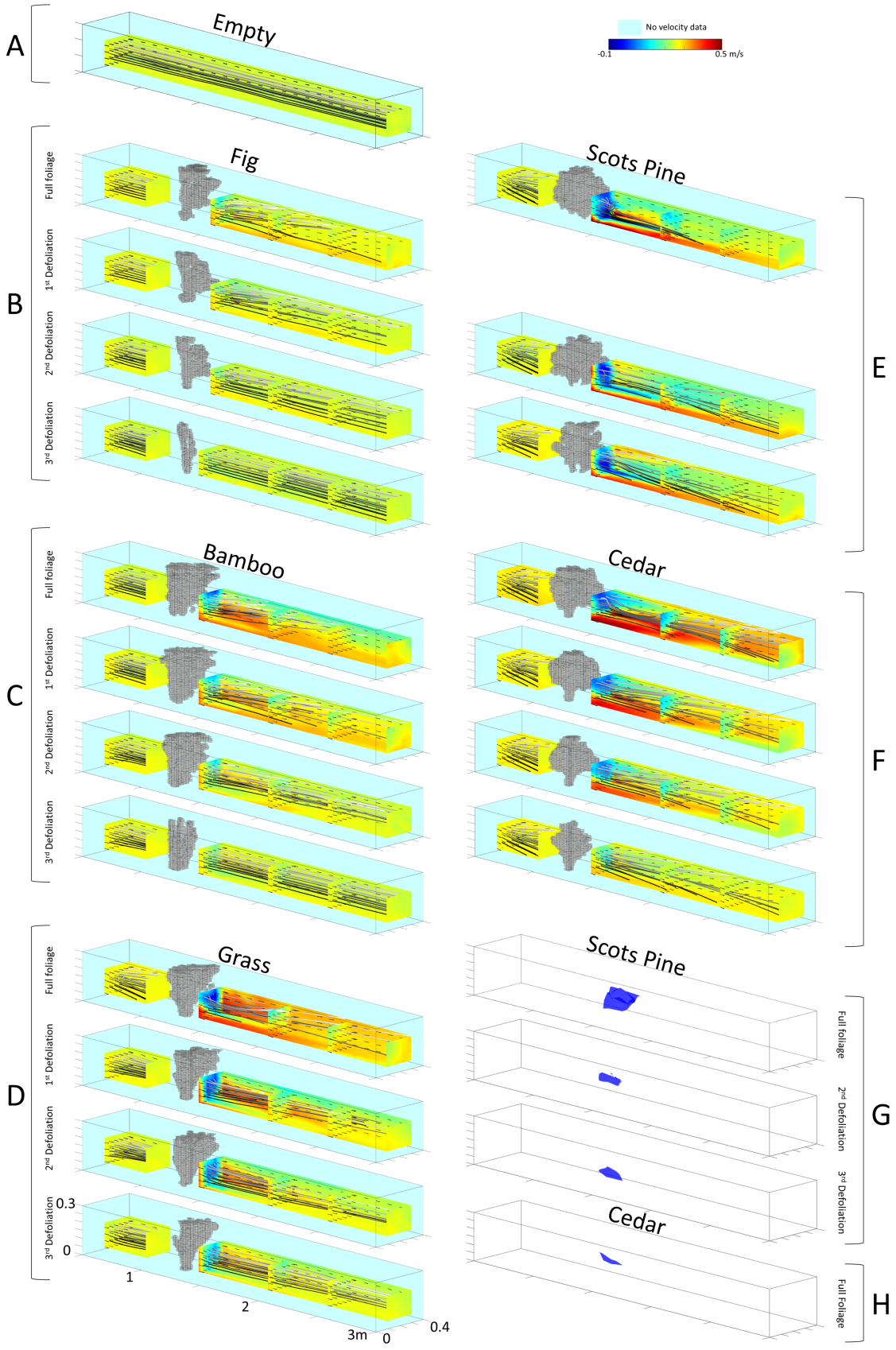

FIGURE 7.1: Flow field during Deep-Slow flow without vegetation (A), and all plant foliage scenario combinations (B-F). The colour scale represents the magnitude of the streamwise velocity vector, while the flow vectors and streamlines were computed using all three velocity vectors. Flow separation zones were developed downstream of the scots pine for all foliage scenarios (G) and the fully foliated cedar (H). Vegetation elements are represented by the extracted 3D porosity arrays.

7.2 Effects of vegetation on the velocity profile

Porosity profiles were extracted from the generated porosity arrays, by calculating the average porosity value for every 0.01 m of plant height. In this way, the variation of plant structure at increasing distances from the flume bed (Z/H) is highlighted. Using the ADV data, the time averaged values of each one of the three velocity vectors ($\bar{u}, \bar{v}, \bar{w}$) were used to calculate spatial velocity averages ($\langle\bar{u}\rangle$,$\langle\bar{v}\rangle$,$\langle\bar{w}\rangle$) for various distances from the flume bed and generate spatially averaged velocity profiles, corresponding to each surveyed cross-section location. The velocity profiles were compared with the ones extracted from the Empty flume run and, for the streamwise velocity vector, the additive residuals ($\langle\bar{u}_{veg}\rangle - \langle\bar{u}_{empty}\rangle$) were computed. The process was repeated for all plant-foliage scenario combinations, under Deep-Slow flow, and the results are presented below (subsections 7.2.1-7.2.5). Moreover, the absolute values of the additive residuals in the form of percentages were plotted against the distance along the flume (Figure 7.17). The area under the curve was used as a proxy of the intensity of the wake region for each plant-foliage scenario combination, while the point at which the curve became approximately horizontal was used to define the wake boundary and thus estimate the streamwise extent of the wake region (see also Section 7.3). Furthermore, the ratio of the transverse over the streamwise velocity $\left(\frac{|\langle\bar{v}\rangle|}{|\langle\bar{u}\rangle|}\right)$, using the absolute values of the spatial averages, was plotted against the distance along the flume (Figure 7.19). This ratio is indicative of secondary currents and associated with the balance between longitudinal and transverse mixing at various distances from the plant elements (see Section 7.4).

7.2.1 Velocity adjustments due to the presence of the fig

Comparison between the streamwise velocity ($\langle\bar{u}\rangle$) profiles upstream of the fig with the ones collected during the empty flume run (Figure 7.2) does not show any variations. This highlights that the fig did not exert any major backwater effects that affect the streamwise velocity vector. Immediately downstream of the plant element, the shape of the streamwise velocity profiles shows some minor adjustments. At the upper level of flow, deceleration occurred, while near the flume bed the flow accelerated, causing the profile to adopt an 'S' shape. This behaviour can be seen clearly at the profiles located at the $x = 1.5$ m cross-section location. At $Z/H = 0.67$ the streamwise flow velocity is decreased by 20% whereas near the flume bed ($Z/H = 0.17$) it is increased by 9%. As the distance downstream of the plant element becomes greater, the observed flow velocity variations become smaller and gradually attenuate. Foliage reduction decreased the magnitude of the streamwise velocity adjustments. However, the extent of the effect remained constant. This can also be seen at the curves of Figure 7.17, where although the area under the curve is decreased after each defoliation step, the point at which the plotted lines become horizontal is at $x = 1.7$ m for all foliage scenarios, except the fully defoliated one. This scenario did not cause any major effects on the streamwise flow

velocity profile.

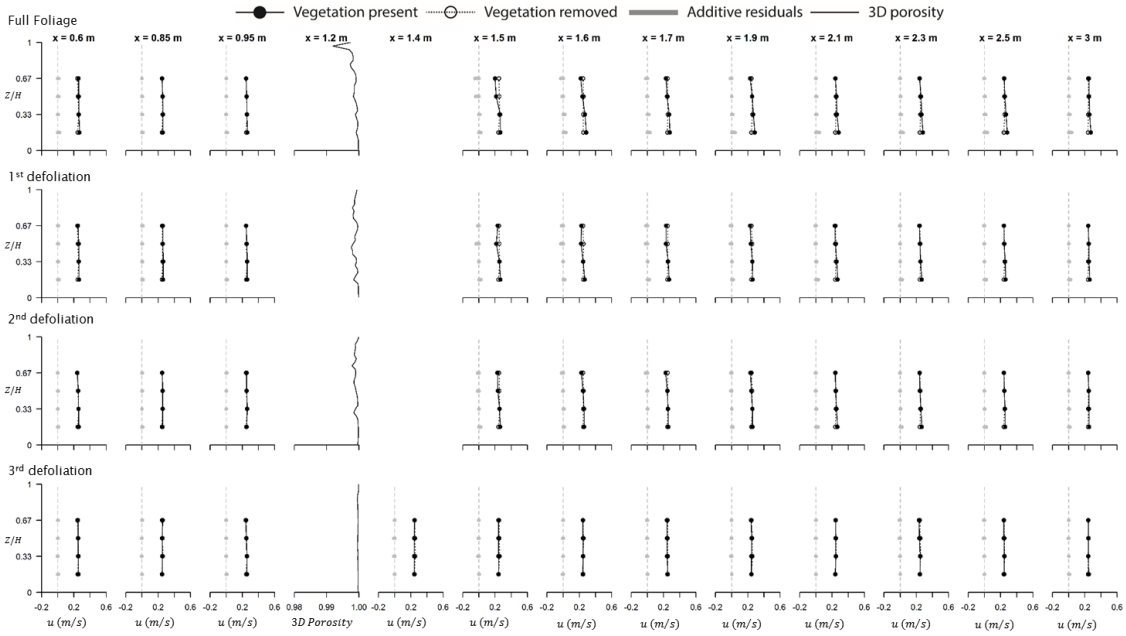

FIGURE 7.2: Cross-stream averages of the streamwise ($\langle\bar{u}\rangle$) velocity vector at increasing distances from the fig, positioned at $x = 1.2\,\text{m}$, for all foliage scenarios. The grey bars represent the additive residuals calculated for the streamwise velocities ($\langle\bar{u}_{veg}\rangle - \langle\bar{u}_{empty}\rangle$). For the first three foliage scenarios ADV data were not collected at $x = 1.4\,\text{m}$ due to a physical obstruction by the plant itself.

The transverse velocity profiles ($\langle\bar{v}\rangle$) (Figure 7.3) show some small variations upstream of the plant element. In some cases, the velocity vector changed direction (e.g. near the bed at the $x = 0.95\,\text{m}$ cross-section location, after the third defoliation). However, the magnitude of the transverse velocity was very small. Downstream of the plant element the velocity vectors show some adjustments. For example at the $x = 1.5\,\text{m}$ cross-section location downstream of the fully foliated fig, the velocity changes direction at $Z/H = 0.33$ and then changes again at $Z/H = 0.5$ while at $Z/H = 0.67$ it is increased by an order of magnitude (from $0.009\,\text{m s}^{-1}$ to $0.04\,\text{m s}^{-1}$). This behaviour propagates downstream, but at greater distances its magnitude decreases. Foliage reduction reduced the magnitude of the transverse velocity profile adjustments.

Velocity adjustments are also observed for the vertical velocity component ($\langle\bar{w}\rangle$) (Figure 7.4). For the empty flume scenario, the direction of the w vector changed frequently, with some levels of flow moving upwards while others are moving in a downward motion. However, upstream of the fig the majority of the measurements reveal that the flow followed a downward motion ($\langle\bar{w}\rangle < 0$). Downstream of the fig plant, for all foliage scenarios except the fully defoliated one, the w velocity vector consistently pointed upwards ($\langle\bar{w}\rangle > 0$). Furthermore, in some locations its value increased by up to two orders of magnitude. For example, at the x =1.5 m cross-section location downstream of the fully foliated fig, at $Z/H = 0.5$ the value of the spatially averaged vertical velocity changes from $0.0007\,\text{m s}^{-1}$ to $0.017\,\text{m s}^{-1}$. These adjustments are propagated downstream but their magnitude is reduced at increased distances. When

the plant foliage was reduced, the downstream distance required for the profiles to converge was shortened.

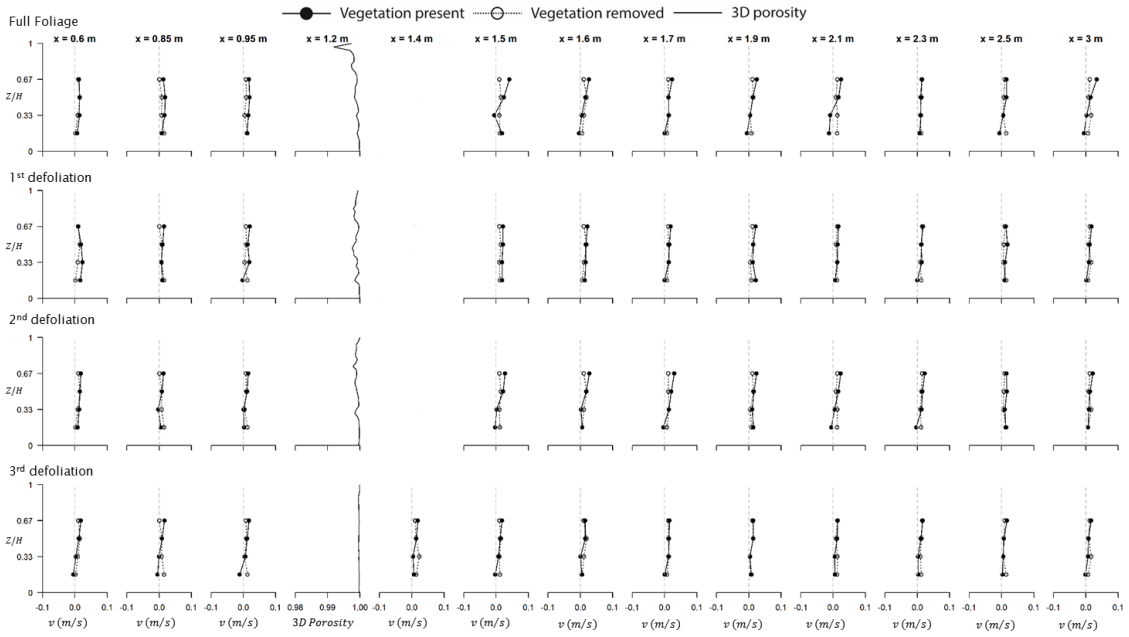

FIGURE 7.3: Cross-stream averages of the transverse ($\langle \bar{v} \rangle$) velocity vector at increasing distances from the fig, positioned at $x = 1.2\,\mathrm{m}$, for all foliage scenarios. For the first three foliage scenarios ADV data were not collected at $x = 1.4\,\mathrm{m}$ due to a physical obstruction by the plant itself.

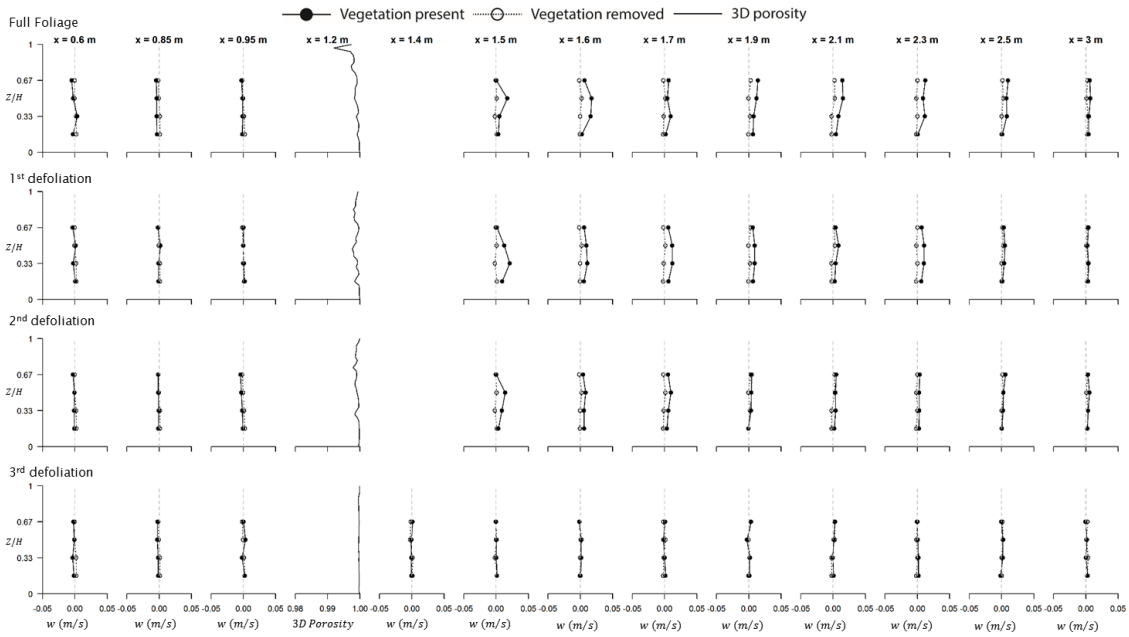

FIGURE 7.4: Cross-stream averages of the vertical ($\langle \bar{w} \rangle$) velocity vector at increasing distances from the fig, positioned at $x = 1.2\,\mathrm{m}$, for all foliage scenarios. For the first three foliage scenarios ADV data were not collected at $x = 1.4\,\mathrm{m}$ due to a physical obstruction by the plant itself.

7.2.2 Velocity adjustments due to the presence of the bamboo

The effects of the bamboo on the streamwise velocity profile ($\langle\bar{u}\rangle$) (Figure 7.5) are greater than those of the fig presented earlier. Immediately downstream of the plant (at $x = 1.4\,\text{m}$) the upper levels of flow decelerated by up to 58% while near the bed the flow accelerated and became up to 35% greater than the streamwise velocity measured at the same location without any vegetation affecting the flow. At increasing distances downstream of the plant element, the decelerated region of the flow gradually attenuated with the streamwise flow velocity returning to its original values. However, the zone of acceleration near the flume bed propagated downstream. For example at the $x = 2.5\,\text{m}$ cross-section location, the velocity at the upper level of the flow is only 14% slower than the background value and at the $x = 3\,\text{m}$ cross-section location the difference has been fully attenuated, while at the lower level of the flow is 24% faster and 21% faster at the same cross-section locations, respectively. Foliage reduction decreases the area under the curve shown in Figure 7.17 signifying a decrease in the intensity of the wake after each defoliation step. However, the extent of the wake region appears to remain constant with the wake border located between the $x = 2.5\,\text{m}$ and $x = 3\,\text{m}$ cross-section locations. The fully defoliated bamboo had a negligible effect on the velocity profile even at the cross-section location that was very near downstream of the plant element (at x =1.4 m).

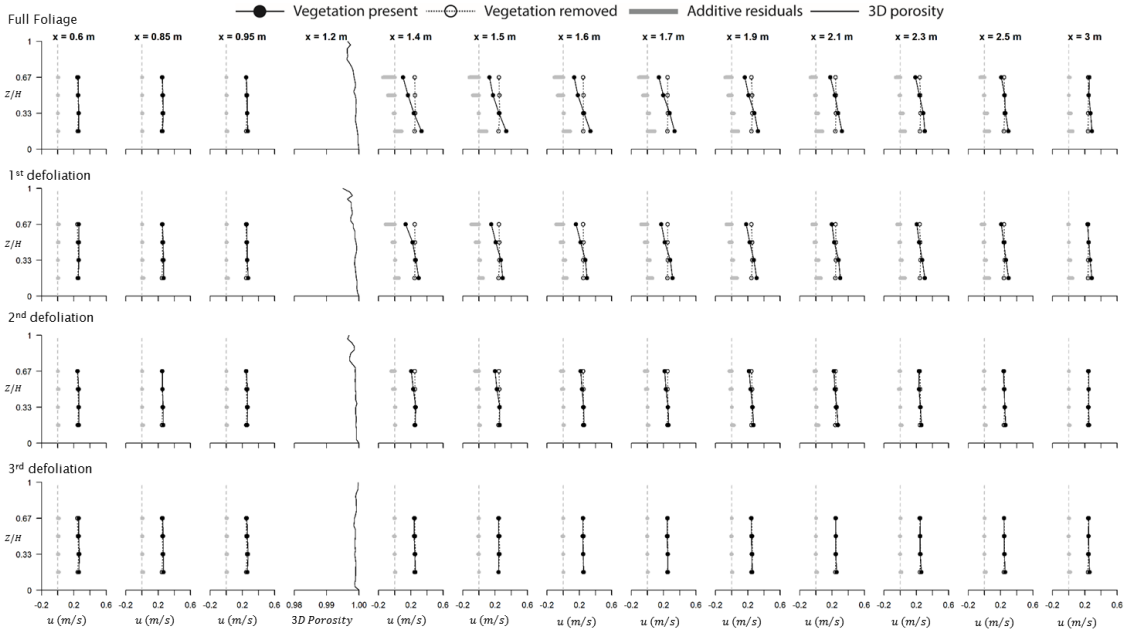

FIGURE 7.5: Cross-stream averages of the streamwise ($\langle\bar{u}\rangle$) velocity vector at increasing distances from the bamboo, positioned at $x = 1.2\,\text{m}$, for all foliage scenarios. The grey bars represent the additive residuals calculated for the streamwise velocities ($\langle\bar{u}_{veg}\rangle - \langle\bar{u}_{empty}\rangle$).

Upstream of the plant element, the profiles of the transverse velocity ($\langle\bar{v}\rangle$) (Figure 7.6) show some minor adjustments and, in some cases, the direction of the vector appears to be opposite to the one observed in absence of vegetation. This occurs near the bed and can be seen at the $x = 0.6\,\text{m}$ and $x = 0.95\,\text{m}$ cross-section locations upstream of the fully

foliated bamboo and at the $x = 0.85\,\mathrm{m}$ and $x = 0.95\,\mathrm{m}$ upstream of the bamboo after the first defoliation. Adjustments of the transverse velocity vector were also observed downstream of the plant. Although, in the majority of observations, the direction of the vector matches the one observed in absence of vegetation, its magnitude was affected downstream of the bamboo. For example, near the bed at the $x = 1.6\,\mathrm{m}$ cross-section location the velocity is increased by an order of magnitude (from $0.006\,\mathrm{m\ s^{-1}}$ to $0.03\,\mathrm{m\ s^{-1}}$).

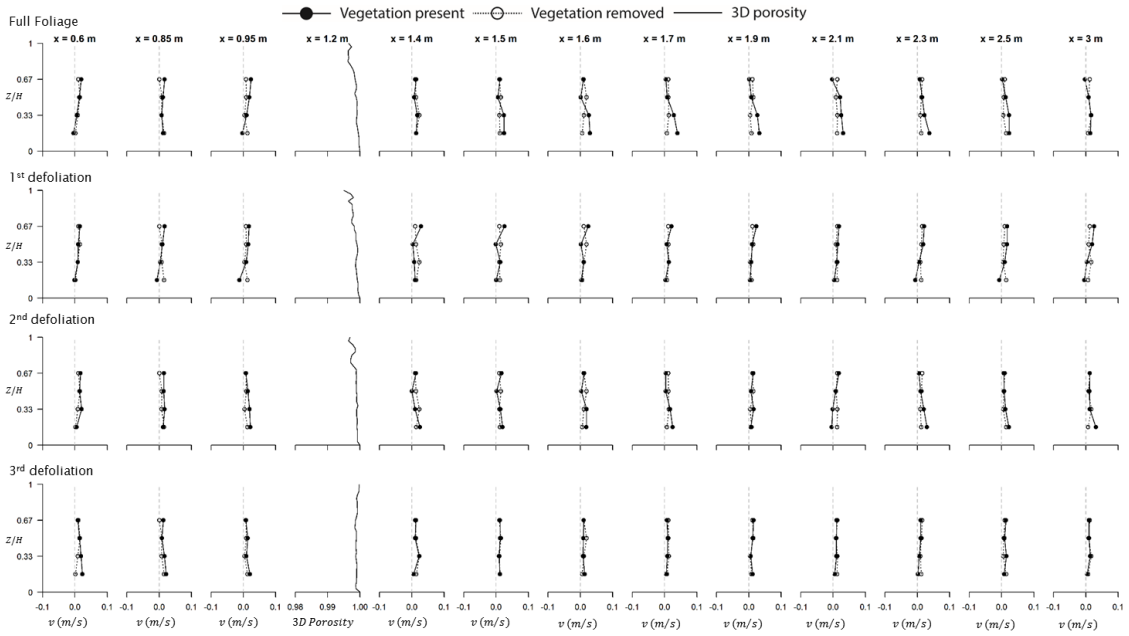

FIGURE 7.6: Cross-stream averages of the transverse ($\langle \bar{v} \rangle$) velocity vector at increasing distances from the bamboo, positioned at $x = 1.2\,\mathrm{m}$, for all foliage scenarios.

The profiles of the vertical velocity vector ($\langle \bar{w} \rangle$) computed upstream of the bamboo show that the flow moved downwards ($\langle \bar{w} \rangle < 0$). Downstream of the plant element, in the majority of the profiles, the flow moved upwards and the magnitude of the vertical velocity was increased, especially for the fully foliated scenario . At $x = 1.4\,\mathrm{m}$ and $Z/H = 0.5$ the vertical velocity vector not only changed direction but also its magnitude increased by a factor of nine (from $-0.002\,\mathrm{m\ s^{-1}}$ to $0.018\,\mathrm{m\ s^{-1}}$). This behaviour propagated downstream, however, its magnitude reduced at greater distances.

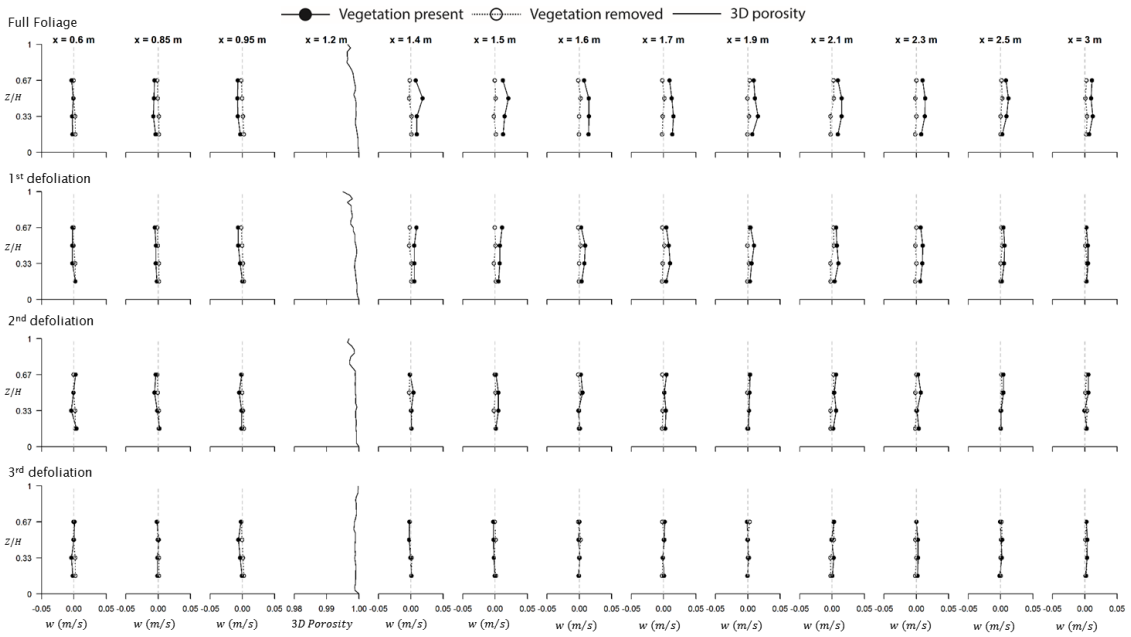

FIGURE 7.7: Cross-stream averages of the vertical ($\langle \bar{w} \rangle$) velocity vector at increasing distances from the bamboo, positioned at $x = 1.2\,\mathrm{m}$, for all foliage scenarios.

7.2.3 Velocity adjustments due to the presence of the grass

The streamwise velocity ($\langle \bar{u} \rangle$) adjustments exerted by the presence of grass are presented in Figure 7.8. Comparison between the profiles obtained upstream of the plant element with those obtained in absence of vegetation at identical cross-section locations does not show any major differences, highlighting that the streamwise velocity vector was not particularly affected by any backwater effects exerted by the presence of the plant element. Downstream the velocity profiles adopt an 'S' shape highlighting that the upper levels of flow decelerated while the lower ones accelerated. In more detail, at $x = 1.4\,\mathrm{m}$ downstream of the fully foliated grass the flow is decelerated by 58% at $Z/H = 0.5$ and by 47% at $Z/H = 0.67$ while at $Z/H = 0.17$ it is accelerated by 28%. At increasing distances downstream, the decelerating region of flow gradually attenuates and reaches the background velocity values between the $x = 2.1\,\mathrm{m}$ and $x = 2.3\,\mathrm{m}$ cross-section locations. The accelerating region propagates downstream with the residual values increasing until they reach their maximum (36%) at the $x = 1.9\,\mathrm{m}$ cross-section location. Beyond that point the residual values decrease gradually but the actual values remain higher than the ones measured in absence of vegetation throughout the extent of the surveyed region. The curves of Figure 7.17 show that the presence of the grass caused a wake region to be developed with its streamwise extent reaching the $x = 2.5\,\mathrm{m}$ cross-section location for all foliage scenarios. Its magnitude however, appears to have decreased after each successive defoliation.

The profiles of the spatially averaged transverse velocity vector ($\langle \bar{v} \rangle$) presented in (Figure 7.9), are majorly adjusted by the presence of grass. Upstream of the fully foliated grass, the direction of the flow changed at half depth, while its magnitude was

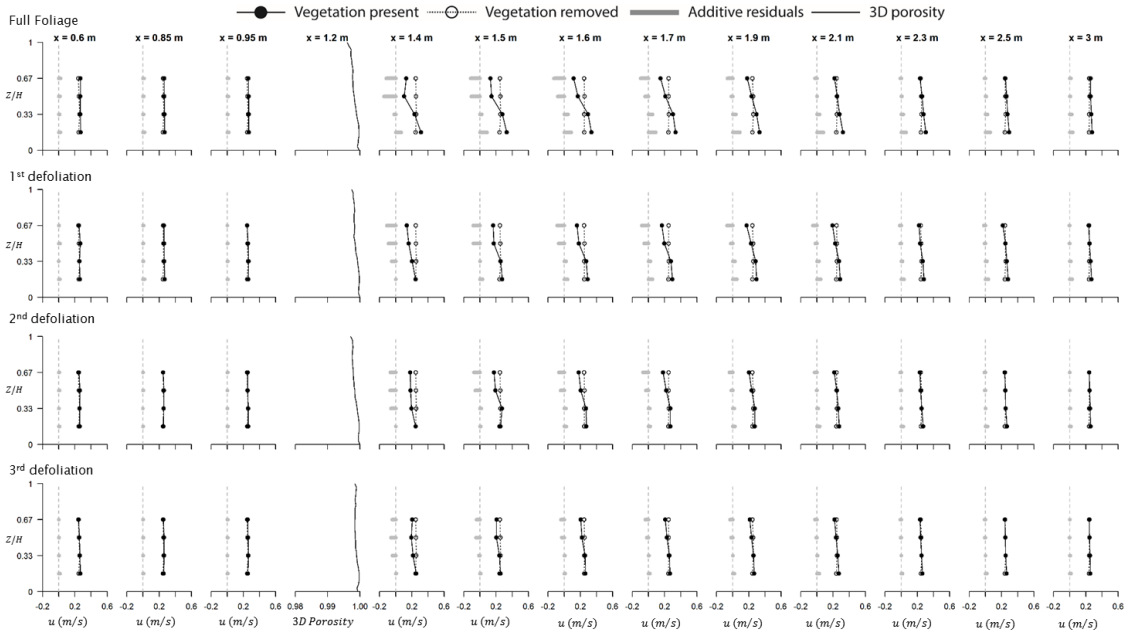

FIGURE 7.8: Cross-stream averages of the streamwise ($\langle\bar{u}\rangle$) velocity vector at increasing distances from the grass, positioned at $x = 1.2\,\text{m}$, for all foliage scenarios. The grey bars represent the additive residuals calculated for the streamwise velocities ($\langle\bar{u}_{veg}\rangle - \langle\bar{u}_{empty}\rangle$).

much greater than the background values. For example at $x = 0.6\,\text{m}$ near the bed, the magnitude of the lateral velocity is decreased almost by a factor of thirty (from $0.0016\,\text{m s}^{-1}$ to $-0.0470\,\text{m s}^{-1}$) while at $Z/H = 0.67$ it is increased by a factor of four (from $0.01\,\text{m s}^{-1}$ to $0.04\,\text{m s}^{-1}$). At short distances downstream of the vegetation, the transverse velocity adjustments were constrained within the lower levels of flow. For example at $x = 1.4\,\text{m}$ the velocities measured with and without vegetation are almost identical at $Z/H = 0.5$ and $Z/H = 0.67$ but vary at $Z/H = 0.17$ and $Z/H = 0.33$. However, at increasing distances the total extent of flow was affected with the motion at the upper levels having the opposite direction than the lower ones. Successive defoliation steps dampened the transverse velocity adjustments.

Although the profiles of the spatially averaged vertical velocity ($\langle\bar{w}\rangle$) (Figure 7.10) show some small variation upstream of the grass, a consistent pattern is not observed. At small distances downstream of the plant ($x = 1.4\,\text{m}$ to $x = 1.6\,\text{m}$ for the fully foliated scenario), the upper levels of flow show a downwards motion while the flow near the bed moved upwards. At longer distances the flow at all distances from the flume bed moved upwards but the magnitude of this behaviour gradually decreased further downstream. When the plant foliage was reduced, the profiles converged to the background values at shorter distances.

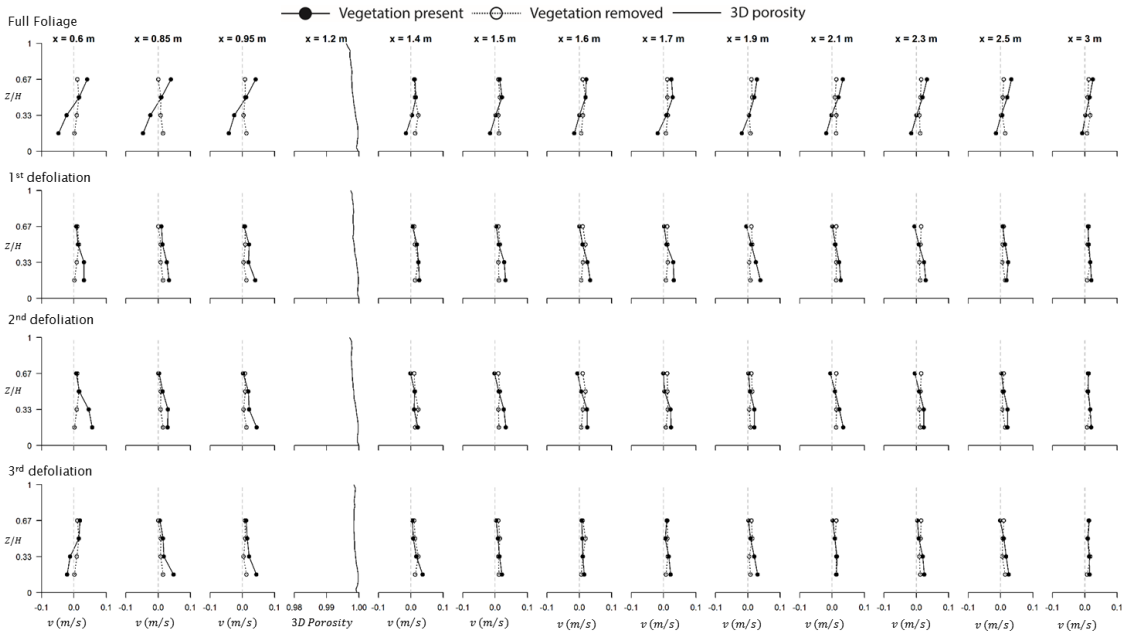

FIGURE 7.9: Cross-stream averages of the transverse ($\langle \bar{v} \rangle$) velocity vector at increasing distances from the grass, positioned at $x = 1.2\,\mathrm{m}$, for all foliage scenarios.

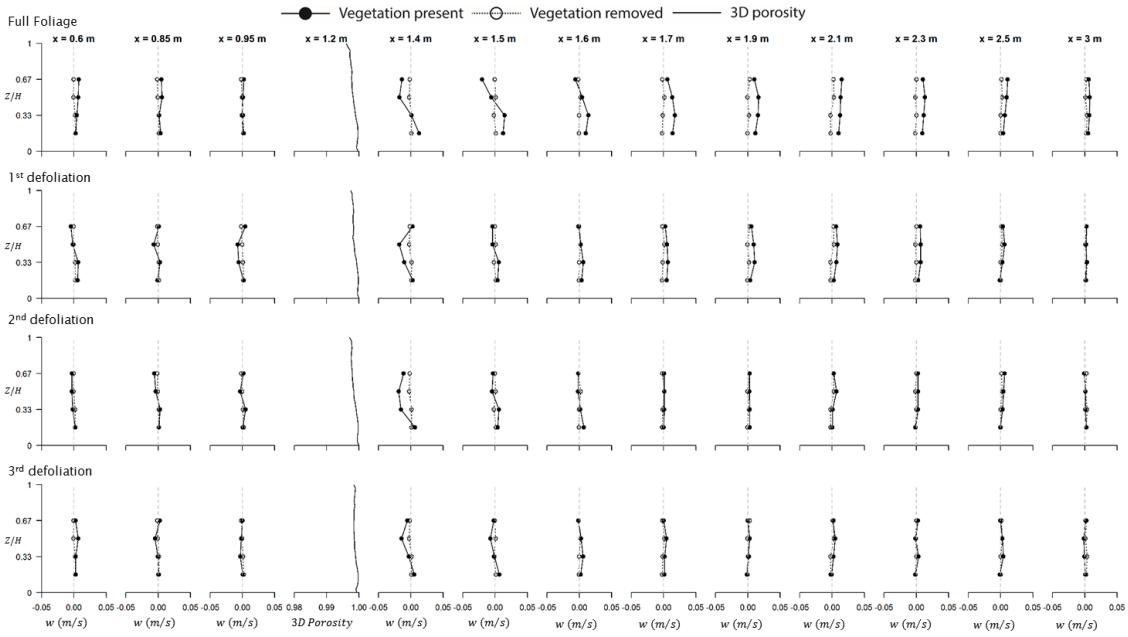

FIGURE 7.10: Cross-stream averages of the transverse ($\langle \bar{w} \rangle$) velocity vector at increasing distances from the grass, positioned at $x = 1.2\,\mathrm{m}$, for all foliage scenarios.

7.2.4 Velocity adjustments due to the presence of the scots pine

The streamwise velocity ($\langle\bar{u}\rangle$) profiles (Figure 7.11) upstream of the scots pine match the ones generated in absence of vegetation. Major flow adjustments occurred downstream. For the fully foliated scenario, near the flume bed ($Z/H = 0.17$), the flow accelerated. Although it is only 7% larger than the background value at $x = 1.4\,\text{m}$ this acceleration increases rapidly further downstream. At $x = 1.5\,\text{m}$ the streamwise velocity is 23% larger than the background value and the flow acceleration propagates further downstream. Above the accelerating region the flow showed a great deceleration. At the $x = 1.4\,\text{m}$ cross-section location the flow is 75% slower at $Z/H = 0.33$, 53% slower at $Z/H = 0.5$ and 62% slower at $Z/H = 0.67$. Although the region of deceleration gradually attenuated further downstream it did not reach the background flow velocity values within the sampled extent of the flow. The profiles of Figure 7.11 are comprised of spatially averaged streamwise velocity values which remain positive throughout the flow region. However, when looking at the individual velocity values, negative velocities are observed at the centre of the flow, revealing a flow separation zone that was developed immediately downstream of the scots pine and reached the $x = 1.7\,\text{m}$ cross-section location (see also Figure 7.1). When the foliage of the scots pine was reduced, the flow downstream of the plant decelerated even at the levels of flow near the flume bed. After the second defoliation, the flow near the flume bed ($Z/H = 0.17$) started to accelerate after the $x = 1.9\,\text{m}$ cross-section location, while after the third defoliation this occurred sooner (at $x = 1.7\,\text{m}$). The upper levels of flow were characterised by flow retardation, although the magnitude of the effect was gradually reduced further downstream. In general, the comparison between the fully foliated scenario of the scots pine and the one after the second defoliation (data of the first defoliation have been discarded, see also Section 6.3 in Chapter 6) reveals a decrease of the wake magnitude and extent. However, the comparison between second and third defoliation does not show any major differences (Figure 7.17). Nevertheless, some differences are observed for the flow separation zone which appears to have decreased after each foliage reduction. After the second defoliation the flow separation zone stops at the $x = 1.6\,\text{m}$ cross-section location, while after the third defoliation it stops at the $x = 1.5\,\text{m}$ cross-section location.

The profiles of the spatially averaged transverse velocity vector ($\langle\bar{v}\rangle$) are presented in Figure 7.12. Upstream of the scots pine the flow shows a great variation with the direction of motion changing at $Z/H = 0.5$ and the velocity near the flume bed being reduced by an order of magnitude. At short distances downstream of the plant element, the velocity profiles adopt an 'S' shape. At increasing distances their shape is changing gradually but instead of converging to the profiles that were computed in the absence of vegetation, they adopt a similar shape to the profiles computed upstream of the plant element. This unexpected behaviour might be the result of discrepancies of the inlet conditions of the flow, but in that case variations would be also expected for the streamwise velocity profiles upstream of the plant element (Figure 7.11).

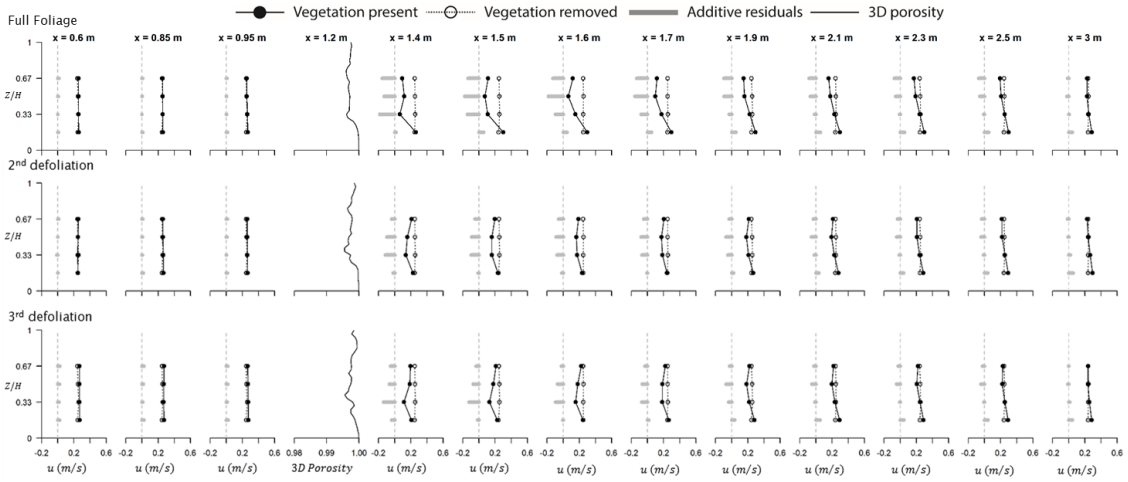

FIGURE 7.11: Cross-stream averages of the streamwise ($\langle \bar{u} \rangle$) velocity vector at increasing distances from the scots pine, positioned at $x = 1.2\,\mathrm{m}$, for all foliage scenarios. The grey bars represent the additive residuals calculated for the streamwise velocities ($\langle \bar{u}_{veg} \rangle - \langle \bar{u}_{empty} \rangle$).

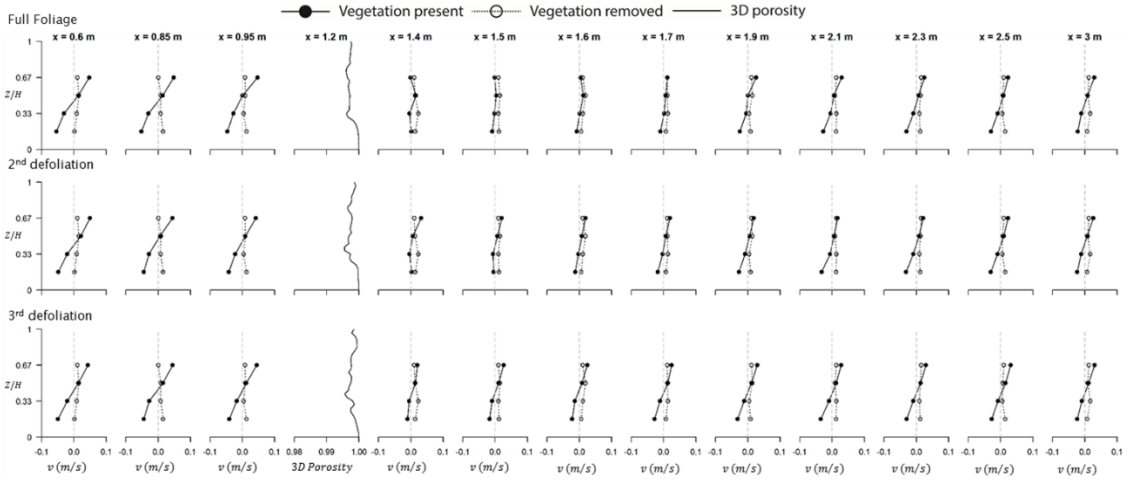

FIGURE 7.12: Cross-stream averages of the transverse ($\langle \bar{v} \rangle$) velocity vector at increasing distances from the scots pine, positioned at $x = 1.2\,\mathrm{m}$, for all foliage scenarios.

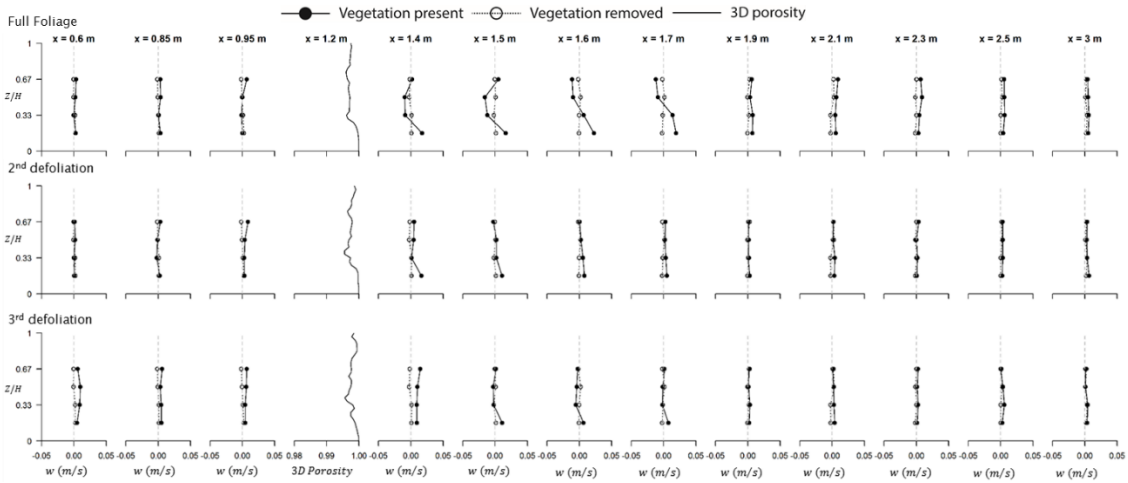

FIGURE 7.13: Cross-stream averages of the transverse ($\langle \bar{w} \rangle$) velocity vector at increasing distances from the scots pine, positioned at $x = 1.2\,\mathrm{m}$, for all foliage scenarios.

Although the profiles of the spatially averaged vertical velocity ($\langle\bar{w}\rangle$) (Figure 7.13) show very little variation upstream of the scots pine, they are substantially altered downstream. Near the plant element, the lower levels of flow followed an upward motion, while the upper ones moved downwards. This behaviour is very prominent up to the $x = 1.7\,\text{m}$ cross-section location (inclusive) for the fully foliated scenario. Foliage removal reduced both the magnitude and extent of this behaviour.

7.2.5 Velocity adjustments due to the presence of the cedar

The profiles of the spatially averaged streamwise velocity vector ($\langle\bar{u}\rangle$) (Figure 7.14) show major flow adjustments downstream of the plant element. At the cross-section locations near the plant, the lower level of flow accelerated. For example at the $x = 1.5\,\text{m}$ cross-section location for the fully foliated cedar, the flow near the bed is 76% faster in comparison to the velocity measured in absence of vegetation at the same location. The region above the accelerating zone was characterised by flow deceleration with the flow at $x = 1.4\,\text{m}$ being 65% slower at $Z/H = 0.33$, 67% slower at $Z/H = 0.5$ and 60% slower at $Z/H = 0.67$. Additionally, a small flow separation zone is observed immediately downstream of the fully foliated plant, which is quickly attenuated between locations $x = 1.5\,\text{m}$ and $x = 1.6\,\text{m}$ (see Figure 7.1). Further downstream the decelerating and accelerating regions gradually diffused within each other and attenuated. After the first defoliation no recirculation zones are observed, and the magnitude of the flow adjustments was gradually reduced after each successive defoliation step. However, the extent of the wake remained constant with the wake boundary being at the $x = 2.5\,\text{m}$ cross-section location. An exception is found for the fully defoliated cedar, the boundary of its wake was at the $x = 1.9\,\text{m}$ cross-section location (see also Figure 7.17).

Upstream of the vegetation element the profiles of the spatially averaged transverse velocity vector ($\langle\bar{v}\rangle$) (Figure 7.15) appear to be similar with the respective profiles upstream of the scots pine that were discussed earlier in subsection 7.2.4. The direction of motion changed at approximately $Z/H = 0.5$ and near the bed the lateral velocity was reduced by an order of magnitude. Changes of the direction of motion are also observed downstream of the plant element throughout the surveyed region of the flow. At short distances this change occurred at $Z/H = 0.33$. However, in successive cross-section locations downstream the inflection point moved upwards and towards the $Z/H = 0.5$. After each defoliation step the inflection point reached the $Z/H = 0.5$ height at shorter distances.

The profiles of the vertical velocity vector ($\langle\bar{w}\rangle$) (Figure 7.16) show small variations upstream of the cedar plant. Most notably at $x = 0.95\,\text{m}$, and especially for the fully foliated scenario, the flow appeared to move downwards. Downstream of the plant element, the flow near the bed showed an upward motion ($\langle\bar{w}\rangle > 0$). The flow above this region had near zero, or slightly negative, vertical velocities meaning that the flow was almost horizontal or flowing slightly downwards.

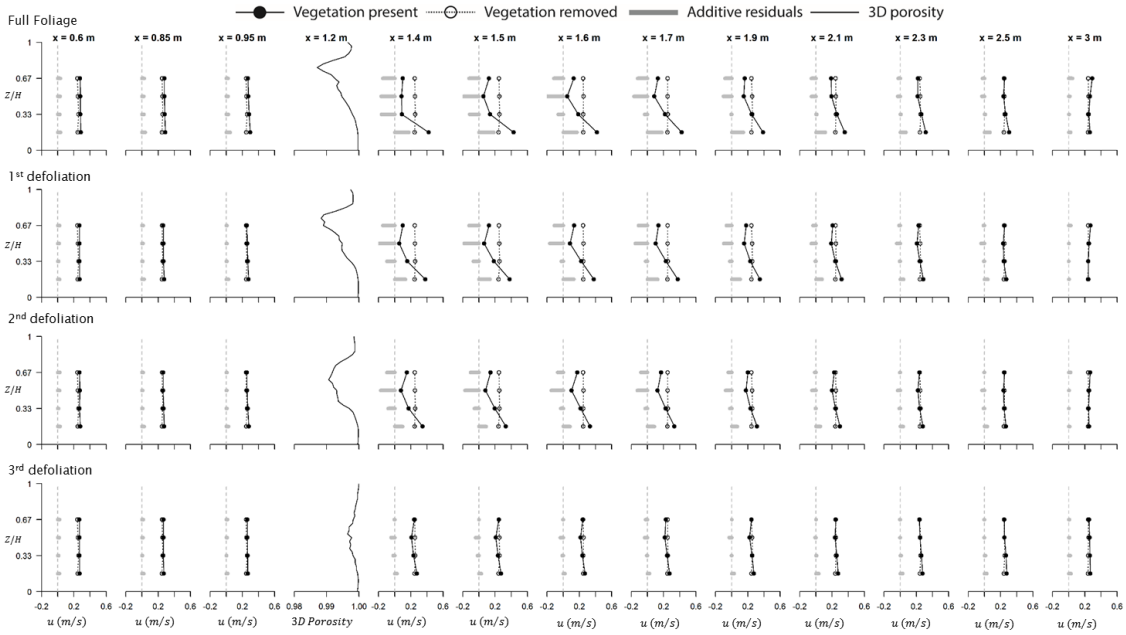

FIGURE 7.14: Cross-stream averages of the streamwise ($\langle \bar{u} \rangle$) velocity vector at increasing distances from the cedar, positioned at $x = 1.2\,\mathrm{m}$, for all foliage scenarios. The grey bars represent the additive residuals calculated for the streamwise velocities ($\langle \bar{u}_{veg} \rangle - \langle \bar{u}_{empty} \rangle$).

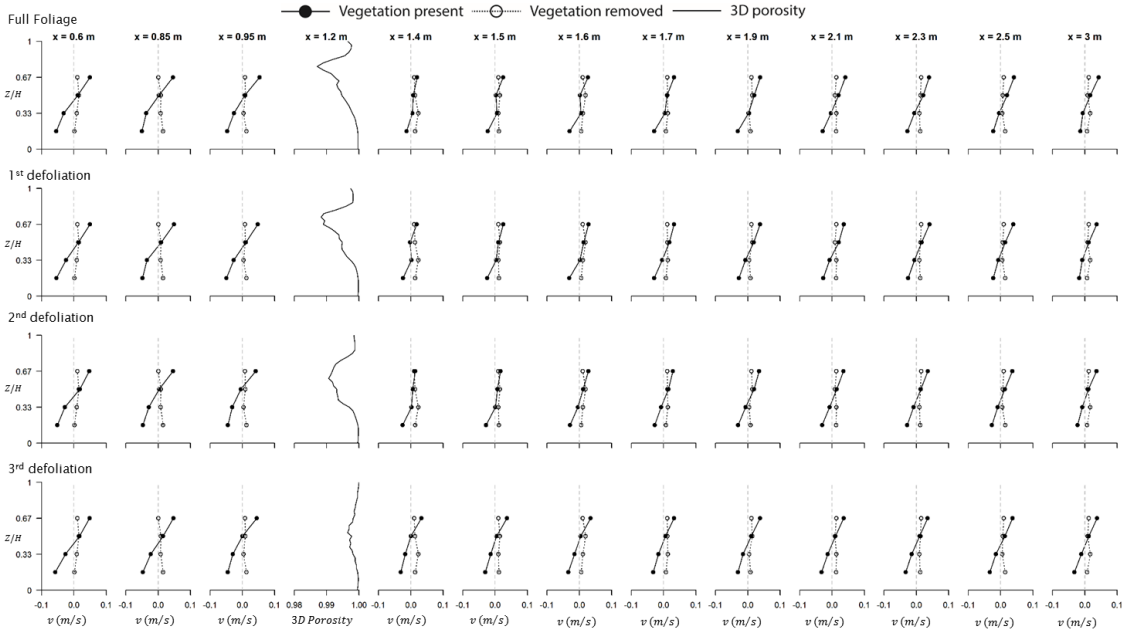

FIGURE 7.15: Cross-stream averages of the transverse ($\langle \bar{v} \rangle$) velocity vector at increasing distances from the cedar, positioned at $x = 1.2\,\mathrm{m}$, for all foliage scenarios.

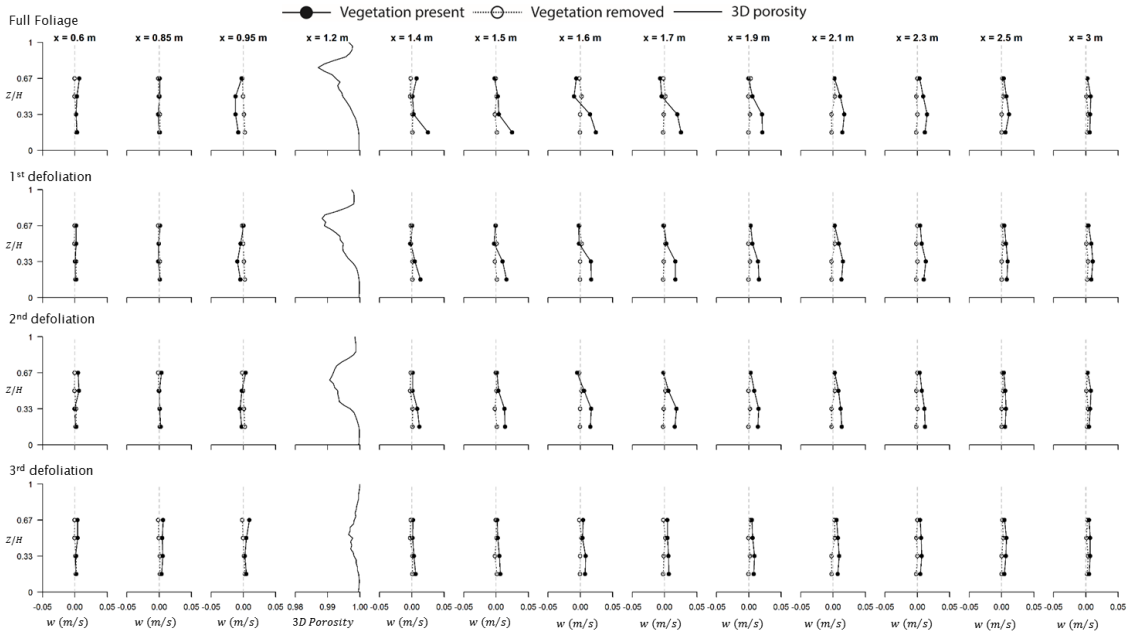

FIGURE 7.16: Cross-stream averages of the transverse ($\langle \bar{w} \rangle$) velocity vector at increasing distances from the cedar, positioned at $x = 1.2\,\mathrm{m}$, for all foliage scenarios.

7.2.6 Summary

The plants investigated during the physical modelling experiments affected the velocity profiles in all three individual components. Downstream of the plant element, the streamwise velocity profiles adopted an 'S' shape, highlighting a flow acceleration region located near the bed and a flow deceleration region occupying the upper levels of flow. For the least porous plant-foliage scenario combinations, a region of localised flow inversion was developed within the flow deceleration zone. This flow structure is in agreement with the spatial configuration of the plant elements, which, as shown from the porosity profiles, were sparsely foliated near the bottom and also agrees with the velocity profile downstream of emergent vegetation described by Nepf (2012) and that was introduced in Section 3.2. Although both the accelerating and decelerating regions of flow appear to attenuate at increasing distances downstream, the region of accelerating flow appears to propagate over longer distances.

The transverse velocity profiles reveal a change of the direction of motion occurring downstream of all plant-foliage scenario combinations. For the least porous scenarios, this behaviour is propagated for longer distances downstream. Conversely, in the most porous scenarios the adjustments of the transverse velocity profiles quickly attenuate. Notably, for all foliage scenarios of the scots pine and the cedar, and the fully foliated grass, this change of motion appears in all of the upstream cross-section locations as well. This is an unexpected behaviour that requires further investigation.

The vertical velocity profiles, reveal that downstream of the plant elements, the lower levels of flow appear to be moving upwards while the upper levels of flow are moving

either downwards or horizontally. Upstream of the vegetation element, negative vertical velocities are observed which are more prominent at the least porous plant-foliage scenario combinations. Therefore, it appears that these scenarios exert a noticeable backwater effect on the flow manifesting with the observed adjustments of the vertical and transverse velocity. In other words, when the flow reaches the dense plant obstruction it is being steered towards the sides of the flume and downwards, seeking the pathways of least resistance to overcome the obstacle.

7.3 Associating plant structure and wake characteristics

Downstream of the plant elements a wake region was developed. In most cases, the extent of the wake does not appear to be related to the reduction of foliage between successive scenarios (Figure 7.17). Boothroyd et al. (2015) undertook numerical modelling simulations with a single plant type (*Prunus laurocerasus*) and report that the extent of the wake region resolved by the CFD model ranged between three and seven plant lengths. The wake extents estimated from the curves of Figure 7.17 fall within the same range. The extent of the wake developed downstream of the fig was approximately two plant lengths. The one developed downstream of the bamboo ranged between five and seven plant lengths, while the extent downstream of the grass was approximately five plant lengths. The wake region downstream of the scots pine had an extent that ranged between five and six plant lengths while the one developed downstream of the cedar had an extent that ranged between three and four plant lengths.

The wake intensity (area under the curve in Figure 7.17) however, appears to have decreased after each successive defoliation step. Therefore the areas under the curve computed from Figure 7.17 are plotted against the bulk plant structure metrics that were earlier identified in Chapter 6 ($P_{2D}/\overline{A_b}$ and $P_{3D}/\overline{A_b}$). The respective plots are presented in Figure 7.18. A power law relationship is found between the variables and the general appearance of the plots as well as the computed R^2 values are similar with the ones found through the investigation of plant structure metrics and hydraulic roughness (see Chapter 6).

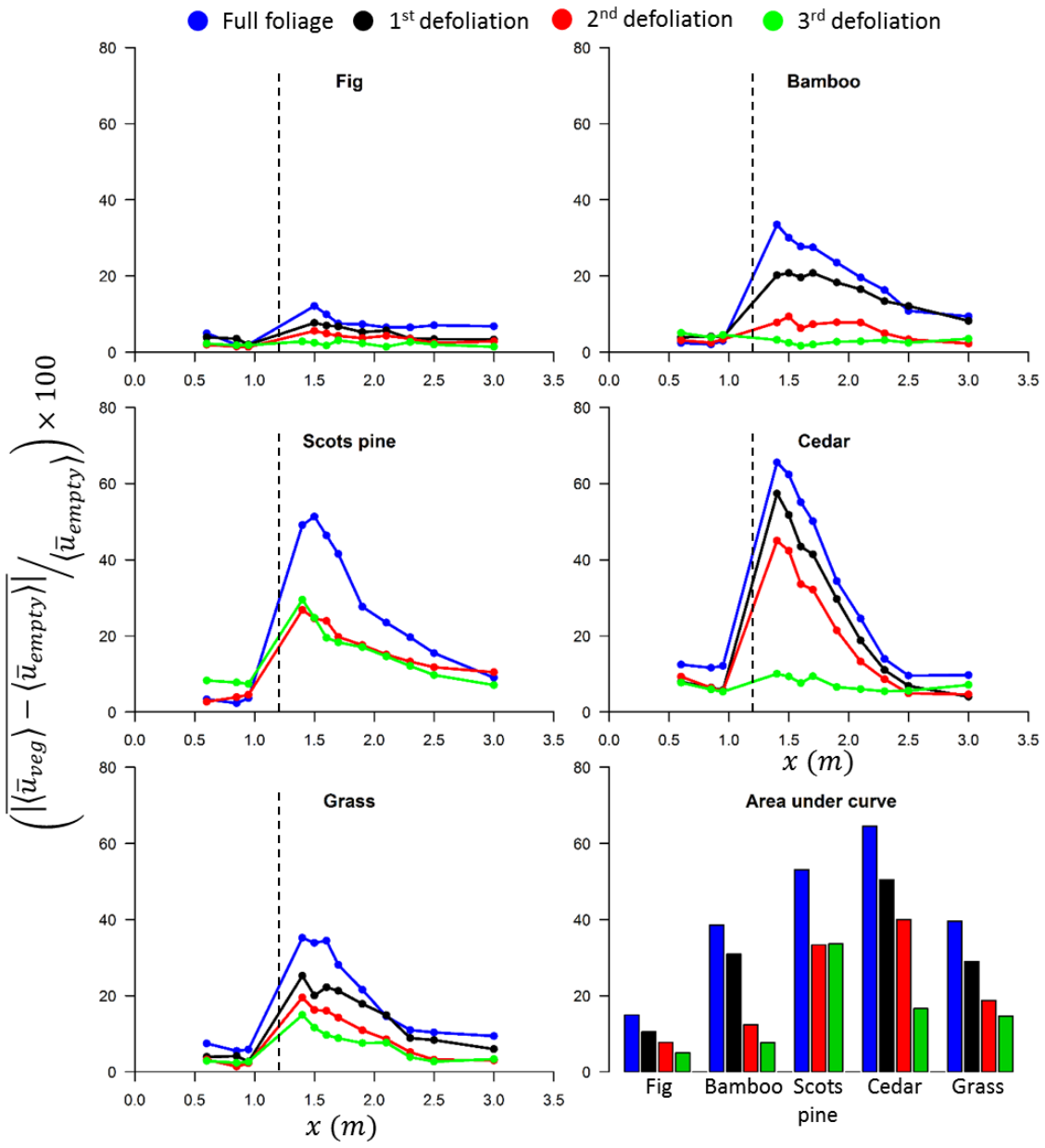

FIGURE 7.17: Comparison of the spatially averaged streamwise velocity ($\langle\bar{u}\rangle$) for all plant-foliage scenario combinations. The plants were mounted at $x = 1.2\,\mathrm{m}$ (dashed line). The bar plot shows the area under the curve computed for each plant-foliage scenario combination.

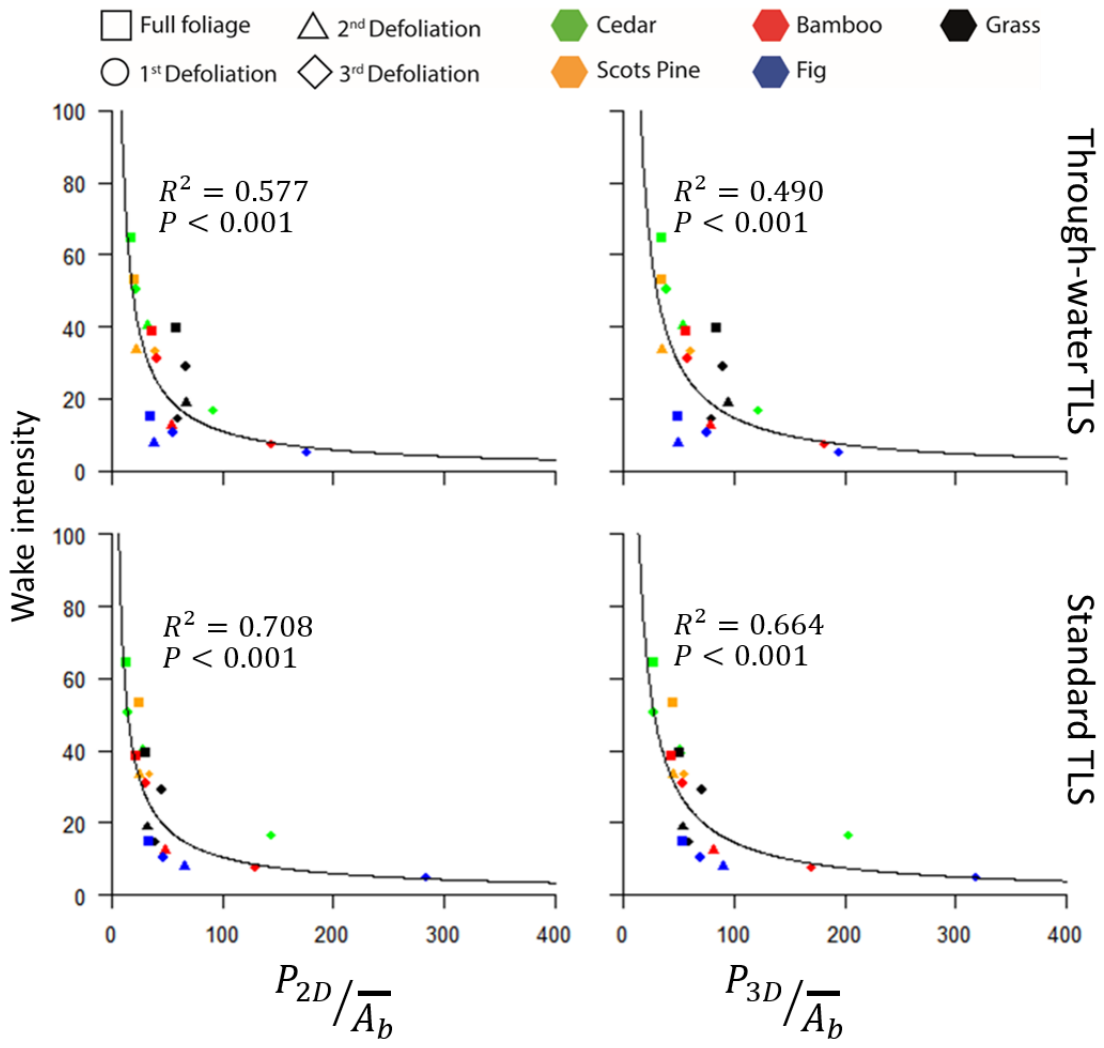

FIGURE 7.18: Relationship between bulk metrics of plant structure, expressed using the combination of bulk 2D or 3D porosity metrics with the mean value of the plant extent, with the wake intensity estimated from the streamwise velocity residuals. Plots correspond to Deep-Slow flow using both 'through-water' and 'standard' TLS data.

7.4 Flow mixing downstream of the plant elements

The ratio of transverse over the streamwise velocity, using spatially averaged absolute values $\left(M = \frac{|\langle\bar{v}\rangle|}{|\langle\bar{u}\rangle|}\right)$ is presented in Figure 7.19. In the absence of vegetation, the value of M appears to fluctuate between the various cross-section locations, with its mean value being equal to $\overline{M} = 0.046$ ($\sigma = 0.007$).

When the fully foliated fig is introduced into the flow, M shows a major increase immediately downstream of the plant element (from 0.06 to 0.102) but at successive cross-section locations it decreases and rapidly returns to the background values. The mean value for this scenario was computed to be equal to 0.057 (($\sigma = 0.02$)). Although after each successive defoliation step, the value of M immediately downstream of the plant element is decreased (0.084, 0.058 and 0.042 are the values of M computed at the $x = 1.5$ m cross-section location for the first, second and third defoliation scenarios,

respectively), the ratio of transverse and streamwise velocity remains large enough at the subsequent cross-section locations to yield larger mean values. In fact, the mean value of M appears to increase slightly after the first defoliation of the fig; it remains approximately constant after the second defoliation while after the third defoliation it shows a major decrease with the mean value being lower than the one computed in the absence of vegetation, but within one standard deviation of the mean.

Immediately downstream of the fully foliated bamboo the value of M is higher than the respective value computed in the absence of vegetation. Although it fluctuates at increasing distances downstream, it remains greater than the empty flume values at all cross-section locations except from the furthermost downstream one. This yields a mean value for this scenario which is greater than the one computed in absence of vegetation ($\overline{M} = 0.066$ ($\sigma = 0.012$ and $\overline{M} = 0.046$ ($\sigma = 0.007$). After the first defoliation, the M value immediately downstream of the plant element is slightly larger than the one computed for the fully foliated scenario of the same plant ($M = 0.718$). However, at the subsequent cross-section location it is reduced to 0.056 and remains approximately constant further downstream. The mean value for this scenario was computed to be equal to 0.056 ($\sigma = 0.006$). At subsequent defoliation steps the values of M at individual cross-section locations are decreased and become similar to the background values, this yields lower mean values with $\overline{M}$ being equal to 0.051 and 0.04 after the second and third defoliation, respectively.

At the $x = 1.4\,\text{m}$ and $x = 1.5\,\text{m}$ cross-section locations downstream of the fully foliated scots pine, the value of M appears to be smaller than the empty flume scenario. However, at increasing distances downstream M is increasing steadily until it reaches its maximum at the $x = 2.1\,\text{m}$ cross-section location. Although it shows a small increase at the further downstream cross-section locations, it always remains much greater than the background values. The mean value of M is equal to 0.064 ($\sigma = 0.018$). The variation of M at subsequent cross-sections downstream of the scots pine after the second and third defoliation is similar to the previous scenario. Initially the value of M is small but increases gradually with increasing distances downstream until it reaches a maximum (at $x = 2.3\,\text{m}$ and $x = 1.9\,\text{m}$ for the second and third defoliation scenarios, respectively). After that point the values are slightly decreasing further downstream. At the furthermost downstream cross-section location, the values of M for each scenario appear to converge with each other. Interestingly, the values computed for the third defoliation scenario are constantly higher than the ones computed for the other foliage scenarios of this plant and this is also revealed by the computed mean values (0.064, 0.062 and 0.09 for full foliage, second and third defoliation, respectively).

The variation of M downstream of the cedar appears to follow a similar trend with the one of the scots pine discussed earlier. Although the values of M immediately downstream of the plant element are greater than the ones computed for the empty flume scenario, they remain relatively small. At increasing distances downstream, they increase gradually until they reach their maximum. This happens at the $x = 1.9\,\text{m}$ cross-section

location for the fully defoliated plant scenario and at the $x = 1.7\,\text{m}$ cross-section location for all other scenarios. Further downstream the values of M decrease and converge with each other. An exception is shown for the fully defoliated scenario; although the values of M appear to fluctuate with an increasing distance, they remain similar to the maximum value observed for this scenario. The mean value of the ratio of transverse and streamwise velocity is equal to 0.095 ($\sigma = 0.015$) for the fully foliated scenario. After the first defoliation the mean value is increased to 0.098 ($\sigma = 0.019$) and decreased to 0.086 ($\sigma = 0.014$) after the second defoliation. For the fully defoliated plant the computed mean value of M is increased and equal to 0.089 ($\sigma = 0.004$).

The values of M downstream of the fully foliated grass show a similar pattern with the one observed for the cedar earlier. The ratio of transverse over the streamwise velocity at the $x = 1.4\,\text{m}$ cross-section location is equal to 0.076 and gradually increases downstream until it reaches a maximum at $x = 1.7\,\text{m}$. After this point the computed value of M decreases at each successive cross-section and reaches the background value at the furthermost cross-section downstream ($x = 3\,\text{m}$). After the first defoliation the pattern appears to be different. The maximum M value occurs immediately downstream of the plant element and although M fluctuates further downstream, it follows a general decreasing trend. After the x =2.3 m cross-section location it appears to remain approximately constant. The same pattern appears after the third defoliation, although the values of M are consistently lower in comparison to the first defoliation scenario and more similar to the empty flume scenario. The mean value of M for the fully foliated grass is equal to 0.074 ($\sigma = 0.013$). Foliage reduction decreases the mean value of the ratio which becomes equal to 0.068 ($\sigma = 0.012$), 0.057 ($\sigma = 0.010$) and 0.053 ($\sigma = 0.009$) after each successive defoliation.

The values of the ratio of transverse over the streamwise velocity vector (M) reveal the existence of secondary flow for all plant-foliage scenario combinations that were investigated. Yang et al. (2012) suggest that for an open rectangular duct with smooth boundaries the magnitude of secondary flow is $\frac{|\langle\overline{v}\rangle|}{|\langle\overline{u}\rangle|} = 1\%$. This value is smaller than the mean values estimated from the experiments conducted in this study, where the smallest $\overline{M}$ value was computed to be equal to 3.8% and it corresponds to the fully defoliated fig, while for the empty flume scenario $\overline{M}$ is equal to 4.6%. The higher value of $\overline{M}$ observed in absence of vegetation, in comparison to the one suggested by Yang et al. (2012), is likely due to the roughness of the false bed that was installed in the flume prior to the experiments. As described in Chapter 6 (see subsection 6.1.1) the bed was covered with sheets of marine plywood that were sealed with adhesive sealant and modelling clay, and three large roughness elements were installed near the inlet to assure a quick transition to a fully turbulent flow. Therefore, it is likely that the surface of this false bed is dissimilar to the ideal conditions of a smooth flume bed associated with many flume experiments. Nevertheless, comparison between the values of $\overline{M}$ computed for the empty flume scenario with those computed for the various plant-foliage scenario combinations reveals that the magnitude of secondary flow increases when vegetation is present. For

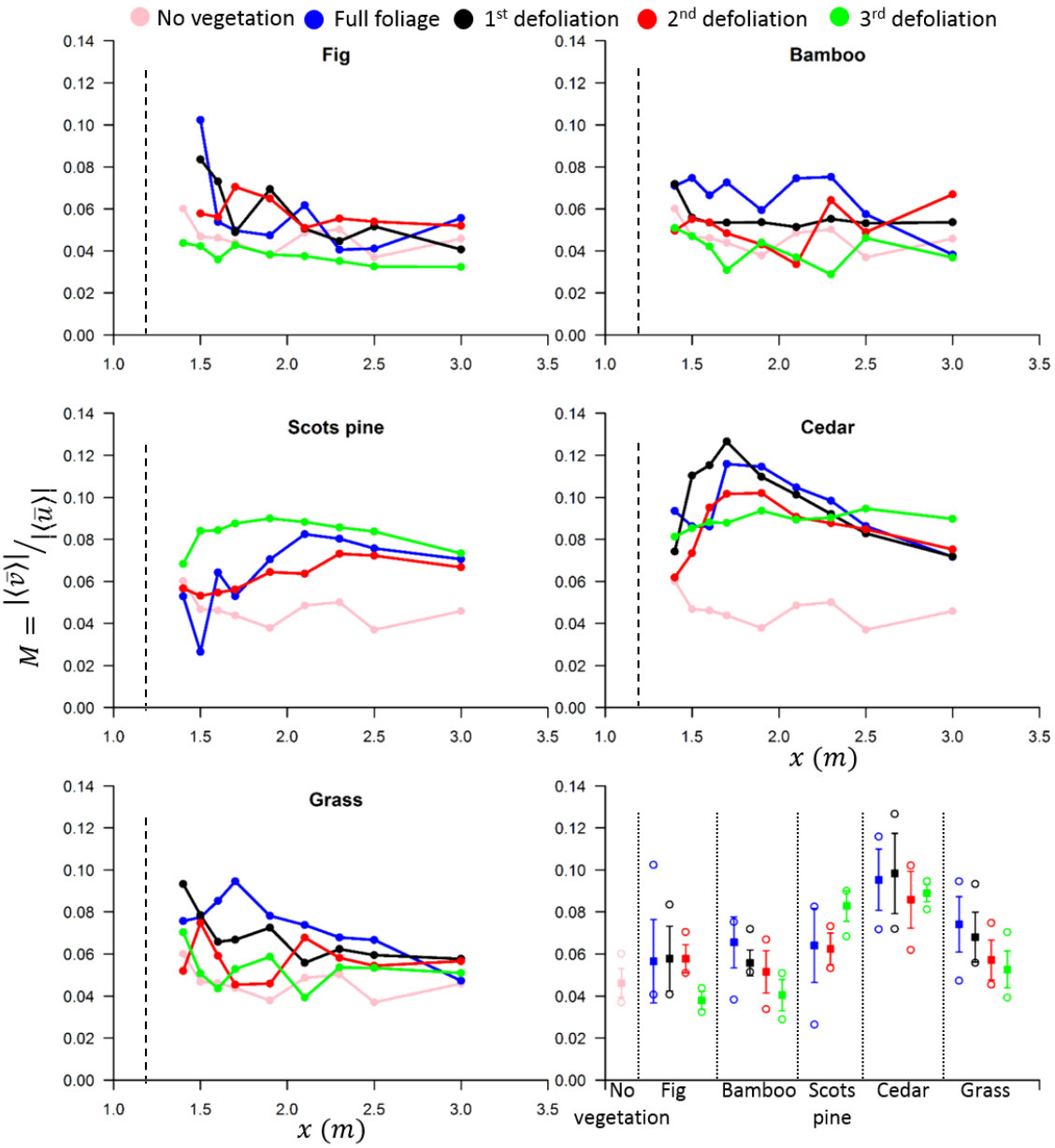

FIGURE 7.19: Ratio of the transverse over the streamwise velocity component, using spatially averaged absolute values, downstream of all plant foliage scenario combinations at various cross-section locations along the flume. The vertical black dashed lines show the position of the vegetation elements ($x = 1.2\,\mathrm{m}$). The bottom right plot presents the mean value (solid squares) computed for each scenario along with the minimum and maximum values (circles), while the vertical bars represent one standard deviation above and below the mean.

some of the investigated plants (i.e. bamboo and grass) foliage reduction appears to be reducing the values of $\overline{M}$. For the remaining ones (i.e. fig, scots pine and cedar) this argument is not clearly supported by the data, with means which are not statistically distinct from one another. Therefore, the bulk plant structure does not appear to be strongly associated with the values of $\overline{M}$ and this is supported by the relatively weak correlation statistics shown in Figure 7.20 between plant structure and $\overline{M}$.

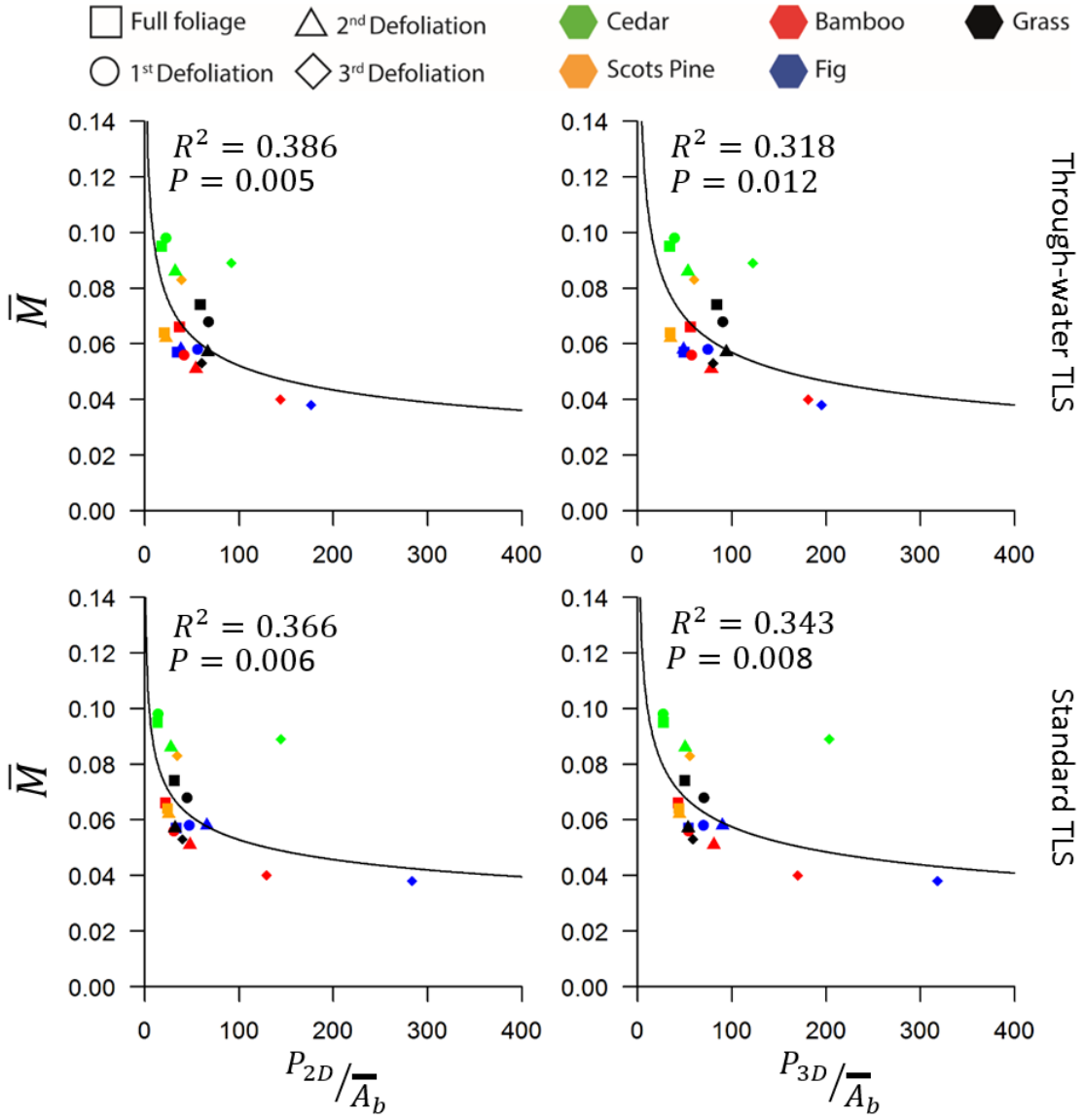

FIGURE 7.20: Relationship between bulk metrics of plant structure, expressed using the combination of bulk 2D or 3D porosity metrics with the mean plant extent, with the mean values of the ratio of transverse over the cross-stream velocity component ($\overline{M}$). Plots correspond to Deep-Slow flow using both 'through-water' and 'standard' TLS data.

There is an extensive body of literature that has looked into the effects of vegetation on the magnitude of secondary flow and the consequent flow mixing. Nepf (1999) suggests that there are two mechanisms of diffusion associated with vegetated flows; turbulent and mechanical. The former is due to the turbulent nature of water flow which accommodates the random scatter of particles by turbulent motion Chau (2000) (see

example in Figure 7.21, I). The latter is common in flows through porous media and it is associated with the dispersal of fluid particles due to variability in flow paths when water travels through vegetation (see example in Figure 7.21, II). The available pathways necessary for the flow to overcome the plant obstruction are related to the spatial arrangement of the plant elements. Therefore, the mechanical diffusion itself must be linked to the spatial arrangement of individual stems and leaves, which is not taken into account in the bulk metrics of plants structure. The occurrence of mechanical diffusion within the vegetation array might explain the relatively weak correlation statistics that were shown in Figure 7.20. Since velocity measurements where not obtained from points within the canopy during the experiments, the mechanical diffusion could not be estimated. Nevertheless, because mechanical and turbulent diffusion are additive, the values of $\overline{M}$ estimated here incorporate both the part of diffusion emanating by the function of vegetation as a physical obstruction (mechanical diffusion) as well as the diffusion emanating by the increased turbulence (turbulent diffusion) which in turn is partially a product of the presence of vegetation. The increased values of $\overline{M}$ with the presence of vegetation highlight that the transverse velocity component becomes larger at the expense of the streamwise one. This indicates that vegetation moderates longitudinal mixing in favour of transverse mixing.

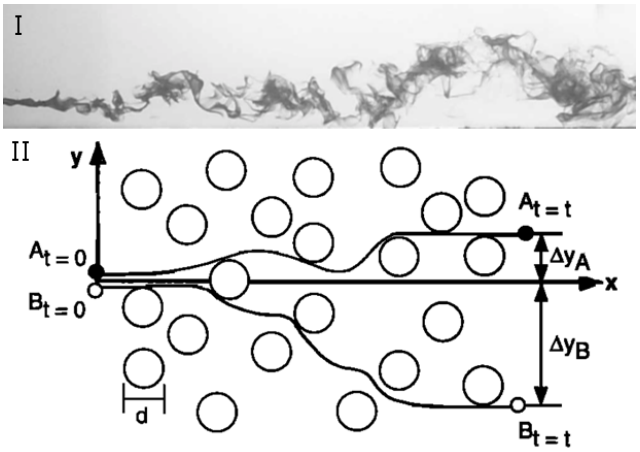

FIGURE 7.21: I: Example of turbulent diffusion, chemical plume released isokinetically into fully developed turbulent open-channel flow (Source: Figure 1 from Roberts and Webster, 2002). II: Concept of mechanical diffusion that arises from the physical obstruction of the flow by stems. When a stem is encountered, the particle must move laterally $\Delta y \tilde{} d$ (Source: Figure 2 from Nepf, 1999).

7.5 Effects of vegetation on the turbulent kinetic energy

Using the 3D velocity fluctuations (u', v', w') that were calculated through the Reynolds decomposition of the ADV data, the turbulent kinetic energy (TKE) was computed from Equation (6.6). This was undertaken for all surveyed cross-section locations downstream of each plant-foliage scenario combination. Subsequently, an average TKE value was computed for each cross-section location and plotted against the corresponding distance

value. The resulting curves for each plant-foliage scenario combination are presented in Figure 7.22. For each curve the minimum, maximum, mean and standard deviation values were extracted and are presented in the bottom-right plot of the same figure.

The mean TKE value in the absence of vegetation is approximately $6 \times 10^{-4}\text{m}^2\ \text{s}^{-2}$ ($\sigma = 1 \times 10^{-4}\text{m}^2\ \text{s}^{-2}$) and it shows only minor deviations at various locations along the flume as shown by the minimum and maximum values which are $4 \times 10^{-4}\text{m}^2\ \text{s}^{-2}$ and $8 \times 10^{-4}\text{m}^2\ \text{s}^{-2}$, respectively. When the fully foliated fig is introduced into the flume flow, the value of the TKE immediately downstream of the plant element ($x = 1.5\,\text{m}$) is increased and becomes equal to $18 \times 10^{-4}\text{m}^2\ \text{s}^{-2}$. However, it gradually decreases as the distance from the plant element increases and at the furthermost downstream cross-section location ($x = 3\,\text{m}$) it becomes similar to the background value ($7 \times 10^{-4}\text{m}^2\ \text{s}^{-2}$). After each successive defoliation the computed TKE values for each cross-section location are reduced, but the general trajectory of the curve remains similar, showing decreasing values of TKE at increasing distances from the plant element. The mean computed values are equal to $13 \times 10^{-4}\text{m}^2\ \text{s}^{-2}$ ($\sigma = 4 \times 10^{-4}\text{m}^2\ \text{s}^{-2}$), $11 \times 10^{-4}\text{m}^2\ \text{s}^{-2}$ ($\sigma = 5 \times 10^{-4}\text{m}^2\ \text{s}^{-2}$), $8 \times 10^{-4}\text{m}^2\ \text{s}^{-2}$ ($\sigma = 3 \times 10^{-4}\text{m}^2\ \text{s}^{-2}$) and $5 \times 10^{-4}\text{m}^2\ \text{s}^{-2}$ ($\sigma = 1 \times 10^{-4}\text{m}^2\ \text{s}^{-2}$) for the fully foliated, first defoliation, second defoliation and fully defoliated scenarios of the fig, respectively. For the fully defoliated fig the TKE values calculated are almost identical with the ones computed in absence of vegetation.

The TKE value calculated immediately downstream of the fully foliated bamboo ($x = 1.4\,\text{m}$) is equal to $18 \times 10^{-4}\text{m}^2\ \text{s}^{-2}$ it then decreases gradually at increasing distances downstream, until it reaches a minimum ($15 \times 10^{-4}\text{m}^2\ \text{s}^{-2}$) at the $x = 1.7\,\text{m}$ cross-section location. After that it shows an increase and at the $x = 2.1\,\text{m}$ cross-section location it reaches a maximum ($19 \times 10^{-4}\text{m}^2\ \text{s}^{-2}$). At further cross-sections downstream it decreases gradually and at the $x = 3\,\text{m}$ cross-section location it becomes equal to $15 \times 10^{-4}\text{m}^2\ \text{s}^{-2}$. The curve after the first defoliation has a more regular pattern with the value of TKE being $13 \times 10^{-4}\text{m}^2\ \text{s}^{-2}$ immediately downstream of the plant element and remaining approximately constant up until the $x = 2.1\,\text{m}$ cross-section location. After this point it starts decreasing gradually and at the $x =3\,\text{m}$ cross-section location it is equal to $9 \times 10^{-4}\text{m}^2\ \text{s}^{-2}$. After the second defoliation the TKE value immediately downstream of the plant element is equal to $14 \times 10^{-4}\text{m}^2\ \text{s}^{-2}$ and remains approximately constant up until the $x = 1.6\,\text{m}$ cross-section location. At the $x =1.7\,\text{m}$ cross-section location it appears to be increased ($15 \times 10^{-4}\text{m}^2\ \text{s}^{-2}2$) and then it decreases until it reaches a low value ($10 \times 10^{-4}\text{m}^2\ \text{s}^{-2}$) at $x = 2.1\,\text{m}$. However, at $x = 2.3\,\text{m}$ it appears to be increased again ($12 \times 10^{-4}\text{m}^2\ \text{s}^{-2}$) and then gradually decreases further downstream until it reaches its minimum ($9 \times 10^{-4}\text{m}^2\ \text{s}^{-2}$) at $x = 3\,\text{m}$. The curve of the fully defoliated bamboo scenario appears to be similar to the one computed in absence of vegetation but the values of TKE calculated for the fully defoliated bamboo are slightly higher than the ones calculated in absence of vegetation. The mean TKE values computed for each foliage scenario are equal to $17 \times 10^{-4}\text{m}^2\ \text{s}^{-2}$ ($\sigma = 1 \times 10^{-4}\text{m}^2\ \text{s}^{-2}$),

13×10^{-4}m^2 s^{-2} ($\sigma = 2 \times 10^{-4}$m^2 s^{-2}), 12×10^{-4}m^2 s^{-2} ($\sigma = 2 \times 10^{-4}$m^2 s^{-2}) and 7×10^{-4}m^2 s^{-2} ($\sigma = 1 \times 10^{-4}$m^2 s^{-2}) for the fully foliated, first defoliation, second defoliation and fully defoliated bamboo scenarios, respectively.

Immediately downstream of the fully foliated scots pine, the computed TKE value is equal to 15×10^{-4}m^2 s^{-2} and it increases very rapidly until it reaches its maximum (62×10^{-4}m^2 s^{-2}) at the $x = 1.7$ m cross-section location. This is followed by a rapid decrease and at the furthermost downstream cross-section location the value of the TKE is equal to 17×10^{-4}m^2 s^{-2}. The same pattern is observed at the other two foliage scenarios of the scots pine. After the second defoliation, the calculated TKE immediately downstream of the plant element ($x = 1.4$ m) is equal to 30×10^{-4}m^2 s^{-2}, then it increases rapidly and it reaches its maximum (37×10^{-4}m^2 s^{-2}) at $x = 1.7$ m and then decreases further downstream. After the third defoliation, the computed value at $x = 1.4$ m is equal to 32×10^{-4}m^2 s^{-2}, the maximum value is 35×10^{-4}m^2 s^{-2} and it is observed at the $x = 1.7$ m cross-section location and the minimum value is observed at the furthermost downstream cross-section location. The mean computed values are equal to 40×10^{-4}m^2 s^{-2}2 ($\sigma = 17 \times 10^{-4}$m^2 s^{-2}), 38×10^{-4}m^2 s^{-2} ($\sigma = 7 \times 10^{-4}$m^2 s^{-2}) and 28×10^{-4}m^2 s^{-2} ($\sigma = 7 \times 10^{-4}$m^2 s^{-2}) for the fully foliated, second defoliation and third defoliation scenarios of the scots pine, respectively.

A similar trend of the TKE fluctuations is observed for the cedar. Immediately downstream of the fully foliated scenario it is equal to 16×10^{-4}m^2 s^{-2} and it increases rapidly until the $x = 1.6$ m cross-section location. This is followed by a minor increase until the x =1.9 m cross-section location where the maximum is reached (43×10^{-4}m^2 s^{-2}). After that the value decreases quickly at increasing distances and at the $x = 3$ m cross-section location it is equal to 18×10^{-4}m^2 s^{-2}. A similar pattern is observed after the first defoliation of the cedar. Immediately downstream of the plant element the value of the TKE is equal to 15×10^{-4}m^2 s^{-2}, it increases rapidly until the $x = 1.6$ m where it becomes equal to 27×10^{-4}m^2 s^{-2} and continues to increase at a smaller rate until the $x = 1.9$ m where it reaches its maximum value (29×10^{-4}m^2 s^{-2}). At further locations downstream it gradually decreases and at $x = 3$ m it is equal to 13×10^{-4}m^2 s^{-2}. After the second defoliation the TKE value computed immediately downstream of the plant element is equal to 15×10^{-4}m^2 s^{-2} and increases rapidly further downstream until it reaches its maximum (28×10^{-4}m^2 s^{-2}) at the $x = 1.7$ m cross-section location. The values of TKE decrease gradually further downstream and reach a minimum (10×10^{-4}m^2 s^{-2}) at the furthermost downstream cross-section location. The value computed for the fully defoliated scenario of the cedar is equal to 10×10^{-4}m^2 s^{-2} immediately downstream of the plant element and it increases to 12×10^{-4}m^2 s^{-2} at the next cross-section location ($x = 1.5$ m). At all successive cross-section locations, a gradual decrease at increasing distances is observed. The mean TKE values computed for the cedar plant are equal to 32×10^{-4}m^2 s^{-2} ($\sigma = 10 \times 10^{-4}$m^2 s^{-2}), 23×10^{-4}m^2 s^{-2} ($\sigma = 6 \times 10^{-4}$m^2 s^{-2}), 20×10^{-4}m^2 s^{-2} ($\sigma = 6 \times 10^{-4}$m^2 s^{-2}) and 10×10^{-4}m^2 s^{-2} ($\sigma = 2 \times 10^{-4}$m^2 s^{-2}) for the fully foliated,

first defoliation, second defoliation and fully defoliated scenarios, respectively.

The computed value of TKE immediately downstream of the fully foliated grass is equal to $34 \times 10^{-4}\text{m}^2\ \text{s}^{-2}$ and it increases further downstream, until it reaches its maximum ($44 \times 10^{-4}\text{m}^2\ \text{s}^{-2}$) at the $x = 1.6\,\text{m}$ cross-section location. After this point the value decreases slightly at first up until the $x = 1.9\,\text{m}$ cross-section location and then rapidly for the rest of the surveyed extent of the flow. The TKE value computed for the $x = 3\,\text{m}$ cross-section location is equal to $15 \times 10^{-4}\text{m}^2\ \text{s}^{-2}$. A similar pattern is observed after the first defoliation. At $x = 1.4\,\text{m}$ the value of TKE is equal to $26 \times 10^{-4}\text{m}^2\ \text{s}^{-2}$, it increases to $32 \times 10^{-4}\text{m}^2\ \text{s}^{-2}$ at the $x = 1.6\,\text{m}$ cross-section location and then decreases at the successive cross-section locations downstream. The magnitude of the decrease is moderate until the $x = 2.1\,\text{m}$ cross-section location and becomes rapid further downstream. After the second defoliation the value of the TKE is equal to $24 \times 10^{-4}\text{m}^2\ \text{s}^{-2}$ immediately downstream of the plant element and it increases to $28 \times 10^{-4}\text{m}^2\ \text{s}^{-2}$ at the $x = 1.5\,\text{m}$. Further downstream the value remains approximately constant until the $x = 1.9\,\text{m}$ cross-section location and then decreases rapidly for the rest of the surveyed flow. After the final defoliation, the TKE value immediately downstream of the grass is $25 \times 10^{-4}\text{m}^2\ \text{s}^{-2}$ and is decreasing rapidly as the distance from the plant element becomes greater. The mean TKE values computed for the grass are equal to $33 \times 10^{-4}\text{m}^2\ \text{s}^{-2}$ ($\sigma = 9 \times 10^{-4}\text{m}^2\ \text{s}^{-2}$), $26 \times 10^{-4}\text{m}^2\ \text{s}^{-2}$ ($\sigma = 6 \times 10^{-4}\text{m}^2\ \text{s}^{-2}$), $23 \times 10^{-4}\text{m}^2\ \text{s}^{-2}$ ($\sigma = 5 \times 10^{-4}\text{m}^2\ \text{s}^{-2}$) and $17 \times 10^{-4}\text{m}^2\ \text{s}^{-2}$ ($\sigma = 6 \times 10^{-4}\text{m}^2\ \text{s}^{-2}$) for the fully foliated, first defoliation, second defoliation and third defoliation scenarios, respectively.

In summary, all plant-foliage scenario combinations appear to increase the magnitude of the flow's turbulent kinetic energy. In some cases, this is decreased as the distance from the plant element becomes greater while in others, the value of TKE appears to be increasing rapidly within a short region downstream of the obstruction until it reaches a maximum. Beyond this point the increased turbulent kinetic energy is gradually attenuated. Foliage reduction appears to be moderating the magnitude of the turbulent kinetic energy. This is further supported by the regression statistics presented in Figure 7.23, where the relationship between bulk plant structure metrics and mean TKE shows a good agreement when standard TLS data are used.

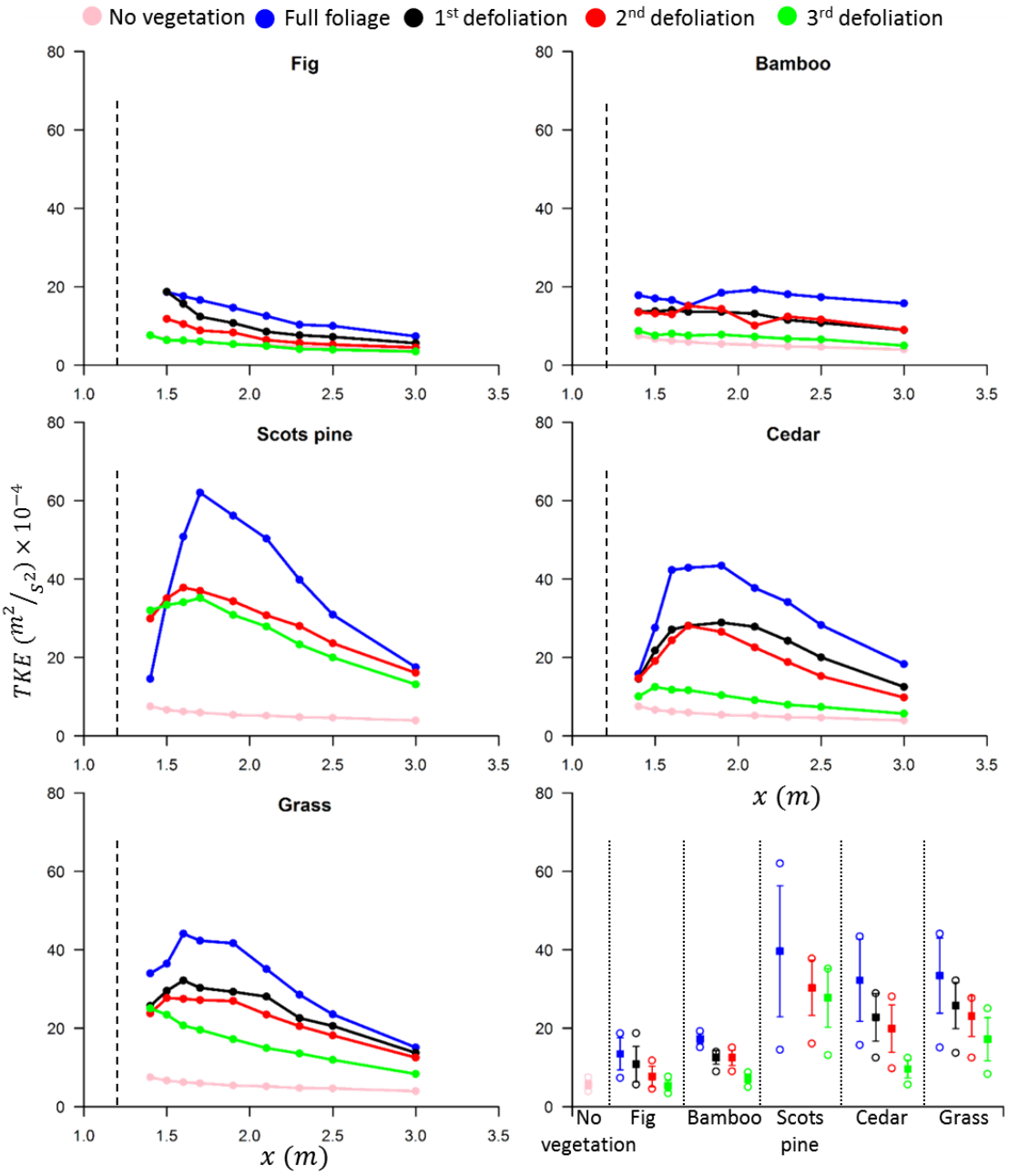

FIGURE 7.22: Spatially averaged turbulent kinetic energy (TKE) estimated for each surveyed cross-section location downstream of the plant elements. The vertical black dashed lines show the position of the plant elements ($x = 1.2\,\mathrm{m}$). The bottom right plot presents the mean value (solid squares) computed for each scenario along with the minimum and maximum values (circles), while the vertical bars represent one standard deviation above and below the mean.

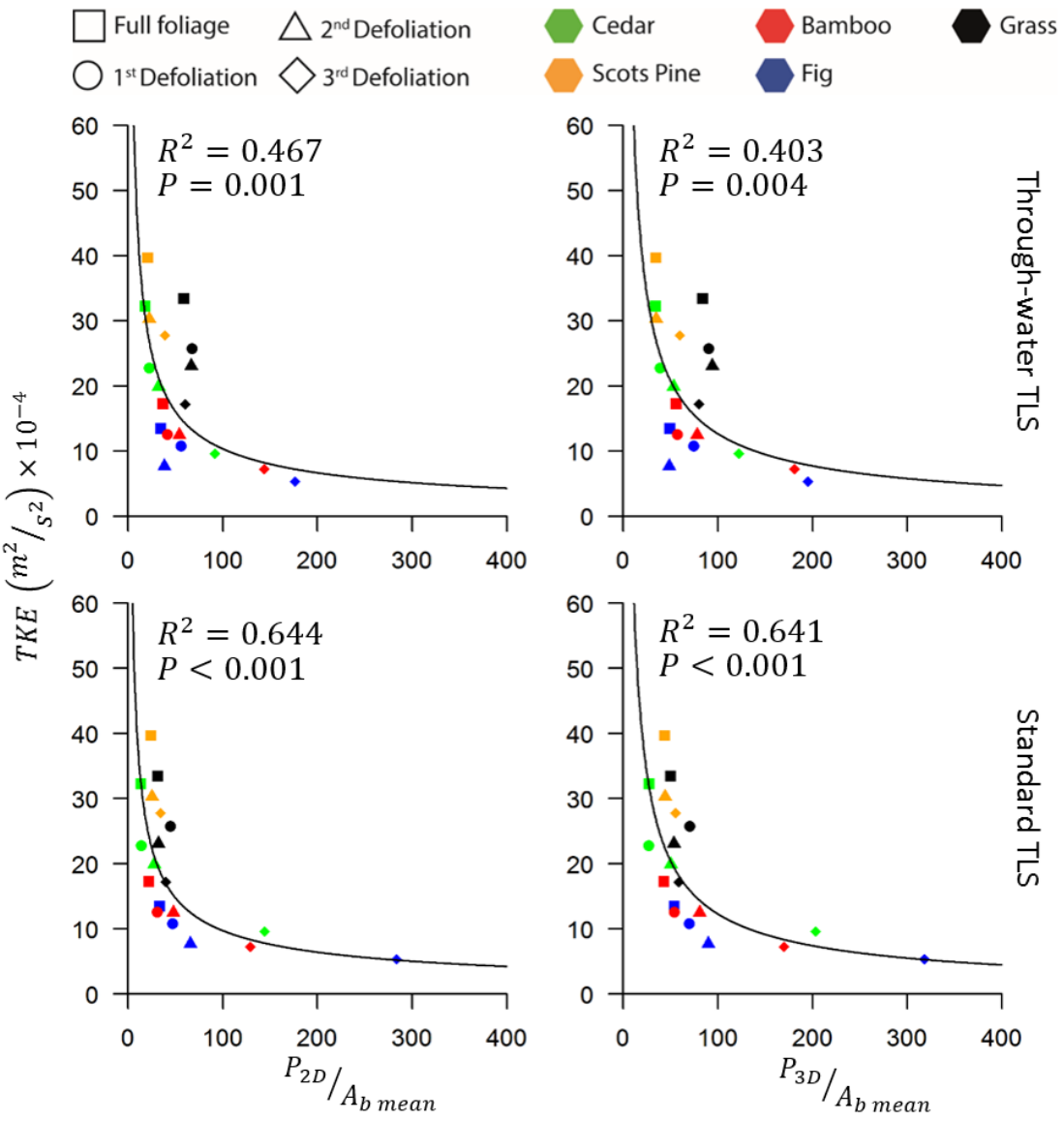

FIGURE 7.23: Relationship between bulk metrics of plant structure, expressed using the combination of bulk 2D or 3D porosity metrics with the mean plant extent, with the mean values of turbulent kinetic energy. Plots correspond to Deep-Slow flow using both 'through-water' and 'standard' TLS data.

7.6 Chapter summary

The present Chapter highlighted that dense vegetation may exert backwater effects on the flow (Figure 7.24, B). Plants essentially function as large-scale obstacles, blocking parts of the flow. At areas where the plant obstruction is dense (e.g. due to increased foliage) the flow decelerates, this, in conjunction with a continuous supply of water from further upstream, leads to water accumulation and consequently to a localised increase of the pressure head. The flow follows preferential flow paths through less obstructed regions (e.g. near the bottom where the plant foliage is minimal) attempting to overcome the obstacle and due to the increased pressure head, in conjunction with the limited available space, accelerates. Downstream of the plant element a wake region is

developed. Inside this region, the layer of flow downstream of less obstructed areas (e.g. near the bottom) accelerates and moves towards the slow moving layers that are situated downstream of the more obstructed areas. Flow acceleration occurring within the lower levels of flow (i.e. below the canopy) has been also observed by Freeman et al. (2000), while an upwelling motion, similar to the one observed during the experiments, has been also observed by Lee and Lee (2012). The movement from the fast region towards the slow one causes the latter to progressively increase its velocity while the former gradually slows down. This exchange increases the amount of turbulence within the wake, dissipating a part of the flow kinetic energy into heat (Figure 7.24, D, E). At increasing distances downstream of the plant obstruction the slow and fast regions of flow are progressively diffused within each other (Figure 7.24, F) and the flow returns to its original, unaffected state when the downstream distance becomes sufficiently large (Figure 7.24, G).

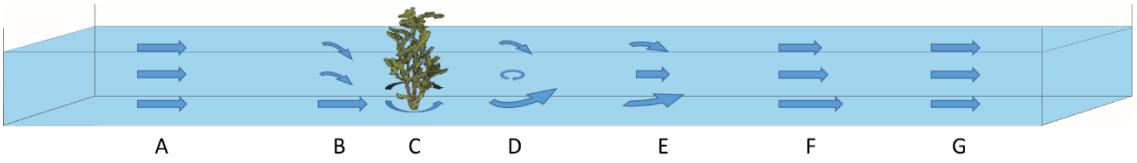

FIGURE 7.24: Example sketch presenting the flow adjustments exerted by the presence of vegetation at different distances from a single plant element.

The above mechanism highlights that the flow through porous vegetation is associated with specific regions of distinct flow behaviour and potentially geomorphological footprint. The flow variations, originating from the vegetative drag, can lead to variations of the skin friction drag, acting on the surface below, and hence alterations of the sediment transport processes. The latter may lead to variations in morphology (Bywater-Reyes et al., 2017). For example, regions that are characterised by flow retardation may be associated with deposition of suspended material, while those characterised by flow acceleration may be associated with localised scouring and erosion. The downstream distance required for the flow to attenuate marks the boundary of the wake region. This was found to be independent of porosity and instead it is a function of the streamwise plant extent. However, the relationship is not clear as the wake extent varied between two and seven plant lengths for the plants that were examined in the study and further research is required in future studies to quantify this. Although the wake extent does not appear to be influenced by porosity, the intensity of the wake region is closely related to the porous structure of plants. This links back to the spatial arrangement of the roughness elements and the concept of wake shading discussed in Chapter 2 (Subsection 2.3.2). For example, a large and very dense plant will generate a wake region of great extent and intensity, affecting significantly the downstream flow, while a large but very porous plant will also generate a similarly large wake but the flow within it will be comparable to the flow in the unaffected flow region. Conversely, a small and dense plant will generate a small but powerful wake region whereas a small and very porous plant will generate a negligible wake. A schematic of this is presented in

Figure 7.25 using the fig as an example. Information on the extent and intensity of the wake region generated by various types of vegetation is pertinent in projects of river restoration and natural flood management applications. It can help to inform decisions regarding the choice of plant types to be used for the reforestation of floodplains as well as the optimal plant spacing for a satisfactory control of flood water during flood events.

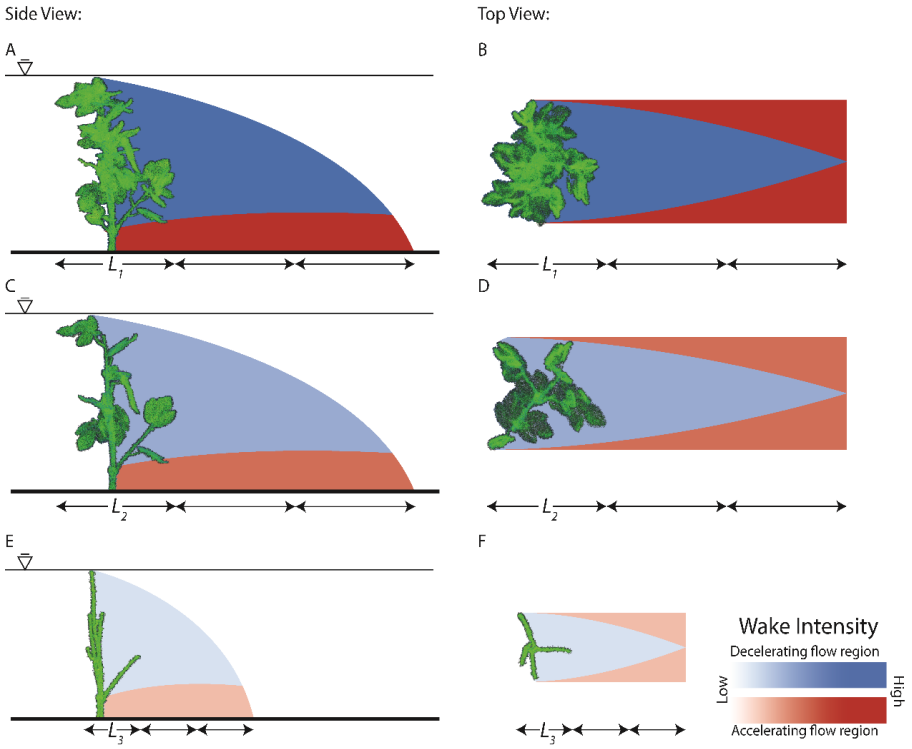

FIGURE 7.25: Example sketch of the effects of plant extent and porosity on the extent and intensity of the wake region. The fully foliated fig (A and B) generates a wake the streamwise extent of which is approximately two plant lengths (L_1). After two successive defoliations (C and D), the streamwise plant extent remained constant ($L_1 = L_2$) and so has the extent of the wake. However, the plant porosity increased leading to a decrease of the wake intensity. After the final defoliation (E and F) the plant extent decreased ($L_3 < L_2$) while the porosity increased greatly, this lead to a smaller wake region of very low intensity.

Chapter 8

Discussion and Conclusions

The details of a method capable of quantifying the 3D from and structure of vegetation were presented in Chapter 5. This was followed by assessment of the relationship between plant structure and bulk hydraulic roughness in Chapter 6 and investigating the associated effects on the flow field in Chapter 7. The present Chapter seeks to draw these lines of research together. It is broadly divided into four sections; the first section sets out the key findings of the research. It focuses on the parameterisation of vegetative roughness, its association with the hydraulic roughness and the consequent effects on flow properties. This is followed by a critique of the research methods and implications in relation to the assessment of vegetation-flow interactions in general. The third section presents thoughts regarding the future directions of related research, while the conclusions of the study are presented in the fourth section.

8.1 Synthesis

Until now, the majority of studies seeking to characterise vegetative hydraulic roughness have mainly focused on extracting measurements to quantify the vegetation frontal area and, more recently, deformation during flow (*e.g.* Västilä and Järvelä, 2014). These 2D metrics have been typically obtained through processing of imaging (*e.g.* Grant and Nickling, 1998) or TLS (*e.g.* Straatsma et al., 2008) data. Although they have provided useful insights, they neglect vegetation heterogeneity in the streamwise direction and are therefore limited, especially where multiple vegetation elements are present or plants have extensive streamwise structure. Laser scanning captures form and structure in 3D at high resolution, and so attempts have been previously undertaken to incorporate the third dimension into vegetative structure metrics and discretise plant form (Hosoi and Omasa, 2006; Béland et al., 2014). However, these examples come from the forestry domain and have concentrated on deriving tree biometrics that are pertinent to photosynthesis, transpiration or CO_2 budgets. In the fluvial domain, attempts to parameterise vegetation in 3D have commonly retreated into substituting plant elements

with cylindrical analogues. It is clear however, that cylindrical analogues neglect plant heterogeneity and as such oversimplify the mechanics of the problem. On the other hand, the few examples where vegetation has been accurately represented in 3D using voxels (Antonarakis et al., 2009, 2010) have associated this with hydraulic roughness values taken from equations that were derived using 2D methods, instead of measuring it directly. More recently, 3D representations of *Prunus laurocerasus* (Boothroyd et al., 2015) and *H. odora* (Boothroyd et al., 2017) were developed from TLS data obtained above water, using binary voxels, and combined with a CFD model. The novelty of the present research lies in the fact that vegetative structure, deformation during flow, hydraulic roughness and flow attributes were all measured simultaneously, allowing a holistic approach to quantifying the interactions. Furthermore, the geometry of individual plant elements (i.e. stems and leaves) was characterised explicitly, allowing the mapping of plants' spatial heterogeneity and associating it with flow field adjustments.

8.1.1 Quantifying plant structure from TLS data

The metric of 2D porosity developed in this research (Section 5.4) is similar to the optical porosity extracted from images by Grant and Nickling (1998) and later from TLS by Straatsma et al. (2008). As such it inherits similar shortcomings. It captures plant frontal area well and converts it to a two dimensional bulk porosity metric, but it assumes that the surveying angle and the flow direction coincide. Whilst this assumption was not unreasonable in the flume experiments undertaken, as the confined flume flow follows a constrained path, in real-world applications it might cause problems in regions of unconstrained flow. Additionally, the metric does not take into account vegetation's streamwise dimension. This could pose implications when heterogeneous vegetation is considered but also if the metric is employed to larger vegetated areas with multiple plants situated at variable spacing. These considerations are addressed by the employment of the 3D porosity metric (Section 5.5), which although following a similar concept, relies on plant volume instead of frontal area and therefore, incorporates the much needed third dimension into the bulk measurement. Therefore, the advantage of 3D porosity in comparison to its 2D equivalent is that it takes into account vegetation heterogeneity both at the plant and reach scale and by doing this, the metric remains pertinent regardless of flow direction, plant geometry and spacing.

It has long been acknowledged that any structural metric extracted from plants standing above water may be irrelevant as soon as they become immersed underwater, due to reconfiguration. Proposed methods to address this issue include normalising the porosity estimates using a 'still air' porosity (Gillies et al., 2002) or coupling plant structure estimates with a reconfiguration parameter (Järvelä, 2004). The former requires surveying of plant structure as it is deformed during flow, for example via the employment of through-water TLS (Smith et al., 2012). However, this method is accompanied by many limitations that render it unrealistic for field applications, at least

with the present state of laser scanning technology. Moreover, it necessitates surveying vegetation during a flood event, which is practically very difficult. The latter relies on experimental measurements to estimate the values of the reconfiguration factor which varies not only among plant species but also seasonally, and at different growth stages or health conditions. Nevertheless, it was shown in Chapter 6 that if the plant extent is incorporated into the porosity estimate, the metrics become robust even when quantified above water. This refutes the considerations arising by vegetation's deforming nature when it is quantified in bulk, at least for the moderate plant deformation examined in this study.

The next consideration that needs to be addressed involves the bulk nature of the metrics. By assigning a single porosity value to describe an individual plant (or vegetated reach) any spatial variation of vegetative structure is disregarded. Effectively, the plant (or reach) is being replaced by a simple, homogeneous rectangle (for the 2D metric) or cuboid (for the 3D metric) that has a constant porosity value assigned to it. Clearly, this representation is far from realistic, and cannot be associated with any small scale flow attributes such as turbulence among vegetation elements, and local adjustments of the flow velocity. Nevertheless, it is useful if it is associated with bulk flow parameters (e.g. Darcy-Weisbach f, Manning's n), which in many cases is the desirable product if the aim is to use numerical models to explore flow dynamics over large areas. When the requirement is a detailed characterisation of the spatial heterogeneity of the flow field around individual plants, or their distinct elements, the methods of extracting 3D porosity arrays can be employed. In this way, vegetation is discretised and single elements, such as stems or leaves, are explicitly accounted for. The extraction of 3D porosity arrays opens up a way for the numerical analysis of vegetation-interactions using Computational Fluid Dynamics (CFD) models. In this way, instead of employing idealised, and frequently simplistic, examples of plants for the numerical modelling of flows, the analysis of real plant structures can be explored, bridging the gap between numerical simulations and real-world scenarios.

If the conceptualised vegetated reach that was considered in Chapter 1 of this thesis (Figure 1.1) is revisited using the methods developed in the study, a porosity metric may be derived at different spatial scales. The reach may be represented using a single porosity value (Figure 8.1, A) allowing the assignment of a crude hydraulic roughness of the entire region. Alternatively, individual plants can be identified, and enclosing cuboids derived (Figure 8.1, B), which can be assigned individual porosities and extent values and in turn hydraulic roughness values. This will also enable a simplistic representation of the preferable flow paths among the various plant obstacles. Transitioning to a finer scale (for example 0.1×0.1 m, Figure 8.1, C), the total extent of the reach is characterised using an array of cubic cells, each one of which is assigned a distinct porosity value. This enables a better representation of plant geometry, as now it is defined by an aggregate of cubic cells instead of a single cuboid, and a refined mapping of hydraulic roughness within the reach. Consequently, it can be used to derive a more detailed representation

of flow variations among the plants. If the cubic cell array is refined at even higher resolution (for example 0.01×0.01 m, Figure 8.1, D), a greater detail can be derived that incorporates the smaller plant elements (e.g. thin stalks, small leaves). In turn, this can be associated with small scale turbulence among individual plant elements.

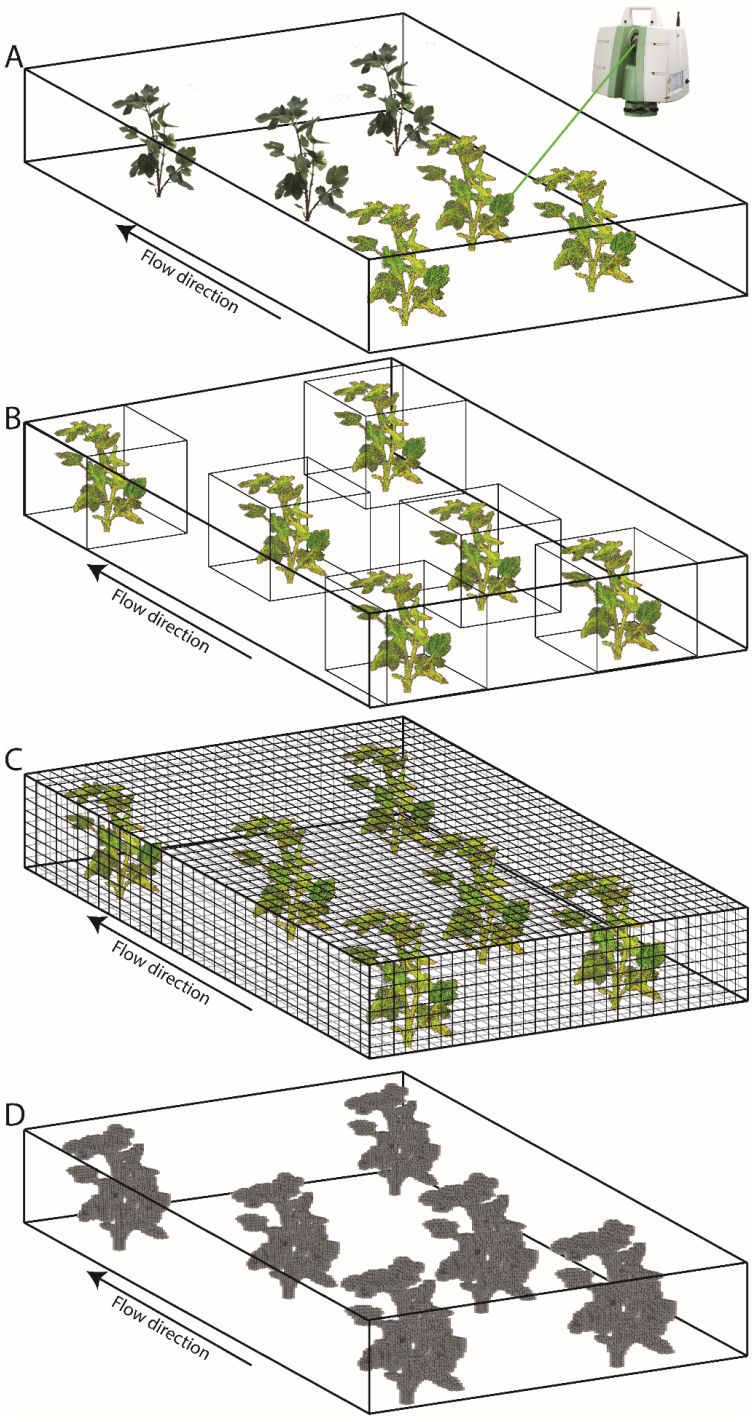

FIGURE 8.1: Concept of characterising the vegetated reach introduced in Figure 1.1 of Chapter 1 at different scales. Using the methods developed in the study the total extent of the reach may be characterised by a single porosity value (A). Single plants can be identified and assigned individual porosity values (B). The reach can be partitioned into cubic cells of a user-defined size (C and D) with each cell being assigned a distinct porosity value.

Considering the various spatial scales for characterising vegetation, presented in Figure 8.1, a question surfaces regarding the optimal scale of the assessment of vegetation-flow interactions. This leads back to the concept of the roughness window which was outlined in Chapter 2 (Section 2.3) and has been thoroughly discussed by Smith (2014). The upper limit of this scale is case-specific. If for example the requirement is to extract bulk hydraulic parameters of a vegetative region, the extent of the reach (Figure 8.1, A) or the size of the plant elements (Figure 8.1, B) may be the deciding factor. At the opposite extreme, the lower limit of the scale window is determined by the measurement capabilities in conjunction with computational constraints. For example, modern TLS systems can obtain data at millimetric resolution. However, CFD models usually work at centimetric or coarser scales due to computational thresholds. Therefore, if there is a requirement to numerically resolve the 3D flow patterns among individual plant elements, TLS data of millimetric resolution could be obtained. These can be used to develop coarser 3D porosity arrays (Figure 8.1, C or D) with a resolution defined by the necessities of the study in conjunction to the capabilities of the CFD model. In this way, each cell of the array is assigned a porosity value to represent the smaller features that are not explicitly represented from the chosen scale. In this context porosity is assuming the role of roughness, aiming to represent these finer characteristics that are not explicitly accounted for.

8.1.2 Evaluation of the models of hydraulic roughness

One of the main questions that this research deals with involves the determination of a suitable metric to quantify plant structure in bulk and identify its relationship with the hydraulic roughness. In Chapter 6 the ratio of porosity over the average plant extent was found to be the best candidate, as it showed a good correlation when 'standard' TLS data were employed. The relationship linking the bulk hydraulic roughness, represented by the Darcy-Weisbach friction factor (f), with the plant structure was given by Equations (6.7) ($f = a_1(P_{2D}/\overline{A_b})^{\beta_1}$) and (6.8) ($f = a_2(P_{3D}/\overline{A_b})^{\beta_2}$), in Chapter 6.

In Chapter 3 of this thesis, three other models of estimating the bulk hydraulic roughness based on the physical characteristics of vegetation were outlined and are revisited here. Equation (3.2) ($n = 0.037 + 0.0239B^A/UR_h$) is an empirical model developed by Huntington and Whitehead (1992) that employs a planar area blockage factor (B^A) to estimate Manning's n. B^A is defined as the size of the vegetated planar area over the reach planar area. Similarly, Equation (3.3) ($n = 0.043B^X - 0.0497$) proposed by Green (2005) estimates Manning's n but this time a frontal area blockage factor (B^X) is employed, defined as the percentage of vegetation's frontal area over the cross-sectional area of the channel. Finally, Equation (3.6) $\left(f = 4C_D LAI \left(\frac{U}{U_\chi}\right)^\chi \frac{h}{H}\right)$ proposed by Järvelä (2004), estimates the Darcy-Weisbach friction factor (f) from the drag coefficient (C_D), Vogel's exponent (χ) and the leaf area index ($LAI = A_f/A_b$), with A_f being the plant frontal area and A_b the ground area.

From the data obtained during the physical modelling experiments and the subsequent analysis described in Chapter 6, the surface area blockage factor can be derived from the TLS data using the planform 2D porosity as $B^A = 1 - P_{2Dpf}$. Similarly, the frontal area blockage factor can be derived using $B^X = 100A_f/A_c$, with A_c being the flume cross-section. Therefore, modelled Manning's n values can be computed from Equations (3.2) and (3.3) and converted to f values using Equation (2.16). This was undertaken using blockage factor estimates from both 'through-water' and 'standard' TLS data.

Employing Järvelä's model is more complicated, as it requires values for C_D and χ. The former was calculated using $f = 4C_D A_f/A_b$ (Wilson and Horritt, 2002). f was substituted with the experimentally measured values of Darcy-Weisbach friction factor, while the plant frontal area (A_f) and the planar area (A_b) were taken from the 'through-water' TLS data. Subsequently the form drag (F_D) was computed using Equation (3.4). With known values of form drag, the Vogel exponent is calculated from Equation (3.5), assuming equality ($F = U^{2+\chi}$). In this way, the necessary parameters for Equation (3.6) were obtained and used to derive modelled estimates of the Darcy-Weisbach friction factor. Following Västilä and Järvelä (2014), U_χ is equal to the lowest flow velocity of the flume scenarios that were investigated (i.e. $0.25\,\mathrm{m\ s^{-1}}$), while LAI was measured from the 'dry' TLS datasets using only the plant portion that encounters flow. The latter means that the ratio h/H, employed in Equation (3.6) to represent the level of inundation, can be discarded.

Figure 8.2 shows the comparison between experimentally measured values of f and the corresponding predicted ones using the models described from Equations (3.2), (3.3), (3.6), (6.7) and (6.8) (for Equations (6.7) and (6.8) the values of Table 6.7 were used). Experimentally measured values are plotted on the y-axis and model predictions on the x-axis. Although the computation of R^2 is not affected by which set of values is plotted on each axis, the slope and the intercept of the regression line are affected by this choice. Piñeiro et al. (2008) demonstrated that the correct way of comparing observed and predicted values, for model evaluation, is by plotting the observed ones on the y-axis. Linear regression between measured and predicted values was performed and the regression statistics are presented in Table 8.1. Additionally, the Root Mean Square Deviation ($RMSD$) from the 1:1 line was computed and also presented in Table 8.1.

Both models derived in the study (Equations (6.7) and (6.8), Figure 8.2, A and B) show a good agreement between predicted and measured f values. The computed $RMSD$ is relatively small for both models (0.698 and 0.723, respectively), while the slope and the intercept of the regression line are approximately equal to 1 and 0, respectively. This highlights that the regression lines of the two models are quite similar to the 1:1 line, although the regression line of Equation (6.8) shows a tendency to slightly under-predict the values of f, for greater values of hydraulic roughness. The model described by Equation (3.2) (Figure 8.2, C) appears to perform poorly, regardless of which mode of plant structure characterisation is employed, and it greatly over-predicts f values. On

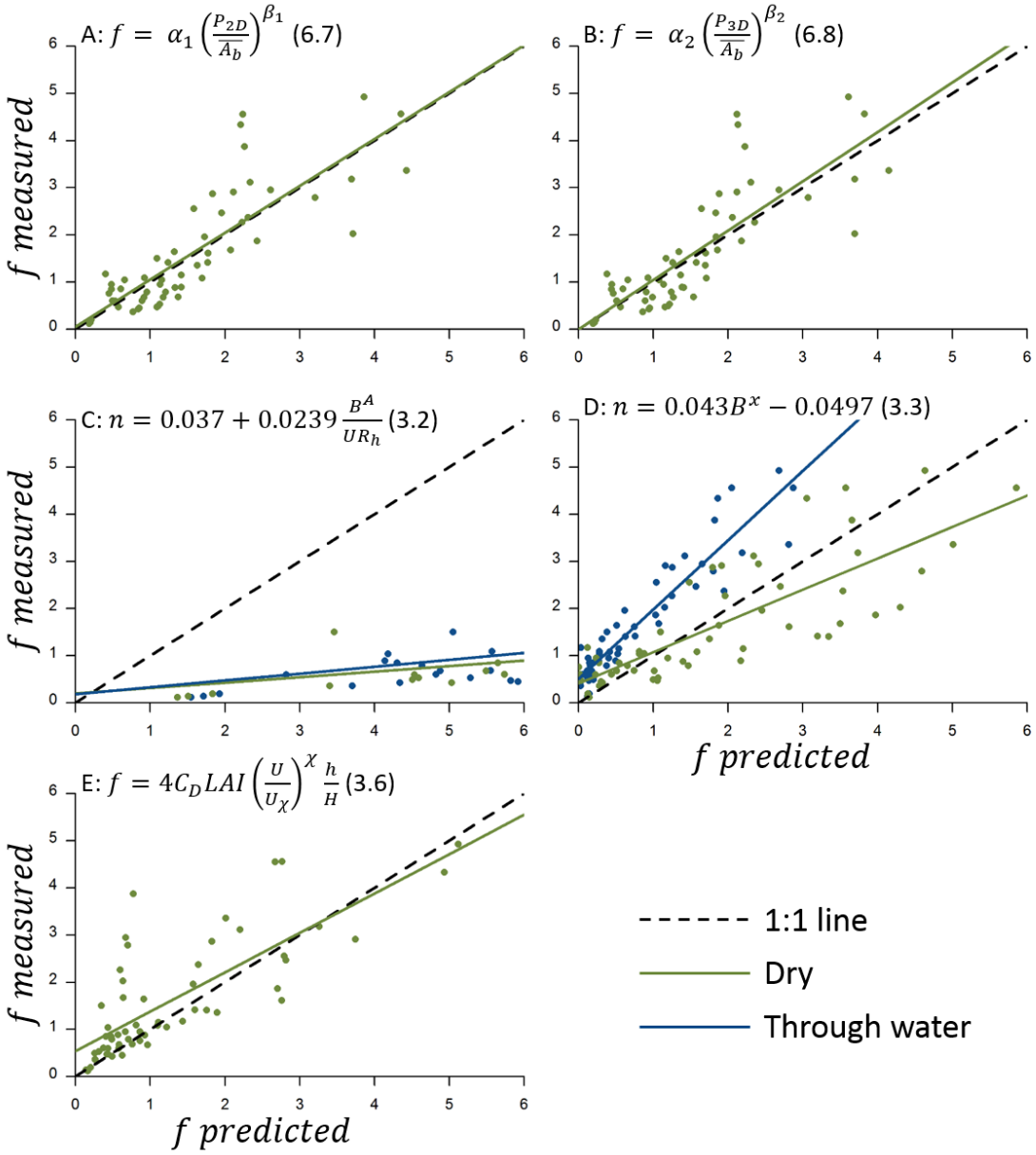

FIGURE 8.2: Comparison between measured values of hydraulic roughness with predicted ones using the models developed in the study in panels A and B (Equations (6.7) and (6.8), respectively), the surface area blockage factor (Equation (3.2)) in panel C, the frontal area blockage factor (Equation (3.3)) in panel D and the theoretical model of Equation (3.6) in panel E. Colours represent the mode of plant structure measurement (i.e. during flow: blue, dry: green), the black, dashed line represent the 1:1 relationship.

the other hand, the model described by Equation (3.3) (Figure 8.2, D) appears to perform better. When the plant structure is quantified during flow, the model appears to under predict the values of f, especially for scenarios of greater hydraulic roughness. When the plant structure is measured under a 'dry' state, the model under-predicts the value of f for scenarios associated with low hydraulic roughness and over-predicts for all other cases. The model described by Equation (3.6) (Figure 8.2, E) performs relatively well, but shows a tendency to under-predict the value of hydraulic roughness for lower f values, the opposite effect occurs at high f values.

TABLE 8.1: Model validation statistics, including the slope and the intercept of the regression lines, the R^2 values as well as the Root Mean Square Deviation ($RMSD$) from the 1:1 line. The values correspond to the models presented in Figure 8.2

Model	**During flow**				**Dry**			
	Slope	**Intercept**	$\boldsymbol{R^2}$	$\boldsymbol{RMSD}$	**Slope**	**Intercept**	$\boldsymbol{R^2}$	$\boldsymbol{RMSD}$
Equation (6.7)	-	-	-	-	0.995	0.054	0.681	0.698
Equation (6.8)	-	-	-	-	1.047	-0.004	0.660	0.723
Equation (3.2)	0.145	0.185	0.591	9.988	0.117	0.197	0.595	12.705
Equation (3.3)	1.469	0.508	0.878	1.028	0.664	0.410	0.651	0.905
Equation (3.6)	-	-	-	-	0.835	0.540	0.596	0.870

Equation (3.2) proposed by Huntington and Whitehead (1992), was empirically derived from measurements obtained from a single river, and as such it was expected to perform poorly. Equation (3.3) proposed by Green (2005) is the product of the analysis of 35 UK river systems and although it performs better than Equation (3.2), its regression line is quite different from the 1:1 line. It must be noted that all of the rivers examined by Green were vegetated with the same species of macrophytes (*Ranunculus*). This demonstrates a weakness of empirically derived models, which is related to the fact that they are derived from a finite sample of measurements and species. The models developed in the present study fall into the category of empirically derived ones. Although they were developed using a range of flow scenarios and structurally variable plant types, additional experiments with different plant types are necessary to further explore their robustness. The theoretical model proposed by Järvelä (Equation (3.6)) shows the best agreement of the models from the literature with the current study. Discrepancies between the regression line for Equation (3.6) and the 1:1 line are likely due to noise within the datasets, affecting the calculations of C_D and χ. This highlights the sensitivity of the method in the selection of correct values for the drag coefficient and Vogel's exponent. The drag coefficient of flexible vegetation is affected not only by the plant structure but also by the flow velocity (due to reconfiguration). In addition, Vogel's exponent varies between species but also at different growth stages of the same species or even with vegetation's health condition. Therefore, choosing the correct values of C_D and χ is not always straightforward.

8.2 Methodological considerations

A range of methods were employed in the research to fulfil the objectives that were outlined at the introduction of this thesis. Some of them are well established in the literature, while others are novel applications. All of them have inherent limitations which are discussed herein.

8.2.1 Plant discretisation

Over the last decade, advances in laser scanning technology have revolutionised our ability to capture the form and structure of features in 3D at very high levels of detail. The superior surveying ability of TLS quickly found applications in the field of geomorphology but also in forestry studies. More recently, approaches have been undertaken to explore the potential of employing TLS in the field of ecohydraulics, aiming to characterise the spatial variation of plant structure, either by converting the 3D point clouds to their 2D equivalents (*e.g.* Straatsma et al., 2008; Manners et al., 2013) or by employing voxels to maintain the 3D nature of the datasets, enabling a more accurate representation of plant structure (*e.g.* Antonarakis et al., 2009, 2010; Jalonen et al., 2015; Boothroyd et al., 2015, 2017). The employment of TLS is accompanied by limitations, especially with regard to increased noise in the datasets when complex plants are surveyed, and occlusions at the inner region of very dense vegetation and large solid stems. Mixed points can be corrected to some extent by the application of filters such as the SOR filter developed by Rusu et al. (2008) and employed in the study. Although the SOR filter is capable of detecting the majority of erroneous points within the datasets, some errors persist and may have an effect on the measured porosity values. Quantifying the errors stemming from the existence of mixed points, necessitates the employment of an independent dataset with similar quality and resolution as a means of comparison (Hodge, 2010). However, no other method exists capable of delivering 3D representations of plant structure at similar levels of detail, at least for field studies. This complicates the application of the SOR or other filters. They typically require user-defined threshold values and the filtered product is evaluated visually. Hence, the selection of the appropriate filtering thresholds is subjective. Occlusions can be partially tackled by surveying plants from multiple viewing angles, although in examples of dense vegetation a complete coverage is not always possible (Pueschel, 2013). The occlusions within the inner parts of solid stems will persist regardless of the number of surveying positions, as the laser beam cannot physically penetrate the solid surface of objects. Ray tracing algorithms (*e.g* Hosoi and Omasa, 2006) may be useful, but are very computationally intensive when applied to datasets consisting of hundreds of millions of voxels and as such their results are not assessed in the study.

Another consideration is in regard to the optimal resolution for the estimation of porosity metrics and it includes both the scanning resolution during the data collection

procedure and also the resolution of the binary grid, employed for the quantification of plant porosity. In the study, plant surveying was conducted using the maximum resolution that the Leica C10 is capable of delivering (i.e. 1 mm). The size of the binary voxels was *de facto* taken equal to this nominal TLS point spacing. 3D point cloud data are essentially an aggregate of volume-less points in the 3D space. The return laser signal indicates that there is a reflective object in the location defined by the 3D point coordinates, without providing any information about the shape, surface area or volume of the object. Converting a 3D point to a binary voxel, during the porosity extraction routine, assumes that each point corresponds to a cubic volume equal to the voxel volume. Certainly, this assumption contains some uncertainty. However, because the plant surveys were undertaken at very high resolution and the voxel size is very small, the uncertainty is expected to be small. It must be acknowledged however, that the thickness of leaves which typically falls in the sub-mm range is exaggerated by this assumption. The effect of scanning resolution and voxel size on the estimate of 3D porosity was examined following the procedure described below.

In order to assess the effect of scanning resolution, the filtered scan datasets that were analysed in Chapter 5 were used. One scan dataset for every plant after it had been defoliated twice, was imported into CloudCompare and systematically degraded by resampling the point cloud a total of ten times, creating datasets of variable point spacing (from 1 to 10 mm). Subsequently the 3D porosity extraction routine, described in Chapter 5, was followed. The voxel size was, each time, taken equal to the point spacing of the input dataset. The results are presented in Figure 8.3, A. In order to assess the effect of the voxel size, the same datasets were examined using the original resolution (i.e. 1 mm). This time, the 3D extraction routine was undertaken ten times, increasing the voxel size by 1 mm after each iteration. The results are presented in Figure 8.3, B.

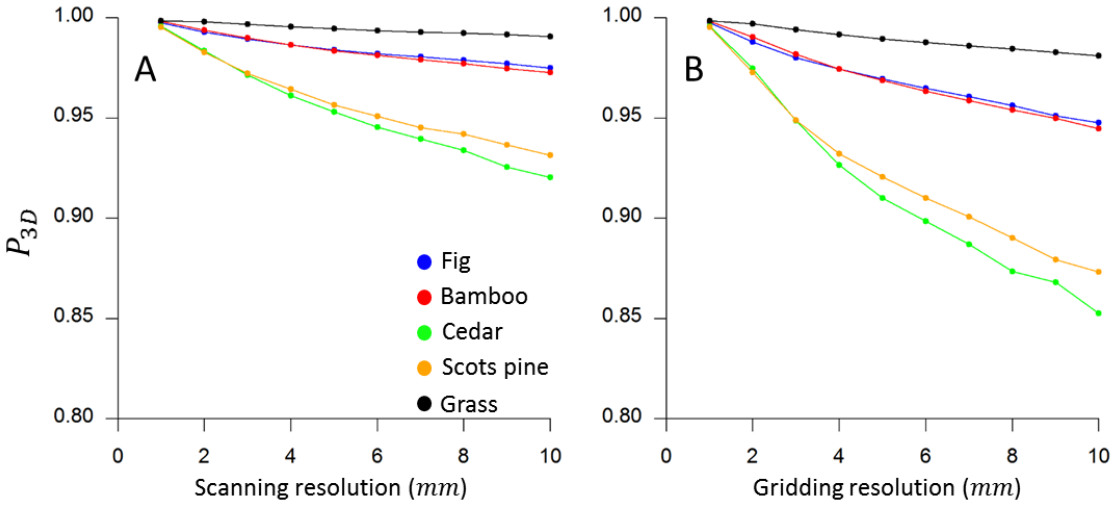

FIGURE 8.3: Effects of scanning (A) and gridding (B) resolution on the estimates of 3D porosity for the plants examined in Chapter 5 after two defoliations.

From Figure 8.3, A it is evident that the scanning resolution has an effect on the estimated porosity, with coarser input datasets associated with lower porosity values.

This was expected as an effect of fractal geometry similar to the coastline paradox (Mandelbrot, 1967). On the other hand, from Figure 8.3, B the increase of the binary voxel size appears to have an even greater effect on reducing the porosity estimate. This is because of the assumption described earlier that converts a volume-less point to a volumetric pixel, and includes an increasing error at every step of the increase of the voxel size. This finding suggests that the size of the binary voxels must be always taken equal to the nominal point spacing of the TLS dataset. Also if Equations (6.7) and (6.8) are to be employed it is necessary that $P_{2D}/\overline{A_b}$ and $P_{3D}/\overline{A_b}$ are measured from point clouds obtained at 1 mm point spacing. Datasets of different resolution may be used, but calibration will be required to correctly evaluate parameters a_1, β_1, a_2, β_2.

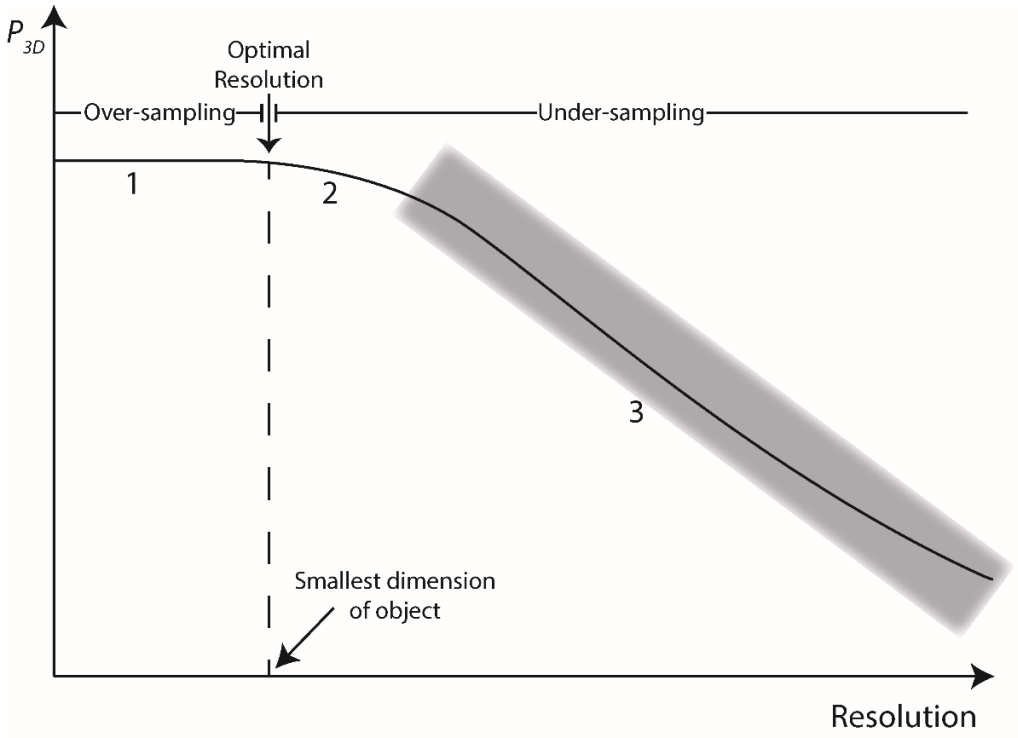

FIGURE 8.4: Sketch diagram showing the effect of scanning resolution on the estimate of 3D porosity. The optimal resolution is defined by the smallest dimension of the surveyed object. Scanning at coarser than the optimal resolution leads to an underestimate of the metric (regions 2 and 3 of the curve) while scanning at finer than the optimal resolution (region 1) does not affect the estimated value but oversampling may lead to much larger datasets.

The effect of scanning resolution on the porosity estimate is conceptualised in Figure 8.4. The optimal scale is defined from the smallest dimension of the smallest element of the surveyed plant. For example, if a leafy plant is surveyed and the thickness of its leaves is 0.1 mm then a 0.1 mm point spacing would be the optimal one. Scanning at even higher resolutions is not expected to have an effect on the porosity estimate, however it will increase the size of the dataset and may make its processing very computationally intensive. Scanning at coarser scales underestimates the porosity value as the size of small elements is exaggerated by the voxelisation routine, as explained above. From the comparison between Figure 8.3, A and Figure 8.4 it is evident that the scales examined

in this study fall within the shaded region (3) of Figure 8.4. Finer resolutions could not be examined due to the specifications of the TLS instrument. Therefore, neither the optimal scale nor the rate of change in region 2 of Figure 8.4 can be assessed. This highlights a limitation of the current state of TLS technology. Although it is able to capture 3D data in great detail, further improvements, in terms of scanning point spacing, are necessary to limit the exaggeration of the size of the minuscule plant elements. Perhaps complementary laboratory measurements using methods capable of delivering ultra-high resolution (μm) (e.g. CT scanning) could be used in future research to assess the optimal resolution for plant scanning and quantify the underestimation of porosity at coarser scales.

8.2.2 Physical modelling

Physical modelling using flumes is one of the main directions of research typically followed in the field of ecohydraulics and it was reviewed in Section 3.4. The other two are field studies and numerical modelling. The advantage of physical modelling over field studies is that variables can be closely monitored and, depending on the necessities of the project, altered through time or remain constant for the duration of the experiment. This allows for a single affecting variable to be isolated each time and its effect to be studied in depth. Like all models, physical ones are mere simplifications of real systems and as such a concern exists whether the replicated process reflects the one occurring in natural systems or oversimplifies the interactions. For example, it has been extensively discussed in this thesis that substituting vegetation elements with rigid cylindrical analogues is likely to be such an oversimplification. Numerical models are useful, because, in comparison to physical ones, they are less labour intensive and, once set up, permit an extensive number of runs to be undertaken, where the affecting variable can be fine-tuned and the result can be examined in detail under a plethora of configurations. However, they may become detached from the natural processes shaping Earth's surface and for this reason it is good practice to validate results drawn from numerical models with physical experimentation (*e.g.* Marjoribanks et al., 2014) or field measurements.

This study has been based on physical modelling experiments, which allowed the careful adjustment of inlet flow conditions, the precise location of vegetation elements and their alteration during successive runs, as well as the precise positioning of process monitoring equipment for the simultaneous and thorough monitoring of plant reconfiguration and flow attributes. The plants employed were 1:1 prototypes and this revoked any considerations in regards to scaling effects. However, it must be acknowledged that because their width was of the same order as the flume width, blockage ratio effects might have influenced the drag acting upon them (Cooper et al., 2007). It is also likely that the flow acceleration observed near the bed and the sides of the flume were exaggerated due to the confined flume flow and the blockage ratio effects. Conducting a flume run in the absence of vegetation allowed for the base flume hydraulics to be fully

characterised and enable the vegetative drag to be distinguished from the drag exerted by the flume itself. However, wall effects must be acknowledged for the discrete flow characteristics. It is likely that the large eddies developed within the wake region were reflecting off the flume walls as they were propagated downstream, and this might have had an effect on the wake extent. Potentially this explains why a clear relationship between plant length and wake extent could not be established in the study.

Throughout the study, artificial plant surrogates were employed both for the development and validation of the porosity extraction routines as well as for the physical modelling experiments that followed. Clearly, the employment of structurally realistic plants is an improvement in comparison to the employment of stiff, or flexible, cylindrical rods, common in many ecohydraulic experiments. The employment of real plants in such experiments has seen an increase in recent years. However, there is a concern regarding the environmental conditions in hydraulic laboratories that may put plants under stress, affecting their physical characteristics and biomechanical properties (see also 3.4.1). This concern is further exacerbated if the duration of the experiments is very long. For these reasons, artificial, but structurally realistic, plants were favoured in the study. This choice permitted the replicability of the experiments and assured consistency throughout the research as identical plants were employed both for the development and validation of the porosity extraction methods, as well as for the physical modelling experiments. It must be acknowledged that although the plants were flexible and realistic in terms of shape, size and structure, they consisted of synthetic materials. Therefore, their flexibility may not fully resemble the biomechanical properties of real vegetation. For this reason, the amount of plant reconfiguration during flow, assessed in Section 6.3 should not be taken as transferable to real species of the artificial plants, rather it was used to better understand the relationship between plant structure and drag under varying flow conditions.

8.3 Recommendations for future research

There are a number of key areas that have arisen from this study which could benefit from further investigation.

The study focused on the effects of individual emergent plants on flow. Although vegetation-flow interactions in the case of multiple plants can be inferred if the wake characteristics that were assessed in Chapter 7 are taken into consideration, any deductions can only be speculative. Physical modelling experiments with arrays of plants in various configurations would be beneficial. They could provide valuable information on the cumulative drag exerted by multiple plants and also enable the exploration of wake shading effects under different scenarios. In this case, supplementary methods for the flow visualisation between plants or even their distinct elements could be employed, for example using Particle Image Velocimetry (PIV). Combining PIV and TLS could

utilise the full potential of the method to extract porous arrays developed in this study, as the plant spatial variability could be directly linked to the small scale flow structures developed in the vicinity of discrete plant elements. This could also enable an in depth analysis of the secondary flow structures and mechanical diffusion originating from plants' spatial variability.

It would also be beneficial to explore the transferability of the metrics developed in the study in natural settings. Floodplain vegetation can be accurately surveyed in high resolution if TLS is employed. Alternatively, recent developments in UAV-LiDAR systems show a promising potential of conducting high resolution surveys over vegetated areas of even larger extent, which is likely to bridge the gap between resolution and coverage in the near future. Bulk drag values over large areas can be measured using dye tracing approaches similar to the ones demonstrated by Richardson and Carling (2006). Discrete flow velocity measurements could be obtained using ADVs or Acoustic Doppler Current Profilers (aDcp). Recently, PIV methods have been applied in field studies and showed promising potential (Creëlle et al., 2016). In this way the robustness of the metrics developed here can be assessed and the effectiveness of vegetation as a means of natural flood management explored.

Finally, it would be interesting to assess the potential of implementing porosity arrays in numerical models. Vegetation-flow interactions have been previously explored using CFD models either using simplified, but flexible, plant models (*e.g.* Ikeda et al., 2001; Marjoribanks et al., 2014) or more recently by employing realistic plant representations obtained with TLS (*e.g.* Boothroyd et al., 2015, 2017). In the latter examples, plants were represented using binary voxels the size of which ranged between 0.5 and 1 cm^3 due to the CFD computational capabilities, and this is likely to have exaggerated the size of smaller plant elements. A porosity approach within the numerical domain has been previously employed by Lane et al. (2004) to represent gravel bed rivers. These methods could be extended to vegetation where the voxel size is assigned according to the capabilities of the CFD model, but instead of a binary representation the voxels are populated with distinct porosity values, using the methods developed here (see also example in Figure 8.1, D.

8.4 Conclusions

This research has sought to expand the knowledge regarding vegetation-flow interactions, pertinent to the study of ecohydraulic processes and fluvial geomorphology in general. In doing so it has developed novel methods to accurately characterise the vegetative structure and link it to the fluvial drag exerted by plants and the consequent adjustments of the flow field at the vicinity of vegetation elements. The present Section summarises they key conclusions of the research, highlights their value in progressing academic knowledge and their potential utility to the practitioner community.

Novel methods to characterise the vegetative structure and deformation both in 2D and 3D were developed in this study. The proposed metrics ($P_{2D}/\overline{A_b}$ and $P_{3D}/\overline{A_b}$) can be obtained at a range of spatial scales spanning from individual plants to extensive reaches. The only limiting factor being the current state of the art of laser scanning technology, in terms of maximum resolution, coverage and the trade-offs between them. Typical TLS instruments are capable of achieving millimetric resolution which allows the explicit defining of very small plant elements. It should be noted though that a sub-mm resolution might be desirable to avoid overestimating certain minute dimensions of plant features (e.g. leaf thickness). On the other hand, TLS has a limited range with most systems typically operating over a few hundreds of metres only. This means that surveying extensive areas with TLS can be difficult, laborious and time consuming. Alternatively, airborne laser scanning (ALS) has the capability to cover large areas, but the typical resolution that ALS instruments can achieve is within the magnitude of decimetres. Recent advances on mobile laser scanning (MLS) has enabled the successful coupling of TLS units with moving vehicles such as cars, boats and more recently UAV platforms. Combining such apparatus with accurate RTK GPS and IMU systems (*e.g.* Leyland et al., 2017) enables the survey of extensive areas at resolutions comparable to those achieved during static TLS surveys, bridging the gap between resolution and coverage.

Two models were developed that are capable of predicting the vegetative hydraulic roughness from the bulk porous plant structure, Equations (6.7) and (6.8). The former relies on a bulk 2D representation of the vegetative structure, while the latter is based on the equivalent 3D metric. Both models perform better than previous ones from related literature (Equations (3.2), (3.3) and (3.6)) with the RMSD values computed for Equations (6.7) and (6.8) being lower that those computed for previously existing models. From the data collected during the research and the RMSD values computed, the 2D model appears to perform slightly better than the 3D one. It must be taken into account that the flume flow during the experiments was well constrained. This means that flow direction and viewing angle for the extraction of P_{2D} coincide and this is potentially responsible for the slightly better performance of Equation (6.7) in comparison to Equation (6.8). But because P_{3D} is not affected by vegetation's orientation relative to the flow direction, it is expected that the model described by Equation (6.8) will remain robust over a wider range of scenarios. Equations (6.7) and (6.8) established a direct link between physically meaningful metrics of plant structure and vegetative hydraulic roughness, independently of plant reconfiguration and the drag coefficient. This implies that the models developed here can be applied to a range of plant types without a need to explicitly determine values of the Vogel exponent χ or the drag coefficient C_D. It must be acknowledged though that the parameters α and β employed in the models are dependent on Reynolds number. The relationship between Re and α, β could not be determined from the limited flow variability associated with the physical modelling experiments that were undertaken. More experiments at a Re range broad enough to cover a series of surface water flows is required to determine

correct values for these parameters under a variety of flow conditions.

Flow adjustments at the vicinity of plant elements were quantified and associated with the explicitly defined plant from. It was highlighted that the flow follows preferential paths in its attempt to overcome the porous plant obstruction. This behaviour, in combination with the increased pressure upstream, causes some flow regions to accelerate while others slow down. This mechanism can be useful in the study of distinct geomorphological features that are frequently observed near vegetation in rivers and floodplains, including scours and tail bars. The wake region developed downstream of the plant elements was found to have an intensity that can be directly associated to the bulk porous plant structure, but its extent appears to be related to the streamwise plant extent. The substantial secondary currents generated within the wake region may be associated to flow mixing and consequently to transport of sediment as well as soluble substances including nutrients and polluters.

There is much scope to expand the exploration undertaken here. The work documented shows that it is possible to utilise high resolution 3D point cloud data to explicitly characterise vegetation's spatial variability and link it to flow characteristics. The methods proposed in this study to quantify plant structure were developed and tested in the laboratory. However, because they rely on surveying equipment that is typically employed in the field, they are readily transferable to field applications. For example, employing ViPER to process 3D point clouds obtained using TLS or MLS from a vegetated floodplain will enable a thorough characterisation of the vegetation elements within the area at a range of spatial scales. Subsequently, ViPER outputs can be combined with Equation (6.8) to quantify the hydraulic roughness of the area, covering a respective range of scales and enabling the explicit representation of spatial variations of the vegetative drag of the floodplain. Combining the spatial variability of vegetative structures and associated hydraulic roughness with the findings stemming from the assessment of flow attributes at the plant scale, can help inform decisions regarding the choice of plant types to be employed for the reforestation of floodplains as well as the optimal plant spacing for the mitigation of flood associated hazards in riverine environments. This makes the work undertaken in this study highly relevant to natural flood management applications.

Appendix A

Vegetative Porosity Extraction Routine in 2D (ViPER2D)

```
function ViPER2D(infile, pointspacing)
%-------------------------------------------------------------------------
%Free for all uses, but please retain the following:
%   Vegetative Porosity Extraction Routine (ViPER)- 2D Version
%   Original Author:
%   Grigorios Vasilopoulos, October-2017
%   g.vasilopoulos@soton.ac.uk
%-------------------------------------------------------------------------

%-------------------------------------------------------------------------
                            %%Description%%
%-------------------------------------------------------------------------
%This function converts an unstructured 3D TLS point cloud to a structured
%2D binary grid and calculates the bulk porosity of the dataset as the
%ratio of emply cells over the total amount of cells. As input data
%requires a '.txt' file containing the 3D point cloud coordinates (in m)
%and the TLS point spacing to be specified by the user (in m).
%The code outputs include:

%1:a text file named '*_P2D' (where * is the file name of the inputdataset)
%that contains the value of the bulk 3D porosity of the dataset as well as
%its frontal area in square mm

%2:a text file named '*_2DGrid' (where * is the file name of the input
%dataset)with the coordinates of the created 2D binary grid (x,z) and
%their binary status (0 for empty, 1 for filled)

%Example of use: ViPER2D(Cedar, 0.001)
%-------------------------------------------------------------------------

%READ DATA--------------------------------------------------------------
input = sprintf('%s.txt',infile);
in = load(input);
d = pointspacing*1000;

%MAKE ALL COORDINATES POSITIVE------------------------------------------
in(:,1) = in(:,1)+1000;
in(:,2) = in(:,2)+1000;
in(:,3) = in(:,3)+1000;
```

```
40
41 %CONVERT ALL COORDINATES TO INTEGERS-------------------------------------
42 in(:,1) = in(:,1)*1000;
43 in(:,2) = in(:,2)*1000;
44 in(:,3) = in(:,3)*1000;
45
46 %ORGANISE POINT CLOUD (SNAP COORDINATES TO GRID)-------------------------
47 k = size(in,1);
48
49 for p = 1:k
50     in(p,4) = in(p,1)-rem(in(p,1),d);
51     in(p,5) = in(p,2)-rem(in(p,2),d);
52     in(p,6) = in(p,3)-rem(in(p,3),d);
53 end
54
55 %SAVE NEW COORDINATES TO MATRIX-------------------------------------------
56 NP = [in(:,4), in(:,5), in(:,6)];
57
58 %CONVERT DATASET TO 2D (DISCARD STREAMWISE COORDINATE)--------------------
59 FC = [NP(:,1), NP(:,3)];
60
61 %DISCARD NON-IDENTICAL COORDINATE PAIRS-----------------------------------
62 FilledCells = unique(FC, 'rows');
63
64 %DERIVE THE MINIMUM BOUNDING GRID THAT CONTAINS THE DATA------------------
65 x = FilledCells(:,1);
66 y = FilledCells(:,2);
67
68 imin = min(x);
69 jmin = min(y);
70
71 imax = max(x);
72 jmax = max(y);
73
74 a = 0:ceil((imax-imin)*(1/d));
75 b = 0:ceil((jmax-jmin)*(1/d));
76
77 amax = max(a);
78 bmax = max(b);
79
80
81 while a <= amax
82     i = imin +a*d;
83     a = amax + 1;
84 end
85
86 while b <= bmax
87     j = jmin +b*d;
88     b = bmax + 1;
89 end
90
91 EmptyGrid = combvec (i,j)';
92
93
94 %CROSS-REFERENCE THE BOUNDING GRID WITH THE ORGANISED POINT DATA IN A
95 %LOCIAL MANNER TO CREATE A BINARY GRID (1 FOR FULL 0 FOR EMPTY) BECAUSE OF
96 %THE POINT DATA ORGANISATION EARLIER, ONLY ONE POINT CORRESPONDS TO A
97 %SINGLE GRID CELL---------------------------------------------------------
98 Logical = ismember(EmptyGrid,FilledCells, 'rows');
99
```

```
100 FinalGrid = [EmptyGrid, Logical];
101
102
103 %CHECK RESULTS. THE TOTAL AMOUNT OF ORGANISED POINTS (l) MUST BE EQUAL TO
104 %THE SUM OF THE LOGICAL OUTPUT (k). IF THE BINARY GRID IS CORRECTLY
105 %EVALUATED CALCULATE BULK POROSITY (USING EMPTY CELLS/TOTAL CELLS). SAVE
106 %THE POROSITY RESULT TO CURRENT DIR. CONVERT THE COORDINATES OF THE BINARY
107 %GRID BACK TO THEIR ORIGINAL FORM (DUE TO THE '+1000' AND '*1000'
108 %CORRECTIONS APPLIED IN THE BEGINING). WRITE BINARY GRIDS TO CURRENT DIR.
109 %--------------------------------------------------------------------------
110 k = sum(Logical, 1);
111 l = size(FilledCells,1);
112
113 if k == l
114     Porosity = (size(FinalGrid,1) - sum(FinalGrid(:,3)))/size(FinalGrid,1);
115     FrontalArea_sqmm = l;
116     %save porosity result to current dir
117     Output(1,1) = Porosity;
118     Output(1,2) = FrontalArea_sqmm;
119     dlmwrite((sprintf('%s_P2D.txt',infile)),Output,'precision',8)
120
121     %apply corrections on the grid coordinates
122     PorosityGrid = [(FinalGrid(:,1)/1000)-1000,...
123         (FinalGrid(:,2)/1000)-1000,FinalGrid(:,3)];
124
125
126     dlmwrite(sprintf('%s_2DGrid.txt',infile),PorosityGrid, 'precision', 8);
127
128
129 else disp('ERROR ERROR ERROR!!!')
130 end
131
132 end
133 %--------------------------------------------------------------------------
134                                   %%END%%
135 %--------------------------------------------------------------------------
```

Appendix B

Vegetative Porosity Extraction Routine in 3D (ViPER3D)

```
function ViPER3D(infile, pointspacing, cellsize)
%-------------------------------------------------------------------------
%Free for all uses, but please retain the following:
%   Vegetative Porosity Extraction Routine (ViPER)- 3D Version
%   Original Author:
%   Grigorios Vasilopoulos, October-2017
%   g.vasilopoulos@soton.ac.uk
%-------------------------------------------------------------------------

%-------------------------------------------------------------------------
                            %%Description%%
%-------------------------------------------------------------------------
%This function converts and unstructured 3D TLS point cloud to a structured
%3D binary grid and calculates the bulk porosity of the dataset as the
%ratio of empty voxels over the total amount of voxels. It also generates a
%coarser (user-specified resolution) 3D porosity array with each cubic
%array cell being assigned a porosity value based on how many empty voxels
%reside within it. As input data it requires a text file containig the 3D
%point cloud coordinates (in m), the TLS point spacing of the input data
%to be speficied by the user (in m) as well as the desired cellsize for the
%coarser porosity array to be specified by the user (in m). The cellsize
%must be chosen accordingly so that cellsize divided by pointspacing
%results to an interger. The code outputs include:

%1:a text file named '*.P3D (where '*' is the file name of the input
%dataset) that contains the amount of the voxels consisting the binary
%grid, the amount of empty binary voxels in the grid, the amount of filled
%voxels in the grid, the bulk 3D porosity of the dataset, and the datasets
%lateral and streamwise extent in the followin order: mean lateral, mean
%streamwise, 80th percentile lateral, 80th percentile streamwise, max
%lateral, max streamwise.

%2:a text file named '*_bin' (where '*' is the file name of the input
%dataset) with the coordinates of the created 3D binary grid (x,y,z) and
%their binary status (0 for empty, 1 for filled).

%3: a text file named '*_por' (where '*' is the file name of the input
%dataset) with the coordinates of the created coarser 3D porosity array
%(x,y,z) and their porosity value ranging between 0 and 1 (0 is a
```

```
%completely filled cell, 1 is an empty cell).

%Example of use: ViPER3D(Cedar, 0.001, 0.02)
%-------------------------------------------------------------------------

%-------------------------------------------------------------------------
%                    FIRST PART - DATA PREPARATION                        %
%-------------------------------------------------------------------------

%READ DATA-------------------------------------------------------------------
input = sprintf('%s.txt', infile);
in = load(input);
d = pointspacing*1000;
D = cellsize*1000;

%CHECK THAT THE USER-DEFINED CELLSIZE MATCHES THE INPUT DATA POINT SPACING-
R = rem(D,d);
if R == 0

%MAKE ALL COORDINATES POSITIVE-----------------------------------------------
in(:,1) = in(:,1)+1000;
in(:,2) = in(:,2)+1000;
in(:,3) = in(:,3)+1000;

%CONVERT ALL COORDINATES TO INTEGERS-----------------------------------------
in(:,1) = in(:,1)*1000;
in(:,2) = in(:,2)*1000;
in(:,3) = in(:,3)*1000;


%ORGANISE POINT CLOUD (SNAP COORDINATES TO GRID)-----------------------------
k = size(in,1);
for p = 1:k
    in(p,4) = in(p,1)-rem(in(p,1),d);
    in(p,5) = in(p,2)-rem(in(p,2),d);
    in(p,6) = in(p,3)-rem(in(p,3),d);
end

%SAVE NEW COORDINATES TO MATRIX----------------------------------------------
NP = [in(:,4), in(:,5), in(:,6)];


%DISCARD NON-IDENTICAL COORDINATE TRIPLETS-----------------------------------
FilledCells = unique(NP, 'rows');

%SPLIT DATA IN 8 SUBDATASETS IN A SPATIAL MANNER-----------------------------
x = FilledCells(:,1);
y = FilledCells(:,2);
z = FilledCells(:,3);

%Find the split points. For consistency the split points must be in
%aggreement with the porosity array that will be built later in this
%process:
xs = ceil(((max(x) - min(x))/D)/2);
ys = ceil(((max(y) - min(y))/D)/2);
zs = ceil(((max(z) - min(z))/D)/2);
xsplit = min(x) + xs*D;
ysplit = min(y) + ys*D;
zsplit = min(z) + zs*D;

```

```
% subdataset #1:
good_1 = FilledCells(:,1) >= min(x) & FilledCells(:,1) < xsplit &...
    FilledCells(:,2) >= min(y) & FilledCells(:,2) < ysplit &...
    FilledCells(:,3) >= min(z) & FilledCells(:,3) < zsplit;
FC_1 = FilledCells(good_1,:);

% subdataset #2:
good_2 = FilledCells(:,1) >= xsplit & FilledCells(:,1) <= max(x) &...
    FilledCells(:,2) >= min(y) & FilledCells(:,2) < ysplit &...
    FilledCells(:,3) >= min(z) & FilledCells(:,3) < zsplit;
FC_2 = FilledCells(good_2,:);

% subdataset #3:
good_3 = FilledCells(:,1) >= min(x) & FilledCells(:,1) < xsplit &...
    FilledCells(:,2) >= min(y) & FilledCells(:,2) < ysplit &...
    FilledCells(:,3) >= zsplit & FilledCells(:,3) <= max(z);
FC_3 = FilledCells(good_3,:);

% subdataset #4:
good_4 = FilledCells(:,1) >= xsplit & FilledCells(:,1) <= max(x) &...
    FilledCells(:,2) >= min(y) & FilledCells(:,2) < ysplit &...
    FilledCells(:,3) >= zsplit & FilledCells(:,3) <= max(z);
FC_4 = FilledCells(good_4,:);

% subdataset #5:
good_5 = FilledCells(:,1) >= min(x) & FilledCells(:,1) < xsplit &...
    FilledCells(:,2) >= ysplit & FilledCells(:,2) <= max(y) &...
    FilledCells(:,3) >= min(z) & FilledCells(:,3) < zsplit;
FC_5 = FilledCells(good_5,:);

% subdataset #6:
good_6 = FilledCells(:,1) >= xsplit & FilledCells(:,1) <= max(x) &...
    FilledCells(:,2) >= ysplit & FilledCells(:,2) <= max(y) &...
    FilledCells(:,3) >= min(z) & FilledCells(:,3) < zsplit;
FC_6 = FilledCells(good_6,:);

% subdataset #7:
good_7 = FilledCells(:,1) >= min(x) & FilledCells(:,1) < xsplit &...
    FilledCells(:,2) >= ysplit & FilledCells(:,2) <= max(y) &...
    FilledCells(:,3) >= zsplit & FilledCells(:,3) <= max(z);
FC_7 = FilledCells(good_7,:);

% subdataset #8:
good_8 = FilledCells(:,1) >= xsplit & FilledCells(:,1) <= max(x) &...
    FilledCells(:,2) >= ysplit & FilledCells(:,2) <= max(y) &...
    FilledCells(:,3) >= zsplit & FilledCells(:,3) <= max(z);
FC_8 = FilledCells(good_8,:);
%-------------------------------------------------------------------------

%-------------------------------------------------------------------------
%                        SECOND PART - BINARISING                         %
%-------------------------------------------------------------------------

%DERIVE THE MINIMUM BOUNDING GRID THAT CONTAIN THE DATA--------------------
%bounding grid #1:
imin = min(x);
jmin = min(y);
hmin = min(z);
imax = xsplit-d;
jmax = ysplit-d;
```

```
160 hmax = zsplit-d;
161
162 a = 0:ceil((imax-imin)*(1/d));
163 b = 0:ceil((jmax-jmin)*(1/d));
164 c = 0:ceil((hmax-hmin)*(1/d));
165 amax = max(a);
166 bmax = max(b);
167 cmax = max(c);
168
169 while a <= amax
170     i = imin +a*d;
171     a = amax + 1;
172 end
173
174 while b <= bmax
175     j = jmin +b*d;
176     b = bmax + 1;
177 end
178
179 while c<=cmax
180     h = hmin +c*d;
181     c = cmax + 1;
182 end
183
184 EG_1 = combvec (i,j,h)';
185
186 %bounding grid #2:
187 imin = xsplit;
188 jmin = min(y);
189 hmin = min(z);
190
191 imax = max(x);
192 jmax = ysplit-d;
193 hmax = zsplit-d;
194
195 a = 0:ceil((imax-imin)*(1/d));
196 b = 0:ceil((jmax-jmin)*(1/d));
197 c = 0:ceil((hmax-hmin)*(1/d));
198 amax = max(a);
199 bmax = max(b);
200 cmax = max(c);
201
202 while a <= amax
203     i = imin +a*d;
204     a = amax + 1;
205 end
206
207 while b <= bmax
208     j = jmin +b*d;
209     b = bmax + 1;
210 end
211
212 while c<=cmax
213     h = hmin +c*d;
214     c = cmax + 1;
215 end
216
217 EG_2 = combvec (i,j,h)';
218
219 %bounding grid #3:
```

```
imin = min(x);
jmin = min(y);
hmin = zsplit;

imax = xsplit-d;
jmax = ysplit-d;
hmax = max(z);

a = 0:ceil((imax-imin)*(1/d));
b = 0:ceil((jmax-jmin)*(1/d));
c = 0:ceil((hmax-hmin)*(1/d));
amax = max(a);
bmax = max(b);
cmax = max(c);

while a <= amax
    i = imin +a*d;
    a = amax + 1;
end

while b <= bmax
    j = jmin +b*d;
    b = bmax + 1;
end

while c<=cmax
    h = hmin +c*d;
    c = cmax + 1;
end

EG_3 = combvec (i,j,h)';

%bounding grid #4:
imin = xsplit;
jmin = min(y);
hmin = zsplit;

imax = max(x);
jmax = ysplit-d;
hmax = max(z);

a = 0:ceil((imax-imin)*(1/d));
b = 0:ceil((jmax-jmin)*(1/d));
c = 0:ceil((hmax-hmin)*(1/d));
amax = max(a);
bmax = max(b);
cmax = max(c);

while a <= amax
    i = imin +a*d;
    a = amax + 1;
end

while b <= bmax
    j = jmin +b*d;
    b = bmax + 1;
end

while c<=cmax
    h = hmin +c*d;
```

```
    c = cmax + 1;
end

EG_4 = combvec (i,j,h)';

%bounding grid #5:
imin = min(x);
jmin = ysplit;
hmin = min(z);

imax = xsplit-d;
jmax = max(y);
hmax = zsplit-d;

a = 0:ceil((imax-imin)*(1/d));
b = 0:ceil((jmax-jmin)*(1/d));
c = 0:ceil((hmax-hmin)*(1/d));
amax = max(a);
bmax = max(b);
cmax = max(c);

while a <= amax
    i = imin +a*d;
    a = amax + 1;
end

while b <= bmax
    j = jmin +b*d;
    b = bmax + 1;
end

while c<=cmax
    h = hmin +c*d;
    c = cmax + 1;
end

EG_5 = combvec (i,j,h)';

%bounding grid #6:
imin = xsplit;
jmin = ysplit;
hmin = min(z);

imax = max(x);
jmax = max(y);
hmax = zsplit-d;

a = 0:ceil((imax-imin)*(1/d));
b = 0:ceil((jmax-jmin)*(1/d));
c = 0:ceil((hmax-hmin)*(1/d));
amax = max(a);
bmax = max(b);
cmax = max(c);

while a <= amax
    i = imin +a*d;
    a = amax + 1;
end

while b <= bmax
```

```
340     j = jmin +b*d;
341     b = bmax + 1;
342 end
343
344 while c<=cmax
345     h = hmin +c*d;
346     c = cmax + 1;
347 end
348
349 EG_6 = combvec (i,j,h)';
350
351 %bounding grid #7:
352 imin = min(x);
353 jmin = ysplit;
354 hmin = zsplit;
355
356 imax = xsplit-d;
357 jmax = max(y);
358 hmax = max(z);
359
360 a = 0:ceil((imax-imin)*(1/d));
361 b = 0:ceil((jmax-jmin)*(1/d));
362 c = 0:ceil((hmax-hmin)*(1/d));
363 amax = max(a);
364 bmax = max(b);
365 cmax = max(c);
366
367 while a <= amax
368     i = imin +a*d;
369     a = amax + 1;
370 end
371
372 while b <= bmax
373     j = jmin +b*d;
374     b = bmax + 1;
375 end
376
377 while c<=cmax
378     h = hmin +c*d;
379     c = cmax + 1;
380 end
381
382 EG_7 = combvec (i,j,h)';
383
384 %bounding grid #8:
385 imin = xsplit;
386 jmin = ysplit;
387 hmin = zsplit;
388
389 imax = max(x);
390 jmax = max(y);
391 hmax = max(z);
392
393 a = 0:ceil((imax-imin)*(1/d));
394 b = 0:ceil((jmax-jmin)*(1/d));
395 c = 0:ceil((hmax-hmin)*(1/d));
396 amax = max(a);
397 bmax = max(b);
398 cmax = max(c);
399
```

```
while a <= amax
    i = imin +a*d;
    a = amax + 1;
end

while b <= bmax
    j = jmin +b*d;
    b = bmax + 1;
end

while c<=cmax
    h = hmin +c*d;
    c = cmax + 1;
end

EG_8 = combvec (i,j,h)';

%CROSS-REFERENCE THE BOUNDING GRIDS WITH THE ORGANISED POINT DATA IN A
%LOGICAL MANNER AND CREATE BINARY SUBGRIDS (1 FOR FULL 0 FOR EMPTY) BECAUSE
%OF THE POINT DATA ORGANISATION EARLIER, ONLY ONE POINT CORRESPONDS TO A
%SINGLE VOXEL-----------------------------------------------------------------
for p = 1:8
    if p==1
        EG = EG_1;
        FilledCells = FC_1;
    elseif p==2
        EG = EG_2;
        FilledCells = FC_2;
    elseif p==3
        EG = EG_3;
        FilledCells = FC_3;
    elseif p==4
        EG = EG_4;
        FilledCells = FC_4;
    elseif p==5
        EG = EG_5;
        FilledCells = FC_5;
    elseif p==6
        EG = EG_6;
        FilledCells = FC_6;
    elseif p==7
        EG = EG_7;
        FilledCells = FC_7;
    elseif p==8
        EG = EG_8;
        FilledCells = FC_8;
    end

    Logical = ismember(EG, FilledCells, 'rows');
    BG = [EG, Logical];

    if p==1
        BG_1 = BG;
    elseif p==2
        BG_2 = BG;
    elseif p==3
        BG_3 = BG;
    elseif p==4
       BG_4 = BG;
    elseif p==5
```

```
460         BG_5 = BG;
461     elseif p==6
462         BG_6 = BG;
463     elseif p==7
464        BG_7 = BG;
465     elseif p==8
466         BG_8 = BG;
467     end
468 end
469 
470 %RELEASE MEMORY------------------------------------------------------------
471 clear EG
472 clear EG_1
473 clear EG_2
474 clear EG_3
475 clear EG_4
476 clear EG_5
477 clear EG_6
478 clear EG_7
479 clear EG_8
480 
481 %CHECK RESULTS. THE TOTAL AMOUNT OF ORGANISED POINTS (l) MUST BE EQUAL TO
482 %THE SUM OF THE LOGICAL OUTPUT (k). IF THE BINARY GRIDS ARE CORRECTLY
483 %EVALUATED CALCULATE BULK POROSITY (EMPTY VOXELS / TOTAL VOXELS) AND PLANT
484 %EXTENT VALUES. SAVE RESULTS TO CURRENT DIR. COBNINE THE BINARY SUBGRIDS
485 %INTO ONE DATASET AND CORRECT ITS COORDINATES BACK TO THE ORIGINAL VALUES
486 %(DUE TO THE '+1000' AND 'x1000' CORRECTIONS APPLIED IN THE BEGINING) WRITE
487 %BINARY GRID TO CURRENT DIR-----------------------------------------------
488 k = sum(BG_1(:,4)) + sum(BG_2(:,4))+sum(BG_3(:,4))+...
489     sum(BG_4(:,4))+sum(BG_5(:,4))+sum(BG_6(:,4))+...
490     sum(BG_7(:,4))+sum(BG_8(:,4));
491 
492 l = size(FC_1,1)+size(FC_2,1)+size(FC_3,1)+size(FC_4,1)+size(FC_5,1)...
493     +size(FC_6,1)+size(FC_7,1)+size(FC_8,1);
494 
495 if k==l
496 
497     %combine the binary grids:
498     AA = [BG_1;BG_2;BG_3;BG_4;BG_5;BG_6;BG_7;BG_8];
499 
500     %find amount of empty binary cells:
501     good = AA(:,4) == 0;
502     empty = AA(good,:);
503 
504     %find amount of filled binary cells:
505     good = AA(:,4) == 1;
506     filled = AA(good,:);
507 
508     %calculate porosity:
509     porosity = size(empty,1)/size(AA,1);
510 
511     %measure streamwise and lateral extent for every mm of heiht:
512     minz = min(filled(:,3));
513     maxz = max(filled(:,3));
514     bb = 1;
515     for aa = minz:1:maxz
516         good = filled(:,3) == aa;
517         temp = filled(good,:);
518         minx = min(temp(:,1));
519         maxx = max(temp(:,1));
```

```
520         miny = min(temp(:,2));
521         maxy = max(temp(:,2));
522 
523         if sum(good) ~= 0
524             xext(bb) = maxx - minx;
525             yext(bb) = maxy - miny;
526         else xext(bb) = 0;
527             yext(bb) = 0;
528         end
529         bb = bb+1;
530     end
531 
532     %calculate mean, max and 80th percentile of plant extent:
533     lat_extent_mean = mean(xext);
534     str_extent_mean = mean(yext);
535     lat_extent_max = max(xext);
536     str_extent_max = max(yext);
537     lat_extent_80 = prctile(xext,80);
538     str_extent_80 = prctile(yext,80);
539 
540     %store porosity and extent values to current dir:
541     out(1,1) = size(AA,1);          %the total amount of binary voxels
542     out(1,2) = size(empty,1);       %the amount of empty binary voxels
543     out(1,3) = size(filled,1);      %the amount of filled binary voxels
544     out(1,4) = porosity;            %the bulk 3D porosity
545     out(1,5) = lat_extent_mean/1000;%the average lateral plant extent
546     out(1,6) = str_extent_mean/1000;%the average streamwise plant extent
547     out(1,7) = lat_extent_80/1000;  %the 80th perc of the lateral plant extent
548     out(1,8) = str_extent_80/1000;  %the 80th perc of the streamwise plant extent
549     out(1,9) = lat_extent_max/1000; %the max lateral plant extent
550     out(1,10) = str_extent_max/1000;%the max streamwise plant extent
551 
552     %apply corrections on the coordinates of the bin grids:
553     BinaryGrid = [(AA(:,1)/1000)-1000,(AA(:,2)/1000)-1000,...
554         (AA(:,3)/1000)-1000, AA(:,4)];
555 
556     %store porosity and extent values to current dir:
557     dlmwrite((sprintf('%s_P3D.txt',infile)),out, 'precision',8);
558 
559     %store binary grid to current dir:
560     dlmwrite((sprintf('%s_bin.txt',infile)),BinaryGrid, 'precision',8);
561 
562     %release memory:
563     clear AA
564     clear filled
565     clear empty
566 
567 end
568 %--------------------------------------------------------------------------
569 
570 %--------------------------------------------------------------------------
571 %                        THIRD PART - POROSITY ARRAYS                     %
572 %--------------------------------------------------------------------------
573 for p = 1:8
574     if p == 1
575         BG = BG_1;
576         FC = FC_1;
577     elseif p == 2
578         BG = BG_2;
579         FC = FC_2;
```

```
580     elseif p == 3
581         BG = BG_3;
582         FC = FC_3;
583     elseif p == 4
584         BG = BG_4;
585         FC = FC_4;
586     elseif p == 5
587         BG = BG_5;
588         FC = FC_5;
589     elseif p == 6
590         BG = BG_6;
591         FC = FC_6;
592     elseif p == 7
593         BG = BG_7;
594         FC = FC_7;
595     elseif p == 8
596         BG = BG_8;
597         FC = FC_8;
598     end
599
600 %DERIVE THE MINIMUM BOUNDING ARRAYS THAT CONTAIN THE DATA------------------
601 Imin = (min(BG(:,1)));
602 Jmin = (min(BG(:,2)));
603 Hmin = (min(BG(:,3)));
604
605 Imax = (max(BG(:,1))-D +d);
606 Jmax = (max(BG(:,2))-D +d);
607 Hmax = (max(BG(:,3))-D +d);
608
609 A = 0:ceil((Imax-Imin)*(1/D));
610 B = 0:ceil((Jmax-Jmin)*(1/D));
611 C = 0:ceil((Hmax-Hmin)*(1/D));
612 Amax = max(A);
613 Bmax = max(B);
614 Cmax = max(C);
615
616 while A <= Amax
617     I = Imin +A*D;
618     A = Amax + 1;
619 end
620
621 while B <= Bmax
622     J = Jmin +B*D;
623     B = Bmax + 1;
624 end
625
626 while C<=Cmax
627     H = Hmin +C*D;
628     C = Cmax + 1;
629 end
630
631 EA = combvec(I,J,H,0)';
632
633 KK = size(EA,1);
634
635 %CROSS-REFERENCE THE EMPTY POROSITY ARRAY WITH THE FILLED BINARY VOXELS AND
636 %COUNT HOW MANY FILLED BINARY VOXELS ARE INSIDE EACH POROSITY ARRAY CELL---
637 for K = 1:KK
638     I = EA(K,1);
639     J = EA(K,2);
```

```
640     H = EA(K,3);
641     Index = find(FC(:,1)>=I & FC(:,1)<(I+D) &...
642         FC(:,2)>=J & FC(:,2)<(J+D) &...
643         FC(:,3)>=H & FC(:,3)<(H+D));
644     EA(K,4) = length(Index);
645 end
646 
647 %POPULATE THE POROSITY ARRAY WITH POROSITY VALUES
648 %(POROSITY = EMPTY VOXELS/TOTAL AMOUNT OF VOXELS)-------------------------
649 %Maximum theoretical amount of voxels within each array celL:
650 TA = (D/d)^3;
651 
652 %Empty voxels within each array cell :
653 EA(:,5) = TA - EA(:,4);
654 
655 %Porosity value for each array cell:
656 EA(:,6) = EA(:,5)/TA;
657 
658 %Save porosity array in new matrix:
659 PA = [EA(:,1), EA(:,2), EA(:,3), EA(:,6)];
660 
661 if p == 1
662     EA_1 = EA;
663     PA_1 = PA;
664     clear BG_1
665 elseif p == 2
666     EA_2 = EA;
667     PA_2 = PA;
668     clear BG_2
669 elseif p == 3
670     EA_3 = EA;
671     PA_3 = PA;
672     clear BG_3
673 elseif p == 4
674     EA_4 = EA;
675     PA_4 = PA;
676     clear BG_4
677 elseif p == 5
678     EA_5 = EA;
679     PA_5 = PA;
680     clear BG_5
681 elseif p == 6
682     EA_6 = EA;
683     PA_6 = PA;
684     clear BG_6
685 elseif p == 7
686     EA_7 = EA;
687     PA_7 = PA;
688     clear BG_7
689 elseif p == 8
690     EA_8 = EA;
691     PA_8 = PA;
692     clear BG_8
693 end
694 
695 end
696 
697 %CHECK RESULTS. THE TOTAL AMOUNT OF POINTS THAT WERE COUNTED INSIDE EACH
698 %POROSITY ARRAY CELL (u) MUST BE EQUAL TO THE TOTAL AMOUNT OF ORGANISED
699 %CELLS (l). IF THE POROSITY ARRAYS ARE CORRECTLY EVALUATED CONVERT THEIR
```

```
%COORDINATES BACK TO THEIR ORIGINAL FORM (DUE T THE '+1000' AND 'x1000'
%TRANSFORMATIONS APPLIED IN THE BEGINING). COMBINE THEM INTO ONE FILE AND
%STORE IT IN THE CURRENT DIR-----------------------------------------------

u = sum(EA_1(:,4),1)+sum(EA_2(:,4),1)+sum(EA_3(:,4),1)+sum(EA_4(:,4),1)+...
    sum(EA_5(:,4),1)+sum(EA_6(:,4),1)+sum(EA_7(:,4),1)+sum(EA_8(:,4),1);

if u ==1
    PorArray_1 = [(PA_1(:,1)/1000)-1000,(PA_1(:,2)/1000)-1000,...
        (PA_1(:,3)/1000)-1000, PA_1(:,4)];

    PorArray_2 = [(PA_2(:,1)/1000)-1000,(PA_2(:,2)/1000)-1000,...
        (PA_2(:,3)/1000)-1000, PA_2(:,4)];

    PorArray_3 = [(PA_3(:,1)/1000)-1000,(PA_3(:,2)/1000)-1000,...
        (PA_3(:,3)/1000)-1000, PA_3(:,4)];

    PorArray_4 = [(PA_4(:,1)/1000)-1000,(PA_4(:,2)/1000)-1000,...
        (PA_4(:,3)/1000)-1000, PA_4(:,4)];

    PorArray_5 = [(PA_5(:,1)/1000)-1000,(PA_5(:,2)/1000)-1000,...
        (PA_5(:,3)/1000)-1000, PA_5(:,4)];

    PorArray_6 = [(PA_6(:,1)/1000)-1000,(PA_6(:,2)/1000)-1000,...
        (PA_6(:,3)/1000)-1000, PA_6(:,4)];

    PorArray_7 = [(PA_7(:,1)/1000)-1000,(PA_7(:,2)/1000)-1000,...
        (PA_7(:,3)/1000)-1000, PA_7(:,4)];

    PorArray_8 = [(PA_8(:,1)/1000)-1000,(PA_8(:,2)/1000)-1000,...
        (PA_8(:,3)/1000)-1000, PA_8(:,4)];

    %combine them:
    PorArray = [PorArray_1;PorArray_2;PorArray_3;PorArray_4;...
        PorArray_5;PorArray_6;PorArray_7;PorArray_8];

    %release memory:
    clear PorArray_1
    clear PorArray_2
    clear PorArray_3
    clear PorArray_4
    clear PorArray_5
    clear PorArray_6
    clear PorArray_7
    clear PorArray_8


 %store porosity array to current dir:
    dlmwrite((sprintf('%s_por.txt',infile)),PorArray, 'precision',8);

else disp('Error in the porosity array calculation')
end
%-------------------------------------------------------------------------

else
    disp('Select appropriate cell size so that cellsize/pointspacing = interger')
end

end
%-------------------------------------------------------------------------
```

```
760                                    %%END%%
761 %--------------------------------------------------------------------------
```

Appendix C

P_{2D}, OP and 3D Porosity Array Figures for all Plant-Foliage Scenarios

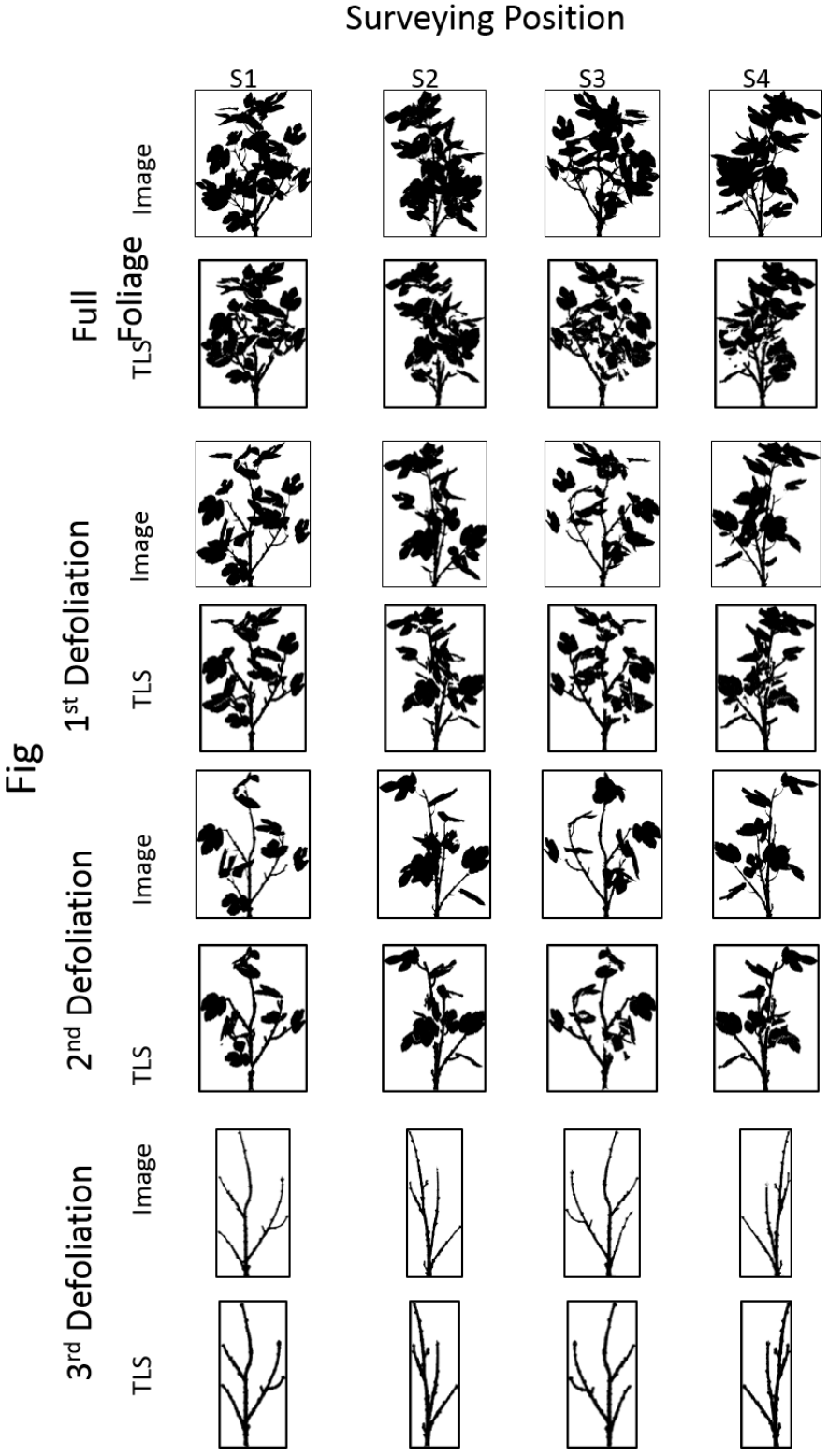

FIGURE C.1: Optical and 2D porosity figures for all scenarios of the fig from all four surveying positions.

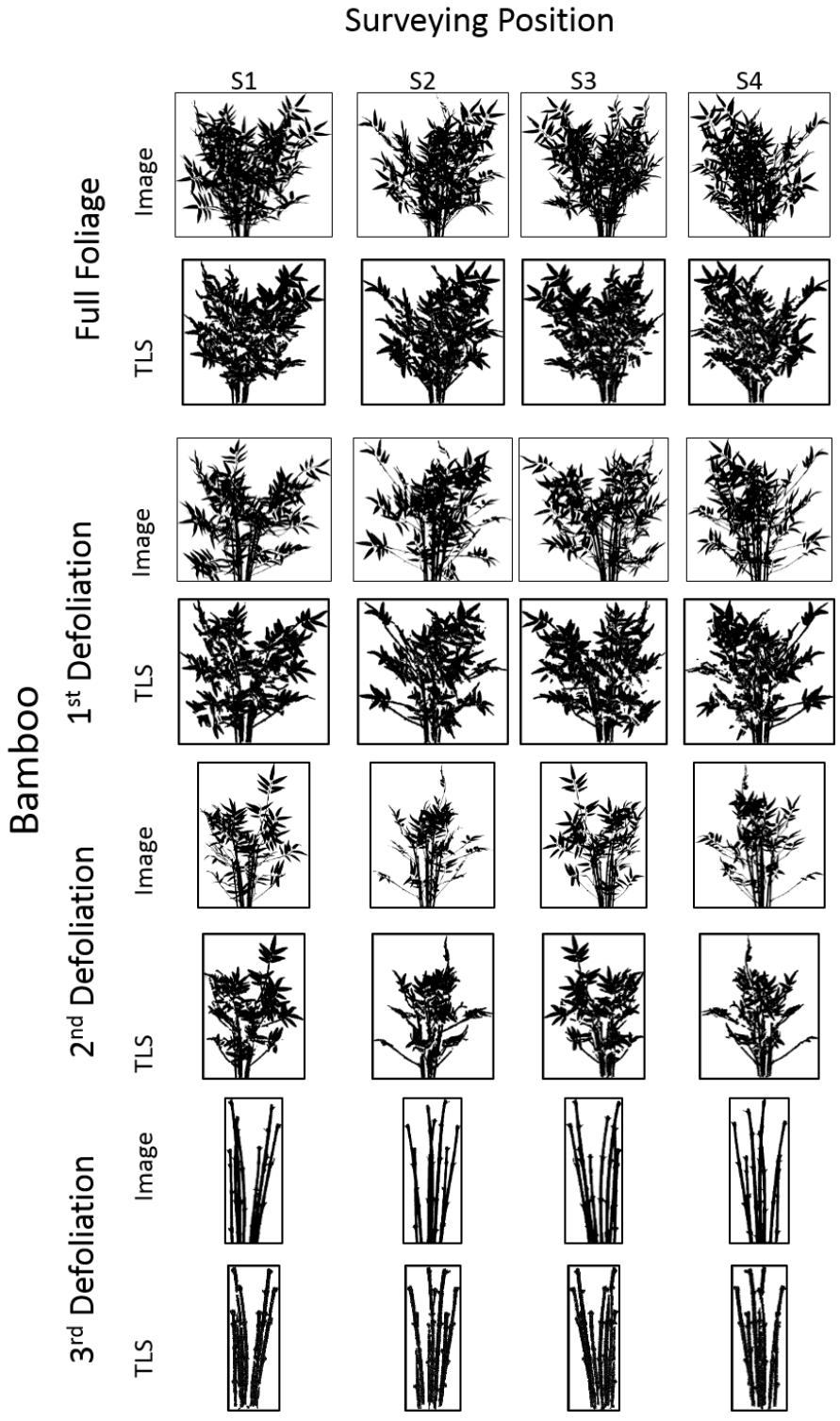

FIGURE C.2: Optical and 2D porosity figures for all scenarios of the bamboo from all four surveying positions.

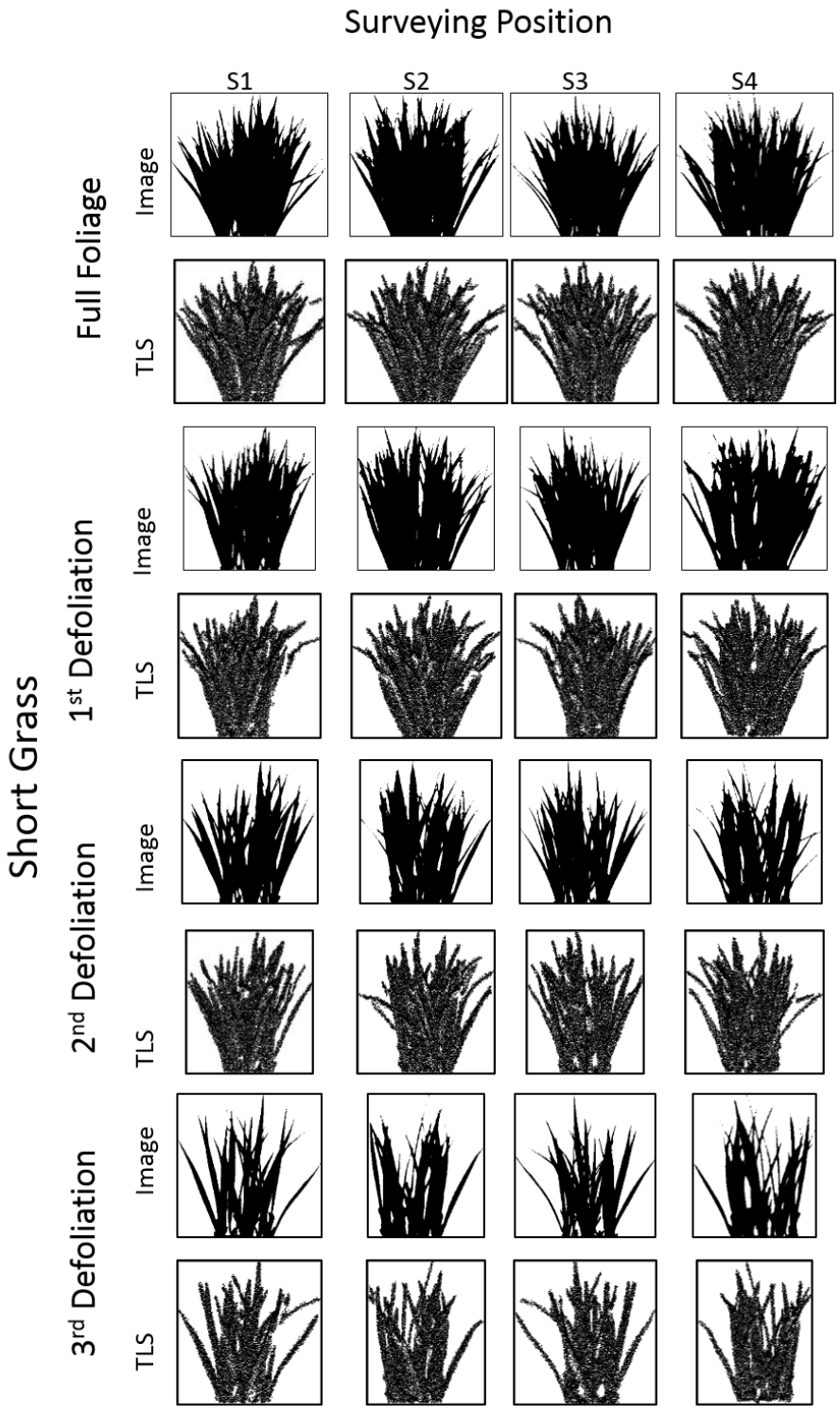

FIGURE C.3: Optical and 2D porosity figures for all scenarios of the short grass from all four surveying positions.

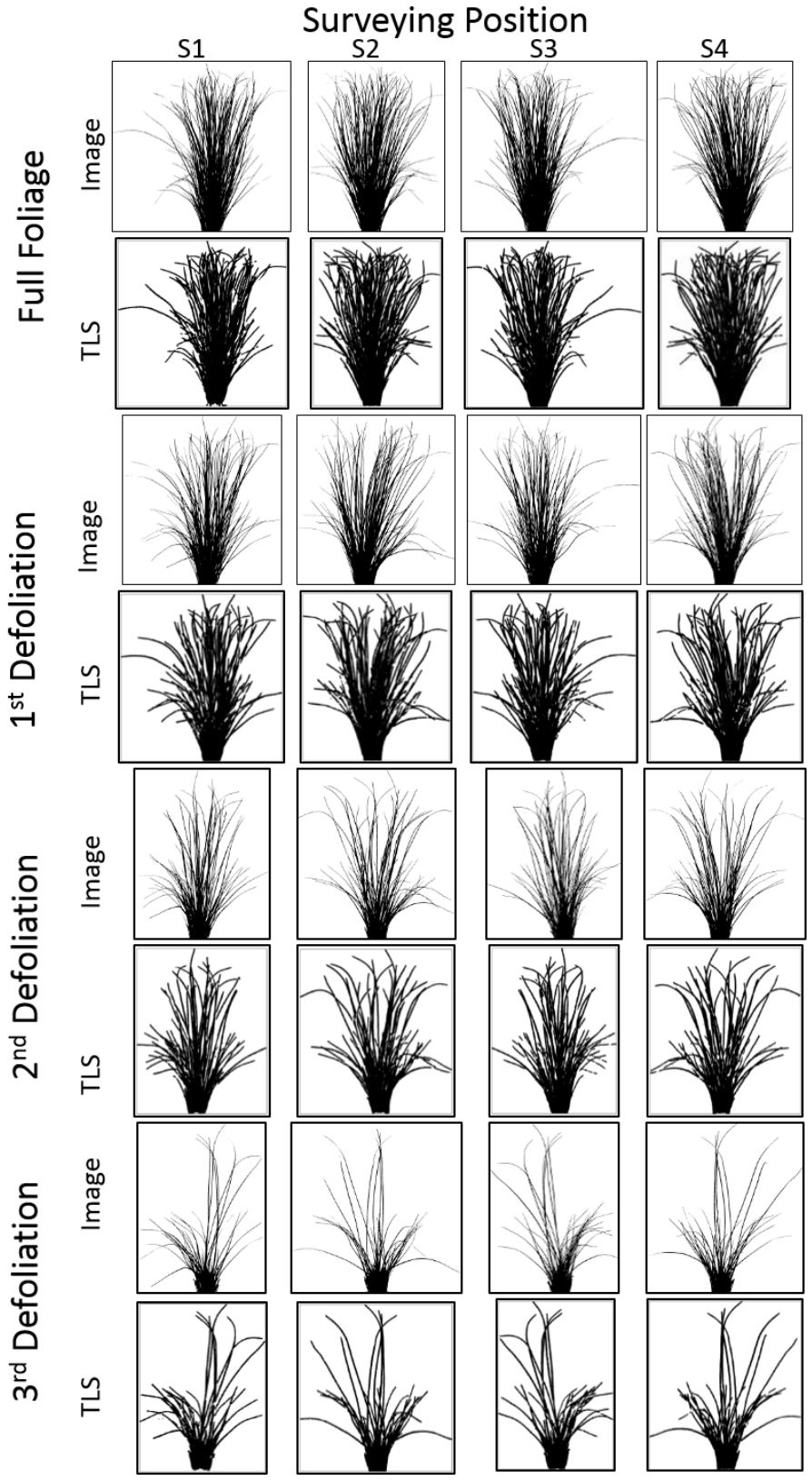

FIGURE C.4: Optical and 2D porosity figures for all scenarios of the tall grass from all four surveying positions.

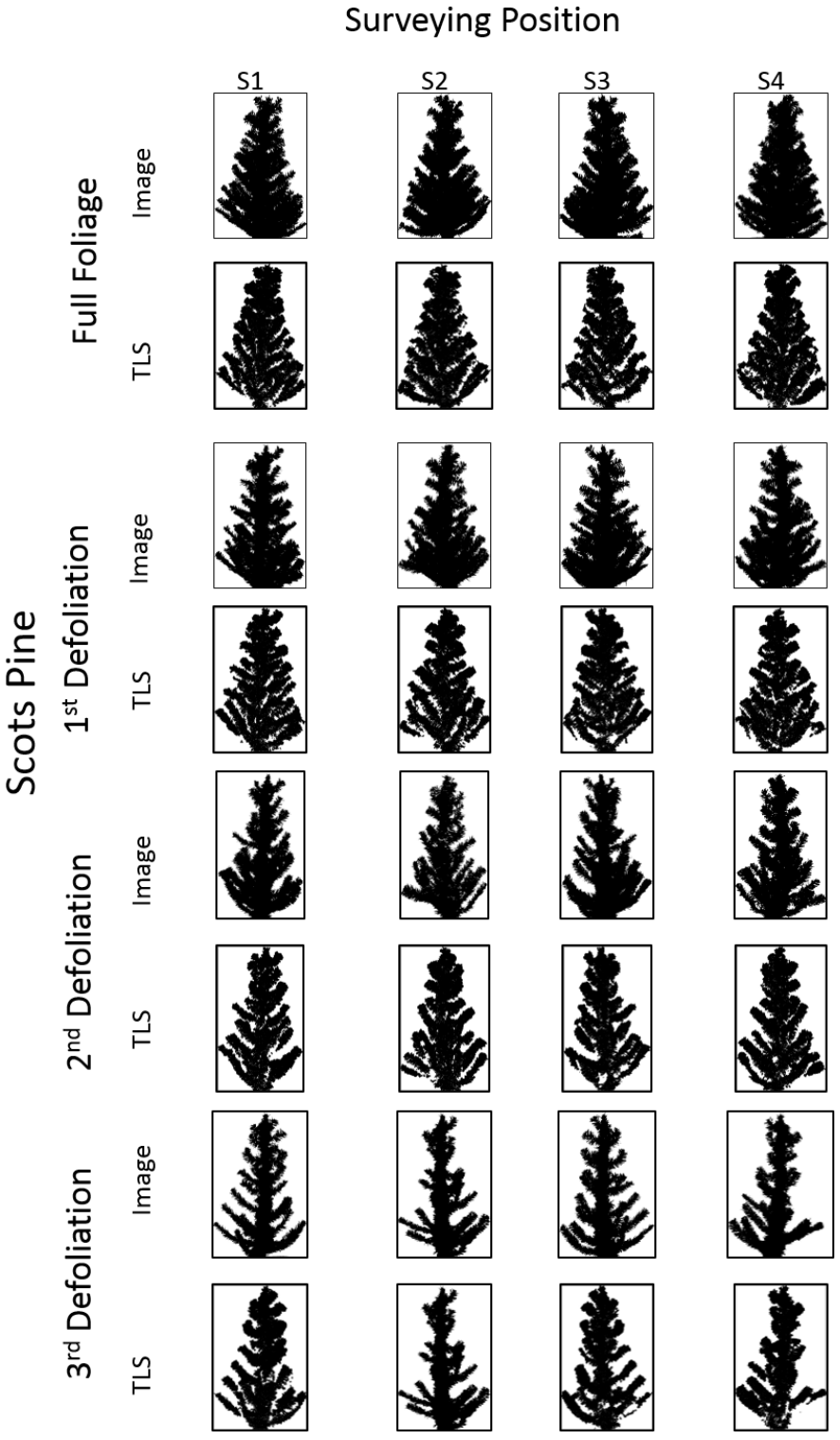

FIGURE C.5: Optical and 2D porosity figures for all scenarios of the scots pine from all four surveying positions.

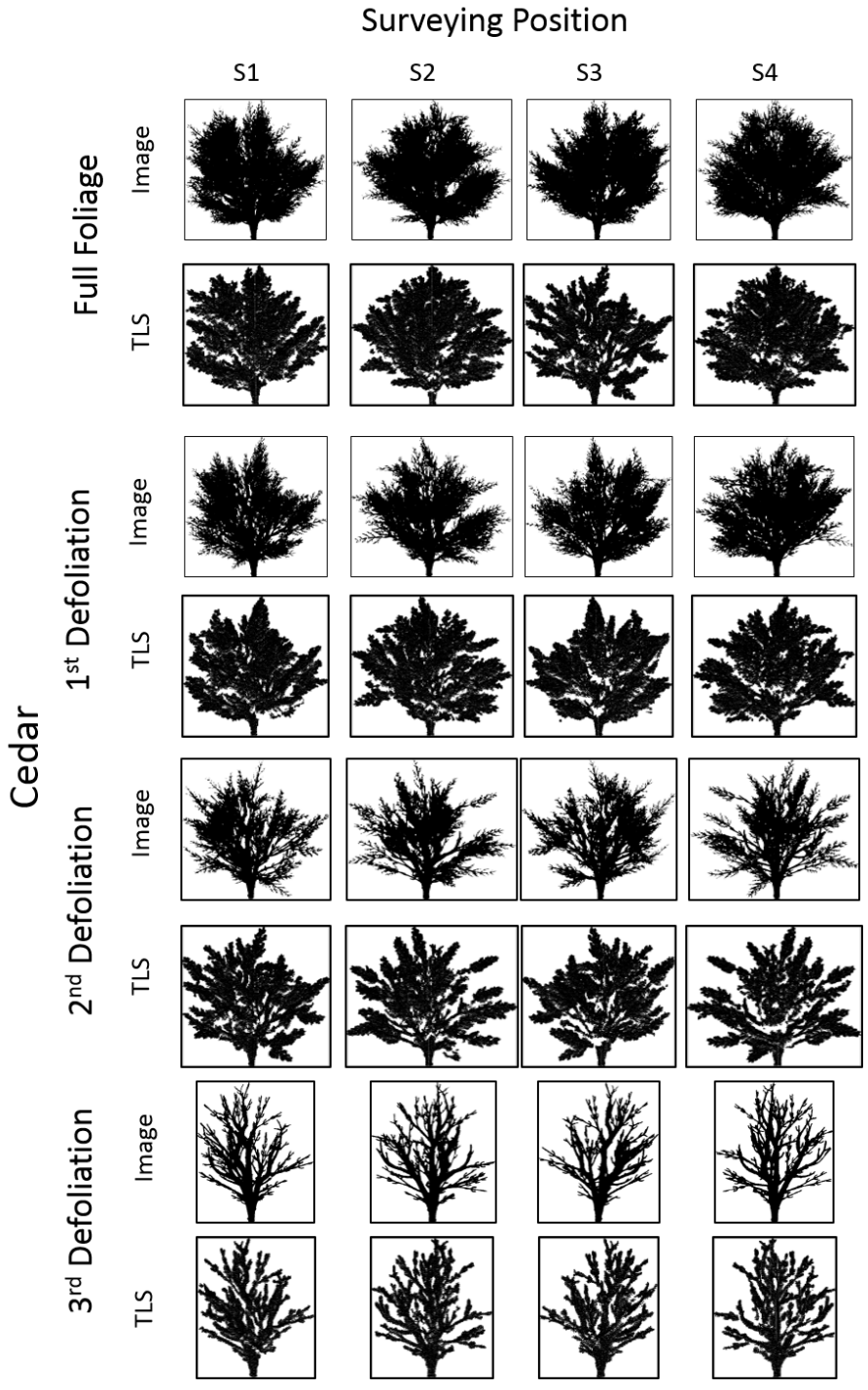

FIGURE C.6: Optical and 2D porosity figures for all scenarios of the cedar from all four surveying positions.

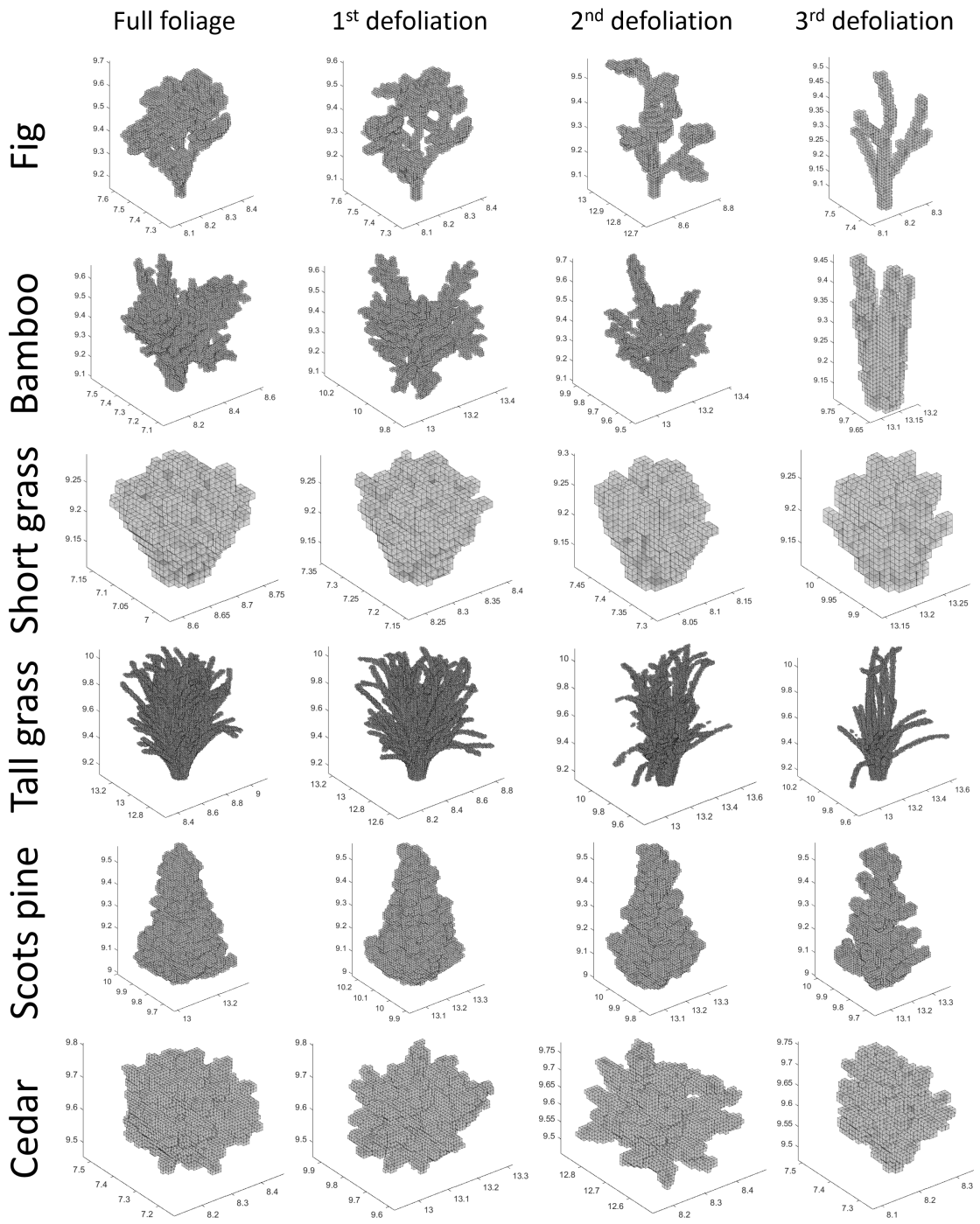

FIGURE C.7: 3D porosity arrays of all plant scenarios.

Appendix D

Extracted Hydraulic Parameters

TABLE D.1: Hydraulic parameters for the physical modelling experiments

Plant	**Foliage**	**Flow**	U	S_f	A_c	P	R_h	f
Bamboo	Full foliage	Deep-Slow	0.246	0.013	0.118	1.000	0.118	1.931
Bamboo	Full foliage	Medium	0.297	0.015	0.097	0.893	0.109	1.447
Bamboo	Full foliage	Shallow-Fast	0.370	0.017	0.078	0.792	0.099	0.944
Bamboo	1st defoliation	Deep-Slow	0.245	0.011	0.118	1.003	0.118	1.688
Bamboo	1st defoliation	Medium	0.294	0.012	0.099	0.899	0.110	1.197
Bamboo	1st defoliation	Shallow-Fast	0.366	0.015	0.079	0.797	0.099	0.857
Bamboo	2nd defoliation	Deep-Slow	0.245	0.007	0.118	1.002	0.118	1.088
Bamboo	2nd defoliation	Medium	0.298	0.008	0.097	0.893	0.109	0.799
Bamboo	2nd defoliation	Shallow-Fast	0.372	0.011	0.078	0.791	0.099	0.633
Bamboo	3rd defoliation	Deep-Slow	0.251	0.005	0.116	0.989	0.117	0.756
Bamboo	3rd defoliation	Medium	0.296	0.006	0.098	0.896	0.109	0.619
Bamboo	3rd defoliation	Shallow-Fast	0.370	0.009	0.078	0.792	0.099	0.498
Cedar	Full foliage	Deep-Slow	0.243	0.033	0.119	1.008	0.118	5.256
Cedar	Full foliage	Medium	0.292	0.048	0.099	0.902	0.110	4.873
Cedar	Full foliage	Shallow-Fast	0.361	0.052	0.080	0.803	0.100	3.155
Cedar	1st defoliation	Deep-Slow	0.246	0.022	0.118	1.000	0.118	3.300
Cedar	1st defoliation	Medium	0.291	0.035	0.100	0.904	0.110	3.605
Cedar	1st defoliation	Shallow-Fast	0.364	0.038	0.080	0.800	0.100	2.244
Cedar	2nd defoliation	Deep-Slow	0.248	0.017	0.117	0.997	0.118	2.525
Cedar	2nd defoliation	Medium	0.293	0.025	0.099	0.901	0.110	2.502
Cedar	2nd defoliation	Shallow-Fast	0.362	0.031	0.080	0.802	0.100	1.868
Cedar	3rd defoliation	Deep-Slow	0.246	0.008	0.118	1.001	0.118	1.217
Cedar	3rd defoliation	Medium	0.296	0.010	0.098	0.896	0.109	0.979
Cedar	3rd defoliation	Shallow-Fast	0.365	0.016	0.079	0.798	0.100	0.922
Fig	Full foliage	Deep-Slow	0.246	0.009	0.118	1.000	0.118	1.400
Fig	Full foliage	Medium	0.295	0.009	0.098	0.898	0.110	0.914
Fig	Full foliage	Shallow-Fast	0.364	0.010	0.080	0.800	0.100	0.583
Fig	1st defoliation	Deep-Slow	0.246	0.005	0.118	1.001	0.118	0.698
Fig	1st defoliation	Medium	0.297	0.005	0.098	0.895	0.109	0.483
Fig	1st defoliation	Shallow-Fast	0.368	0.009	0.079	0.794	0.099	0.529
Fig	2nd defoliation	Deep-Slow	0.247	0.003	0.117	0.998	0.118	0.462
Fig	2nd defoliation	Medium	0.294	0.004	0.099	0.899	0.110	0.447
Fig	2nd defoliation	Shallow-Fast	0.364	0.007	0.080	0.799	0.100	0.397
Fig	3rd defoliation	Deep-Slow	0.245	0.001	0.118	1.002	0.118	0.202
Fig	3rd defoliation	Medium	0.293	0.001	0.099	0.900	0.110	0.145
Fig	3rd defoliation	Shallow-Fast	0.367	0.002	0.079	0.796	0.099	0.124
Grass	Full foliage	Deep-Slow	0.247	0.013	0.118	0.999	0.118	2.021
Grass	Full foliage	Medium	0.297	0.017	0.098	0.894	0.109	1.690
Grass	Full foliage	Shallow-Fast	0.369	0.028	0.079	0.794	0.099	1.619
Grass	1st defoliation	Deep-Slow	0.243	0.010	0.119	1.009	0.118	1.621
Grass	1st defoliation	Medium	0.292	0.011	0.099	0.903	0.110	1.069
Grass	1st defoliation	Shallow-Fast	0.357	0.019	0.081	0.807	0.101	1.189
Grass	2nd defoliation	Deep-Slow	0.244	0.007	0.119	1.005	0.118	1.136
Grass	2nd defoliation	Medium	0.294	0.010	0.099	0.899	0.110	0.989
Grass	2nd defoliation	Shallow-Fast	0.363	0.016	0.080	0.801	0.100	0.940
Grass	3rd defoliation	Deep-Slow	0.245	0.005	0.118	1.002	0.118	0.714
Grass	3rd defoliation	Medium	0.297	0.007	0.098	0.894	0.109	0.695
Grass	3rd defoliation	Shallow-Fast	0.365	0.011	0.079	0.798	0.100	0.649
Scots Pine	Full foliage	Deep-Slow	0.243	0.029	0.119	1.008	0.118	4.611
Scots Pine	Full foliage	Medium	0.297	0.049	0.098	0.894	0.109	4.734
Scots Pine	Full foliage	Shallow-Fast	0.371	0.075	0.078	0.791	0.099	4.218
Scots Pine	2nd defoliation	Deep-Slow	0.242	0.020	0.120	1.009	0.118	3.104
Scots Pine	2nd defoliation	Medium	0.294	0.033	0.099	0.899	0.110	3.283
Scots Pine	2nd defoliation	Shallow-Fast	0.365	0.056	0.080	0.799	0.100	3.291
Scots Pine	3rd defoliation	Deep-Slow	0.249	0.017	0.116	0.993	0.117	2.581
Scots Pine	3rd defoliation	Medium	0.295	0.030	0.098	0.898	0.110	3.001
Scots Pine	3rd defoliation	Shallow-Fast	0.370	0.043	0.078	0.793	0.099	2.444

Appendix E

Extracted Vegetation Structure Metrics

TABLE E.1: Plant structure metrics extracted from the through-water TLS data

Plant scenario		Flow	through-water									
			W_{max}	L_{max}	$\overline{W}$	$\overline{L}$	W_{80}	L_{80}	A_f	P_{2D}	P_{2Dpf}	P_{3D}
Bamboo	Full foliage	Deep-Slow	0.348	0.376	0.154	0.116	0.268	0.199	0.049	0.663	0.738	0.9982
	Full foliage	Medium	0.318	0.356	0.145	0.107	0.262	0.170	0.045	0.666	0.757	0.9980
	Full foliage	Shallow-Fast	0.352	0.257	0.159	0.116	0.256	0.171	0.040	0.730	0.815	0.9982
	1st defoliation	Deep-Slow	0.384	0.300	0.155	0.113	0.282	0.183	0.018	0.723	0.755	0.9983
	1st defoliation	Medium	0.317	0.260	0.140	0.105	0.229	0.167	0.043	0.695	0.740	0.9979
	1st defoliation	Shallow-Fast	0.354	0.204	0.154	0.111	0.252	0.171	0.037	0.744	0.799	0.9978
	2nd defoliation	Deep-Slow	0.263	0.268	0.120	0.106	0.194	0.194	0.035	0.693	0.722	0.9979
	2nd defoliation	Medium	0.274	0.257	0.108	0.097	0.179	0.180	0.030	0.730	0.787	0.9982
	2nd defoliation	Shallow-Fast	0.222	0.212	0.114	0.103	0.161	0.164	0.026	0.713	0.795	0.9978
	3rd defoliation	Deep-Slow	0.199	0.158	0.082	0.067	0.139	0.121	0.028	0.794	0.792	0.9980
	3rd defoliation	Medium	0.199	0.154	0.085	0.072	0.141	0.124	0.022	0.766	0.776	0.9976
	3rd defoliation	Shallow-Fast	0.186	0.148	0.087	0.070	0.150	0.119	0.035	0.725	0.768	0.9971
Cedar	Full foliage	Deep-Slow	0.332	0.333	0.176	0.165	0.303	0.279	0.032	0.533	0.512	0.9951
	Full foliage	Medium	0.345	0.329	0.176	0.166	0.311	0.293	0.025	0.550	0.511	0.9947
	Full foliage	Shallow-Fast	0.351	0.332	0.151	0.153	0.296	0.299	0.012	0.633	0.648	0.9963
	1st defoliation	Deep-Slow	0.336	0.314	0.164	0.154	0.303	0.262	0.026	0.568	0.523	0.9952
	1st defoliation	Medium	0.342	0.313	0.174	0.156	0.307	0.268	0.021	0.545	0.522	0.9946
	1st defoliation	Shallow-Fast	0.330	0.306	0.131	0.132	0.272	0.277	0.017	0.660	0.631	0.9959
	2nd defoliation	Deep-Slow	0.326	0.290	0.148	0.126	0.284	0.245	0.005	0.603	0.578	0.9953
	2nd defoliation	Medium	0.321	0.288	0.152	0.132	0.275	0.252	0.041	0.572	0.557	0.9946
	2nd defoliation	Shallow-Fast	0.321	0.283	0.132	0.116	0.260	0.250	0.041	0.655	0.650	0.9961
	3rd defoliation	Deep-Slow	0.229	0.210	0.095	0.086	0.176	0.158	0.036	0.750	0.711	0.9976
	3rd defoliation	Medium	0.237	0.210	0.108	0.093	0.179	0.166	0.018	0.712	0.700	0.9972
	3rd defoliation	Shallow-Fast	0.219	0.213	0.098	0.094	0.185	0.173	0.035	0.673	0.686	0.9965
Fig	Full foliage	Deep-Slow	0.279	0.366	0.128	0.157	0.230	0.297	0.032	0.703	0.698	0.9980
	Full foliage	Medium	0.298	0.385	0.123	0.141	0.228	0.250	0.031	0.731	0.763	0.9983
	Full foliage	Shallow-Fast	0.269	0.302	0.132	0.128	0.231	0.229	0.024	0.753	0.780	0.9982
	1st defoliation	Deep-Slow	0.279	0.353	0.106	0.127	0.212	0.256	0.025	0.751	0.754	0.9985
	1st defoliation	Medium	0.255	0.313	0.132	0.146	0.210	0.240	0.023	0.728	0.714	0.9981
	1st defoliation	Shallow-Fast	0.242	0.310	0.103	0.112	0.210	0.228	0.019	0.681	0.718	0.9976
	2nd defoliation	Deep-Slow	0.262	0.346	0.125	0.164	0.206	0.279	0.026	0.788	0.809	0.9987
	2nd defoliation	Medium	0.266	0.352	0.119	0.151	0.200	0.271	0.024	0.800	0.827	0.9988
	2nd defoliation	Shallow-Fast	0.261	0.310	0.098	0.109	0.177	0.253	0.018	0.789	0.825	0.9984
	3rd defoliation	Deep-Slow	0.182	0.218	0.060	0.086	0.107	0.166	0.012	0.904	0.910	0.9993
	3rd defoliation	Medium	0.180	0.214	0.073	0.093	0.118	0.163	0.021	0.890	0.910	0.9992
	3rd defoliation	Shallow-Fast	0.166	0.189	0.069	0.079	0.115	0.150	0.018	0.892	0.908	0.9992
Grass	Full foliage	Deep-Slow	0.336	0.245	0.125	0.095	0.264	0.191	0.014	0.703	0.732	0.9980
	Full foliage	Medium	0.311	0.266	0.124	0.107	0.252	0.208	0.005	0.702	0.762	0.9981
	Full foliage	Shallow-Fast	0.300	0.250	0.103	0.090	0.197	0.152	0.027	0.712	0.790	0.9980
	1st defoliation	Deep-Slow	0.330	0.269	0.113	0.098	0.260	0.195	0.024	0.746	0.782	0.9985
	1st defoliation	Medium	0.334	0.293	0.142	0.127	0.290	0.243	0.023	0.710	0.778	0.9983
	1st defoliation	Shallow-Fast	0.326	0.306	0.139	0.131	0.289	0.243	0.015	0.720	0.810	0.9983
	2nd defoliation	Deep-Slow	0.309	0.255	0.119	0.089	0.267	0.176	0.026	0.708	0.749	0.9981
	2nd defoliation	Medium	0.333	0.246	0.117	0.085	0.263	0.169	0.026	0.735	0.771	0.9982
	2nd defoliation	Shallow-Fast	0.313	0.198	0.117	0.085	0.236	0.138	0.024	0.780	0.807	0.9982
	3rd defoliation	Deep-Slow	0.285	0.257	0.133	0.094	0.224	0.181	0.017	0.753	0.816	0.9985
	3rd defoliation	Medium	0.292	0.254	0.127	0.087	0.221	0.184	0.019	0.753	0.815	0.9984
	3rd defoliation	Shallow-Fast	0.295	0.255	0.112	0.081	0.222	0.155	0.015	0.766	0.855	0.9985
Scots Pine	Full foliage	Deep-Slow	0.364	0.330	0.171	0.167	0.298	0.274	0.014	0.598	0.632	0.9973
	Full foliage	Medium	0.351	0.323	0.182	0.176	0.306	0.274	0.019	0.581	0.644	0.9971
	Full foliage	Shallow-Fast	0.357	0.308	0.159	0.149	0.298	0.270	0.018	0.622	0.717	0.9973
	2nd defoliation	Deep-Slow	0.358	0.355	0.169	0.168	0.274	0.285	0.012	0.642	0.656	0.9976
	2nd defoliation	Medium	0.357	0.350	0.158	0.149	0.264	0.271	0.010	0.637	0.685	0.9976
	2nd defoliation	Shallow-Fast	0.359	0.337	0.179	0.170	0.290	0.289	0.014	0.623	0.730	0.9975
	3rd defoliation	Deep-Slow	0.342	0.319	0.141	0.118	0.267	0.229	0.015	0.649	0.730	0.9977
	3rd defoliation	Medium	0.345	0.320	0.156	0.139	0.271	0.233	0.011	0.636	0.742	0.9976
	3rd defoliation	Shallow-Fast	0.342	0.318	0.169	0.146	0.269	0.243	0.004	0.637	0.760	0.9975

TABLE E.2: Plant structure metrics extracted from the standard TLS data

Plant scenario		Flow	standard									
			W_{max}	L_{max}	$\overline{W}$	$\overline{L}$	W_{80}	L_{80}	A_f	P_{2D}	P_{2Dpf}	P_{3D}
Bamboo	Full foliage	Deep-Slow	0.376	0.383	0.184	0.125	0.336	0.251	0.060	0.507	0.690	0.9972
	Full foliage	Medium	0.361	0.284	0.172	0.101	0.320	0.171	0.055	0.530	0.672	0.9966
	Full foliage	Shallow-Fast	0.361	0.226	0.169	0.091	0.315	0.154	0.048	0.596	0.712	0.9967
	1st defoliation	Deep-Slow	0.381	0.273	0.173	0.107	0.321	0.188	0.021	0.566	0.657	0.9967
	1st defoliation	Medium	0.363	0.250	0.160	0.095	0.266	0.155	0.051	0.590	0.695	0.9967
	1st defoliation	Shallow-Fast	0.355	0.208	0.155	0.090	0.261	0.144	0.044	0.640	0.723	0.9966
	2nd defoliation	Deep-Slow	0.269	0.303	0.116	0.106	0.203	0.200	0.039	0.590	0.690	0.9971
	2nd defoliation	Medium	0.269	0.303	0.111	0.095	0.188	0.165	0.047	0.619	0.745	0.9974
	2nd defoliation	Shallow-Fast	0.269	0.240	0.115	0.091	0.182	0.153	0.044	0.659	0.771	0.9972
	3rd defoliation	Deep-Slow	0.209	0.164	0.087	0.067	0.142	0.120	0.041	0.758	0.748	0.9970
	3rd defoliation	Medium	0.209	0.159	0.088	0.072	0.144	0.126	0.032	0.737	0.755	0.9967
	3rd defoliation	Shallow-Fast	0.186	0.147	0.094	0.074	0.148	0.119	0.056	0.690	0.737	0.9957
Cedar	Full foliage	Deep-Slow	0.372	0.351	0.199	0.181	0.338	0.308	0.050	0.488	0.446	0.9935
	Full foliage	Medium	0.372	0.351	0.210	0.180	0.339	0.311	0.034	0.453	0.455	0.9929
	Full foliage	Shallow-Fast	0.372	0.351	0.191	0.163	0.338	0.310	0.015	0.514	0.549	0.9944
	1st defoliation	Deep-Slow	0.369	0.339	0.201	0.183	0.329	0.282	0.042	0.522	0.476	0.9936
	1st defoliation	Medium	0.369	0.339	0.220	0.185	0.333	0.290	0.035	0.478	0.481	0.9929
	1st defoliation	Shallow-Fast	0.369	0.339	0.211	0.174	0.336	0.295	0.025	0.519	0.547	0.9939
	2nd defoliation	Deep-Slow	0.346	0.289	0.156	0.126	0.296	0.242	0.006	0.545	0.533	0.9932
	2nd defoliation	Medium	0.346	0.289	0.162	0.134	0.299	0.246	0.053	0.507	0.534	0.9924
	2nd defoliation	Shallow-Fast	0.344	0.289	0.160	0.125	0.301	0.251	0.051	0.518	0.566	0.9932
	3rd defoliation	Deep-Slow	0.240	0.197	0.076	0.064	0.166	0.147	0.045	0.708	0.637	0.9959
	3rd defoliation	Medium	0.240	0.197	0.084	0.067	0.171	0.152	0.020	0.675	0.640	0.9954
	3rd defoliation	Shallow-Fast	0.240	0.189	0.085	0.065	0.180	0.154	0.043	0.667	0.660	0.9951
Fig	Full foliage	Deep-Slow	0.363	0.329	0.151	0.122	0.292	0.269	0.038	0.618	0.684	0.9972
	Full foliage	Medium	0.363	0.321	0.144	0.108	0.300	0.242	0.034	0.646	0.750	0.9976
	Full foliage	Shallow-Fast	0.363	0.310	0.142	0.097	0.324	0.200	0.035	0.678	0.799	0.9978
	1st defoliation	Deep-Slow	0.360	0.322	0.138	0.104	0.236	0.211	0.033	0.673	0.741	0.9978
	1st defoliation	Medium	0.360	0.322	0.136	0.097	0.246	0.213	0.031	0.670	0.766	0.9977
	1st defoliation	Shallow-Fast	0.360	0.307	0.146	0.093	0.261	0.178	0.024	0.677	0.802	0.9977
	2nd defoliation	Deep-Slow	0.323	0.306	0.111	0.100	0.215	0.219	0.042	0.730	0.787	0.9982
	2nd defoliation	Medium	0.323	0.306	0.113	0.097	0.256	0.225	0.038	0.734	0.810	0.9982
	2nd defoliation	Shallow-Fast	0.318	0.290	0.115	0.088	0.263	0.198	0.025	0.739	0.835	0.9982
	3rd defoliation	Deep-Slow	0.183	0.226	0.046	0.068	0.093	0.145	0.014	0.891	0.914	0.9991
	3rd defoliation	Medium	0.177	0.222	0.045	0.065	0.089	0.140	0.032	0.884	0.919	0.9990
	3rd defoliation	Shallow-Fast	0.164	0.188	0.047	0.058	0.090	0.121	0.029	0.880	0.917	0.9988
Grass	Full foliage	Deep-Slow	0.416	0.382	0.153	0.130	0.349	0.288	0.021	0.624	0.745	0.9980
	Full foliage	Medium	0.376	0.382	0.133	0.113	0.288	0.261	0.005	0.625	0.769	0.9980
	Full foliage	Shallow-Fast	0.361	0.382	0.125	0.107	0.240	0.225	0.038	0.679	0.836	0.9983
	1st defoliation	Deep-Slow	0.398	0.309	0.135	0.105	0.313	0.228	0.038	0.633	0.698	0.9974
	1st defoliation	Medium	0.385	0.304	0.116	0.093	0.238	0.189	0.035	0.654	0.734	0.9976
	1st defoliation	Shallow-Fast	0.346	0.256	0.099	0.081	0.187	0.144	0.016	0.686	0.755	0.9974
	2nd defoliation	Deep-Slow	0.327	0.350	0.143	0.130	0.302	0.282	0.033	0.596	0.705	0.9975
	2nd defoliation	Medium	0.326	0.343	0.121	0.107	0.264	0.196	0.029	0.633	0.754	0.9977
	2nd defoliation	Shallow-Fast	0.297	0.259	0.094	0.078	0.191	0.159	0.027	0.685	0.771	0.9975
	3rd defoliation	Deep-Slow	0.321	0.304	0.141	0.120	0.277	0.241	0.023	0.678	0.776	0.9978
	3rd defoliation	Medium	0.307	0.271	0.116	0.099	0.209	0.180	0.022	0.700	0.800	0.9977
	3rd defoliation	Shallow-Fast	0.241	0.221	0.087	0.073	0.147	0.131	0.019	0.688	0.801	0.9971
Scots Pine	Full foliage	Deep-Slow	0.373	0.337	0.154	0.147	0.302	0.251	0.016	0.551	0.595	0.9968
	Full foliage	Medium	0.373	0.337	0.156	0.144	0.318	0.258	0.029	0.539	0.621	0.9968
	Full foliage	Shallow-Fast	0.373	0.337	0.160	0.147	0.331	0.276	0.026	0.558	0.682	0.9970
	2nd defoliation	Deep-Slow	0.340	0.342	0.149	0.150	0.267	0.287	0.018	0.573	0.586	0.9966
	2nd defoliation	Medium	0.340	0.342	0.156	0.156	0.279	0.290	0.011	0.556	0.607	0.9964
	2nd defoliation	Shallow-Fast	0.340	0.342	0.164	0.169	0.287	0.293	0.024	0.566	0.660	0.9965
	3rd defoliation	Deep-Slow	0.345	0.324	0.144	0.125	0.261	0.228	0.023	0.619	0.720	0.9971
	3rd defoliation	Medium	0.345	0.324	0.156	0.130	0.266	0.242	0.017	0.597	0.737	0.9970
	3rd defoliation	Shallow-Fast	0.345	0.314	0.170	0.145	0.267	0.252	0.004	0.596	0.753	0.9969

Appendix F

Regression Plots

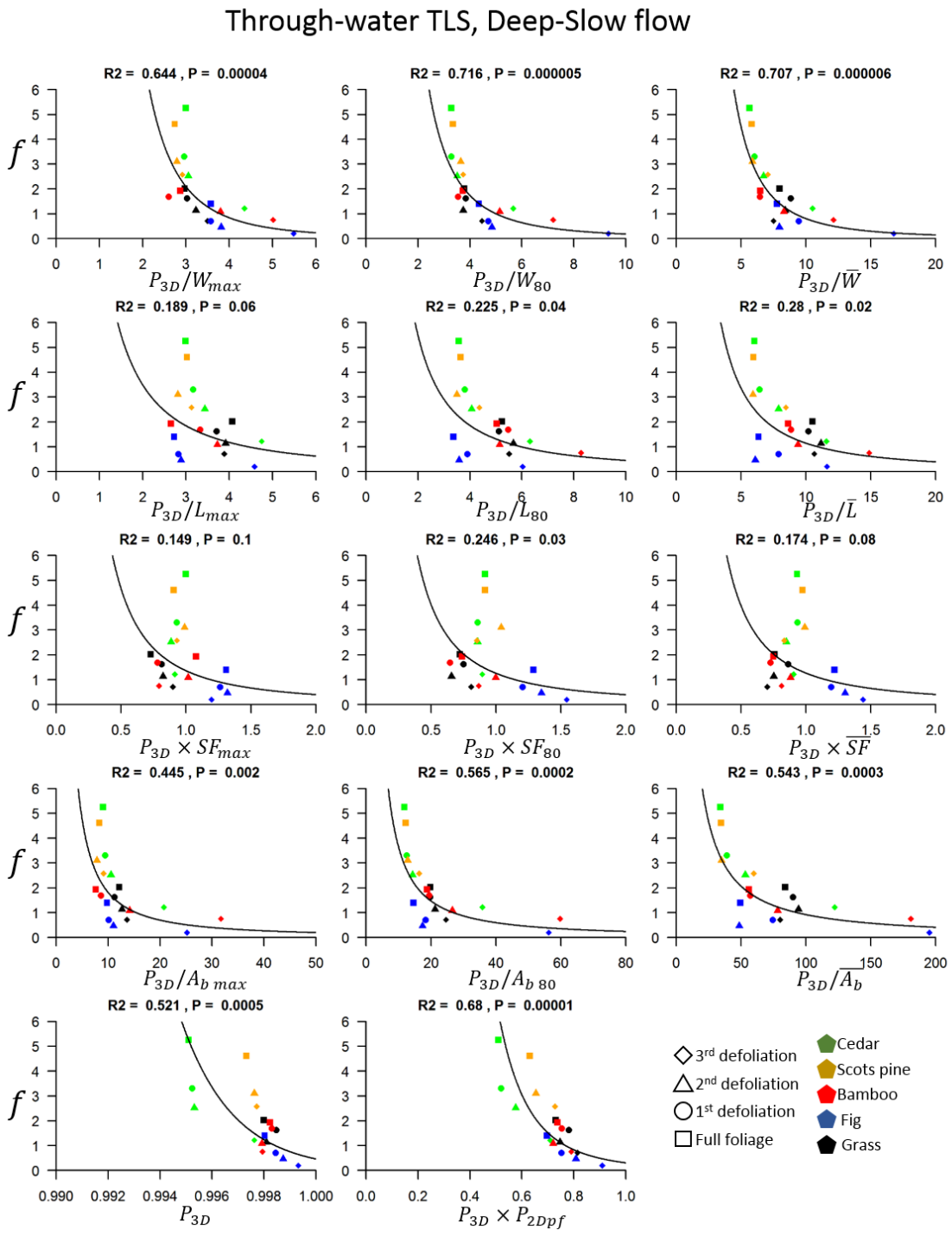

FIGURE F.1: Regression plots for all bulk 3D plant structure metric combinations extracted from the through-water TLS datasest, against the hydraulic roughness for the Deep-Slow flow scenario.

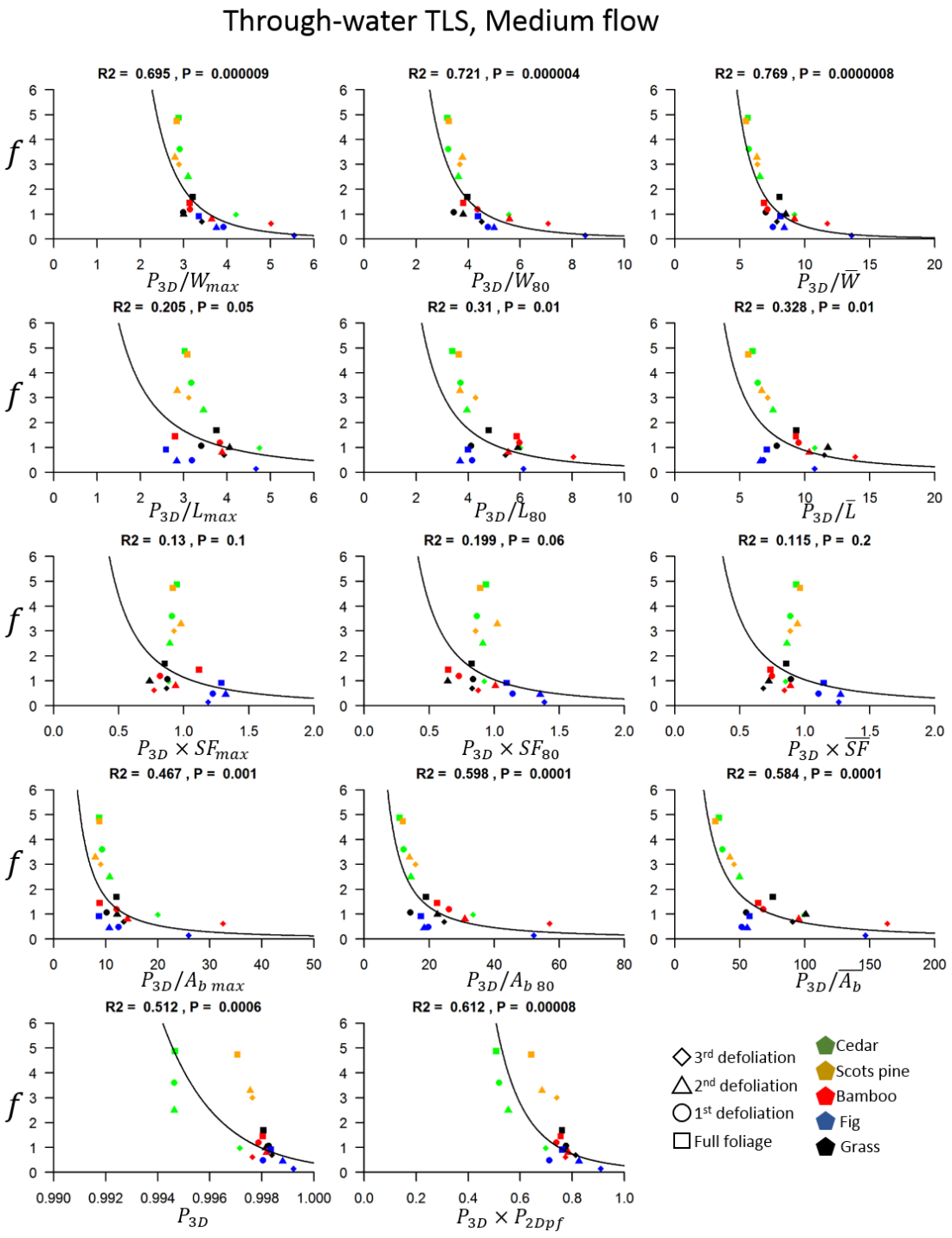

FIGURE F.2: Regression plots for all bulk 3D plant structure metric combinations extracted from the through-water TLS datasest, against the hydraulic roughness for the Medium flow scenario.

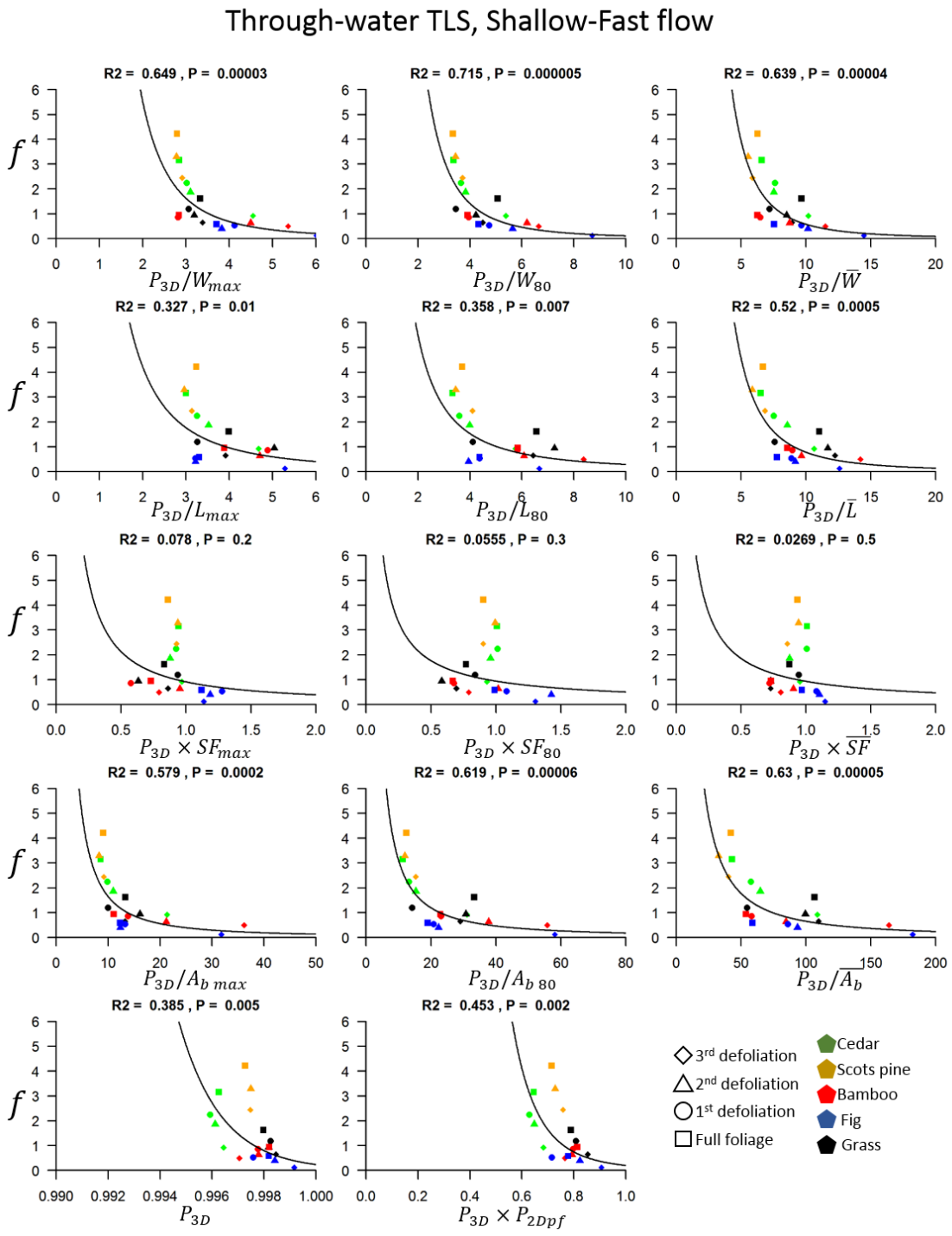

FIGURE F.3: Regression plots for all bulk 3D plant structure metric combinations extracted from the through-water TLS datasest, against the hydraulic roughness for the Shallow-Fast flow scenario.

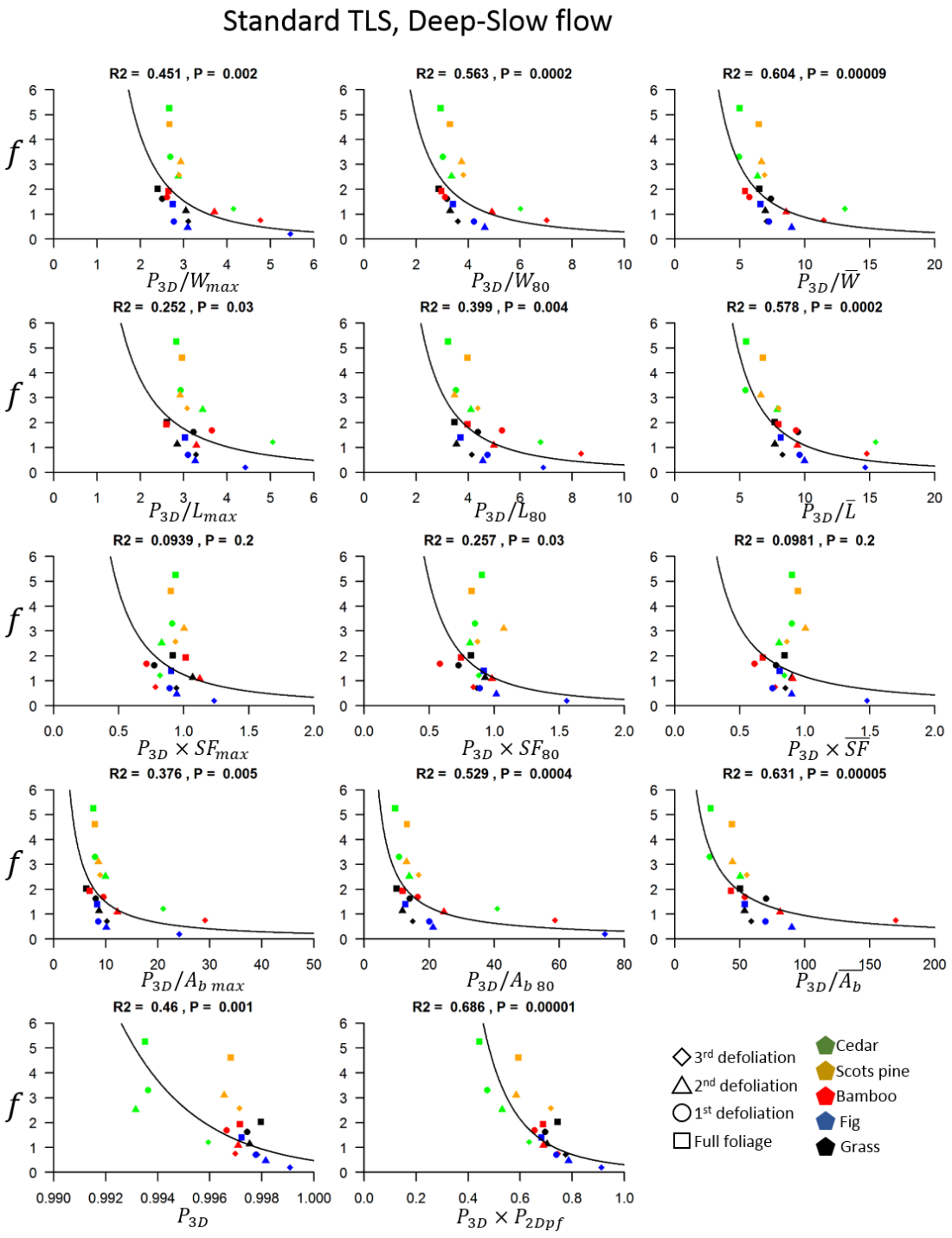

FIGURE F.4: Regression plots for all bulk 3D plant structure metric combinations extracted from the standard TLS datasest, against the hydraulic roughness for the Deep-Slow flow scenario.

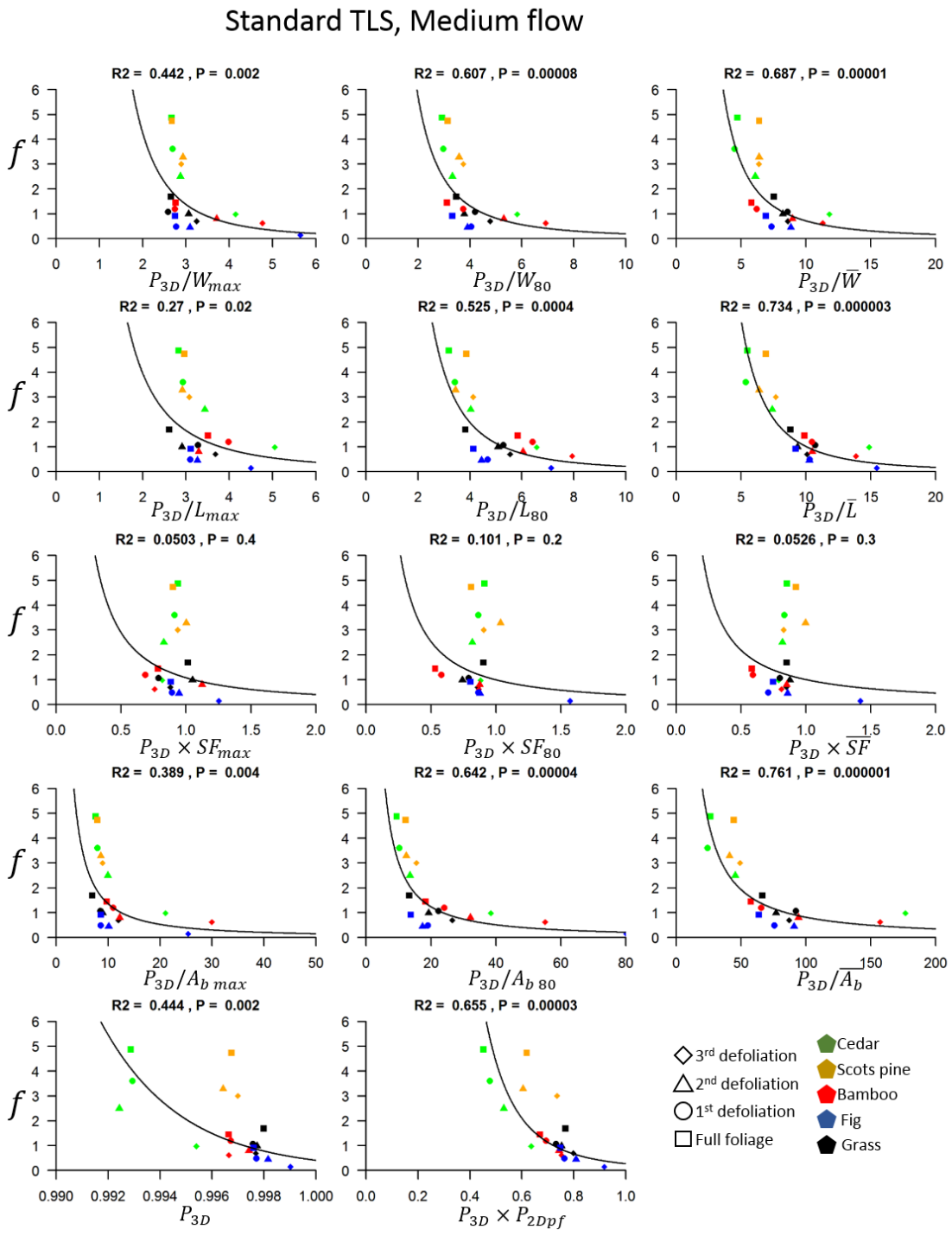

FIGURE F.5: Regression plots for all bulk 3D plant structure metric combinations extracted from the standard TLS datasest, against the hydraulic roughness for the Medium flow scenario.

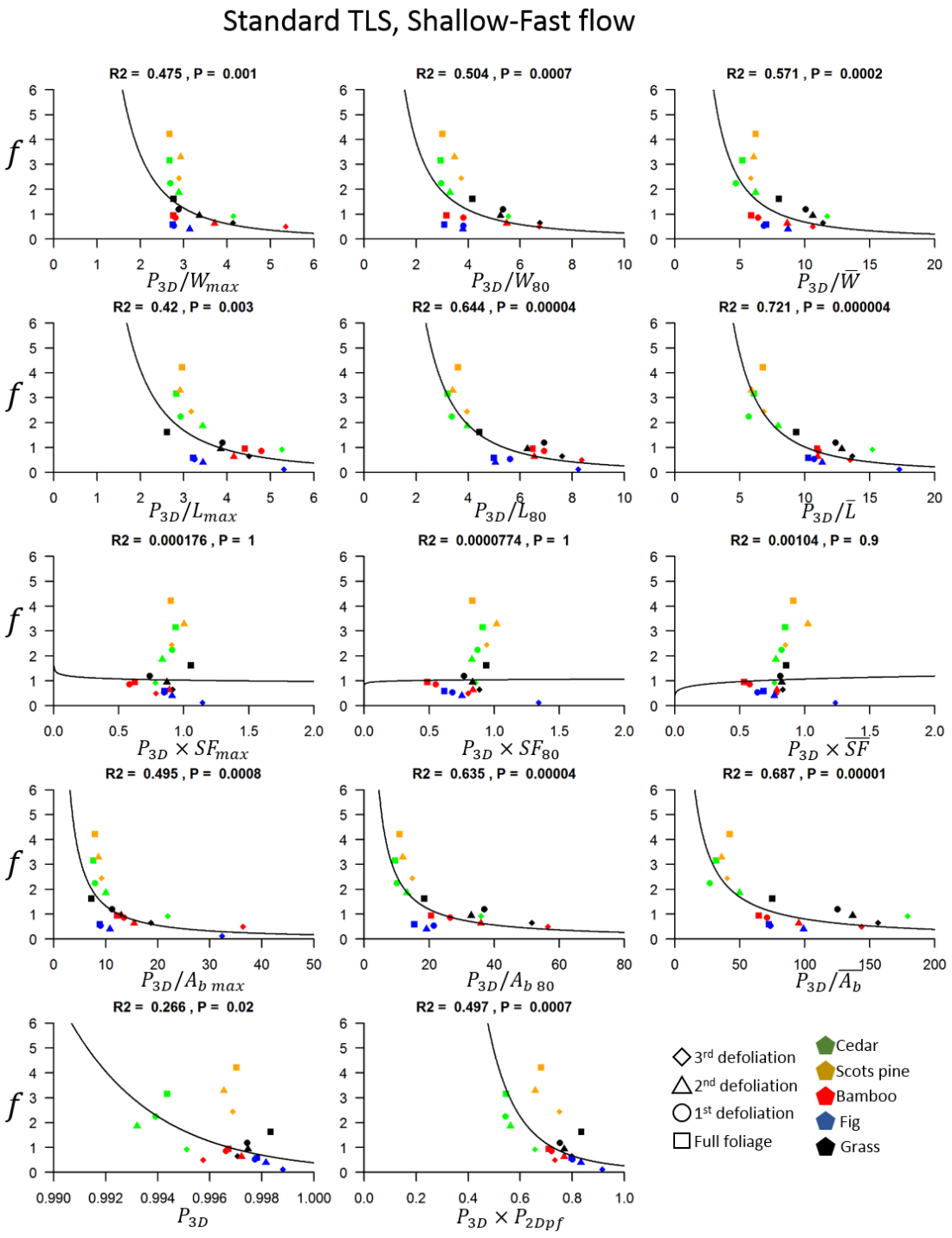

FIGURE F.6: Regression plots for all bulk 3D plant structure metric combinations extracted from the standard TLS datasest, against the hydraulic roughness for the Shallow-Fast flow scenario.

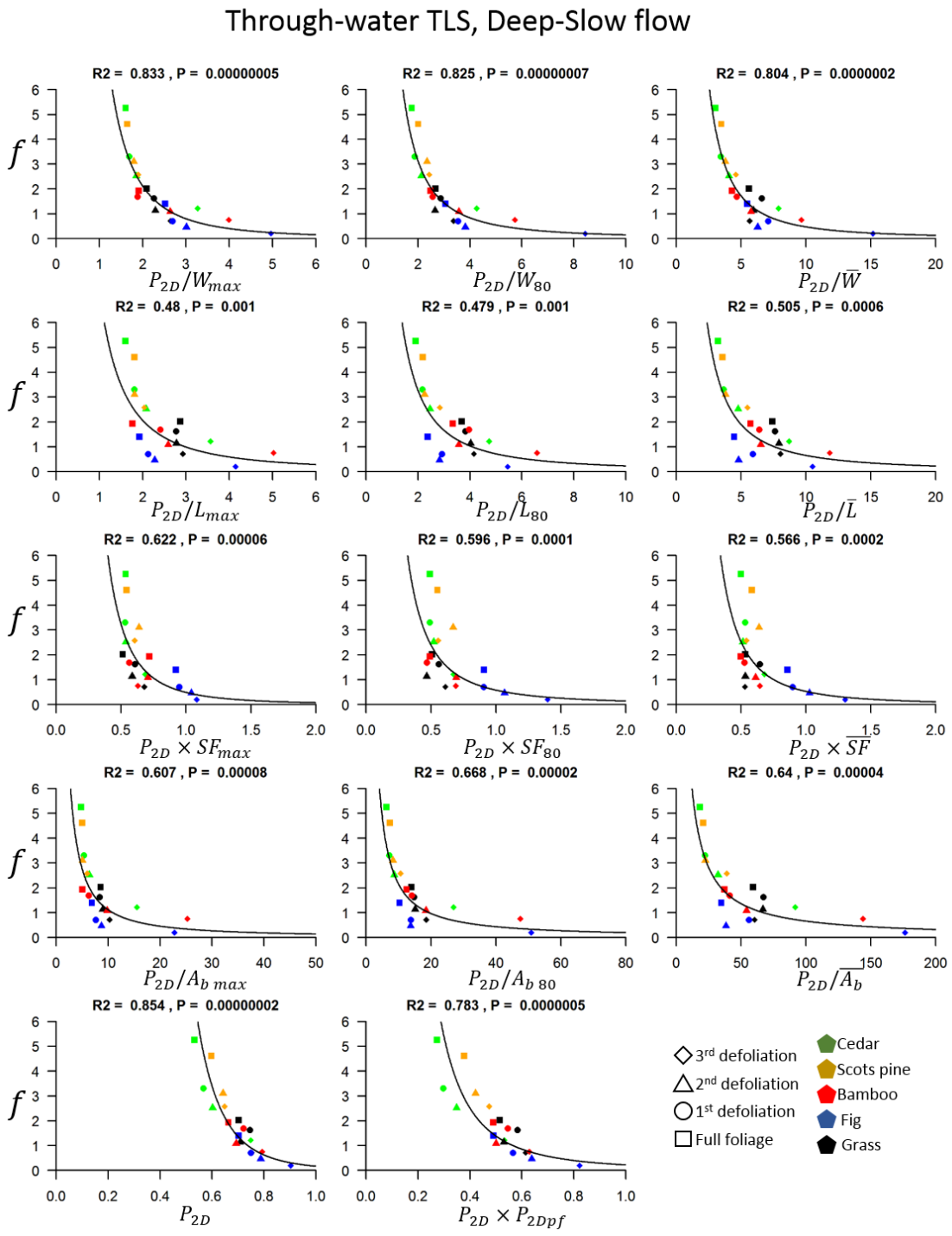

FIGURE F.7: Regression plots for all bulk 2D plant structure metric combinations extracted from the through-water TLS datasest, against the hydraulic roughness for the Deep-Slow flow scenario.

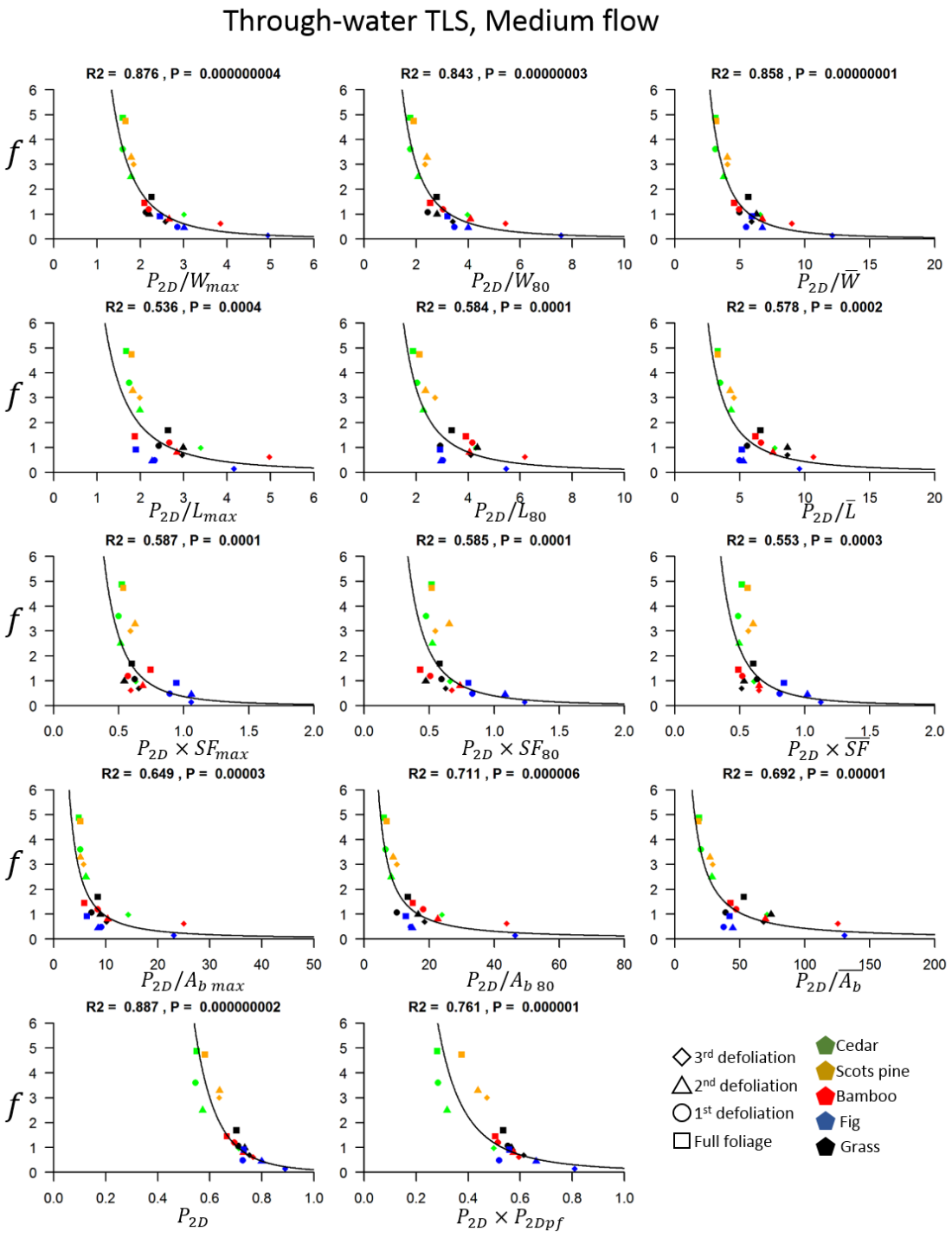

FIGURE F.8: Regression plots for all bulk 2D plant structure metric combinations extracted from the through-water TLS datasest, against the hydraulic roughness for the Medium flow scenario.

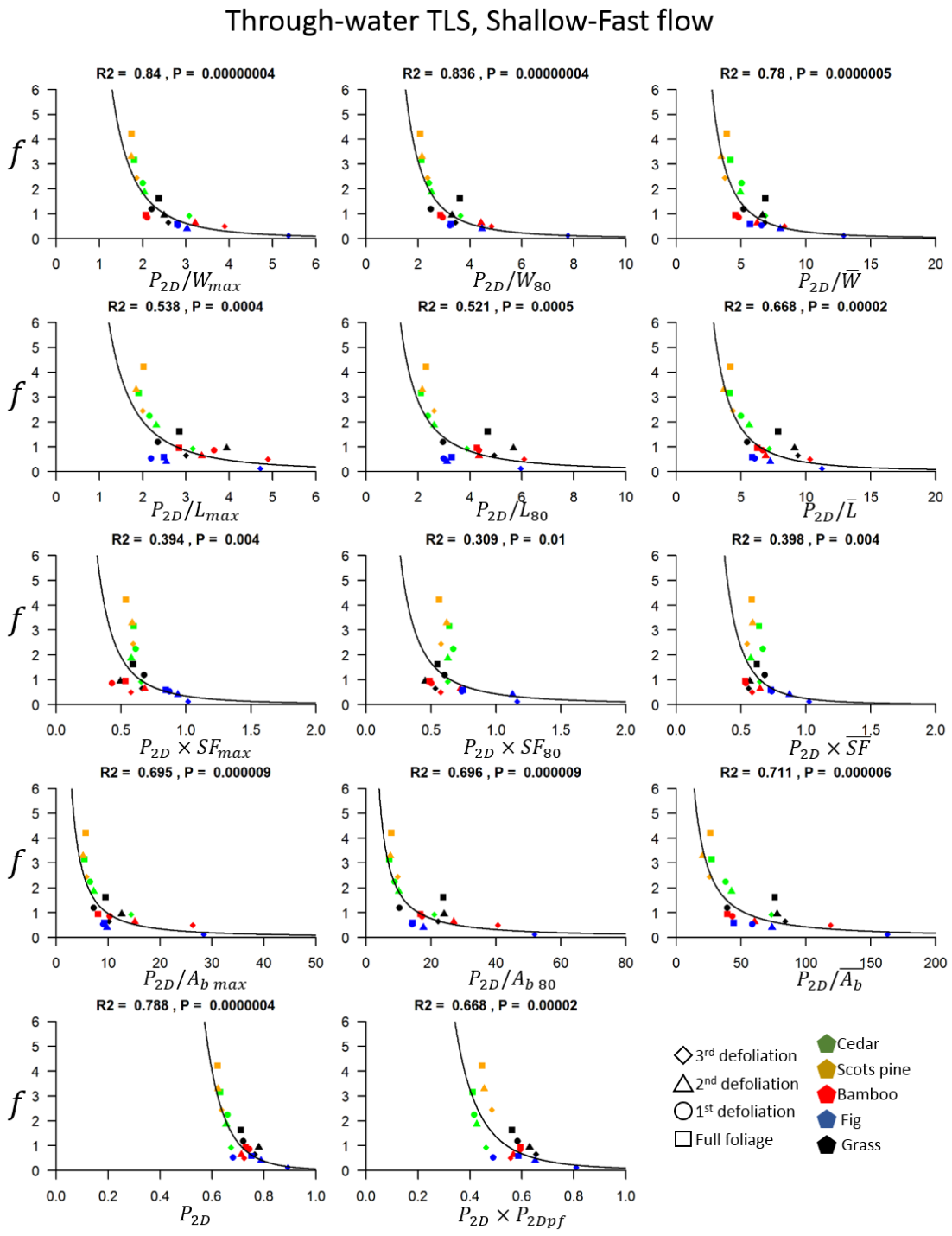

FIGURE F.9: Regression plots for all bulk 2D plant structure metric combinations extracted from the through-water TLS datasest, against the hydraulic roughness for the Shallow-Fast flow scenario.

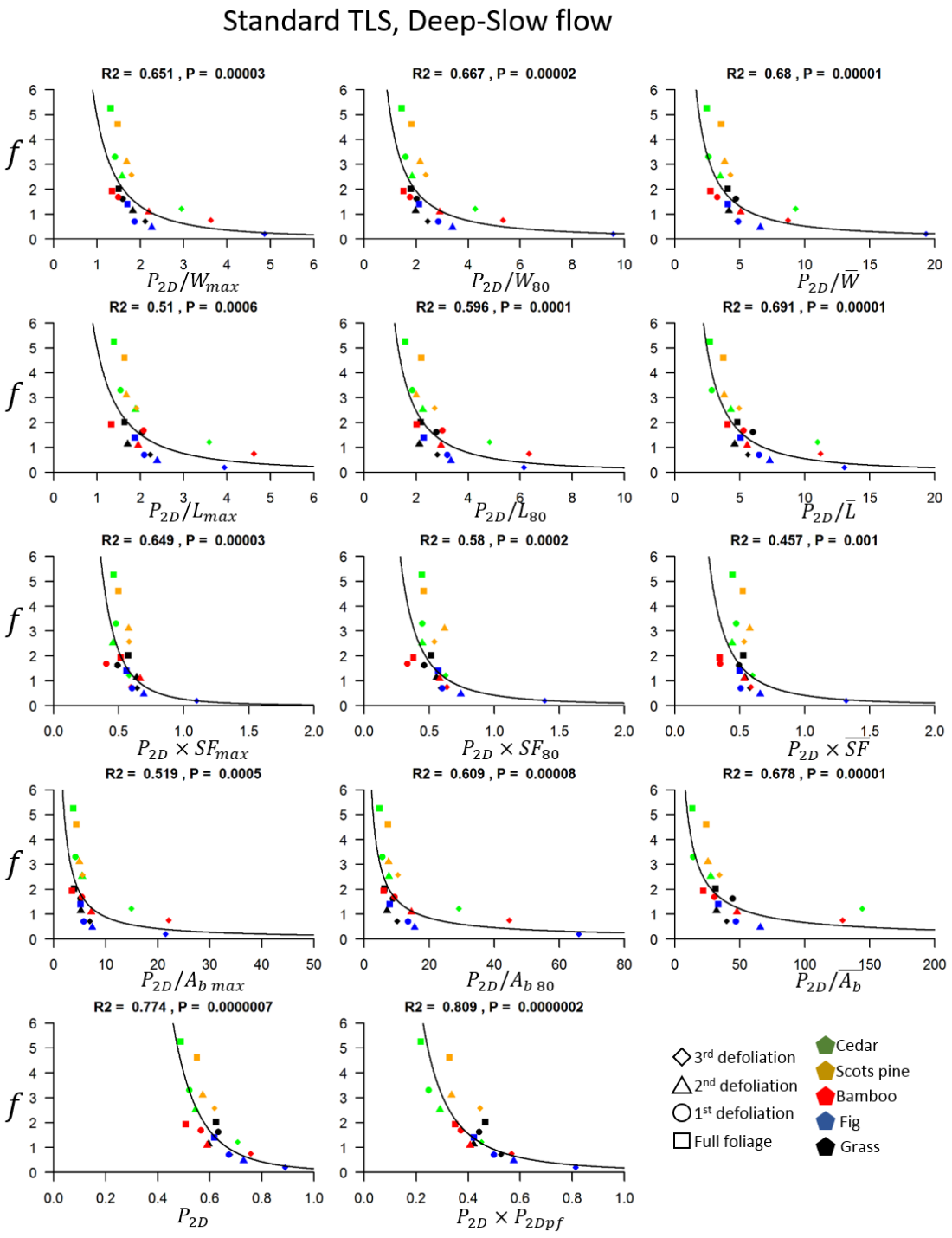

FIGURE F.10: Regression plots for all bulk 2D plant structure metric combinations extracted from the standard TLS datasest, against the hydraulic roughness for the Deep-Slow flow scenario.

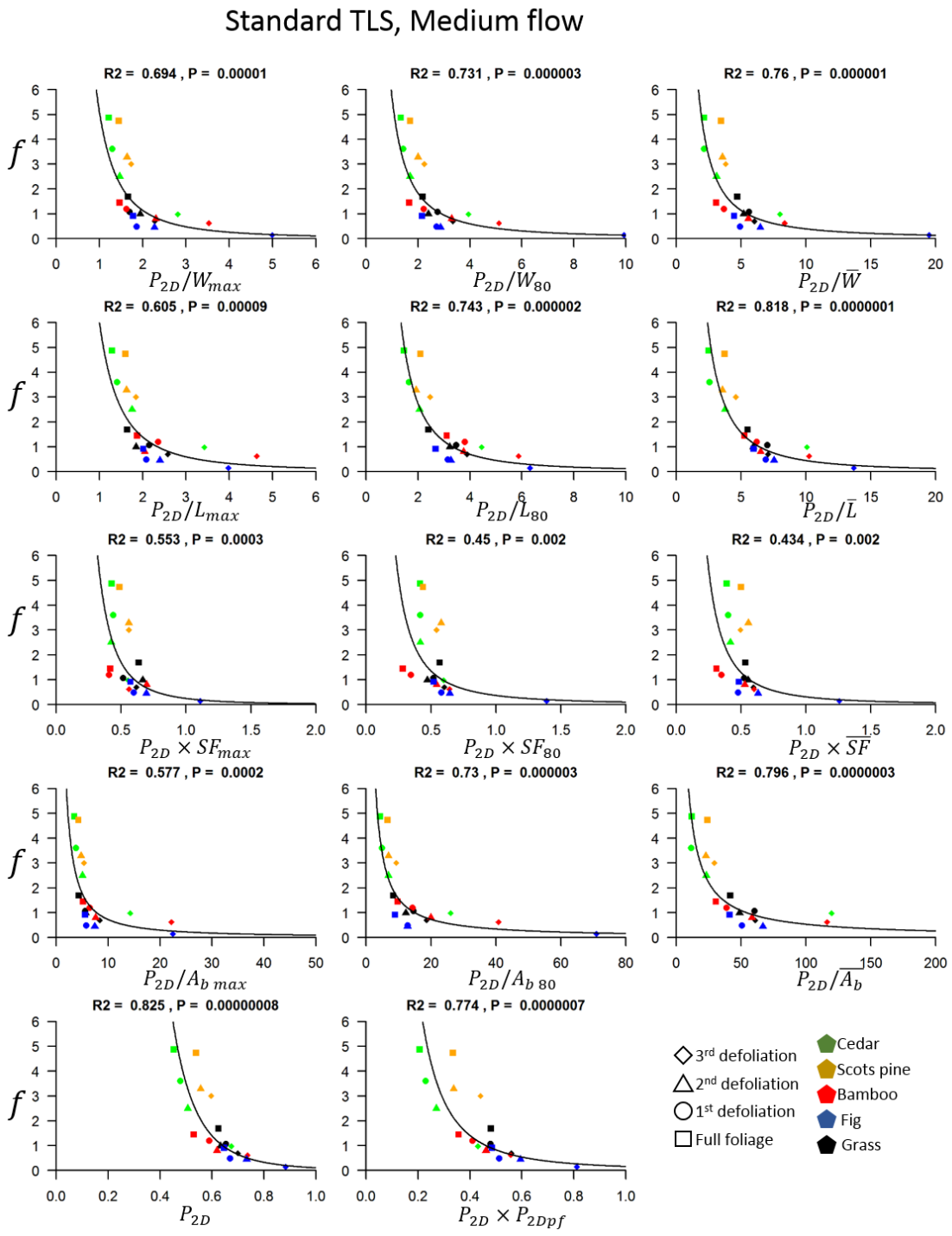

FIGURE F.11: Regression plots for all bulk 2D plant structure metric combinations extracted from the standard TLS datasest, against the hydraulic roughness for the Medium flow scenario.

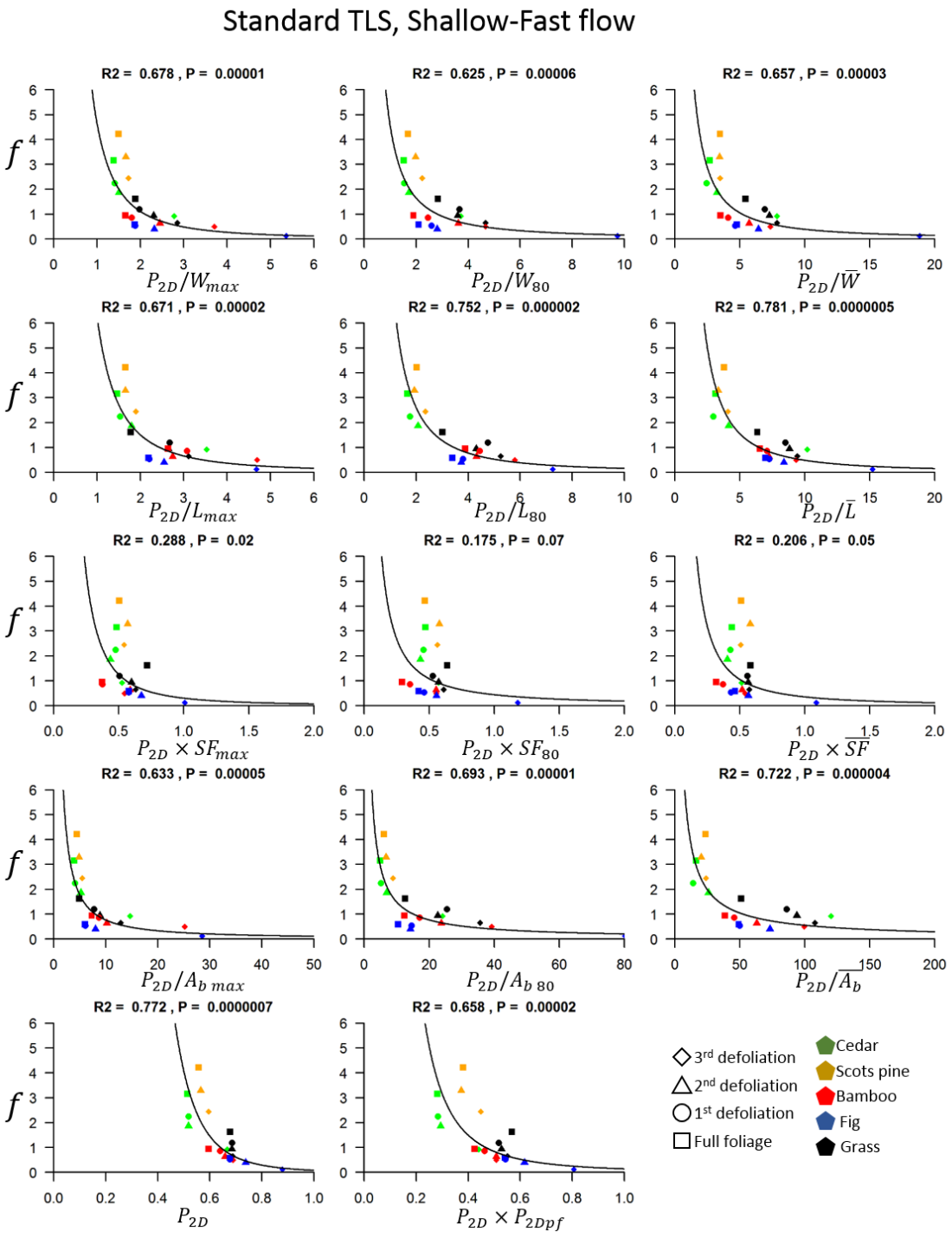

FIGURE F.12: Regression plots for all bulk 2D plant structure metric combinations extracted from the standard TLS datasest, against the hydraulic roughness for the Shallow-Fast flow scenario.

Appendix G

Theil-Sen Regression Results

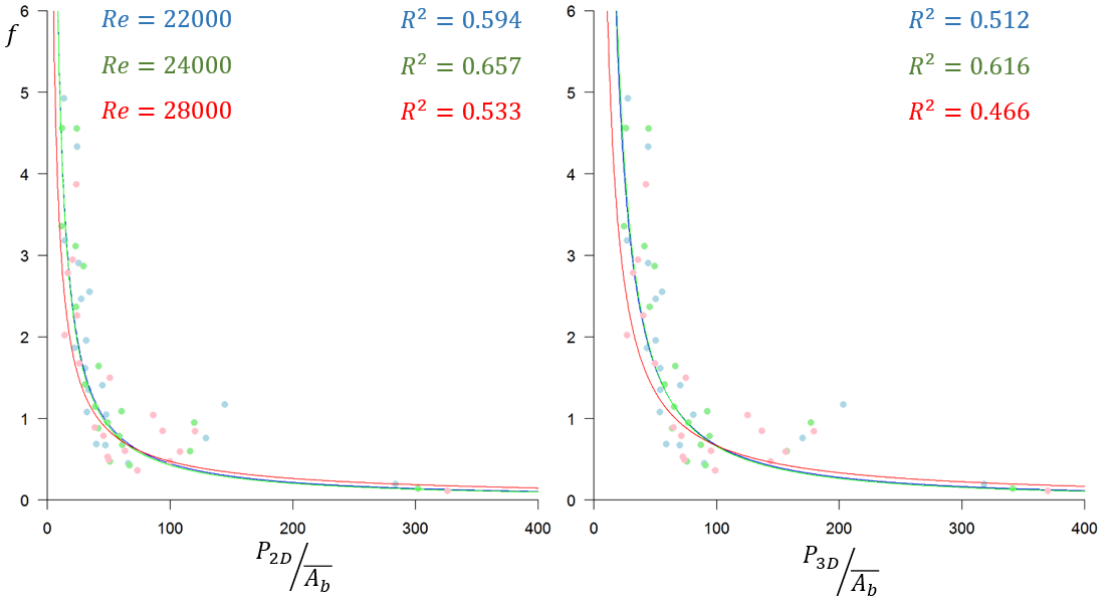

FIGURE G.1: Theil-Sen regression plots relating plant structure and bulk hydraulic roughness using Equations (6.7) and (6.8).

```
Kendall-Theil Robust Line (KTRLine--version 1.0) Output:


*****************************************
2D Metric| Standard TLS | Deep-Slow Flow
*****************************************

Independent Variable (X): 2.608348232
Dependent Variable (Y): 1.594580493
********************
Linear model all data:
 Number of points: 19 Number of pairs: 171
```

```
 Number of ties in X: 0
 Minimum X: 2.608348
 Maximum X: 5.647548
 Minimum Y: -1.637889
 Maximum Y: 1.594581
 Median of X's: 3.511184
 Median of Y's: 0.3435577
 Median of Slopes: -1.051214
  Upper 95th percent confidence interval of slope: -0.6494313
  Lower 95th percent confidence interval of slope: -1.623095
 Linear intercept: 4.034564
 Kendall-Theil Line for all linear data: Y = 4.034564 + -1.051214 * X
Information on independent random errors (deviations from line):
 Median Deviation (error): 0.2643294
 Median Absolute Deviation (error) (MAD): 0.3100368
 Root Mean Square Error (RMSE): 0.5353453
 NonParametric PRediction Error Sum of Squares (NPPRESS): 7.118544
 Bias Correction Factor (BCF): 0.1934813
Note: This is a Duan (1983) smearing estimator.
********************

****************************************
2D Metric| Standard TLS | Medium Flow
****************************************

Independent Variable (X): 2.482767237
Dependent Variable (Y): 1.517693112
********************
Linear model all data:
 Number of points: 19 Number of pairs: 171
 Number of ties in X: 0
 Minimum X: 2.464984
 Maximum X: 5.710702
 Minimum Y: -1.973305
 Maximum Y: 1.517693
 Median of X's: 3.728883
 Median of Y's: 8.592172E-02
 Median of Slopes: -1.06603
  Upper 95th percent confidence interval of slope: -0.7903346
  Lower 95th percent confidence interval of slope: -1.472726
 Linear intercept: 4.061022
 Kendall-Theil Line for all linear data: Y = 4.061022 + -1.06603 * X
```

```
Information on independent random errors (deviations from line):
 Median Deviation (error): 5.345106E-02
 Median Absolute Deviation (error) (MAD): 0.2233011
 Root Mean Square Error (RMSE): 0.4553238
 NonParametric PRediction Error Sum of Squares (NPPRESS): 4.384633
 Bias Correction Factor (BCF): 0.1525632
Note: This is a Duan (1983) smearing estimator.
********************

****************************************
2D Metric| Standard TLS | Shallow-Fast Flow
****************************************

Independent Variable (X): 2.802690551
Dependent Variable (Y): 1.025124351
********************
Linear model all data:
 Number of points: 19 Number of pairs: 171
 Number of ties in X: 0
 Minimum X: 2.649626
 Maximum X: 5.786419
 Minimum Y: -2.161158
 Maximum Y: 1.353466
 Median of X's: 3.912059
 Median of Y's: -0.1626274
 Median of Slopes: -0.8425888
  Upper 95th percent confidence interval of slope: -0.5496904
  Lower 95th percent confidence interval of slope: -1.237258
 Linear intercept: 3.13363
 Kendall-Theil Line for all linear data: Y = 3.13363 + -0.8425888 * X
Information on independent random errors (deviations from line):
 Median Deviation (error):   0.1273047
 Median Absolute Deviation (error) (MAD): 0.4192152
 Root Mean Square Error (RMSE): 0.4865377
 NonParametric PRediction Error Sum of Squares (NPPRESS): 5.078016
 Bias Correction Factor (BCF): 0.1201724
Note: This is a Duan (1983) smearing estimator.
********************

****************************************
3D Metric| Standard TLS | Deep-Slow Flow
****************************************
```

```
Independent Variable (X): 3.319013492
Dependent Variable (Y): 1.594580493
********************
Linear model all data:
 Number of points: 19 Number of pairs: 171
 Number of ties in X: 0
 Minimum X: 3.299445
 Maximum X: 5.762496
 Minimum Y: -1.637889
 Maximum Y: 1.594581
 Median of X's: 3.990183
 Median of Y's: 0.3435577
 Median of Slopes: -1.238111
  Upper 95th percent confidence interval of slope: -0.7006838
  Lower 95th percent confidence interval of slope: -2.025219
 Linear intercept: 5.283846
 Kendall-Theil Line for all linear data: Y = 5.283846 + -1.238111 * X
Information on independent random errors (deviations from line):
 Median Deviation (error): 0.2128741
 Median Absolute Deviation (error) (MAD): 0.4200411
 Root Mean Square Error (RMSE): 0.5788697
 NonParametric PRediction Error Sum of Squares (NPPRESS): 8.540751
 Bias Correction Factor (BCF): 0.2285775
Note: This is a Duan (1983) smearing estimator.
********************


****************************************
3D Metric| Standard TLS | Medium Flow
****************************************

Independent Variable (X): 3.267950461
Dependent Variable (Y): 1.517693112
********************
Linear model all data:
 Number of points: 19 Number of pairs: 171
 Number of ties in X: 0
 Minimum X: 3.196093
 Maximum X: 5.832554
 Minimum Y: -1.973305
 Maximum Y: 1.517693
 Median of X's: 4.196759
```

```
 Median of Y's: 8.592172E-02
 Median of Slopes: -1.291698
  Upper 95th percent confidence interval of slope: -0.8518212
  Lower 95th percent confidence interval of slope: -1.841101
 Linear intercept: 5.506865
 Kendall-Theil Line for all linear data: Y = 5.506865 + -1.291698 * X
Information on independent random errors (deviations from line):
 Median Deviation (error): 0.1241167
 Median Absolute Deviation (error) (MAD): 0.2886847
 Root Mean Square Error (RMSE): 0.4993356
 NonParametric PRediction Error Sum of Squares (NPPRESS): 5.412227
 Bias Correction Factor (BCF): 0.1847628
Note: This is a Duan (1983) smearing estimator.
********************

****************************************
3D Metric| Standard TLS | Shallow-Fast Flow
****************************************

Independent Variable (X): 3.462976693
Dependent Variable (Y): 1.025124351
********************
Linear model all data:
 Number of points: 19 Number of pairs: 171
 Number of ties in X: 0
 Minimum X: 3.298985
 Maximum X: 5.913467
 Minimum Y: -2.161158
 Maximum Y: 1.353466
 Median of X's: 4.299259
 Median of Y's: -0.1626274
 Median of Slopes: -0.9861524
  Upper 95th percent confidence interval of slope: -0.6606023
  Lower 95th percent confidence interval of slope: -1.492431
 Linear intercept: 4.077097
 Kendall-Theil Line for all linear data: Y = 4.077097 + -0.9861524 * X
Information on independent random errors (deviations from line):
 Median Deviation (error):   0.2926869
 Median Absolute Deviation (error) (MAD): 0.4066746
 Root Mean Square Error (RMSE): 0.5319638
 NonParametric PRediction Error Sum of Squares (NPPRESS): 6.102798
 Bias Correction Factor (BCF): 0.1798356
```

```
Note: This is a Duan (1983) smearing estimator.
********************
```

Bibliography

Aberle, J. (2007). Measurements of armour layer roughness geometry function and porosity. *Acta Geophysica 55*, 23–32.

Aberle, J. and V. Nikora (2006). Statistical properties of armored gravel bed surfaces. *Water Resources Research 42*.

Aberle, J., V. Nikora, M. Henning, B. Ettmer, and B. Hentschel (2010). Statistical characterization of bed roughness due to bed forms: A field study in the Elbe River at Aken, Germany. *Water resources research 46*.

Abernethy, B. and I. D. Rutherfurd (2001). The distribution and strength of riparian tree roots in relation to riverbank reinforcement. *Hydrological processes 15*, 63–79.

Abt, S. R., W. P. Clary, and C. I. Thornton (1992). Ability of streambed vegetation to entrap fine sediments. *Interdisciplinary Approaches in Hydrology and Hydrogeology. American Institute of Hydrology*, 249–259.

Abt, S. R., W. P. Clary, and C. I. Thornton (1994). Sediment deposition and entrapment in vegetated streambeds. *Journal of Irrigation and Drainage Engineering 120*, 1098–1111.

Ackerman, J. D. and A. Okubo (1993). Reduced mixing in a marine macrophyte canopy. *Functional Ecology*, 305–309.

Allmaras, R. R., E. A. Hallauer, W. W. Nelson, and S. D. Evans (1977). Surface energy balance and soil thermal property modifications by tillage-induced soil structure.

Anderson, K., H. Croft, E. J. Milton, and N. J. Kuhn (2012). A simple spectro-goniometer for collection of multiple view angle reflectance factors. *Remote Sensing Letters 3*, 131–140.

Anderson, M. C. (1964). Studies of the woodland light climate: I. The photographic computation of light conditions. *The Journal of Ecology*, 27–41.

Andrews, E. D. (1984). Bed-material entrainment and hydraulic geometry of gravel-bed rivers in Colorado. *Geological Society of America Bulletin 95*, 371–378.

Antonarakis, A. S., K. S. Richards, J. Brasington, and M. Bithell (2009). Leafless roughness of complex tree morphology using terrestrial lidar. *Water Resources Research 45*.

Antonarakis, A. S., K. S. Richards, J. Brasington, and E. Muller (2010). Determining leaf area index and leafy tree roughness using terrestrial laser scanning. *Water Resources Research 46*.

Arcement, G. J. and V. R. Schneider (1989). *Guide for selecting Manning's roughness coefficients for natural channels and flood plains*. US Government Printing Office Washington, DC, USA.

Bagnold, R. A. (1938). The measurement of sand storms. *Proceedings of the Royal Society of London. Series A, Mathematical and Physical Sciences*, 282–291.

Banke, E. G. and S. D. Smith (1973). Wind stress on Arctic sea ice. *Journal of Geophysical Research 78*, 7871–7883.

Bates, P. D., M. S. Horritt, C. N. Smith, and D. Mason (1997). Integrating remote sensing observations of flood hydrology and hydraulic modelling. *Hydrological Processes 11*, 1777–1795.

Bathurst, J. C. (1993). Flow resistance through the channel network. *Channel network hydrology*, 69–98.

Beasom, S. L., E. P. Wiggers, and J. R. Giardino (1983). A technique for assessing land surface ruggedness. *The Journal of Wildlife Management*, 1163–1166.

Béland, M., J.-L. Widlowski, and R. A. Fournier (2014). A model for deriving voxel-level tree leaf area density estimates from ground-based LiDAR. *Environmental Modelling & Software 51*, 184–189.

Bennett, S. J., W. Wu, C. V. Alonso, and S. S. Y. Wang (2008). Modeling fluvial response to in - stream woody vegetation: implications for stream corridor restoration. *Earth Surface Processes and Landforms 33*, 890–909.

Beraldin, J. A., F. Blais, and U. Lohr (2010). Laser Scanning Technology. In G. Vosselman and H. G. Maas (Eds.), *Airborne and terrestrial laser scanning*, pp. 1–39. Whittles.

Bergeron, N. E. (1996). Scale-space analysis of stream-bed roughness in coarse gravel-bed streams. *Mathematical geology 28*, 537–561.

Biggs, B. J. F., D. G. Goring, and V. I. Nikora (1998). Subsidy and stress responses of stream periphyton to gradients in water velocity as a function of community growth form. *Journal of Phycology 34*, 598–607.

Boothroyd, R. J., R. J. Hardy, J. Warburton, and T. I. Marjoribanks (2015). The importance of accurately representing submerged vegetation morphology in the numerical prediction of complex river flow. *Earth Surface Processes and Landforms*.

Boothroyd, R. J., R. J. Hardy, J. Warburton, and T. I. Marjoribanks (2017). Modeling complex flow structures and drag around a submerged plant of varied posture. *Water Resources Research*.

Borges, A. R. and D. X. Viegas (1988). Shelter effect on a row of coal piles to prevent wind erosion. *Journal of Wind Engineering and Industrial Aerodynamics 29*, 145–154.

Brasington, J., D. Vericat, and I. Rychkov (2012). Modeling river bed morphology, roughness, and surface sedimentology using high resolution terrestrial laser scanning. *Water Resources Research 48*.

Brayshaw, A. C. (1985). Bed microtopography and entrainment thresholds in gravel-bed rivers. *Geological Society of America Bulletin 96*, 218–223.

Briggs, K. B. (1989). Microtopographical roughness of shallow-water continental shelves. *Oceanic Engineering, IEEE Journal of 14*, 360–367.

Brown, H. E. and R. M. Forest (1962). The canopy camera.

Brown, S., W. G. Nickling, and J. A. Gillies (2008). A wind tunnel examination of shear stress partitioning for an assortment of surface roughness distributions. *Journal of Geophysical Research: Earth Surface (2003 - 2012) 113*.

Buffin-Bélanger, T. and A. G. Roy (2005). 1 min in the life of a river: selecting the optimal record length for the measurement of turbulence in fluvial boundary layers. *Geomorphology 68*, 77–94.

Burwell, R. E. and W. E. Larson (1969). Infiltration as influenced by tillage-induced random roughness and pore space. *Soil Science Society of America Journal 33*, 449–452.

Bywater-Reyes, S., A. C. Wilcox, and R. M. Diehl (2017). Multiscale influence of woody riparian vegetation on fluvial topography quantified with ground-based and airborne lidar. *Journal of Geophysical Research: Earth Surface 122*(6), 1218–1235. 2016JF004058.

Candela, T., F. Renard, M. Bouchon, A. Brouste, D. Marsan, J. Schmittbuhl, and C. Voisin (2009). Characterization of fault roughness at various scales: Implications of three-dimensional high resolution topography measurements. *Pure and Applied Geophysics 166*, 1817–1851.

Cataño-Lopera, Y. A. and M. H. García (2006). Geometry and migration characteristics of bedforms under waves and currents: Part 2: Ripples superimposed on sandwaves. *Coastal Engineering 53*, 781–792.

Chan, S. S., R. W. McCreight, J. D. Walstad, and T. A. Spies (1986). Notes: Evaluating Forest Vegetative Cover with Computerized Analysis of Fisheye Photographs. *Forest Science 32*, 1085–1091.

Chapman, J. A., B. N. Wilson, and J. S. Gulliver (2015). Drag force parameters of rigid and flexible vegetal elements. *Water Resources Research*.

Chatzinikos, A., T. A. Gemtos, and S. Fountas (2013). The use of a laser scanner for measuring crop properties in three different crops in Central Greece. In *Precision agriculture'13*, pp. 129–136. Springer.

Chau, K. W. (2000). Transverse mixing coefficient measurements in an open rectangular channel. *Advances in Environmental Research 4*, 287–294.

Chen, J. M., T. A. Black, and R. S. Adams (1991). Evaluation of hemispherical photography for determining plant area index and geometry of a forest stand. *Agricultural and forest meteorology 56*, 129–143.

Chow, V. T. (1959). Open-channel hydraulics.

Clifford, N. J., A. Robert, and K. S. Richards (1992). Estimation of flow resistance in gravel-bedded rivers: A physical explanation of the multiplier of roughness length. *Earth Surface Processes and Landforms 17*, 111–126.

Cloudcompare.org (2015). CloudCompare - Open Source project.

Cooper, G. G., F. M. CallaGhan, V. I. Nikora, N. Lamouroux, B. Statzner, and P. Sagnes (2007). Effects of flume characteristics on the assessment of drag on flexible macrophytes and a rigid cylinder.

Courtwright, J. and S. E. G. Findlay (2011). Effects of microtopography on hydrology, physicochemistry, and vegetation in a tidal swamp of the Hudson River. *Wetlands 31*, 239–249.

Cowan, W. L. (1956). Estimating hydraulic roughness coefficients. *Agricultural Engineering 37*, 473–475.

Creëlle, S., R. Roldan, A. Herremans, D. Meire, K. Buis, P. Meire, T. Van Oyen, T. De Mulder, and P. Troch (2016). Validation of large-scale particle image velocimetry to acquire free-surface flow fields in vegetated rivers. *Journal of Applied Water Engineering and Research*, 1–12.

Daimon, M. and A. Masumura (2007). Measurement of the refractive index of distilled water from the near-infrared region to the ultraviolet region. *Applied optics 46*, 3811–3820.

Danson, F. M., R. Gaulton, R. P. Armitage, M. Disney, O. Gunawan, P. Lewis, G. Pearson, and A. F. Ramirez (2014). Developing a dual-wavelength full-waveform

terrestrial laser scanner to characterize forest canopy structure. *Agricultural and Forest Meteorology 198*, 7–14.

Danson, F. M., D. Hetherington, F. Morsdorf, B. Koetz, and B. Allgöwer (2007). Forest canopy gap fraction from terrestrial laser scanning. *Geoscience and Remote Sensing Letters, IEEE 4*, 157–160.

Darby, S. E. (1999). Effect of riparian vegetation on flow resistance and flood potential. *Journal of Hydraulic Engineering-Asce 125*, 443–454.

Darby, S. E., J. Leyland, M. Kummu, T. A. Räsänen, and H. Lauri (2013). Decoding the drivers of bank erosion on the Mekong river: The roles of the Asian monsoon, tropical storms, and snowmelt. *Water Resources Research*.

Darby, S. E., H. Q. Trieu, P. A. Carling, J. Sarkkula, J. Koponen, M. Kummu, I. Conlan, and J. Leyland (2010). A physically based model to predict hydraulic erosion of fine-grained riverbanks: The role of form roughness in limiting erosion. *Journal of Geophysical Research-Earth Surface 115*, 1–20.

Deligianni, D. D., N. D. Katsala, P. G. Koutsoukos, and Y. F. Missirlis (2001). Effect of surface roughness of hydroxyapatite on human bone marrow cell adhesion, proliferation, differentiation and detachment strength. *Biomaterials 22*, 87–96.

Digicamdb.com (2017). Canon EOS 350D Sensor Info & Specs.

Dingman, L. (2009). *Fluvial Hydraulics*. Oxford University Press, USA.

Douglas, J. F., J. M. Gasoriek, J. Swaffield, and L. Jack (2005). *Fluid Mechanics*. Prentice Hall.

Dunne, T., K. X. Whipple, and B. F. Aubry (2013). Microtopography of Hillslopes and Initiation of Channels by Horton Overland Flow. In *Natural and Anthropogenic Influences in Fluvial Geomorphology*, pp. 27–44. American Geophysical Union.

Eitel, J. U. H., T. S. Magney, L. A. Vierling, T. T. Brown, and D. R. Huggins (2014). LiDAR based biomass and crop nitrogen estimates for rapid, non-destructive assessment of wheat nitrogen status. *Field Crops Research 159*, 21–32.

El-Hakim, O. and M. M. Salama (1992). Velocity distribution inside and above branched flexible roughness. *Journal of irrigation and drainage engineering 118*, 914–927.

Engman, E. T. (1986). Roughness coefficients for routing surface runoff. *Journal of Irrigation and Drainage Engineering 112*, 39–53.

Fathi-Maghadam, M., M. Kashefipour, N. Ebrahimi, and S. Emamgholizadeh (2011). Physical and Numerical Modeling of Submerged Vegetation Roughness in Rivers and Flood Plains. *Journal of Hydrologic Engineering 16*, 858–864.

Fathi-Maghadam, M. and N. Kouwen (1997). Nonrigid, nonsubmerged, vegetative roughness on floodplains. *Journal of Hydraulic Engineering 123*, 51–57.

Ferguson, R. (2010). Time to abandon the Manning equation? *Earth Surface Processes and Landforms 35*, 1873–1876.

Fiji.sc (2015). Fiji Is Just ImageJ.

Folkard, A. M. (2005). Hydrodynamics of model Posidonia oceanica patches in shallow water. *Limnology and Oceanography 50*, 1592.

Foufoula-Georgiou, E. and P. Kumar (1994). *Wavelets in geophysics*, Volume 4. Academic Press.

Fraccascia, S., C. Winter, V. B. Ernstsen, and D. Hebbeln (2011). Bedform evolution in a tidal inlet inferred from wavelet analysis. *Journal of Coastal Research*, 751–755.

Frankel, K. L. and J. F. Dolan (2007). Characterizing arid region alluvial fan surface roughness with airborne laser swath mapping digital topographic data. *Journal of Geophysical Research: Earth Surface (2003 - 2012) 112*.

Freeman, G. E., W. H. Rahmeyer, and R. R. Copeland (2000). Determination of resistance due to shrubs and woody vegetation. Technical report.

Frei, S., G. Lischeid, and J. H. Fleckenstein (2010). Effects of micro-topography on surface-subsurface exchange and runoff generation in a virtual riparian wetland – A modeling study. *Advances in Water Resources 33*, 1388–1401.

Frostick, L. E., R. E. Thomas, M. F. Johnson, S. P. Rice, and S. J. McLelland (2014). *Users Guide to Ecohydraulic Modelling and Experimentation: Experience of the Ecohydraulic Research Team (PISCES) of the HYDRALAB Network*. CRC Press.

Gadelmawla, E. S., M. M. Koura, T. M. A. Maksoud, I. M. Elewa, and H. H. Soliman (2002). Roughness parameters. *Journal of Materials Processing Technology 123*, 133–145.

Ghisalberti, M. (2009). Obstructed shear flows: similarities across systems and scales. *Journal of Fluid Mechanics 641*, 51–61.

Ghisalberti, M. and H. Nepf (2006). The structure of the shear layer in flows over rigid and flexible canopies. *Environmental Fluid Mechanics 6*, 277–301.

Ghisalberti, M. and H. M. Nepf (2002). Mixing layers and coherent structures in vegetated aquatic flows. *Journal of Geophysical Research: Oceans (1978 - 2012) 107*, 3–11.

Ghisalberti, M. and H. M. Nepf (2004). The limited growth of vegetated shear layers. *Water Resources Research 40*.

Gille, S. T., M. M. Yale, and D. T. Sandwell (2000). Global correlation of mesoscale ocean variability with seafloor roughness from satellite altimetry. *Geophysical research letters 27*, 1251–1254.

Gillies, J. A., N. Lancaster, W. G. Nickling, and D. M. Crawley (2000). Field determination of drag forces and shear stress partitioning effects for a desert shrub (Sarcobatus vermiculatus, greasewood). *Journal of Geophysical Research: Atmospheres (1984 - 2012) 105*, 24871–24880.

Gillies, J. A., W. G. Nickling, and J. King (2002). Drag coefficient and plant form response to wind speed in three plant species: Burning Bush (Euonymus alatus), Colorado Blue Spruce (Picea pungens glauca.), and Fountain Grass (Pennisetum setaceum). *Journal of Geophysical Research: Atmospheres (1984 - 2012) 107*, ACL 10–1–ACL 10–15.

Gillies, J. A., J. M. Nield, and W. G. Nickling (2014). Wind speed and sediment transport recovery in the lee of a vegetated and denuded nebkha within a nebkha dune field. *Aeolian Research 12*, 135–141.

GiMey, J. E., E. R. Kottwitz, and G. A. Wieman (1991). Roughness coefficients for selected residue materials. *Journal of irrigation and drainage engineering 117*, 503–514.

Glenn, N. F., D. R. Streutker, D. J. Chadwick, G. D. Thackray, and S. J. Dorsch (2006). Analysis of LiDAR-derived topographic information for characterizing and differentiating landslide morphology and activity. *Geomorphology 73*, 131–148.

Gomez, B. (1993). Roughness of stable, armored gravel beds. *Water resources research 29*, 3631–3642.

Goring, D. G. and V. I. Nikora (2002). Despiking acoustic Doppler velocimeter data. *Journal of Hydraulic Engineering 128*, 117–126.

Grant, P. F. and W. G. Nickling (1998). Direct field measurement of wind drag on vegetation for application to windbreak design and modelling. *Land Degradation & Development 9*, 57–66.

Gray, D. H. and A. T. Leiser (1982). *Biotechnical slope protection and erosion control*. Van Nostrand Reinhold Company Inc.

Greeley, R. and J. D. Iversen (1985). Wind as a Geological Process, 333 pp. *Cambridge Univ. Process, New York*.

Green, J. C. (2005). Comparison of blockage factors in modelling the resistance of channels containing submerged macrophytes. *River research and applications 21*, 671–686.

Griffin, E. R., J. W. Kean, K. R. Vincent, J. D. Smith, and J. M. Friedman (2005). Modeling effects of bank friction and woody bank vegetation on channel flow and boundary shear stress in the Rio Puerco, New Mexico. *Journal of Geophysical Research-Earth Surface 110*.

Griffin, E. R. and J. D. Smith (2004). *Floodplain stabilization by woody riparian vegetation during an extreme flood*, Volume 8. US Geol Survey, Boulder, CO 80303 USA. Griffin, ER (reprint author), US Geol Survey, 3215 Marine St,Suite E-127, Boulder, CO 80303 USA.: Amer Geophysical Union.

Grohmann, C. H., M. J. Smith, and C. Riccomini (2011). Multiscale Analysis of Topographic Surface Roughness in the Midland Valley, Scotland. *Geoscience and Remote Sensing, IEEE Transactions on 49*, 1200–1213.

Hackney, C., J. Best, J. Leyland, S. E. Darby, D. Parsons, R. Aalto, and A. Nicholas (2015). Modulation of outer bank erosion by slump blocks: Disentangling the protective and destructive role of failed material on the three-dimensional flow structure. *Geophysical Research Letters 42*(24).

Hallab, N. J., K. J. Bundy, K. O'Connor, R. L. Moses, and J. J. Jacobs (2001). Evaluation of metallic and polymeric biomaterial surface energy and surface roughness characteristics for directed cell adhesion. *Tissue Engineering 7*, 55–71.

Haubrock, S.-N., M. Kuhnert, S. Chabrillat, A. Güntner, and H. Kaufmann (2009). Spatiotemporal variations of soil surface roughness from in-situ laser scanning. *CATENA 79*, 128–139.

Heritage, G. and D. Hetherington (2005). The use of highresolution field laser scanning for mapping surface topography in fluvial systems. *Int. Assoc. Hydrol. Sci 291*, 269–277.

Hey, R. D. (1979). Flow resistance in gravel bed rivers. *J. HYDRAUL. DIV. : PROC. ASCE 105 , no.H*, 365–379.

Hey, R. D. and C. R. Thorne (1986). STABLE CHANNELS WITH MOBILE GRAVEL BEDS. *Journal of Hydraulic Engineering-Asce 112*, 671–689.

Hodge, R., J. Brasington, and K. Richards (2009a). Analysing laser-scanned digital terrain models of gravel bed surfaces: linking morphology to sediment transport processes and hydraulics. *Sedimentology 56*, 2024–2043.

Hodge, R., J. Brasington, and K. Richards (2009b). In situ characterization of grain - scale fluvial morphology using Terrestrial Laser Scanning. *Earth Surface Processes and Landforms 34*, 954–968.

Hodge, R. A. (2010). Using simulated Terrestrial Laser Scanning to analyse errors in high-resolution scan data of irregular surfaces. *ISPRS Journal of Photogrammetry and Remote Sensing 65*, 227–240.

Hoffmann, M. R. (2004). Application of a simple space-time averaged porous media model to flow in densely vegetated channels. *Journal of Porous Media 7*.

Hoover, M. D. (1944). Effect of removal forest vegetation upon water-yields. *Eos, Transactions American Geophysical Union 25*, 969–977.

Hopkinson, C., L. Chasmer, C. Young-Pow, and P. Treitz (2004). Assessing forest metrics with a ground-based scanning lidar. *Canadian Journal of Forest Research 34*, 573–583.

Hosoi, F. and K. Omasa (2006). Voxel-based 3-D modeling of individual trees for estimating leaf area density using high-resolution portable scanning lidar. *Geoscience and Remote Sensing, IEEE Transactions on 44*, 3610–3618.

Huai, W. X., C. G. Li, Y. H. Zeng, Z. D. Qian, and Z. H. Yang (2012). CURVED OPEN CHANNEL FLOW ON VEGETATION ROUGHENED INNER BANK. *Journal of Hydrodynamics 24*, 124–129.

Hubbard, B., M. J. Siegert, and D. McCarroll (2000). Spectral roughness of glaciated bedrock geomorphic surfaces: implications for glacier sliding. *Journal of Geophysical Research: Solid Earth (1978 - 2012) 105*, 21295–21303.

Huntington, S. W. and E. Whitehead (1992). The hydraulic roughness of vegetated channels.

Hwang, P. A. (2008). Observations of swell influence on ocean surface roughness. *Journal of Geophysical Research: Oceans (1978 - 2012) 113*.

Ikeda, S., T. Yamada, and Y. Toda (2001). Numerical study on turbulent flow and honami in and above flexible plant canopy. *International Journal of Heat and Fluid Flow 22*, 252–258.

Inoue, E. (1955). Studies of the Phenomena of Waving Plants ("HONAMI") Caused by Wind. Part 2: Spectra of Waving Plants and Plants Vibration. *Journal of Agricultural Meteorology (Tokyo) 11*, 87–90.

ITC. (2011). *The Core of GIScience: A Process-based Approach*. ITC, Faculty of geo-information Science and Earth Observation.

Jalonen, J., J. Järvelä, J.-P. Virtanen, M. Vaaja, M. Kurkela, and H. Hyyppä (2015). Determining Characteristic Vegetation Areas by Terrestrial Laser Scanning for Floodplain Flow Modeling. *Water 7*, 420–437.

James, M. R. and S. Robson (2014). Mitigating systematic error in topographic models derived from UAV and ground - based image networks. *Earth Surface Processes and Landforms 39*, 1413–1420.

Järvelä, J. (2002a). Determination of flow resistance of vegetated channel banks and floodplains. In *River flow*, Volume 2002, pp. 311–318.

Järvelä, J. (2002b). Flow resistance of flexible and stiff vegetation: a flume study with natural plants. *Journal of Hydrology 269*, 44–54.

Järvelä, J. (2004). Determination of flow resistance caused by non - submerged woody vegetation. *International journal of river basin management 2*, 61–70.

Jenness, J. S. (2004). Calculating landscape surface area from digital elevation models. *Wildlife Society Bulletin 32*, 829–839.

Jones, A. J. and G. S. Campbell (1979). Machine analysis of fisheye photographs for assessment of radiation penetration in plant canopies. In *A paper presented before the West. Soc. Soil Sci.*

Kalbermatten, M., D. Van De Ville, P. Turberg, D. Tuia, and S. Joost (2012). Multiscale analysis of geomorphological and geological features in high resolution digital elevation models using the wavelet transform. *Geomorphology 138*, 352–363.

Kamb, B. (1970). Sliding motion of glaciers: Theory and observation. *Reviews of Geophysics 8*, 673–728.

Kamphorst, E. C., V. Jetten, J. Guérif, J. Pitk a ÂÍ nen, B. V. Iversen, J. T. Douglas, and A. Paz (2000). Predicting Depressional Storage from Soil Surface Roughness. *Soil Science Society of America Journal 64*, 1749–1758.

Katul, G., P. Wiberg, J. Albertson, and G. Hornberger (2002). A mixing layer theory for flow resistance in shallow streams. *Water Resources Research 38*, 32–38.

Kean, J. W. and J. D. Smith (2006a). Form drag in rivers due to small-scale natural topographic features: 2. Irregular sequences. *Journal of Geophysical Research-Earth Surface 111*.

Kean, J. W. and J. D. Smith (2006b). Form drag in rivers due to small-scale natural topographic features: 2. Irregular sequences. *Journal of Geophysical Research-Earth Surface 111*(F4).

Knighton, D. (1998). *Fluvial Forms and Processes: A New Perspective*. Taylor & Francis.

Kouwen, N. and M. Fathi-Maghadam (2000). Friction factors for coniferous trees along rivers. *Journal of hydraulic engineering 126*, 732–740.

Kouwen, N., T. E. Unny, and H. M. Hill (1969). Flow retardance in vegetated channels.

Kreslavsky, M. A., J. W. Head, G. A. Neumann, M. A. Rosenburg, O. Aharonson, D. E. Smith, and M. T. Zuber (2013, oct). Lunar topographic roughness maps from Lunar Orbiter Laser Altimeter (LOLA) data: Scale dependence and correlation with geologic features and units. *Icarus 226*, 52–66.

Kuipers, H. (1957). A relief meter for soil cultivation studies. *Neth. J. Agric. Sci 5*, 255–262.

Lakso, A. N. (1980). Correlations of fisheye photography to canopy structure, light climate, and biological responses to light in apple trees. *Journal of the American Society for Horticultural Science 105*, 43–46.

Lampkin, D. J. and J. VanderBerg (2011). A preliminary investigation of the influence of basal and surface topography on supraglacial lake distribution near Jakobshavn Isbrae, western Greenland. *Hydrological Processes 25*, 3347–3355.

Lancaster, N. and A. Baas (1998). Influence of vegetation cover on sand transport by wind: field studies at Owens Lake, California. *Earth Surface Processes and Landforms 23*, 69–82.

Landy, J. C., D. Isleifson, A. S. Komarov, and D. G. Barber (2015). Parameterization of Centimeter-Scale Sea Ice Surface Roughness Using Terrestrial LiDAR. *Ieee Transactions on Geoscience and Remote Sensing 53*, 1271–1286.

Lane, S. N. (1998). Hydraulic modelling in hydrology and geomorphology: a review of high resolution approaches. *Hydrological Processes 12*, 1131–1150.

Lane, S. N. (2005). Roughness - time for a re - evaluation? *Earth Surface Processes and Landforms 30*, 251–253.

Lane, S. N., P. M. Biron, K. F. Bradbrook, J. B. Butler, J. H. Chandler, M. D. Crowell, S. J. McLelland, K. S. Richards, and A. G. Roy (1998). Three - dimensional measurement of river channel flow processes using acoustic Doppler velocimetry. *Earth Surface Processes and Landforms 23*, 1247–1267.

Lane, S. N., R. J. Hardy, L. Elliott, and D. B. Ingham (2004). Numerical modeling of flow processes over gravelly surfaces using structured grids and a numerical porosity treatment. *Water Resources Research 40*.

Large, A. R. G. and G. L. Heritage (2007). Terrestrial laser scanner based instream habitat quantification using a random field approach. In *Proceedings of the 2007 Annual Conference of the Remote Sensing and Photogrammetry Society (RSPSoc2007), Newcastle Upon Tyne*, pp. 11–14.

Law, S. S. and X. Q. Zhu (2005). Bridge dynamic responses due to road surface roughness and braking of vehicle. *Journal of Sound and Vibration 282*, 805–830.

Le Bouteiller, C. and J. G. Venditti (2015). Sediment transport and shear stress partitioning in a vegetated flow. *Water Resources Research*.

Lee, J. P. and S. J. Lee (2012). PIV analysis on the shelter effect of a bank of real fir trees. *Journal of Wind Engineering and Industrial Aerodynamics 110*, 40–49.

Lee, S.-J. and C.-W. Park (1998). Surface-pressure variations on a triangular prism by porous fences in a simulated atmospheric boundary layer. *Journal of Wind Engineering and Industrial Aerodynamics 73*, 45–58.

Lee, S. Y., C. W. Fong, and R. S. S. Wu (2001). The effects of seagrass (Zostera japonica) canopy structure on associated fauna: a study using artificial seagrass units and sampling of natural beds. *Journal of Experimental Marine Biology and Ecology 259*, 23–50.

Lemmens, M. (2011). *Geo-information: Technologies, Applications and the Environment.* Springer Netherlands.

Lettau, H. (1969). Note on aerodynamic roughness-parameter estimation on the basis of roughness-element description. *Journal of Applied Meteorology 8*, 828–832.

Leyland, J., S. E. Darby, L. Teruggi, M. Rinaldi, and D. Ostuni (2015). A self-limiting bank erosion mechanism? Inferring temporal variations in bank form and skin drag from high resolution topographic data. *Earth Surface Processes and Landforms*, n/a–n/a.

Leyland, J., C. R. Hackney, S. E. Darby, D. R. Parsons, J. L. Best, A. P. Nicholas, R. Aalto, and D. Lague (2017). Extreme flood-driven fluvial bank erosion and sediment loads: direct process measurements using integrated mobile laser scanning (mls) and hydro-acoustic techniques. *Earth Surface Processes and Landforms 42*(2), 334–346.

Lichti, D. D., S. J. Gordon, and T. Tipdecho (2005). Error models and propagation in directly georeferenced terrestrial laser scanner networks. *Journal of surveying engineering*.

Lindsay, R. W., D. B. Percival, and D. Rothrock (1996). The discrete wavelet transform and the scale analysis of the surface properties of sea ice. *Geoscience and Remote Sensing, IEEE Transactions on 34*, 771–787.

Luhar, M., J. Rominger, and H. Nepf (2008). Interaction between flow, transport and vegetation spatial structure. *Environmental Fluid Mechanics 8*, 423–439.

Lyford, W. H. and D. W. MacLean (1966). *Mound and pit microrelief in relation to soil disturbance and tree distribution in New Brunswick, Canada.* Harvard University Massachusetts.

Lyons, A. P., W. L. J. Fox, T. Hasiotis, and E. Pouliquen (2002). Characterization of the two-dimensional roughness of wave-rippled sea floors using digital photogrammetry. *Oceanic Engineering, IEEE Journal of 27*, 515–524.

Malcangio, D. and M. Mossa (2016). A laboratory investigation into the influence of a rigid vegetation on the evolution of a round turbulent jet discharged within a cross flow. *Journal of Environmental Management 173*, 105–120.

Mandelbrot, B. B. (1967). How long is the coast of Britain. *Science 156*(3775), 636–638.

Mandelbrot, B. B. (1983). *The fractal geometry of nature.* Macmillan.

Manners, R., J. Schmidt, and J. M. Wheaton (2013). Multiscalar model for the determination of spatially explicit riparian vegetation roughness. *Journal of Geophysical Research: Earth Surface 118*, 65–83.

Marjoribanks, T. (2013). *High resolution modelling of flexible submerged vegetation in rivers*. Ph. D. thesis.

Marjoribanks, T. I., R. J. Hardy, S. N. Lane, and D. R. Parsons (2014). High-resolution numerical modelling of flow-vegetation interactions. *Journal of Hydraulic Research 52*(6), 775–793.

Martin, L. A. and W. R. C. Myers (1991). Measurement of overbank flow in a compound river channel.

Massey, B. S. (1998). *Mechanics of fluids*, Volume 1. Taylor & Francis.

McCoy, S. W., J. W. Kean, J. A. Coe, D. M. Staley, T. A. Wasklewicz, and G. E. Tucker (2010). Evolution of a natural debris flow: In situ measurements of flow dynamics, video imagery, and terrestrial laser scanning. *Geology 38*, 735–738.

McKean, J. and J. Roering (2004). Objective landslide detection and surface morphology mapping using high-resolution airborne laser altimetry. *Geomorphology 57*, 331–351.

Micheletti, N., J. H. Chandler, and S. N. Lane (2014). Investigating the geomorphological potential of freely available and accessible structure - from - motion photogrammetry using a smartphone. *Earth Surface Processes and Landforms 40*, 473–486.

Micheletti, N., J. H. Chandler, and S. N. Lane (2015). Structure from Motion (SfM) Photogrammetry.

Milan, D. J. (2009). Terrestrial laser scan-derived topographic and roughness data for hydraulic modelling of gravelbed rivers. In G. L. Heritage and A. R. G. Large (Eds.), *Laser Scanning for the Environmental Sciences.*, pp. 133–146. Wiley-Blackwell.

Milan, D. J., G. L. Heritage, and D. Hetherington (2007). Application of a 3D laser scanner in the assessment of erosion and deposition volumes and channel change in a proglacial river. *Earth surface processes and landforms 32*, 1657–1674.

Miwa, M., A. Nakajima, A. Fujishima, K. Hashimoto, and T. Watanabe (2000). Effects of the surface roughness on sliding angles of water droplets on superhydrophobic surfaces. *Langmuir 16*, 5754–5760.

Montes, F., A. Rubio, I. Barbeito, and I. Cañellas (2008). Characterization of the spatial structure of the canopy in Pinus silvestris L. stands in Central Spain from hemispherical photographs. *Forest Ecology and Management 255*, 580–590.

Morgan, R. P. C., J. N. Quinton, R. E. Smith, G. Govers, J. W. A. Poesen, K. Auerswald, G. Chisci, D. Torri, and M. E. Styczen (1998). The European Soil

Erosion Model (EUROSEM): a dynamic approach for predicting sediment transport from fields and small catchments. *Earth Surface Processes and Landforms 23*, 527–544.

Morris, A. R., F. S. Anderson, P. J. Mouginis Mark, A. F. C. Haldemann, B. A. Brooks, and J. Foster (2008). Roughness of Hawaiian volcanic terrains. *Journal of Geophysical Research: Planets (1991 - 2012) 113*.

Morris, H. M. (1955). Flow in rough conduits. *Transactions of the American Society of Civil Engineers 120*, 373–398.

Morvan, H., D. Knight, N. Wright, X. Tang, and A. Crossley (2008, mar). The concept of roughness in fluvial hydraulics and its formulation in 1D, 2D and 3D numerical simulation models. *Journal of Hydraulic Research 46*, 191–208.

Moser, K., C. Ahn, and G. Noe (2007). Characterization of microtopography and its influence on vegetation patterns in created wetlands. *Wetlands 27*, 1081–1097.

Moulin, F. Y., K. Guizien, G. Thouzeau, G. Chapalain, K. Mülleners, and C. Bourg (2007). Impact of an invasive species, Crepidula fornicata, on the hydrodynamics and transport properties of the benthic boundary layer. *Aquatic Living Resources 20*, 15–31.

Munro, D. S. (1989). Surface roughness and bulk heat transfer on a glacier: comparison with eddy correlation. *Journal 0/Glaciology 35*.

Musick, H. B., S. M. Trujillo, and C. R. Truman (1996). Wind-tunnel modelling of the influence of vegetation structure on saltation threshold. *Earth Surface Processes and Landforms 21*, 589–605.

Nepf, H. and M. Ghisalberti (2008). Flow and transport in channels with submerged vegetation. *Acta Geophysica 56*, 753–777.

Nepf, H. M. (1999). Drag, turbulence, and diffusion in flow through emergent vegetation. *Water resources research 35*, 479–489.

Nepf, H. M. (2012). Flow and transport in regions with aquatic vegetation. *Annual Review of Fluid Mechanics 44*, 123–142.

Nepf, H. M. and E. W. K. Koch (1999). Vertical secondary flows in submersed plant - like arrays. *Limnology and Oceanography 44*, 1072–1080.

Nepf, H. M. and E. R. Vivoni (2000). Flow structure in depth - limited, vegetated flow. *Journal of Geophysical Research: Oceans (1978 - 2012) 105*, 28547–28557.

Nield, J. M., R. C. Chiverrell, S. E. Darby, J. Leyland, L. H. Vircavs, and B. Jacobs (2013). Complex spatial feedbacks of tephra redistribution, ice melt and surface roughness modulate ablation on tephra covered glaciers. *Earth Surface Processes and Landforms 38*, 95–102.

Nield, J. M., J. King, and B. Jacobs (2014). Detecting surface moisture in aeolian environments using terrestrial laser scanning. *Aeolian Research 12*, 9–17.

Nield, J. M., J. King, G. F. S. Wiggs, J. Leyland, R. G. Bryant, R. C. Chiverrell, S. E. Darby, F. D. Eckardt, D. S. G. Thomas, L. H. Vircavs, and R. Washington (2013). Estimating aerodynamic roughness over complex surface terrain. *Journal of Geophysical Research: Atmospheres 118*, 2013JD020632.

Nield, J. M. and G. F. S. Wiggs (2011). The application of terrestrial laser scanning to aeolian saltation cloud measurement and its response to changing surface moisture. *Earth Surface Processes and Landforms 36*, 273–278.

Nield, J. M., G. F. S. Wiggs, M. C. Baddock, and M. H. T. Hipondoka (2017). Coupling leeside grainfall to avalanche characteristics in aeolian dune dynamics. *Geology*, G38800–1.

Nield, J. M., G. F. S. Wiggs, and R. S. Squirrell (2011). Aeolian sand strip mobility and protodune development on a drying beach: examining surface moisture and surface roughness patterns measured by terrestrial laser scanning. *Earth Surface Processes and Landforms 36*, 513–522.

Nikuradse, J. (1950). *Laws of flow in rough pipes*. National Advisory Committee for Aeronautics Washington.

Nyander, A., P. S. Addison, I. McEwan, and G. Pender (2003). Analysis of river bed surface roughnesses using 2D wavelet transform-based methods. *Arabian Journal for Science and Engineering 28*, 107–121.

Oliver, M. A. and R. Webster (1986). Semi-variograms for modelling the spatial pattern of landform and soil properties. *Earth Surface Processes and Landforms 11*, 491–504.

Pelletier, J. D., H. Mitasova, R. S. Harmon, and M. Overton (2009). The effects of interdune vegetation changes on eolian dune field evolution: a numerical - modeling case study at Jockey's Ridge, North Carolina, USA. *Earth Surface Processes and Landforms 34*, 1245–1254.

Perera, M. (1981). Shelter behind two-dimensional solid and porous fences. *Journal of Wind Engineering and Industrial Aerodynamics 8*, 93–104.

Perfect, E. and B. D. Kay (1995). Applications of fractals in soil and tillage research: a review. *Soil and Tillage Research 36*, 1–20.

Piñeiro, G., S. Perelman, J. P. Guerschman, and J. M. Paruelo (2008). How to evaluate models: observed vs. predicted or predicted vs. observed? *Ecological Modelling 216*, 316–322.

Plate, E. J. and A. A. Quraishi (1965). Modeling of velocity distributions inside and above tall crops. *Journal of Applied Meteorology 4*, 400–408.

Pommerol, A., S. Chakraborty, and N. Thomas (2012). Comparative study of the surface roughness of the Moon, Mars and Mercury. *Planetary and Space Science 73*, 287–293.

Powell, D. M. (2014). Flow resistance in gravel-bed rivers: Progress in research. *Earth-Science Reviews 136*, 301–338.

Power, W. L., T. E. Tullis, S. R. Brown, G. N. Boitnott, and C. H. Scholz (1987). Roughness of natural fault surfaces. *Geophysical Research Letters 14*, 29–32.

Prandtl, L. (1904). Über Flüssigkeitsbewegung bei sehr kleiner Reibung. *Int. Math. Kongr Heidelberg. Leipzig*.

Pueschel, P. (2013). The influence of scanner parameters on the extraction of tree metrics from FARO Photon 120 terrestrial laser scans. *ISPRS Journal of Photogrammetry and Remote Sensing 78*, 58–68.

Raju, K. G. R., R. J. Garde, S. K. Singh, and N. Singh (1988). Experimental study on characteristics of flow past porous fences. *Journal of Wind Engineering and Industrial Aerodynamics 29*, 155–163.

Raumonen, P., M. Kaasalainen, M. Åkerblom, S. Kaasalainen, H. Kaartinen, M. Vastaranta, M. Holopainen, M. Disney, and P. Lewis (2013). Fast automatic precision tree models from terrestrial laser scanner data. *Remote Sensing 5*, 491–520.

Raupach, M. (1992). Drag and drag partition on rough surfaces. *Boundary-Layer Meteorology 60*, 375–395.

Raupach, M., J. J. Finnigan, and Y. Brunei (1996). Coherent eddies and turbulence in vegetation canopies: the mixing-layer analogy. *Boundary-Layer Meteorology 78*, 351–382.

Raupach, M. R., D. A. Gillette, and J. F. Leys (1993). The effect of roughness elements on wind erosion threshold. *Journal of Geophysical Research: Atmospheres 98*, 3023–3029.

Raupach, M. R. and R. H. Shaw (1982). Averaging procedures for flow within vegetation canopies. *Boundary-Layer Meteorology 22*, 79–90.

Reynolds, O. (1883). An experimental investigation of the circumstances which determine whether the motion of water shall be direct or sinuous, and of the law of resistance in parallel channels. *Proceedings of the Royal Society of London 35*, 84–99.

Rhee, D. S., H. Woo, B. Kwon, and H. K. Ahn (2008). Hydraulic resistance of some selected vegetation in open channel flows. *River research and applications 24*, 673–687.

Richards, K. S. (1982). *Rivers, Form and Process in Alluvial Channels*. Methuen.

Richardson, K. and P. A. Carling (2006). The hydraulics of a straight bedrock channel: Insights from solute dispersion studies. *Geomorphology 82*(1), 98–125.

Richardson, S. (1973). On the no-slip boundary condition. *J. Fluid Mech 59*, 707–719.

Riley, S. J., S. D. DeGloria, and R. Elliot (1999). A terrain ruggedness index that quantifies topographic heterogeneity. *intermountain Journal of sciences 5*, 23–27.

Robert, A. (1988). Statistical properties of sediment bed profiles in alluvial channels. *Mathematical Geology 20*, 205–225.

Roberts, P. J. W. and D. R. Webster (2002). *Turbulent diffusion.* ASCE Press, Reston, Virginia.

Rosenburg, M. A., O. Aharonson, J. W. Head, M. A. Kreslavsky, E. Mazarico, G. A. Neumann, D. E. Smith, M. H. Torrence, and M. T. Zuber (2011). Global surface slopes and roughness of the Moon from the Lunar Orbiter Laser Altimeter. *Journal of Geophysical Research: Planets (1991 - 2012) 116.*

Rosser, N. J., D. N. Petley, M. Lim, S. A. Dunning, and R. J. Allison (2005). Terrestrial laser scanning for monitoring the process of hard rock coastal cliff erosion. *Quarterly Journal of Engineering Geology and Hydrogeology 38*, 363–375.

Rusu, R. B., Z. C. Marton, N. Blodow, M. Dolha, and M. Beetz (2008). Towards 3D point cloud based object maps for household environments. *Robotics and Autonomous Systems 56*, 927–941.

Sankey, J. B., N. F. Glenn, M. J. Germino, A. I. N. Gironella, and G. D. Thackray (2010). Relationships of aeolian erosion and deposition with LiDAR-derived landscape surface roughness following wildfire. *Geomorphology 119*, 135–145.

Sargent, R. J. (1979). Variation of Manning's n roughness coefficient with flow in open river channels. *Journal of the Institution of Water Engineers and Scientists 33.*

Sen, P. K. (1968). Estimates of the regression coefficient based on Kendall's tau. *Journal of the American Statistical Association 63*, 1379–1389.

Senix (2015). ToughSonic Ultrasonic Distance Sensors, Installation and Operating Instructions.

Shepard, M. K., B. A. Campbell, M. H. Bulmer, T. G. Farr, L. R. Gaddis, and J. J. Plaut (2001). The roughness of natural terrain: A planetary and remote sensing perspective. *Journal of Geophysical Research: Planets 106*, 32777–32795.

Shlyakhter, I., M. Rozenoer, J. Dorsey, and S. Teller (2001). Reconstructing 3d tree models from instrumented photographs. *IEEE Computer Graphics and Applications*, 53–61.

Shucksmith, J. D., J. B. Boxall, and I. Guymer (2011). Determining longitudinal dispersion coefficients for submerged vegetated flow. *Water Resources Research 47.*

Siegert, M. J., J. Taylor, A. J. Payne, and B. Hubbard (2004). Macro-scale bed roughness of the siple coast ice streams in West Antarctica. *Earth Surface Processes and Landforms 29*, 1591–1596.

Siwabessy, P. J. W. (2001). An investigation of the relationship between seabed type and benthic and bentho-pelagic biota using acoustic techniques.

Smith, J. D. and S. R. McLean (1977). Spatially averaged flow over a wavy surface. *Journal of Geophysical Research-Oceans and Atmospheres 82*, 1735–1746.

Smith, M., D. Vericat, and C. Gibbins (2012). Through-water terrestrial laser scanning of gravel beds at the patch scale. *Earth Surface Processes and Landforms 37*, 411–421.

Smith, M. W. (2014). Roughness in the earth sciences. *Earth-Science Reviews 136*, 202–225.

Smith, M. W. and D. Vericat (2014). EVALUATING SHALLOW-WATER BATHYMETRY FROM THROUGH-WATER TERRESTRIAL LASER SCANNING UNDER A RANGE OF HYDRAULIC AND PHYSICAL WATER QUALITY CONDITIONS. *River Research and Applications 30*, 905–924.

SonTek (2016). SonTek -16MHz MicroADV.

Stephan, U. and D. Gutknecht (2002). Hydraulic resistance of submerged flexible vegetation. *Journal of Hydrology 269*, 27–43.

Stokes, G. G. (1851). *On the effect of the internal friction of fluids on the motion of pendulums*, Volume 9. Pitt Press.

Stone, R. O. and J. Dugundji (1965). A study of microrelief-its mapping, classification, and quantification by means of a Fourier analysis. *Engineering Geology 1*, 89–187.

Straatsma, M. W., J. J. Warmink, and H. Middelkoop (2008). Two novel methods for field measurements of hydrodynamic density of floodplain vegetation using terrestrial laser scanning and digital parallel photography. *International Journal of Remote Sensing 29*, 1595–1617.

Takken, I. and G. Govers (2000). Hydraulics of interrill overland flow on rough, bare soil surfaces. *Earth Surface Processes and Landforms 25*, 1387–1402.

Tan, P., G. Zeng, J. Wang, S. B. Kang, and L. Quan (2007). Image-based tree modeling. In *ACM Transactions on Graphics (TOG)*, Volume 26, pp. 87. ACM.

Tanino, Y. and H. M. Nepf (2008). Laboratory investigation of mean drag in a random array of rigid, emergent cylinders. *Journal of Hydraulic Engineering 134*, 34–41.

Taylor, J., M. J. Siegert, A. J. Payne, and B. Hubbard (2004). Regional-scale bed roughness beneath ice masses: measurement and analysis. *Computers & Geosciences 30*, 899–908.

Theil, H. (1950). A rank-invariant method of linear and polynomial regression analysis, 3; confidence regions for the parameters of polynomial regression equations. *Stichting Mathematisch Centrum. Statistische Afdeling*, 1–16.

Thorne, C. (1990). Effects of vegetation on river bank erosion and stability.

Thorne, S. D. and D. J. Furbish (1995). Influences of coarse bank roughness on flow within a sharply curved river bend. *Geomorphology 12*, 241–257.

Tilly, N., D. Hoffmeister, Q. Cao, S. Huang, V. Lenz-Wiedemann, Y. Miao, and G. Bareth (2014). Multitemporal crop surface models: Accurate plant height measurement and biomass estimation with terrestrial laser scanning in paddy rice. *Journal of Applied Remote Sensing 8*, 83671.

Tinoco, R. O. and E. A. Cowen (2009). Experimental study of flow through macrophyte canopies. In *Water Engineering for a Sustainable Environment, Proceedings of the 33rd IAHR Congress, Vancouver BC, Canada*, pp. 6160–6166.

Tinoco, R. O. and E. A. Cowen (2013). The direct and indirect measurement of boundary stress and drag on individual and complex arrays of elements. *Experiments in fluids 54*, 1–16.

Torrence, C. and G. P. Compo (1998). A practical guide to wavelet analysis. *Bulletin of the American Meteorological society 79*, 61–78.

Torri, D., J. Poesen, L. Borselli, R. Bryan, and M. Rossi (2012). Spatial variation of bed roughness in eroding rills and gullies. *CATENA 90*, 76–86.

Turcotte, D. L. (1997). *Fractals and chaos in geology and geophysics*. Cambridge university press.

Västilä, K. and J. Järvelä (2014). Modeling the flow resistance of woody vegetation using physically based properties of the foliage and stem. *Water Resources Research*, 229–245.

Vionnet, C. A., P. A. Tassi, and J. P. Martín Vide (2004). Estimates of flow resistance and eddy viscosity coefficients for 2D modelling on vegetated floodplains. *Hydrological Processes 18*, 2907–2926.

Vogel, S. (1984). Drag and flexibility in sessile organisms. *American Zoologist 24*, 37–44.

Vogel, S. (1989). Drag and reconfiguration of broad leaves in high winds. *Journal of Experimental Botany 40*, 941–948.

Von Karman, T. (1930). Mechanische Ähnlichkeit und Turbulenz. Nachr. Ges. Wiss. Göt-tingen, math.-phys. Kl.(1930) 58 - 76. *Proc. 3. Int. Cong. Appl. Mech*, 322–346.

Vosselman, G. V. and H.-G. Maas (2010). *Airborne and terrestrial laser scanning*. Whittles.

Wahl, T. L. (2000). Analyzing ADV data using WinADV. In *Proc., Joint Conf. on Water Resources Engineering and Water Resources Planning and Management*, pp. 1–10. ASCE Reston, Va.

Waldron, L. J. (1977). The shear resistance of root-permeated homogeneous and stratified soil. *Soil Science Society of America Journal 41*, 843–849.

Watt, P. J. and D. N. M. Donoghue (2005). Measuring forest structure with terrestrial laser scanning. *International Journal of Remote Sensing 26*, 1437–1446.

Webb, R. L., E. R. G. Eckert, and Goldstei.Rj (1971). HEAT TRANSFER AND FRICTION IN TUBES WITH REPEATED-RIB ROUGHNESS. *International Journal of Heat and Mass Transfer 14*, 601–&.

Werner, K. J. and J. B. Zedler (2002). How sedge meadow soils, microtopography, and vegetation respond to sedimentation. *Wetlands 22*, 451–466.

Westoby, M. J., J. Brasington, N. F. Glasser, M. J. Hambrey, and J. M. Reynolds (2012). âĂŸStructure-from-Motion' photogrammetry: A low-cost, effective tool for geoscience applications. *Geomorphology 179*, 300–314.

White, F. M. (2011). *Fluid Mechanics*. McGraw-Hill Education.

Whitehouse, D. J. (1982). The parameter rash - is there a cure? *Wear 83*, 75–78.

Wilson, C. and M. S. Horritt (2002). Measuring the flow resistance of submerged grass. *Hydrological Processes 16*, 2589–2598.

Wilson, C., T. Stoesser, P. D. Bates, and A. B. Pinzen (2003). Open channel flow through different forms of submerged flexible vegetation. *Journal of Hydraulic Engineering 129*, 847–853.

Wilson, N. R. and R. H. Shaw (1977). A higher order closure model for canopy flow. *Journal of Applied Meteorology 16*, 1197–1205.

Wolfe, S. A. and W. G. Nickling (1993). The protective role of sparse vegetation in wind erosion. *Progress in physical geography 17*, 50.

Yagci, O. and M. S. Kabdasli (2008). The impact of single natural vegetation elements on flow characteristics. *Hydrol. Processes 22*, 4310–4321.

Yan, X.-F., W.-H. O. Wai, and C.-W. Li (2016). Characteristics of flow structure of free-surface flow in a partly obstructed open channel with vegetation patch. *Environmental Fluid Mechanics*, 1–26.

Yang, S. Q., S. K. Tan, and X. K. Wang (2012). Mechanism of secondary currents in open channel flows. *Journal of Geophysical Research: Earth Surface 117*.

Zhao, C.-h., J.-e. Gao, M.-j. Zhang, F. Wang, and T. Zhang (2016). Sediment deposition and overland flow hydraulics in simulated vegetative filter strips under varying vegetation covers. *Hydrological Processes 30*, 163–175.